

AD-A265 364



2

NAVAL POSTGRADUATE SCHOOL MONTEREY, CALIFORNIA



THESIS

S DTIC
ELECTE
JUN 02 1993 **D**
E

**COMPARISON OF MULTIREOLUTION
TECHNIQUES FOR DIGITAL SIGNAL PROCESSING**

by

Neil A. Hamlett

March 1993

Thesis Co-Advisors:

Ralph Hippenstiel
Monique P. Fargues

Approved for public release; distribution is unlimited

93 0 01 001

93-12353



REPORT DOCUMENTATION PAGE

Form Approved
OMB No. 0704-0188

Public reporting burden for this collection of information is estimated to average 1 hour per response, including the time for reviewing instructions, searching existing data sources, gathering and maintaining the data needed, and completing and reviewing the collection of information. Send comments regarding this burden estimate or any other aspect of this collection of information, including suggestions for reducing this burden, to Washington Headquarters Services, Directorate for Information Operations and Reports, 1215 Jefferson Davis Highway, Suite 1204, Arlington, VA 22202-4302, and to the Office of Management and Budget, Paperwork Reduction Project (0704-0188), Washington, DC 20503.

1. AGENCY USE ONLY (Leave blank)	2. REPORT DATE March 1993	3. REPORT TYPE AND DATES COVERED Master's Thesis	
4. TITLE AND SUBTITLE Comparison of Multiresolution Techniques for Digital Signal Processing		5. FUNDING NUMBERS	
6. AUTHOR(S) HAMLETT, Neil A.			
7. PERFORMING ORGANIZATION NAME(S) AND ADDRESS(ES) Naval Postgraduate School Monterey, CA 93943-5000		8. PERFORMING ORGANIZATION REPORT NUMBER	
9. SPONSORING/MONITORING AGENCY NAME(S) AND ADDRESS(ES)		10. SPONSORING/MONITORING AGENCY REPORT NUMBER	
11. SUPPLEMENTARY NOTES The views expressed in this thesis are those of the author and do not reflect the official policy or position of the Department of Defense or the U.S. Government.			
12a. DISTRIBUTION/AVAILABILITY STATEMENT Approved for public release; distribution is unlimited		12b. DISTRIBUTION CODE	
13. ABSTRACT (Maximum 200 words) A comprehensive study of multiresolution techniques is conducted. Background material in functional analysis and Quadrature Mirror Filter (QMF) banks is presented. The development of Mallat's algorithm for multiresolution decomposition and reconstruction is outlined and demonstrated to be equivalent to QMF banks. The Laplacian pyramid and the a trous algorithm are described and demonstrated. General multiresolution structures are constructed from cascades of QMF and pseudo-QMF banks and are demonstrated for applications in signal decomposition and reconstruction and for signal detection and identification.			
14. SUBJECT TERMS Functional Analysis, Quadrature Mirror Filter (QMF) banks, Multiresolution Analysis, Wavelet Transforms, Spectral Estimation, Detection Theory, Signal Identification		15. NUMBER OF PAGES 237	16. PRICE CODE
17. SECURITY CLASSIFICATION OF REPORT Unclassified	18. SECURITY CLASSIFICATION OF THIS PAGE Unclassified	19. SECURITY CLASSIFICATION OF ABSTRACT Unclassified	20. LIMITATION OF ABSTRACT UL

Approved for public release: distribution is unlimited.

Comparison of Multiresolution Techniques
for Digital Signal Processing

by

Neil A. Hamlett
Lieutenant, United States Navy
B.S.E.E, University of Kansas, 1985

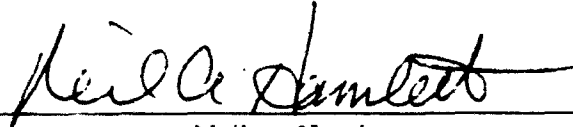
Submitted in partial fulfillment
of the requirements for the degree of

MASTER OF SCIENCE IN ELECTRICAL ENGINEERING

from the

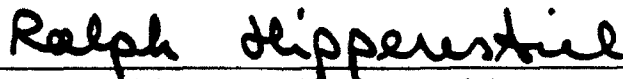
NAVAL POSTGRADUATE SCHOOL
March 1993

Author:

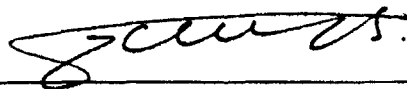


Neil A. Hamlett

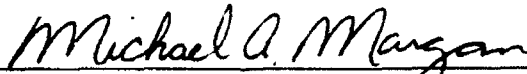
Approved by:



Ralph Hippenstiel, Thesis Co-Advisor



Monique P. Fargues, Thesis Co-Advisor



Michael A. Morgan, Chairman
Department of Electrical and Computer Engineering

ABSTRACT

A comprehensive study of multiresolution signal processing techniques is conducted. Background material in functional analysis and Quadrature Mirror Filter (QMF) banks is presented. The development of Mallat's algorithm for multiresolution decomposition and reconstruction is outlined and demonstrated to be equivalent to QMF banks. The Laplacian pyramid and the à trous algorithm are described and demonstrated. General multiresolution structures are constructed from cascades of QMF and pseudo-QMF banks and are demonstrated for applications in signal decomposition and reconstruction and signal detection and identification.

DTIC QUALITY INSPECTED 3

Accession For	
NTIS CRA&I	<input checked="" type="checkbox"/>
DTIC TAB	<input type="checkbox"/>
Unannounced	<input type="checkbox"/>
Justification	
By	
Distribution /	
Availability Codes	
Dist	Avail and/or Special
A-1	

TABLE OF CONTENTS

I.	INTRODUCTION	1
	A. MOTIVATION FOR STUDY	1
	B. OUTLINE OF STUDY	2
II.	RESULTS FROM FUNCTIONAL ANALYSIS	4
	A. INTRODUCTION	4
	B. NORMS AND NORMED SPACES	4
	C. LINEAR OPERATORS AND TRANSFORMATIONS	8
	D. REPRESENTATION IN INNER PRODUCT SPACES	11
III.	A SURVEY OF MULTIRATE SYSTEM THEORY	16
	A. INTRODUCTION	16
	B. BASIC MULTIRATE SYSTEM OPERATIONS	16
	C. TWO-CHANNEL QUADRATURE MIRROR FILTER BANKS	24
	D. M-CHANNEL FILTER BANKS	39
IV.	THE THEORY OF MULTIREOLUTION SIGNAL PROCESSING	54
	A. INTRODUCTION	54
	B. THEORY OF MULTIREOLUTION ANALYSIS	58
	C. MALLAT'S ALGORITHM FOR MULTIREOLUTION ANALYSIS	71
	D. EARLY MULTIREOLUTION ALGORITHMS	77
	E. MULTIREOLUTION ALGORITHMS FROM CASCADED FILTER BANKS	101
V.	BASIS FUNCTIONS AND FILTERS FOR MULTIREOLUTION DECOMPOSITION	127
	A. INTRODUCTION	127
	B. TWO-SCALE DIFFERENCE EQUATIONS	128
	C. DAUBECHIES' FAMILY OF ORTHONORMAL WAVELETS	136
	D. DESIGN OF FILTERS FOR QMF BANKS	141

VI.	EVALUATION OF MULTIREOLUTION TECHNIQUES FOR DETECTION APPLICATIONS	153
A.	INTRODUCTION	153
B.	COMPUTATIONAL EFFICIENCY OF SIGNAL DECOMPOSITION TECHNIQUES	155
C.	PERFORMANCE OF DECOMPOSITIONS IN THE PRESENCE OF NOISE	164
D.	DECOMPOSITION OF STEADY-STATE HARMONICS AND FM CHIRPS	172
VII.	CONCLUSION	182
A.	SUMMARY OF RESULTS	182
B.	RECOMMENDATIONS FOR FURTHER STUDY	183
APPENDIX A	DETAILS OF DEVELOPMENT OF MALLAT'S ALGORITHM	186
APPENDIX B	<i>MATLAB</i> SOURCE CODE	189
A.	LAPLACIAN PYRAMID	189
B.	À TROUS ALGORITHM	191
C.	MULTIREOLUTION DECOMPOSITIONS FROM CASCADES OF FILTER BANKS	195
D.	SPECTROGRAM DECOMPOSITION	200
E.	DYADIC EXPANSION OF TWO-SCALE DIFFERENCE EQUATIONS	201
F.	GENERATION OF RECEIVER OPERATING CHARACTERISTICS	205
G.	GENERAL-PURPOSE ROUTINES CALLED BY OTHER ROUTINES	209
	REFERENCES	215
	INITIAL DISTRIBUTION LIST	219

LIST OF FIGURES

Figure 3.1:	Block diagram of M-fold decimator.	16
Figure 3.2:	Time plot of 129-point test sequence generated by (3.2).	17
Figure 3.3:	Plot of sequence obtained by decimation of sequence (3.2).	17
Figure 3.4	Plots of power spectral density of test sequence and its decimated version.	19
Figure 3.5	Block diagram of M-fold expander.	20
Figure 3.6	Time plot of expanded, decimated test sequence (3.2).	20
Figure 3.7	Power spectral densities of decimated and decimated, expanded sequence (3.2).	22
Figure 3.8	Superimposed time plots of sequence (3.2) and its decimated, expanded, interpolated version.	23
Figure 3.9	Superimposed plots of power spectral density of test sequence (3.2), its interpolated version and of interpolator filter frequency response.	24
Figure 3.10	Block diagram of two-channel Quadrature Mirror Filter (QMF) bank.	25
Figure 3.11	Time plot of 256-point test sequence.	31
Figure 3.12	Power spectral density of 256-point test sequence.	32
Figure 3.13	Impulse responses of filters used for two-channel QMF bank.	32
Figure 3.14	Superimposed plots of equivalent two-channel QMF impulse response and its deviation from ideal response.	33
Figure 3.15	Superimposed plots of frequency responses of QMF bank filters and deviation from power complementary property.	34
Figure 3.16	Time plot of low-frequency channel decimator output for two-channel QMF bank.	35

Figure 3.17	Time plot of high-frequency channel decimator output for two-channel QMF bank.	35
Figure 3.18	Superimposed plots of power spectral densities of original 256-point test sequence and two-channel QMF decimator outputs.	36
Figure 3.19	Superimposed plots of power spectral densities of original 256-point test sequence and two-channel QMF expander outputs.	37
Figure 3.20	Superimposed plots of power spectral densities of original 256-point test sequence and two-channel QMF synthesis filter outputs.	38
Figure 3.21	Time plot of reconstruction of 256-point test sequence.	38
Figure 3.22	Block diagram of M-channel filter bank.	39
Figure 3.23	Time-plot of 256-point test sequence.	44
Figure 3.24	Plot of power spectral density of 256-point test sequence.	44
Figure 3.25	Superimposed plots of impulse responses of three-channel QMF bank analysis filters.	45
Figure 3.26	Equivalent impulse response of three-channel QMF bank and its deviation from ideal response.	46
Figure 3.27	Superimposed plots of three-channel QMF bank filter frequency responses and deviation from power complementary property.	46
Figure 3.28a	Time plot of low-frequency channel decimator output for three-channel QMF bank.	47
Figure 3.28b	Time plot of medium-frequency channel decimator output for three-channel QMF bank.	48
Figure 3.28c	Time plot of high-frequency channel decimator output for three-channel QMF bank.	48
Figure 3.29	Superimposed plots of power spectral densities of original 256-point test sequence and decimator outputs for each channel of three-channel QMF bank.	49

Figure 3.30	Superimposed plots of power spectral densities of original 256-point test sequence and expander outputs for each channel of three-channel QMF bank.	50
Figure 3.31a	Superimposed plots of power spectral densities of original 256-point test sequence and synthesis filter outputs for each channel of three-channel QMF bank.	52
Figure 3.31b	Superimposed plots of power spectral densities of original 256-point test sequence reconstructed by three-channel QMF bank.	53
Figure 3.32	Time plot of sequence reconstructed by three-channel QMF bank.	53
Figure 4.1	Venn diagram illustration of concept of embedded vector spaces.	57
Figure 4.2	Illustration by frequency spectrum partition of concept of embedded vector spaces.	59
Figure 4.3	Superimposed time plots of Daubechies' orthonormal scaling function on $[0, 11]$ at scales of zero and -1.	63
Figure 4.4	Block diagram of single-stage multiresolution decomposition.	66
Figure 4.5	Illustration by spectral partition of concept of complementary subspaces.	67
Figure 4.6	Block diagram for signal detail extraction by Laplacian pyramid.	78
Figure 4.7a	Block diagram for three-stage decomposition by Laplacian pyramid.	79
Figure 4.7b	Block diagram for reconstruction of sequence decomposed by three-stage Laplacian pyramid.	79
Figure 4.8	Lattice illustrating concept behind generation of kernel used for Laplacian pyramid decomposition and reconstruction.	79
Figure 4.9	Equivalent tree-structure for one-stage decomposition by Laplacian pyramid.	83
Figure 4.10	Partition of frequency spectrum resulting from three-stage decomposition by Laplacian pyramid.	84
Figure 4.11	Block diagram of full expansion by channel of sequence decomposed by Laplacian pyramid.	85

Figure 4.12	Time plot of 256-point, low-frequency transient test sequence.	86
Figure 4.13	Plot of power spectral density of 256-point, low-frequency transient test sequence.	86
Figure 4.14a	Surface plot of full expansion by channel of low-frequency transient decomposed by Laplacian pyramid.	88
Figure 4.14a	Surface plot of full expansion by channel of high-frequency transient decomposed by Laplacian pyramid.	89
Figure 4.15	Plot of mean-square reconstruction error versus number of stages for sequence decomposed by Laplacian pyramid.	90
Figure 4.16	Block diagram of one-stage decomposition by à trous algorithm.	93
Figure 4.17	Spectral partitioning resulting from three-stage decomposition by à trous algorithm using four-voice Morlet analyzing wavelet.	98
Figure 4.18a	Surface plot of decomposition resulting from eight-stage decomposition of 256-point, low-frequency transient by à trous algorithm.	99
Figure 4.18b	Surface plot of decomposition resulting from eight-stage decomposition of 256-point, high-frequency transient by à trous algorithm.	100
Figure 4.19	Block diagram of three-stage, two-channel, zero-subchannel structure for multiresolution decomposition.	102
Figure 4.20	Partition of frequency spectrum resulting from five-stage decomposition by two-channel, zero-subchannel multiresolution decomposition.	103
Figure 4.21	Block diagram for one-stage, two-channel, three-subchannel multiresolution decomposition.	104
Figure 4.22	Partition of frequency spectrum resulting from four-stage decomposition by two-channel, three-subchannel multiresolution decomposition.	105
Figure 4.23	Block diagram for one-stage, three-channel, zero-subchannel multiresolution decomposition.	106
Figure 4.24	Partition of frequency spectrum resulting from four-stage decomposition by three-channel, zero-subchannel multiresolution decomposition.	107

Figure 4.25	Block diagram illustrating equivalence of two-stage, two-channel decomposition-reconstruction structure with one-stage, two-channel decomposition-reconstruction with delay in each channel.	107
Figure 4.26	Block-diagrams indicating development of equivalent delay system resulting from two-channel decomposition-reconstruction QMF bank structure with delay in each channel.	108
Figure 4.27	Block diagrams of structure necessary for full expansion by channel of sequence decomposed by multiresolution structure.	110
Figure 4.28a	Plots of reconstruction error versus number of stages for various multiresolution structures applied to low-frequency 256-point transient.	112
Figure 4.28b	Plots of reconstruction error versus number of stages for various multiresolution structures applied to high-frequency 256-point transient.	113
Figure 4.29a	Surface plot of decomposition of 256-point low-frequency transient decomposed by eight-stage, two-channel, zero-subchannel structure.	115
Figure 4.29b	Surface plot of decomposition of 256-point high-frequency transient decomposed by eight-stage, two-channel, zero-subchannel structure.	117
Figure 4.30a	Surface plot of decomposition of 256-point low-frequency transient decomposed by eight-stage, two-channel, three-subchannel structure.	118
Figure 4.30b	Surface plot of decomposition of 256-point high-frequency transient decomposed by eight-stage, two-channel, three-subchannel structure.	119
Figure 4.31a	Surface plot of decomposition of 256-point low-frequency transient decomposed by eight-stage, two-channel, four-subchannel structure.	120
Figure 4.31b	Surface plot of decomposition of 256-point high-frequency transient decomposed by eight-stage, two-channel, four-subchannel structure.	121
Figure 4.32a	Surface plot of decomposition of 256-point low-frequency transient decomposed by five-stage, three-channel, zero-subchannel structure.	123
Figure 4.32b	Surface plot of decomposition of 256-point high-frequency transient decomposed by five-stage, three-channel, zero-subchannel structure.	125
Figure 5.1a	Time plot of function generated from four-stage dyadic expansion of 20-point lowpass filter with cutoff frequency of $0.375 \cdot f_c$.	134

Figure 5.1b	Time plot of function generated from four-stage dyadic expansion of 20-point lowpass filter with cutoff frequency of $0.5 \cdot f_s$.	135
Figure 5.2a	Superimposed plots of Daubechies' orthonormal scaling function and orthonormal wavelet on $[0, 3]$.	136
Figure 5.2b	Polar plot of zero locations for generating filter for Daubechies' orthonormal scaling function and orthonormal wavelet on $[0, 3]$.	137
Figure 5.3	Two-channel, zero-subchannel multiresolution decomposition of 256-point low-frequency transient.	137
Figure 5.4	Superimposed plots of Daubechies' orthonormal scaling function and orthonormal wavelet on $[0, 1]$.	138
Figure 5.5	Polar plot of zero locations for generating filter for Daubechies' orthonormal scaling function and orthonormal wavelet on $[0, 11]$.	139
Figure 5.6	Equivalent impulse response of two-channel QMF bank constructed from generating filter for Daubechies' orthonormal wavelet and scaling function on $[0, 11]$ and deviation from ideal performance.	139
Figure 5.7	Superimposed plots of frequency responses for generating filters for Daubechies' orthonormal wavelet and scaling function on $[0, 11]$ and deviation from power complementary property.	141
Figure 5.8	Impulse response of 30-point, lowpass filter designed from spectral factorization of Kaiser window for two-channel QMF bank.	145
Figure 5.9	Equivalent impulse response for two-channel QMF bank constructed from 30-point filter designed from spectral factorization of Kaiser window and deviation of structure from ideal response.	146
Figure 5.10	Superimposed plots of frequency responses of 30-point QMF bank analysis filters constructed from spectral factorization of Kaiser window and deviation of bank from power complementary property.	146
Figure 5.11	Superimposed time plots of <i>pseudo</i> -scaling function and <i>pseudo</i> -wavelet generated by four-stage dyadic expansion of 30-point filters constructed by spectral factorization of Kaiser window.	148

Figure 5.12	Impulse responses of lowpass and bandpass filters constructed by spectral factorization of McClellan-Parks filters for four-channel pseudo-QMF bank.	151
Figure 5.13	Equivalent impulse response of four-channel pseudo-QMF bank and its deviation from ideal response.	151
Figure 5.14	Superimposed plots of frequency responses of filters for four-channel pseudo-QMF bank and their deviation from power complementary property.	152
Figure 6.1a	Periodogram decomposition of 256-point, low-frequency transient.	154
Figure 6.1b	Periodogram decomposition of 256-point, high-frequency transient.	155
Figure 6.2a	Receiver operating characteristics for various decompositions of 256-point, low-frequency transient in noise with -3 dB SNR.	168
Figure 6.2b	Receiver operating characteristics for various decompositions of 256-point, high-frequency transient in noise with -3 dB SNR.	169
Figure 6.3a	Receiver operating characteristics for various decompositions of 256-point, low-frequency transient in noise with -6 dB SNR.	170
Figure 6.3b	Receiver operating characteristics for various decompositions of 256-point, high-frequency transient in noise with -6 dB SNR.	171
Figure 6.4a	Time-frequency plot of evolution of first 256-point test sequence constructed from steady-state harmonic and quadratic FM chirp.	174
Figure 6.4b	Time-frequency plot of evolution of second 256-point test sequence constructed from steady-state harmonic and quadratic FM chirp.	174
Figure 6.5a	Periodogram decomposition of first 256-point test sequence constructed from steady-state harmonic and quadratic FM chirp.	175
Figure 6.5b	Periodogram decomposition of second 256-point test sequence constructed from steady-state harmonic and quadratic FM chirp.	176
Figure 6.6a	Two-channel, three-subchannel multiresolution decomposition of first 256-point test sequence constructed from steady-state harmonic and quadratic FM chirp.	177

Figure 6.6b	Two-channel, three-subchannel multiresolution decomposition of first 256-point test sequence constructed from steady-state harmonic and quadratic FM chirp.	178
Figure 6.7a	Two-channel, four-subchannel multiresolution decomposition of first 256-point test sequence constructed from steady-state harmonic and quadratic FM chirp.	179
Figure 6.7b	Two-channel, four-subchannel multiresolution decomposition of first 256-point test sequence constructed from steady-state harmonic and quadratic FM chirp.	180

I. INTRODUCTION

A. MOTIVATION FOR STUDY

In recent years a novel approach to the field of digital signal processing has received significant attention. This new approach, the wavelet transform, has displayed the potential for applications in the fields of speech and image processing, in particular. Techniques based on the wavelet transform have been praised for, among other things, their efficiency of computation.

Unfortunately for the electrical engineer specializing in the field of digital signal processing, the concepts on which the wavelet transform have been based have been somewhat elusive. Pioneers of the field have been specialized in such diverse fields as geophysics, mathematical physics, and a branch of applied mathematics known as functional analysis. Not completely unrelated to the familiar Fourier transform methods, wavelet transforms extend the concept of signal decomposition through basis function expansion to a more general and abstract realm. Such abstract mathematical disciplines as set theory are invoked within the context of embedded vector spaces and their relationships to each other.

Included among the purposes of this present study is an attempt to bridge the gap between the mathematician and engineer. It is intended to provide a rudimentary enough understanding of some of the concepts of functional analysis to facilitate a more in depth understanding. Additionally, a strong tie is demonstrated between wavelet-based methods of decomposition and areas within the field of electrical engineering which may be more familiar

Finally, an additional purpose of the present study is to evaluate wavelet transform methods for detection and identification applications. Wavelet processing methods will be applied to familiar signal processing problems such as the detection of signals in noise and the resolving of disparate frequency components of which a signal is composed.

B. OUTLINE OF STUDY

Chapter II will introduce concepts from functional analysis which commonly appear in the literature on wavelet transforms. Not intended to provide an in depth introduction into the field of functional analysis, the chapter provides a few basic tools to support further study. In Chapter III, the basics of multirate system theory will be explored. In particular, the Quadrature Mirror Filter (QMF) bank for two and more channels will be demonstrated. Chapter IV will introduce the theory of multiresolution analysis. From the definitions introduced, Mallat's algorithm for the discrete wavelet transform will be introduced and shown to be equivalent to the QMF bank. Two earlier multiresolution decompositions--the Laplacian pyramid and the à trous algorithm for the wavelet transform--will then be reviewed prior to extending the concepts of multiresolution analysis to general structures constructed from cascaded QMF banks. In the Chapter V, the basis functions of the wavelet transform and filters for QMF banks will be considered in greater depth. The chapter will include a discussion of two-scale difference equations and some basic filter design methods for QMF banks. Chapter VI will demonstrate for detection and identification applications the application of some multiresolution structures introduced in Chapter VI. Multiresolution structures will be compared with the periodogram

decomposition from the perspective of computational efficiency, robustness with respect to noise, and the ability to resolve proximate spectral components.

II. RESULTS FROM FUNCTIONAL ANALYSIS

A. INTRODUCTION

In essence, wavelet transformation represents a recent development in the field of *functional analysis*. Consequently, a brief study of this branch of mathematics provides an appropriate starting point for a study of Wavelet Transform (WT) analysis.

In mathematical terminology, a *functional* is defined as [1] "a function that has a domain whose elements are functions, sets, or the like and that assumes [scalar] numerical values." Fourier transformation--an operation familiar to electrical engineers working in the field of signal processing--is an example of a functional analysis technique. The Fourier transform integral

$$\hat{f}(\omega) = \mathcal{F}\{f(x)\}(\omega) = \int_{-\infty}^{\infty} f(x) e^{-j\omega x} dx \quad (2.1)$$

is a functional which, through projection on a set of basis functions " $e^{-j\omega x}$," maps a continuous function to a specific value for a given value of " ω ." Similarly, the Discrete Fourier Transform (DFT) is an example of a discrete functional. For a discrete sequence $\mathbf{x}^T = [x[0] \ x[1] \ \dots \ x[M-1]]$, the DFT

$$\mathbf{X} = \mathbf{W}_M \cdot \mathbf{x}, \quad (2.2)$$

where $[\mathbf{W}_M]_{k,m} = W_M^{k \cdot m} = e^{-j2\pi k \cdot m / M}$ maps the vector \mathbf{x} to a discrete set of points $X[k]$.

B. NORMS AND NORMED SPACES [2]

Linear transformations generally involve the mapping of a function (or vector) from one vector space to another. The study of these transformations requires the capacity to quantify

distances within these spaces. Measures for functional spaces possess analogies in geometry--such as length of a vector, distance between the points defined by two vectors, and the scalar product of two vectors. These measures, or *norms*, provide the ability to transform each element u in a vector space V into a real number. For a linear vector space V over the real number field \mathbb{R} , the norm $\|u\|$ for every element $u \in V$ satisfies the following conditions:

$$\|u\| \geq 0, \text{ and } \|u\| = 0 \text{ if and only if } u = 0. \quad (\text{positivity})$$

$$\|\alpha \cdot u\| = |\alpha| \cdot \|u\| \text{ for } \alpha \in \mathbb{R}. \quad (\text{homogeneity}) \quad (2.3)$$

$$\|u + v\| \leq \|u\| + \|v\| \quad (\text{triangular inequality}).$$

Examples of norms which sometimes arise within the context of functional analysis follow. The most common norm is the L^2 -norm. Pythagorean theorem represents a special case of the L^2 -norm. For a function " $x(t)$ " defined in the closed interval $C[0, T]$, the L^2 -norm--denoted by $\|x\|_2$ --is defined as

$$\|x\|_2 = \left[\int_0^T |x(t)|^2 dt \right]^{1/2}. \quad (2.4)$$

Another norm is the *sup-norm* or supremum norm. The supremum of a function or functional is defined as the least upper bound of a function. The concept of supremum is similar to the concept of maximum, however a function does not necessarily ever assume the value of the supremum. For example, consider a function $f(x)=x^2$. If the domain of $f(x)$ includes the closed interval $[0, 1]$, then the extremum (and, incidentally, the supremum) of $f(x)$ occurs for $f(x)=1$. If however, the domain of $f(x)$ is restricted to the open interval $(0, 1)$, then the function $f(x)$ has no extremum. At its limit, $f(x)$ approaches unity, however it can never assume that

value. In this case, however, $f(x)$ does possess a supremum, since $f(x)$ is bounded above by unity.

To applying the concept of supremum to define a sup-norm, consider the vector space $V=C[0, t_0]$, the set of all real-valued, once-differentiable, continuous functions of t in the closed interval $[0, t_0]$. The sup-norm of x , $\|x\|_\infty$ is defined as the supremum of the function " $x(t)$ " on its domain, or

$$\|x\|_\infty = \sup \{ |x(t)|: 0 \leq t \leq t_0 \}. \quad (2.5)$$

The Lebesgue *norm* represents another norm which is related to the L^2 -norm. For a real number $p \in [0, \infty) \cap \mathbb{R}$, the Lebesgue norm for the function $u(t)$ defined on the interval $[0, T]$ is defined as

$$\|u\|_p = \left[\int_0^T |u(t)|^p dt \right]^{1/p} < \infty. \quad (2.6)$$

If a norm can be defined in a given space, then that space can be characterized by that norm. for instance, if the Lebesgue norm is defined for a space of interest, than that space can be classified as a *Lebesgue space*. Furthermore, the space by which a norm is characterized is indicated in the subscript of the norm operator symbol. In some cases, such as for Lebesgue spaces, the subscript indicates the metric of the space. In others, such as sup-norm spaces, subscripts less indicative of the norm operation appear. In general, for some arbitrary, unspecified space U , the norm operator for that space is denoted by

$$\| \cdot \|_U.$$

This notation will be used throughout the remainder of this section to indicate general normed spaces.

Inner product spaces are of significant interest to signal processing. An *inner product space* is defined to be a linear vector space on which an inner product can be defined. The concept of inner product is related to the definition of the norm of a space. For instance, the L^2 -inner product $(u, v)_2$ is evaluated as

$$(u, v)_2 = \int_{\Omega} u(x) \cdot v^*(x) dx \quad (2.7)$$

for two vectors $u, v \in L^2(\Omega)$. Unless otherwise indicated, throughout the remainder of this paper, inner products will be assumed to be L^2 inner products and the corresponding distinguishing operator subscripts will be suppressed. Additionally, inner product operations possess the following properties:

- | | | | |
|----|--|------------------------------------|-------|
| 1. | $(u, v) = (v, u)$ | <i>Symmetry</i> | |
| 2. | $(\alpha u, v) = \alpha(u, v)$ | <i>Homogeneity</i> | |
| 3. | $(u_1 + u_2, v) = (u_1, v) + (u_2, v)$ | <i>Additivity</i> | (2.8) |
| 4. | $(u, u) > 0$, and $(u, u) = 0$ if and only if $u = 0$. | <i>Positive Definite.</i> | |
| 5. | $ (u, v) \leq \sqrt{(u, u)(v, v)} = \ u\ \ v\ $ | <i>Cauchy-Schwartz inequality.</i> | |

Given an inner product space V , the concept of orthogonality is also important for characterizing the space. Two vectors $u, v \in V$ are said to be orthogonal if $(u, v) = 0$. Furthermore, it is possible to partition an inner product space into orthogonally complementary subspaces. For instance, consider the inner product space V_k . If V_{k-1} is a subset of V_k (denoted in mathematical symbology by $V_{k-1} \subset V_k$), then the orthogonal complement W_{k-1} of V_{k-1} is defined as

$$W_{k-1} = V_{k-1}^\perp = \{u \in V_k : (u, v) = 0 \quad \forall v \in V_{k-1}\}. \quad (2.9)$$

Additionally, the union of two orthogonally complementary subspaces V_{k-1} and W_{k-1} to obtain a third is denoted $V_{k-1} \oplus W_{k-1} = V_k$. The concept of an orthogonally complementary subspaces proves critical when defining a multiresolution analysis.

The *Hilbert Space* represents perhaps the most important inner product space for signal processing applications. An abstract Hilbert space is an inner product space which possesses the following characteristics [3]:

1. Linearity--The operations of addition and of multiplication by real or complex numbers are defined for its elements:
2. The metric of an Hilbert space is derived from its inner product. Consequently, for any two elements u and v , there is an associated real or complex number.
3. Completeness--If a sequence of elements $\{u_n\}$ satisfies the condition $\|u_n - u_m\| \rightarrow 0 \quad \forall m, n \rightarrow \infty$, then there exists an element, u , such that $\|u_n - u\| \rightarrow 0 \quad \forall n \rightarrow \infty$.

C. LINEAR OPERATORS AND TRANSFORMATIONS [2]

Many signal processing applications of interest involve linear transformations from one linear vector space U to another linear vector space V . If for some vector u in inner product space U , there is a corresponding vector v in image space V , then the operation T , by which u and v are related, constitutes the corresponding transformation. Mathematically, a mapping by T from space U to space V is denoted by $T: U \rightarrow V$.

With respect to some arbitrary linear transformation $T: U \rightarrow V$, the following properties apply:

1. $T\{\alpha u_1 + \beta u_2\} = \alpha T\{u_1\} + \beta T\{u_2\}$ *Linearity*
2. $\|T\{u_1\} - T\{u_2\}\|_V \leq M \|u_1 - u_2\|_U$ for some arbitrary $M > 0$ *Continuity*
3. $\|T\{u\}\|_V \leq M \|u\|_U$ for some $M > 0$ *Boundedness from Above* (2.10)
4. $\|T\{u\}\|_V \geq C \|u\|_U$ for some $C > 0$ *Boundedness from Below*

Two important consequences for linear operators result from the properties of (2.10). The first states that for some invertible, linear operator $T: U \rightarrow V$ which is bounded from below,

$$\|T^{-1}\{v\}\| \leq \|v\|_V / C. \quad (2.11)$$

Equation (2.11), proven in [2], expresses the *Bounded Inverse Theorem*. In other words, the inverse of a linear operation bounded from below is bounded from above.

The second significant result stems from the linear property. Given $T: U \rightarrow V$, for finite-dimensional vector spaces U and V , constituent vectors u and v , respectively, and bases $\{\phi_1, \phi_2, \dots, \phi_n\}$ for U and $\{\psi_1, \psi_2, \dots, \psi_m\}$ for V , then u and v can be represented as

$$\begin{aligned} u &= \sum_{k=1}^n \alpha_k \phi_k \\ v &= \sum_{k=1}^m \beta_k \psi_k \end{aligned} \quad (2.12)$$

Now, writing down the form of the transformation, $T: U \rightarrow V$, the terms in (2.12) are related by

$$v = \sum_{j=1}^m \beta_j \psi_j = \sum_{k=1}^n \alpha_k T\{\phi_k\} = T\{u\}. \quad (2.13)$$

Since $\phi_k \in U$ and $\psi_j \in V$, the mapping of $\{\phi_k\} \rightarrow \{\psi_j\}$ can be expressed as

$$T\{\phi_k\} = \sum_{j=1}^m t_{j,k} \psi_j. \quad (2.14)$$

In vector-matrix notation, $\{\alpha_k\}$, $\{\beta_j\}$ and $\{t_{j,k}\}$ are related by

$$\begin{bmatrix} \beta_1 \\ \beta_2 \\ \vdots \\ \beta_m \end{bmatrix} = \begin{bmatrix} t_{1,1} & t_{1,2} & \cdots & t_{1,n} \\ t_{2,1} & t_{2,2} & \cdots & t_{2,n} \\ \vdots & \vdots & \ddots & \vdots \\ t_{m,1} & t_{m,2} & \cdots & t_{m,n} \end{bmatrix} \begin{bmatrix} \alpha_1 \\ \alpha_2 \\ \vdots \\ \alpha_n \end{bmatrix}. \quad (2.15)$$

Equation (2.15) represents a linear transformation of the projections onto the bases of U and V.

In signal processing, and other sciences involving representation in terms of linear transformations, mappings which are one-to-one are of significant interest. Given $T: U \rightarrow V$, if for each $u \in U$ there exists a unique $v \in V$, then the transformation T is defined to be *isomorphic*. Furthermore, for $T\{u\} = v$, given an isomorphic operator T, there exists a unique inverse operator T^{-1} such that $u = T^{-1}\{v\}$ [4]. Isomorphic operators are particularly useful because they can be inverted. With respect to signal processing, if a signal is decomposed by an invertible operator, then it can be reconstructed to recover the original signal or process.

Before the final concept can be defined, elaboration on the definition of a functional is necessary. Linear functionals consist of a subset of linear transformations $T: U \rightarrow V$ in which the transform space V represents a scalar field [5]. In the case of functionals, the transform space V represents the *dual* or *conjugate space* of U. The dual space of U is assigned a special notation U^* . The notion of a dual space differs from that of a biorthogonal, or Riesz space which shall be addressed in a later section.

Finally, the concept of adjoint operators occasionally plays a role in functional representation of sequences. Given a bounded, linear operator $T: U \rightarrow V$ for normed, linear spaces U and V , a linear functional ϕ can be defined such that $\phi(v) = \phi(T\{u\}) = l(u)$. The resultant functional l --for u --is linear since ϕ and T are linear. It is possible, therefore, to define an *adjoint operator* T^* , such that $l(u) = l(T^*\{v\}) = \phi(v)$. The functional l , by definition, lies in U^* . Additionally, omitting the argument vectors, the transform T^* can be expressed as $l = T^* \phi$. In the case of Hilbert spaces, an operator and its adjoint are related by inner products. Specifically, for $u, v \in \mathcal{H}$, a Hilbert space,

$$(T\{u\}, v) = (u, T^*\{v\}). \quad (2.16)$$

D. REPRESENTATION IN INNER PRODUCT SPACES

Representation theory consists of the theory of representing sequences or sets in terms of projections upon sets of vectors. The *Riesz Representation Theorem* provides the foundation for representation theory for functionals. If l represents a bounded linear operator in an Hilbert space \mathcal{H} , the Riesz representation theorem [2] states that there exists a unique vector $v_0 \in \mathcal{H}$ such that

$$l(w) = (v_0, w) \quad \forall \quad w \in \mathcal{H}.$$

This vector v_0 is called the *representation* for operator l .

The *Fourier Series Theorem* [2] provides concepts fundamental to representation of a function in a Hilbert space. For a countably infinite, orthonormal vector set $\{u_n\}_{n=0}^{\infty} \in \mathcal{H}$, then a series of the

form $\sum_{n=0}^{\infty} \xi_n u_n$ converges if and only if $\sum_{n=0}^{\infty} |\xi_n|^2 < \infty$. In this case, the series $\sum_{n=0}^{\infty} \xi_n u_n$ converges to the same element x irregardless of the ordering of the terms. Furthermore, the element x , the orthogonal set $\{u_n\}$ and the weighting factors $\{\xi_n\}$ are related by

$$\xi_n = (x, u_n) \quad (2.17a)$$

and

$$x = \sum_{n=0}^{\infty} \xi_n u_n. \quad (2.17b)$$

By linearity, *Parsevals Equality* follows directly from (2.17):

$$(y, x) = \sum_{n=0}^{\infty} (x, u_n) (y, u_n). \quad (2.18)$$

Finally, if $x = y$, another relationship is obvious:

$$\|x\|^2 = (x, x) = \sum_{n=0}^{\infty} |(x, u_n)|^2. \quad (2.19)$$

At this point, consideration of additional concepts is justified. The concept of *closure* arises in representation theory [2]. A subset S of a normed space is said to be *closed* if it contains all its limit points. If S is a closed set, and if a sequence converges, then the limit to which the sequences converges is contained in S . The concept of *denseness* is related to closure. If S is an open set (not closed), the set of all additional points necessary to obtain a closed set including S is denoted by \bar{S} . Consequently, the union of the sets $S \cup \bar{S}$ results in a closed set. A space S is said to be dense if for any vector v in \bar{S} , there is an element in S which is arbitrarily close to v . Practically speaking, within a dense space S , it is, therefore, possible to define a representation with arbitrary precision if enough basis vectors are employed.

Finally, in representation theory, the concept of *completeness* of an orthonormal set represents an important concept. Orthonormality, in the usual sense, refers to a set of vectors

$\{u_n\}_{n=1}^N$ such that $(u_n, u_m) = \delta_{m,n}$ where $\delta_{m,n}$ represents Kronecker's delta function. If an orthonormal basis $\{u_n\}_{n=1}^N \in \mathcal{H}$ is *complete*, then the only vector $v \in \mathcal{H}$ such that $(v, u_n) = 0 \forall$ integer $n \in [1, N]$ is a vector such that $\|v\| = 0$.

In representation by summing projections on a set of orthonormal basis functions U , one of three cases can exist [6]:

1. The set of basis functions is incomplete.
2. The set of basis functions is complete.
3. Some subset U_s of the basis functions constitutes a complete set where the complementary subset $\overline{U_s} \neq \emptyset$.

In case 1, it is not possible to obtain a complete representation from U . In other words, (2.17) does not hold. Since U is incomplete, for the set of basis functions $\{u_n\}_{n=1}^N$, there is some non-zero vector v such that $(v, u_n) = 0$ for any integer n on $[1, N]$. The set of Rademacher functions [7] represents one such example.

In case 2, a complete representation is obtainable and (2.17) does hold. Classical Fourier expansion represents an example for case 2.

The third case is less common but does arise occasionally. In the third case, some arbitrary basis vector u_n may lie in the closed linear span of all others in the set:

$$u_n = \sum_{k \neq n} \alpha_k u_k. \quad (2.20)$$

Such an occurrence is referred to as a *frame*. In the case of a frame, (2.17) does not hold. Due to (2.20), evaluation of (2.17b) would result in a representation of vector x containing redundant information. Representation by Fourier expansion with overlapping subdomain basis functions

exemplifies the use of a frame. Specifically, representation by expansion on integer translates of polynomial splines is employed for some signal processing applications [9].

The concept of a frame originates from a theorem outlined by Riesz and Sz.-Nagy addressing biorthogonal systems [3]. The present term, however, was introduced by Duffin and Schaeffer in work related to nonharmonic Fourier analysis [8]. In contrast to expansion by sets of complete orthonormal bases, expansions by frames do not converge to a specific vector. Instead, such expansions converge to a specified range:

$$A \|x\|^2 \leq \sum_k |(\phi_k, x)|^2 \leq B \|x\|^2 \quad \forall x \in \mathcal{H} \quad (2.21)$$

where \mathcal{H} represents the set of all integers. The constant factors $A, B \in \mathbb{R}$ are called the *frame bounds*. In order the operation to be invertible (or even, possibly, nontrivial), the requirement exists that $A > 0$ and $B < \infty$. Daubechies [6] presents detailed descriptions of the procedures for calculating frame bounds for various situations.

Employing concepts from linear operator theory, the projection operation, T , of some vector, x onto a set of basis functions $\{\phi_m\} \quad \forall m \in \mathcal{H}$ is characterized as a mapping from a Hilbert space \mathcal{H} to the sequence of all square summable sequences $\ell^2(\mathcal{H})$:

$$T: \mathcal{H} \rightarrow \ell^2(\mathcal{H}).$$

Specifically, the projection operation T , defined to be the *frame operator*, is defined as

$$(T\{x\})_k = (\phi_k, x). \quad (2.22a)$$

The adjoint frame operator, T^* , results in the expansion on the basis set $\{\phi_k\}$

$$T^*\{c\} = \sum_k c_k \phi_k. \quad (2.22b)$$

Combining (2.22a) and (2.22b), (2.21) can be expressed in its most abstract form as

$$A \mathbb{1} \leq T^* T \leq B \mathbb{1}$$

where $\mathbb{1}$ denotes the identity operator.

A decomposition by frames can be reconstructed exactly if a *biorthogonal system*, also occasionally referred to as a *Riesz basis* [9], is constructed. The form of such a reconstruction appears as

$$x = \sum_k (\phi_k, x) \tilde{\phi}_k = \sum_k (\tilde{\phi}_k, x) \phi_k. \quad (2.23)$$

In (2.23), the vector set $\{\tilde{\phi}_k\}$ is referred to the biorthogonal basis of $\{\phi_k\}$. The basis function for the biorthogonal set is related to the fundamental set by

$$\tilde{\phi}_k = (T^* T)^{-1} \phi_k \quad (2.24)$$

Occasionally, in literature, the Riesz basis will be referred to as the *dual frame*. This term should not be confused with the concept of dual or conjugate space previously discussed.

Daubechies [6] describes and proves three generalities regarding biorthogonal systems. These include:

1. The family $\{\tilde{\phi}_k\}_{\forall k}$ with $\tilde{\phi}_k = (T^* T)^{-1} \phi_k$ constitutes a frame with bounds B^{-1} and A^{-1} .
2. The frame operator \tilde{T} associated with $\tilde{\phi}_k$ is given by $\tilde{T} = T(T^* T)^{-1}$ and satisfies

$$\begin{aligned} \tilde{T}^* \tilde{T} &= (T^* T)^{-1} \\ \text{and} \\ \tilde{T}^* T &= T^* \tilde{T} = \mathbb{1}, \end{aligned} \quad (2.25)$$

or, equivalently

$$(T^*)^{-1} = \tilde{T}.$$

3. And finally,

$$\tilde{T} T^* = T (T^* T)^{-1} T^* = T \tilde{T}^*. \quad (2.26)$$

III. A SURVEY OF MULTIRATE SYSTEM THEORY

A. INTRODUCTION

Multiresolution analysis implementations frequently reduce to structures composed of multirate system building blocks. Consequently, prior to addressing the construction of multiresolution structures, multirate system theory will be briefly reviewed. Section B will address basic multirate system operations and representations. The simplest multirate system--the two-channel Quadrature Mirror Filter (QMF) bank--will be discussed in Section C. In Section D, the results from the preceding sections will be extended to an arbitrary number of channels.

B. BASIC MULTIRATE SYSTEM OPERATIONS

Multirate systems are comprised of three fundamental operators [10]--decimators, expanders, and linear (usually Finite Impulse Response (FIR)), digital filters. In this section, time- and Fourier-domain consequences of decimation and expansion will be demonstrated.

Decimation consists of subsampling a discrete sequence, retaining only samples at integer intervals. Figure 3.1 presents the block diagram symbol for a decimator. In mathematical



Figure 3.1--Block diagram for M-fold decimator.

notation, decimation of a discrete sequence by a factor of "M" is denoted by

$$x_{\downarrow M}(n) = x(M \cdot n).$$

To illustrate the consequences of decimation, consider the bandpass, transient sequence plotted below in Figure 3.2. Figure 3.2 displays a lineplot of a 128-point sequence constructed from the real part of an exponentially-modulated, Kaiser windowed, *sinc* (sine-over-argument) pulse:

$$\text{Re}\{s(n)\} = \frac{\sin(\pi n 8)}{\pi n} \frac{I_0\left[\pi^2 \sqrt{1 - \left(\frac{n}{64}\right)^2}\right]}{I_0(\pi^2)} \text{Re}\{e^{j\pi n 3}\}. \quad (3.2)$$

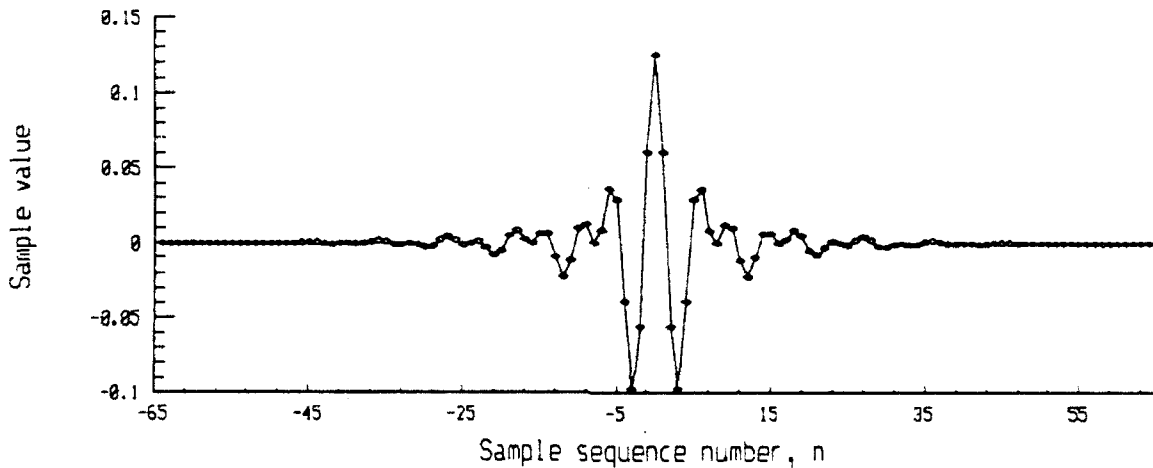


Figure 3.2--Time plot of discrete sequence described by equation (3.2).

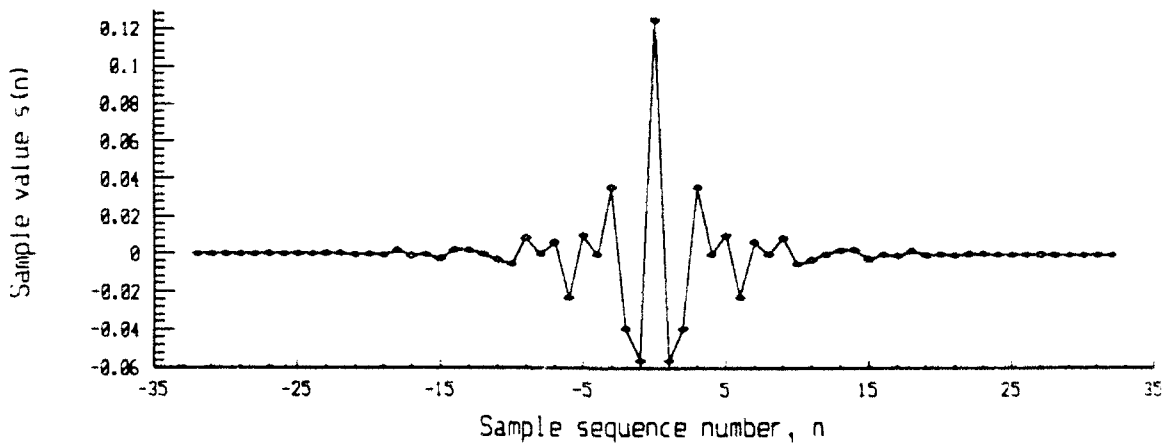


Figure 3.3--Plot of sequence obtained from decimation by a factor of two of sequence (3.2).

Decimation by a factor of two, $s_{\downarrow 2}(n)$, of the sequence in Figure 3.2, produces sequence plotted in Figure 3.3. The length of sequence $s_{\downarrow 2}(n)$ is one half the length of sequence $s(n)$.

Furthermore, the sequences are related by

$$s_{\downarrow 2}(n) = s(2 \cdot n). \quad (3.3)$$

To consider the Fourier-domain consequences of the decimation operation, the Z-transform of the decimated sequence must first be evaluated. For the decimated sequence,

$$\begin{aligned} S_{\downarrow 2}(z) &= \sum_n s(2n) z^{-n} \\ &= \sum_{\text{even } n} s(n) z^{-n/2} \end{aligned} \quad (3.4)$$

Evaluation of the second summation in (3.4a) requires the definition of a sequence $\eta_2(n)$ whose values are unity for even elements and zero for odd elements [11]:

$$\eta_2(n) = [1 + (-1)^n]/2 \quad (3.5)$$

Inserting (3.5) into (3.4) produces

$$\begin{aligned} S_{\downarrow 2}(z) &= \sum_{\text{even } n} s(n) z^{-n/2} \\ &= \frac{1}{2} \sum_n s(n) \left(1 + (-1)^n\right) z^{-n/2} \\ &= \frac{1}{2} [S(z^{1/2}) + S(-z^{1/2})] \end{aligned} \quad (3.6)$$

The effect of decimation on the spectral content of the sequence $s(n)$ is obtained from evaluation of $S_{\downarrow 2}(z)$ on the unit circle:

$$\begin{aligned} S_{\downarrow 2}(e^{j\omega}) &= \frac{1}{2} [S(e^{j\omega/2}) + S(-e^{j\omega/2})] \\ &= \frac{1}{2} [S(e^{j\omega/2}) + S(e^{j(\omega+2\pi)/2})] \end{aligned} \quad (3.7)$$

Decimation, therefore, causes the frequency spectrum of a frequency to become spread become by a factor of two. Additionally, the location of a spectral peak or any other distinguishable

feature will be translated by a factor of two with respect to its original spectral location. The Fourier transform indicated by (3.7) is a 4π -periodic member of $L^2([0, 4\pi])$.

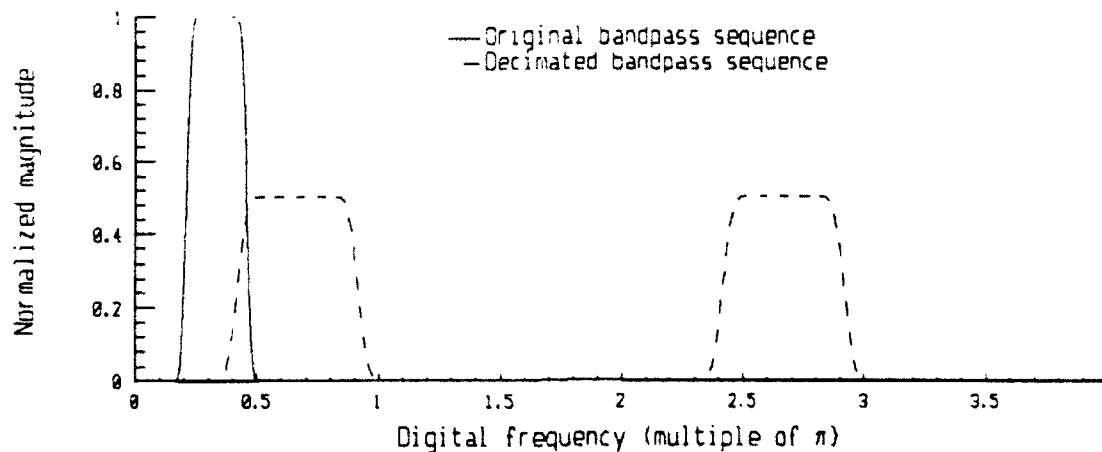


Figure 3.4--Plots of magnitudes of $S(e^{j\omega})$ and $S_{1/2}(e^{j\omega})$.

Figure 3.4 compares the Fourier transforms of a sequence $S(e^{j\omega})$ and its decimated version $S_{1/2}(e^{j\omega})$. The plots in Figure 3.4 illustrate the test sequence power distribution relative to its sampling frequency. The changes to sequence power distribution which occur from decimation are a consequence of a change in the equivalent sampling frequency. In discarding each separate sample, as is done in the decimation operation, the resultant sequence is equivalent to sampling the original sequence at a sample frequency of $f_{s_{1/2}} = 0.5 \cdot f_s$.

As predicted by (3.7), decimation causes a spreading of a bandpass about its center frequency. Furthermore, distance between the center frequency $f_{c_{1/2}}$ of the decimated sequence and $\omega=0$ has been doubled with respect to that of the original sequence. In the example illustrated, the original sequence $s(n)$ was constructed to be an analytic, bandpass process whose

center frequency f_c was related to its sampling frequency f_s by $f_c = f_s/6$ and whose bandwidth $B=0.125 \cdot f_s$. The decimation operation shifts the center frequency $f_{c,12} = f_s/3$ and enlarges the bandwidth to $B_{12} = .25 f_s$, or by a factor of two. The spreading and shifting effects occur because of the subsampling nature of the decimation operation: Decimation results in a change in the sampling frequency. The sequence $s_{12}(n)$ is equivalent to $s(n)$ sampled at one half of its original sampling frequency. The peak magnitude of $S_{12}(e^{j\omega})$ is one half the magnitude of $S(e^{j\omega})$ because of the factor of one half introduced by the sifting sequence (3.5).



Figure 3.5--Block diagram of an expansion operator.

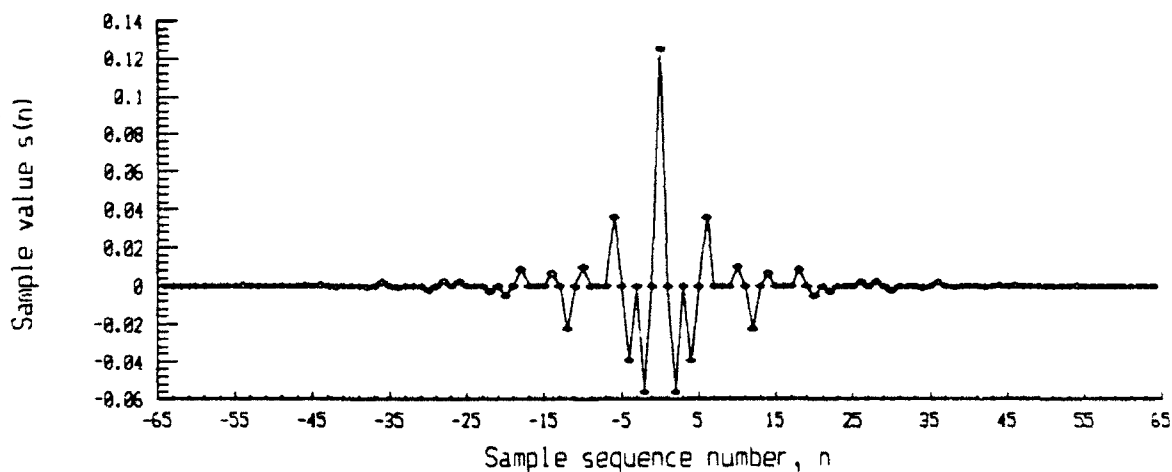


Figure 3.6--Discrete plot of expanded version of $s_{12}(n)$.

The operation of expansion (or upsampling) represents, in a sense, the inversion of the decimation operation. Figure 3.5 presents the signal processing block diagram symbol for an expander. The mathematical notation for a two-fold expansion operation is given by:

$$\begin{aligned}
s_{\uparrow 2}(n) &= \begin{cases} s(n/2) \forall \text{ even 'n'} \\ 0 \forall \text{ odd 'n'} \end{cases} \\
&= \frac{1}{2} \left(1 + (-1)^n \right) s(n/2)
\end{aligned} \tag{3.8}$$

Consequently, expansion entails the insertion of a zero between each sample in a sequence.

Figure 3.6 presents a discrete line plot of the expansion of the sequence $s_{\downarrow 2}(n)$. Expansion restores the length of the decimated sequence to that of the original sequence. However, all odd-number elements of the sequence $s_{\uparrow 2}(n)$ are zero.

Considering the Z-transform and Fourier transform of the expanded sequence provides further insight into the relationship between the expansion and decimation operations. The Z-transform of $s_{\uparrow 2}(n)$ is evaluated as:

$$\begin{aligned}
S_{\uparrow 2}(z) &= \frac{1}{2} \sum_n \left(1 + (-1)^n \right) s\left(\frac{n}{2}\right) z^{-n} \\
&= \frac{1}{2} \sum_n \left(1 + (-1)^{2n} \right) s(n) z^{-2n} \\
&= \sum_n s(n) z^{-2n} \\
&= S\left(z^2\right)
\end{aligned} \tag{3.9}$$

Consequently, in the Z-domain, expansion of the decimated sequence $s_{\downarrow 2}(n)$ produces

$$[S_{\downarrow 2}]_{\uparrow 2}(z) = \frac{1}{2} [S(z) + S(-z)]. \tag{3.10a}$$

In other words, expansion of a decimated sequence reproduces the original sequence plus an additional term. This term is referred to as the *aliasing term* [12]. Evaluating (3.10a) on the unit circle yields:

$$\begin{aligned}
 [S_{1/2}]_{\uparrow 2}(e^{j\omega}) &= \frac{1}{2}[S(e^{j\omega}) + S(-e^{j\omega})] \\
 &= \frac{1}{2}S[(e^{j\omega}) + S(e^{j(\omega-\pi)})]
 \end{aligned}
 \tag{3.10b}$$

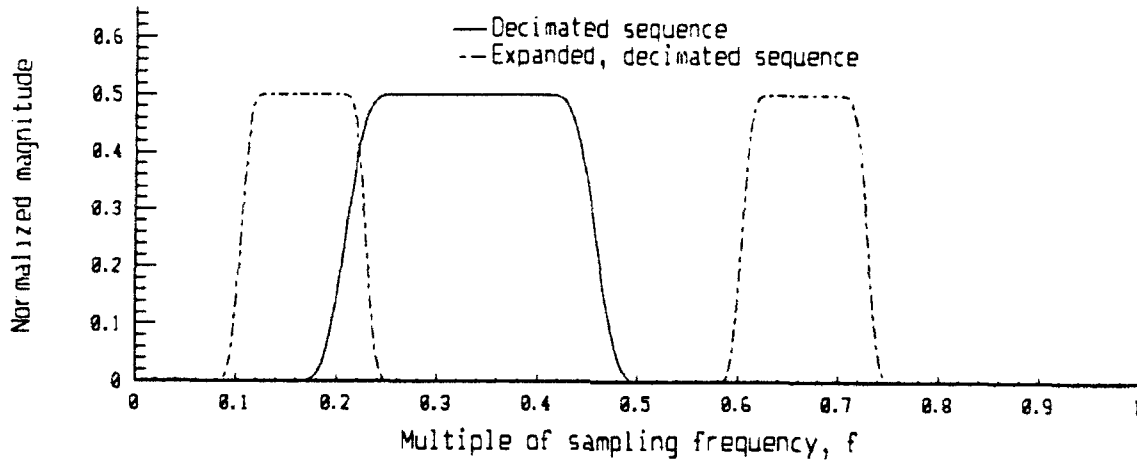


Figure 3.7--Magnitude plots of $S_{1/2}(e^{j\omega})$ and $[S_{1/2}]_{\uparrow 2}(e^{j\omega})$.

The aliasing term, therefore, consists of the original term shifted by π radians. The magnitude plots of $S_{1/2}(e^{j\omega})$ and $[S_{1/2}]_{\uparrow 2}(e^{j\omega})$ presented in Figure 3.7 illustrate this occurrence. The left side of the plot illustrates the restoration of the decimated sequence to its original center frequency and bandwidth while the right side of the plot demonstrates the generation of an aliasing term. The aliasing term illustrated in Figure 3.7 can be reduced through the use of a linear, lowpass filter. Such a filter is often referred to as an *interpolation filter*.

Figure 3.8 illustrates the time-domain results of applying an interpolation filter to the sequence plotted in Figure 3.6. The sequence in Figure 3.8 differs from the original sequence by a normalized mean-squared error of -11.52 dB where the normalized mean-square error is defined as

$$\hat{\epsilon} = \frac{\sum_{n=0}^{N-1} (s(n) - \hat{s}(n))^2}{\sum_{n=0}^{N-1} |s(n)|^2} \quad (3.11)$$

The interpolation filter whose response is shown in Figure 3.9 was constructed using a procedure outlined by Vaidyanathan [12]. A zero-phase, half-band, FIR filter was constructed using the McClellan-Parks algorithm and its characteristic polynomial factored. The minimum-phase zeros of the original polynomial were expanded to form a new characteristic polynomial for the filter whose frequency response appears in Figure 3.9.

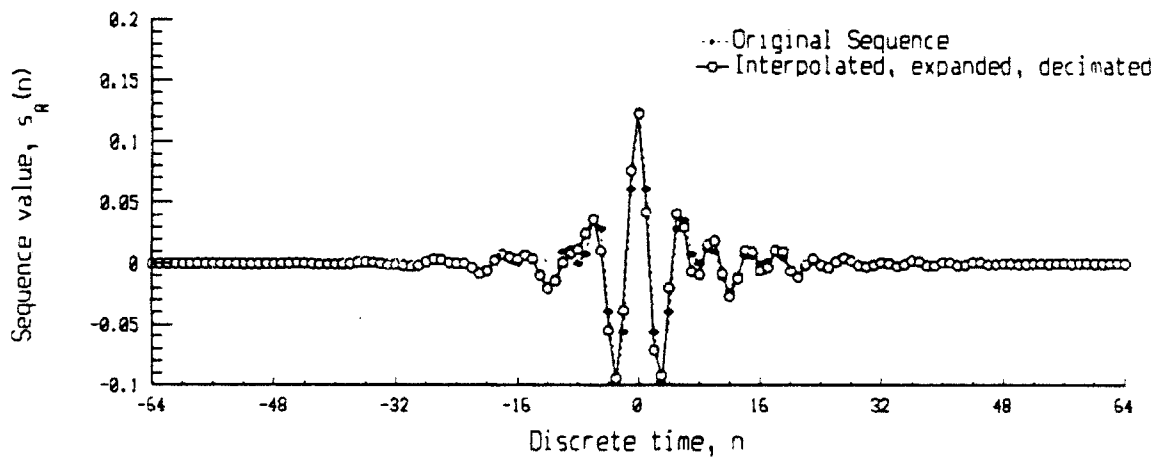


Figure 3.8--Superimposed plots of original sequence $\text{Re}\{s(n)\}$ and of real part of interpolated, expanded, decimated sequence, $\text{Re}\{h_0 * [s_{1/2}]_{\uparrow 2}(n)\}$ where $h_0(n)$ represents the impulse response of the interpolation filter.

The source of the error between the original sequence and its interpolated versions is readily apparent in Figure 3.9. The spectral content of the interpolated sequence almost exactly coincides with that of the original sequence in the region below the Nyquist frequency. However, since the interpolation filter consisted strictly of real coefficients, its frequency response included an image in the half of the spectrum above the Nyquist frequency. The

location of the image coincided with the location of the aliasing term generated by expansion. As a result of partial transmission of the aliasing component, the interpolated sequence whose spectrum is plotted in Figure 3.9 is no longer an analytical sequence. This accounts for the loss of symmetry evident in the plot of the interpolated sequence presented in Figure 3.8.

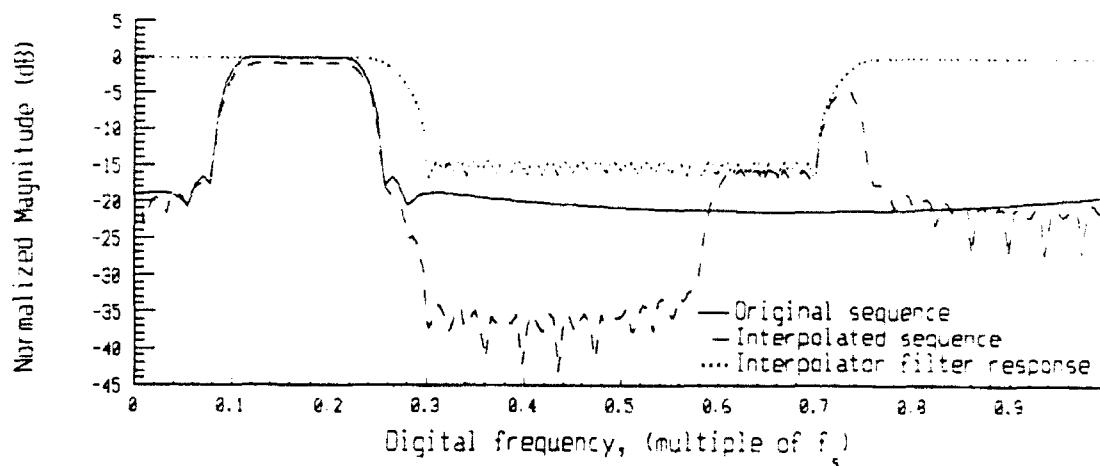


Figure 3.9--Superimposed plots of spectral content of original sequence and interpolated sequence and of interpolator frequency response.

C. TWO-CHANNEL QUADRATURE MIRROR FILTER BANKS

The primary objective of the present section is to introduce the Quadrature Mirror Filter (QMF) bank. QMF bank theory is a well-developed area within the field of electrical engineering and can be understood with a grasp of basic linear systems theory. The purpose for the study of QMF banks in this chapter is to prepare for the construction of multiresolution structures in the next chapter. In Chapter IV, Mallat's algorithm for the discrete wavelet transform will be shown to be exactly equivalent to the QMF bank. Thereafter, multiresolution analysis structures will be constructed from QMF banks of various numbers of channels.

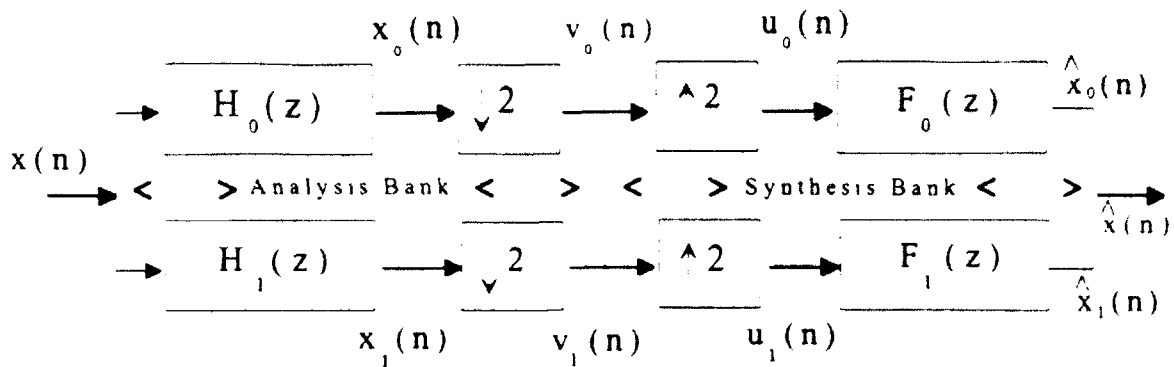


Figure 3.10--Block diagram of two-channel, Quadrature Mirror Filter (QMF) bank. (After [12])

Having considered the basic building blocks of a linear, multirate system, attention in this section will be directed towards assembling those components into a basic system. Two-channel, quadrature mirror filter (QMF) banks represent the most basic structures for transmultiplexers, sub-band coders, and discrete wavelet transforms. Figure 3.10 presents a block diagram of a basic, two-channel QMF bank. The vertical, dotted line in Figure 3.10 divides the system into *analysis* and *synthesis* banks. Each of the filters in the structure is a half-band filter. The analysis section divides the signal, by frequency, into two channels. The synthesis bank then recombines the channels and generates an approximation $\hat{x}(n)$ of the original signal. In general, $\hat{x}(n)$ will differ from the original sequence because of three sources of error [13]: aliasing, amplitude distortion, and phase distortion. The Z-transform analysis presented in the previous section permits precise characterization of these errors.

If a filter bank is designed such that each of these errors is exactly cancelled, then the structure is called a *perfect reconstruction* filter bank. More specifically, the perfect reconstruction criterion is expressed mathematically as

$$\hat{x}(n) = c \cdot x(n - n_0) \tag{3.12}$$

for some non-zero constant c and positive integer n_0 . In other words, for a perfect reconstruction filter bank, the reconstructed sequence will differ from the original sequence only by a constant factor and a delay.

Beginning Z-transform analysis of the structure illustrated in Figure 3.11 [12], the output of the synthesis filter for channel k ($k = 0, 1$) is expressed as

$$X_k(z) = H_k(z)X(z). \quad (3.13)$$

By (3.6), the decimator output is described by

$$\begin{aligned} V_k(z) &= \frac{1}{2} [X_k(z^{1/2}) + X_k(-z^{1/2})] \\ &= \frac{1}{2} [H_k(z^{1/2})X(z^{1/2}) + H_k(-z^{1/2})X(-z^{1/2})] \end{aligned} \quad (3.14)$$

Applying (3.9) and (3.10),

$$\begin{aligned} U_k(z) &= V_k(z^2) \\ &= \frac{1}{2} [H_k(z)X(z) + H_k(-z)X(-z)] \end{aligned} \quad (3.15)$$

describes the decimator output. Finally, the reconstruction component for channel k is given by

$$\begin{aligned} \hat{X}_k(z) &= F_k(z)U_k(z) \\ &= \frac{1}{2} F_k(z) [H_k(z)X(z) + H_k(-z)X(-z)] \end{aligned} \quad (3.16)$$

Since the reconstructed signal is simply the sum of the synthesis filter bank channels, the overall transfer function for the filter bank, in matrix form, becomes

$$\hat{X}(z) = \frac{1}{2} \begin{bmatrix} X(z) & X(-z) \end{bmatrix} \begin{bmatrix} H_0(z) & H_1(z) \\ H_0(-z) & H_1(-z) \end{bmatrix} \begin{bmatrix} F_0(z) \\ F_1(z) \end{bmatrix}. \quad (3.17)$$

Now, (3.17) can be expanded and expressed as

$$\hat{X}(z) = \frac{1}{2} \left(F_0(z)H_0(z) + F_1(z)H_1(z) \right) X(z) + \frac{1}{2} \left(F_0(z)H_0(-z) + F_1(z)H_1(-z) \right) X(-z).$$

When written in this manner, two categories of components are evident: the desired reconstructed components composed of $X(z)$ and its factor, and an aliasing term consisting of $X(-z)$ and its factor. Evaluated on the unit circle, the spectrum of the aliasing terms consist of a replica of the spectrum of the original sequence only shifted by π .

In order to separately represent the components in the QMF bank output in terms of the reconstructed signal component and an undesired aliasing component, it is possible to represent (3.17) as a double-input, single output transfer function:

$$\begin{bmatrix} T(z) \\ A(z) \end{bmatrix} = \frac{1}{2} \begin{bmatrix} H_0(z) & H_1(z) \\ H_0(-z) & H_1(-z) \end{bmatrix} \begin{bmatrix} F_0(z) \\ F_1(z) \end{bmatrix} = \frac{1}{2} \begin{bmatrix} F_0(z)H_0(z) + F_1(z)H_1(z) \\ F_0(z)H_0(-z) + F_1(z)H_1(-z) \end{bmatrix}. \quad (3.18)$$

To satisfy the perfect reconstruction criteria, it is necessary that

$$A(e^{j\omega}) = 0 \quad \forall \quad \omega \quad (3.19a)$$

and

$$T(e^{j\omega}) = e^{-j\omega n_0} |T(e^{j\omega})| = c \cdot e^{-j\omega n_0} \quad (3.19b)$$

where c constitutes a positive constant and n_0 is a positive integer.

Vaidyanathan [12] points out that, given a filter $H_0(z) = \sum_{n=0}^N h_0(n)z^{-n}$, the remaining filters required to construct a two-channel, perfect reconstruction QMF bank are obtained from

$$\begin{aligned} H_1(z) &= -z^{-N} H_0^*(-1/z^*) \\ F_0(z) &= z^{-N} H_0^*(1/z^*) \\ &\text{and} \\ F_1(z) &= z^{-N} H_1^*(1/z^*) \end{aligned} \quad (3.20a)$$

coupled with the constraint that

$$|H_0(e^{j\omega})|^2 + |H_0(e^{j(\omega-\pi)})|^2 = c \quad (3.20b)$$

for some positive constant c (not-necessarily the same constant as in (3.19b)) satisfy the perfect reconstruction criterion. A set of filters characterized by (3.20b) is said to be *power complementary*. Given (3.20), the problem of designing a two-channel, perfect reconstruction QMF filter bank reduces to the problem of selecting a valid analysis filter $h_0(n)$. Some of the details of selecting good filters for these applications will be addressed in Chapter V.

At this juncture, it is appropriate to introduce some additional concepts. The matrix

$$\mathbf{H}(z) = \begin{bmatrix} H_0(z) & H_1(z) \\ H_0(-z) & H_1(-z) \end{bmatrix} \quad (3.21)$$

constitutes the *alias compensation matrix*. If

$$\mathbf{H}^H(e^{j\omega}) \mathbf{H}(e^{j\omega}) = d \mathbf{I}, \quad (3.22)$$

where the superscript H denotes the transpose-conjugate of a matrix, \mathbf{I} represents an identity matrix, and d is a positive constant, then the matrix $\mathbf{H}(e^{j\omega})$ is said to be *unitary*. By definition, unitary operators are operators which, when applied to their inverses, produce an identity operation. Within the context of linear algebra, a matrix is unitary if each of its columns is linearly independent from all of the other columns in the matrix. Consequently, for a QMF bank with an alias compensation matrix which is unitary, the aliasing component of the output is linearly independent of the reconstructed component and the two components are, therefore, separable.

Using the *tilde* notation introduced by Vaidyanathan [12] where $\tilde{\mathbf{H}}(z) \triangleq \mathbf{H}^H(1/z^*)$, and where each element of $\mathbf{H}(z)$ is stable, if

$$\tilde{\mathbf{H}}(z) \mathbf{H}(z) = d \mathbf{I} \quad (3.23)$$

then $\mathbf{H}(z)$ is said to satisfy the *paraunitary* property and the system characterized by $\mathbf{H}(z)$ can be described as a *paraunitary system*. A paraunitary Z-transform matrix will be unitary when evaluated on the unit circle. Furthermore, if the coefficients of $\mathbf{H}(z)$ are all real, then $\mathbf{H}(z)$ is *lossless bounded real*. Additionally, Vaidyanathan lists three important properties for paraunitary systems:

1. The determinant of a square, FIR, paraunitary system produces an allpass polynomial. That is,

$$\det\{\mathbf{H}(z)\} = az^{-K}, K \geq 0, a \neq 0. \quad (3.24)$$

2. Paraunitary systems are power complementary. If $\mathbf{h}(e^{j\omega}) = [H_0(e^{j\omega}) \quad H_1(e^{j\omega})]^T$

$$|H_0(e^{j\omega})|^2 + |H_1(e^{j\omega})|^2 = \tilde{\mathbf{h}}(e^{j\omega}) \mathbf{h}(e^{j\omega}) = c \quad \forall \omega \quad (3.25)$$

3. The submatrices of $\mathbf{H}(z)$ are paraunitary.

Another concept which becomes useful in multirate system theory is the *polyphase representation*. This representation will be introduced for a two-channel system here and extended in the next section to a structure entailing an arbitrary number of channels. It is possible to express the Z-transform of a sequence $h_k(n)$ as

$$\begin{aligned} H_k(z) &= \sum_n h_k(n) z^{-n} \\ &= \sum_n h_k(2n) z^{-2n} + z^{-1} \sum_n h_k(2n+1) z^{-2n} \end{aligned} \quad (3.24)$$

If subsets of the sequence $h_k(n)$ are defined as

$$\begin{aligned} e_{k,0}(n) &= h_k(2n) \\ e_{k,1}(n) &= h_k(2n+1) \end{aligned} \quad (3.25)$$

then it is possible to represent the two-channel, multirate system described in this channel in an additional manner. A z -dependent column vector $\mathbf{h}(z)$ can be defined such that

$$\mathbf{h}(z) = \begin{bmatrix} H_0(z) \\ H_1(z) \end{bmatrix} = \begin{bmatrix} E_{0,0}(z^2) & E_{0,1}(z^2) \\ E_{1,0}(z^2) & E_{1,1}(z^2) \end{bmatrix} \begin{bmatrix} 1 \\ z^{-1} \end{bmatrix} = \mathbf{E}(z^2) \begin{bmatrix} 1 \\ z^{-1} \end{bmatrix} \quad (3.26a)$$

where

$$\mathbf{E}(z^2) \triangleq \begin{bmatrix} E_{0,0}(z^2) & E_{0,1}(z^2) \\ E_{1,0}(z^2) & E_{1,1}(z^2) \end{bmatrix}.$$

Furthermore, upon comparing (3.26a) and (3.21), the following relationship arises:

$$\mathbf{H}^T(z) = \begin{bmatrix} \mathbf{h}(z) & \mathbf{h}(-z) \end{bmatrix}. \quad (3.26b)$$

Therefore, in terms of the polyphase matrix $\mathbf{E}(z^2)$ of (3.26a), (3.26b) becomes

$$\begin{bmatrix} \mathbf{h}(z) & \mathbf{h}(-z) \end{bmatrix} = \begin{bmatrix} 1 & 1 \\ z^{-1} & -z^{-1} \end{bmatrix} \mathbf{E}(z^2) = \begin{bmatrix} 1 & 0 \\ 0 & z^{-1} \end{bmatrix} \begin{bmatrix} 1 & 1 \\ 1 & -1 \end{bmatrix} \mathbf{E}(z^2).$$

Consequently, a simple relationship between $\mathbf{H}(z)$ and $\mathbf{E}(z^2)$ exists:

$$\mathbf{H}^T(z) = \mathbf{E}(z^2) \begin{bmatrix} 1 & 0 \\ 0 & z^{-1} \end{bmatrix} \begin{bmatrix} 1 & 1 \\ 1 & -1 \end{bmatrix}. \quad (3.27)$$

Obviously, the right-most matrix on the right-hand side of (3.27) is simply the transformation \mathbf{W}_2 matrix for a two-point DFT. The middle matrix is simply a diagonal matrix of delays and can be expressed as

$$\mathbf{D}_2(z) = \begin{bmatrix} 1 & 0 \\ 0 & z^{-1} \end{bmatrix}.$$

Finally, it is not difficult to demonstrate that if the alias compensation matrix is paraunitary, then so is the polyphase matrix:

$$\begin{aligned}
\bar{\mathbf{H}}(z) \mathbf{H}(z) &= \mathbf{E}((z^{-2})^*) \mathbf{D}_2(1/z) \mathbf{W}_2 \mathbf{W}_2^H \mathbf{D}_2(z) \mathbf{E}^T(z^2) \\
&= \mathbf{E}^*((z^{-2})^*) \mathbf{E}^T(z^2) \\
&= d \mathbf{I}
\end{aligned} \tag{3.28a}$$

or equivalently,

$$\mathbf{E}(z^2) \bar{\mathbf{E}}(z^2) = d \mathbf{I}. \tag{3.28b}$$

Equation (3.28a) follows since $\mathbf{W}_2 \mathbf{W}_2^H = \mathbf{I}$ and $\mathbf{D}_2(z) \mathbf{D}_2(1/z) = \mathbf{I}$. Equation (3.28b) follows from (3.28a) by making the substitution $\zeta = z^{-1}$ followed by evaluating the complex conjugate of each side of the equation.

Vaidyanathan delineates four important properties of paraunitary filter banks satisfying (3.20a) [12]:

1. Where N represents the order of the filters from which the structure is constructed, filter banks satisfying (3.20a) result in perfect reconstruction with

$$\hat{x}(n) = 0.5 x(n - N); \tag{3.29a}$$

2. The analysis filters are power complementary and satisfy the condition

$$|H_1(e^{j\omega})| = |H_0(e^{j(\omega-\pi)})|; \tag{3.29b}$$

3. The synthesis filters are also complementary and, furthermore, they also satisfy

$$|F_k(e^{j\omega})| = |H_k(e^{j\omega})|; \tag{3.29c}$$

4. and, all filters have order $N=2J+1$ for integer J . This condition ensures even filter lengths.

To demonstrate the operation of a two-channel, QMF bank, a simple, 256-point sequence was constructed. The sequence was comprised of two sinusoids windowed by a complicated,

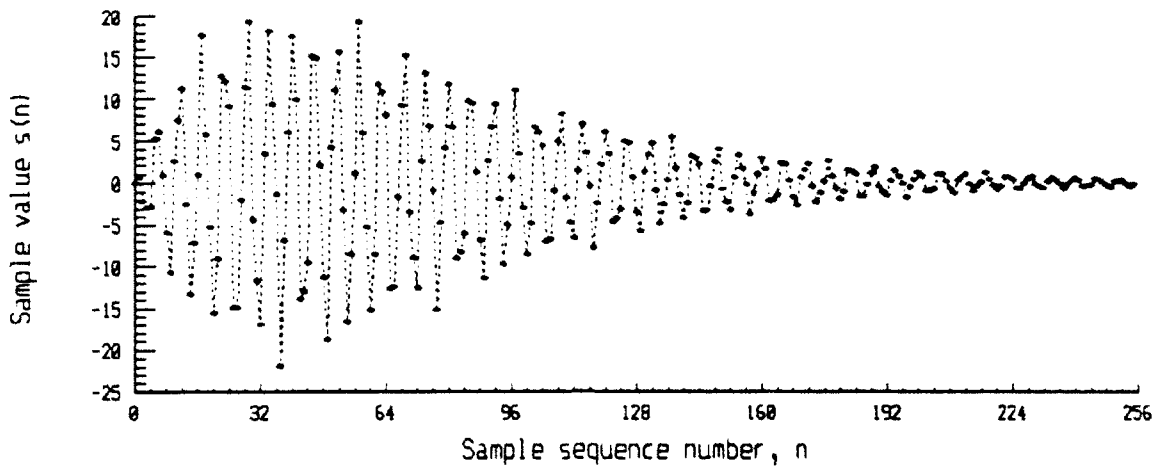


Figure 3.11--Time-domain plot of 256-point test sequence generated using (3.30).

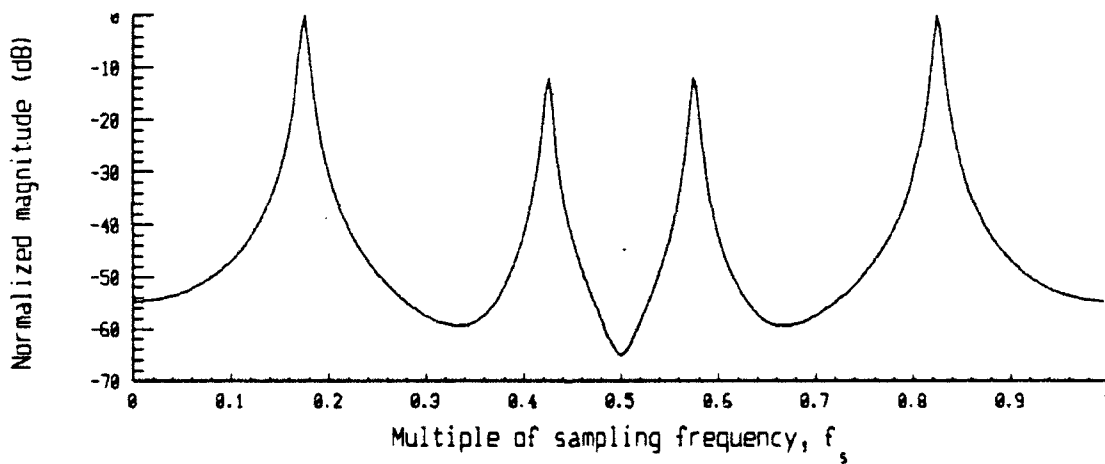


Figure 3.12--Plot of normalized power spectral density of 256-point test sequence generated using (3.30).

exponential window:

$$s(n) = \left(1 - e^{-n/64}\right) \cdot e^{-(n-94)/21} \cdot e^{2n/75} \cdot \sin\left(\frac{7\pi}{20}n\right) + \frac{1}{4} \cos\left(\frac{17\pi}{20}n\right). \quad (3.30)$$

A time plot of the 256-point test sequence (3.30) is presented in Figure 3.11 and the power spectral density of the test sequence appears in figure 3.12. The test sequence contains harmonic

components at digital frequencies of $7\cdot\pi/20 (\approx 0.175\cdot f_s)$ and $17\cdot\pi/20 (\approx 0.425\cdot f_s)$. The components were selected such that one appears in each half of the frequency spectrum.

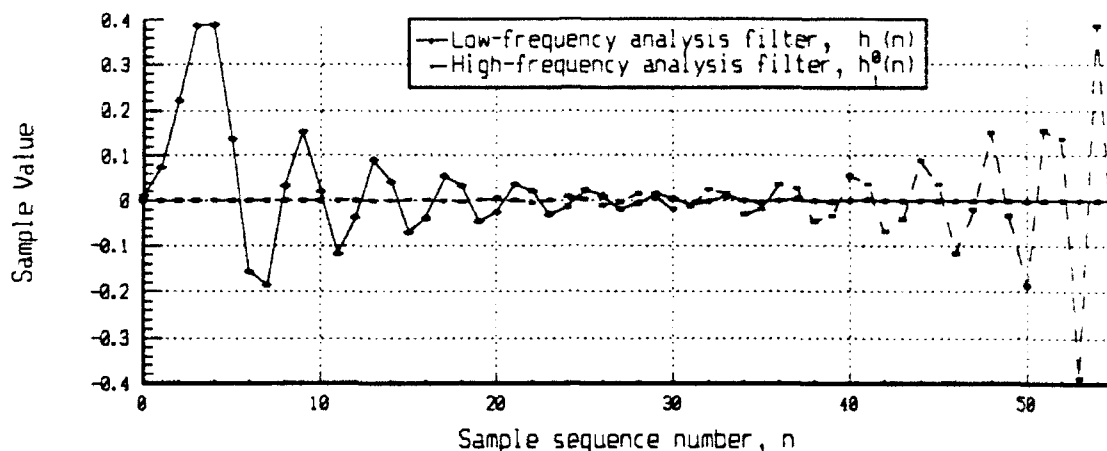


Figure 3.13--Impulse responses for 57th-order FIR filters used in two-channel QMF analysis bank.

Figures 3.13, 3.14 and 3.15 characterize the filter bank to which test sequence (3.30) was applied. The impulse response of the analysis filters for each channel are plotted in Figures 3.13a and 3.13b. The low-frequency channel analysis filter, $H_0(z)$, a 57th-order FIR filter, is a minimum-phase spectral factor of a zero-phase, lowpass, half-band filter designed using the McClellan-Parks technique. From $H_0(z)$, the low-frequency channel synthesis filter $F_0(z)$ and both high-frequency channel filters were designed using (3.20a).

The equivalent transfer function, $t(n)$, whose Z-transform was defined in (3.18), is plotted in Figure 3.14. It has been asserted in (3.12) and (3.19b) that, for perfect reconstruction, $t(n)$ will be of the form

$$t(n)=\delta(n-N), \quad (3.31)$$

where N is the order of the filters from which the QMF bank was constructed. Superimposed with a dashed-line plot, is a plot of the sequence $t(n) - \delta(n-N)$. The axis for the superimposed plot is graduated on the right-hand side of the plot. From the superimposed plot, it is evident that the sequence $t(n)$ approaches the form of (3.31) with a maximum error of less than 2×10^{-5} .

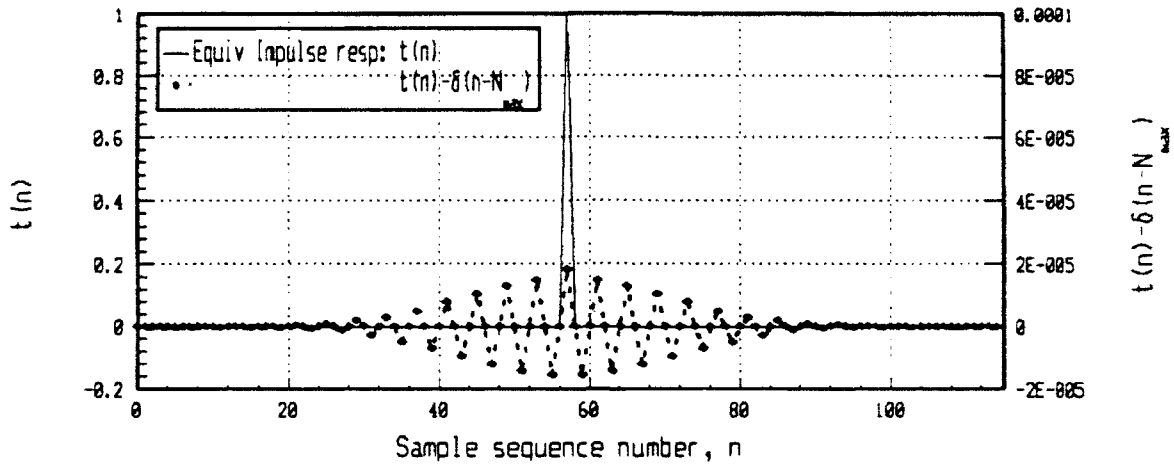


Figure 3.14--Superimposed plots of equivalent impulse response for QMF bank, $t(n)$ (defined as in (3.18)), and of $t(n) - \delta(n - N_{\max})$.

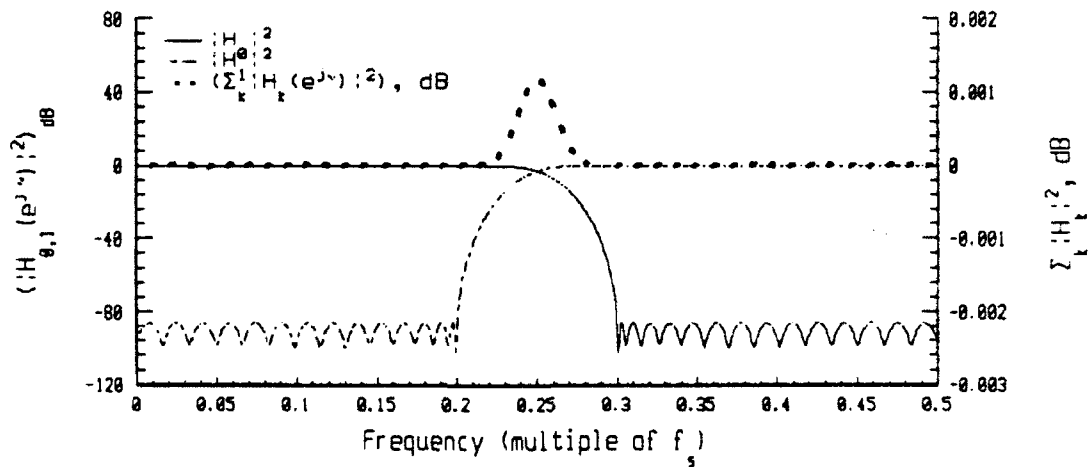


Figure 3.15--Superimposed plots of frequency responses (in dB) of low- and high-frequency filters for QMF bank. Also superimposed is a plot of $|H_0(e^{j\omega})|^2 + |H_1(e^{j\omega})|^2$.

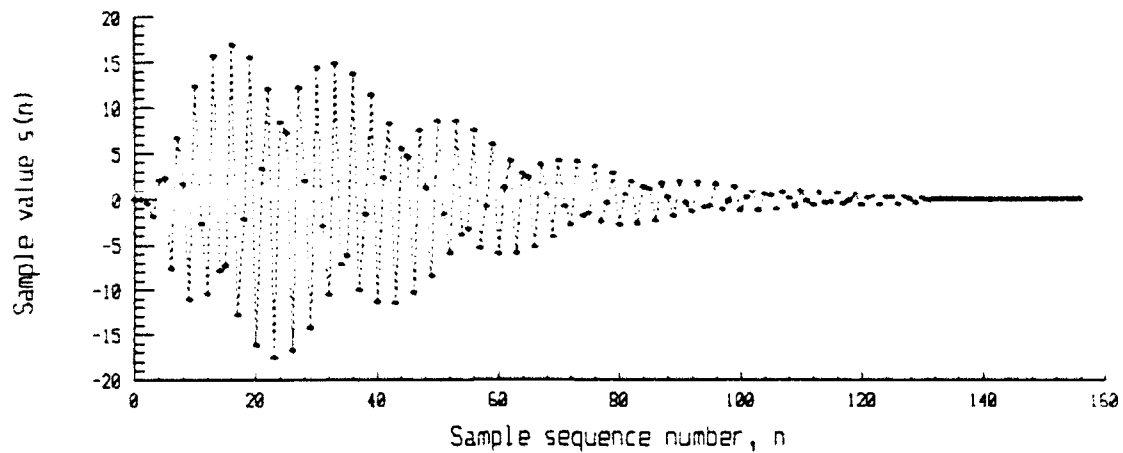


Figure 3.16--Time-domain plot of low-frequency channel decimator output for 256-point test sequence.

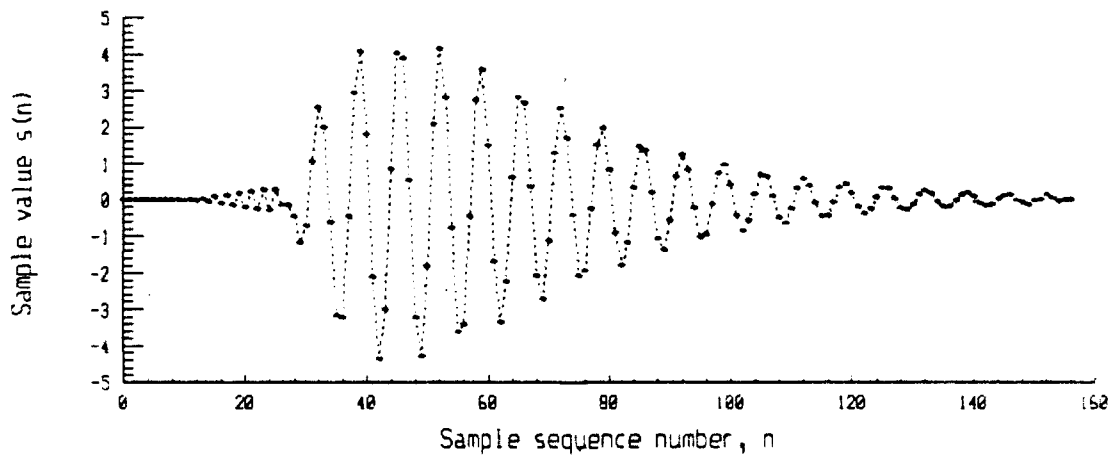


Figure 3.17--Time-domain plot of high-frequency channel decimator output for 256-point test sequence generated by (3.30).

The frequency responses of the filters are plotted in Figure 3.15. Only two frequency responses are shown because of the condition described in (3.29c). Also superimposed on Figure 3.15 is a plot of $|H_0(e^{j\omega})|^2 + |H_1(e^{j\omega})|^2$. This last plot demonstrates the degree to which the filter bank satisfies the power complementary property, (3.20b).

Time plots of the low- and high-frequency channel decimator outputs are presented in Figures 3.16 and 3.17. As a consequence of the decimation-induced translation of the spectral peaks for each component, the plots appear to reflect harmonics whose frequencies are quite close together. Additionally, due to the shape of the filter, the flat segment in the trailing edge of the sequence plotted in Figure 3.16 converges sharply to zero. The flat segment in Figure 3.17 is on the leading edge of the sequence. Since the synthesis filter for channel is the time reversal of the analysis filter, the relative locations of the flat regions will be reversed, resulting in a flat segment on either side. This represents the source of the delay. The difference occurs since, by (3.20a), the low-frequency and high-frequency channel analysis filters are modulated time-reversals of each other. Also worth notice, the relative magnitudes of the low-frequency and high-frequency channel decimator outputs have maintained the proportions established in (3.30). As expected, the decimator output of the low-frequency in figure 3.16 channel maintains a peak amplitude greater, by a factor of four, than the peak if the envelope for the high-frequency channel in figure 3.17.

Figure 3.18 presents superimposed, normalized power spectral density plots for the decimator outputs and the original sequence. As discussed previously, decimation changes the sampling frequency. The sampling frequency $f_{s\downarrow 2}$ for a decimated sequence is related to the sampling frequency f_s for the original frequency by

$$f_{s\downarrow 2} = f_s/2.$$

As expected from (3.7), the peak at $7\pi/20$ ($= 0.175 f_s$) has been translated to $7\pi/10$ ($= 0.35 f_{s\downarrow 2}$).

The peak which was originally at $17\pi/20$ ($= 0.425 f_s$) was shifted to $17\pi/10$. Due to aliasing, the spectral peak located at $17\pi/10$ appears at $20\pi/10 - 17\pi/10 = 3\pi/10$ ($= 0.15 f_{s\downarrow 2}$). Additionally, each of the peaks has been widened.

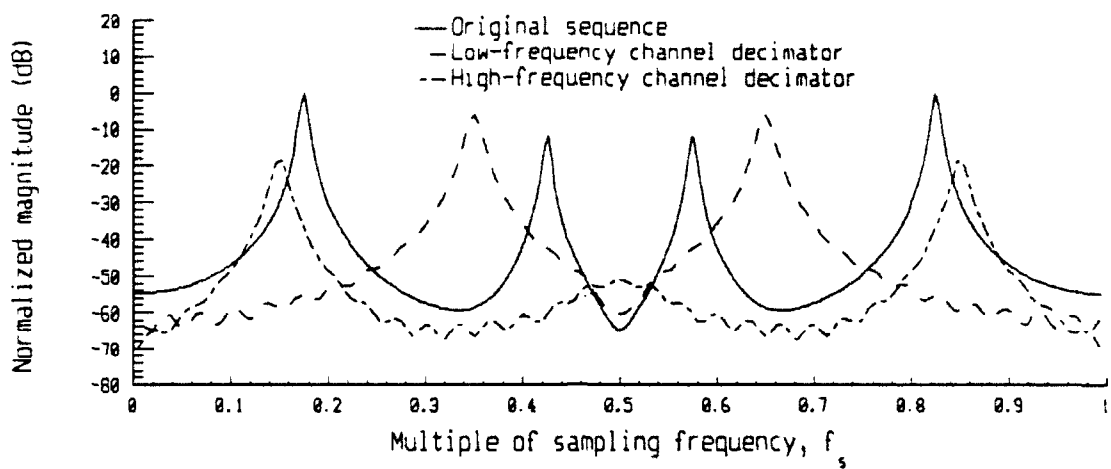


Figure 3.18--Superimposed plots of normalized power spectral densities of the high- and low-frequency channel decimator outputs and the original sequence.

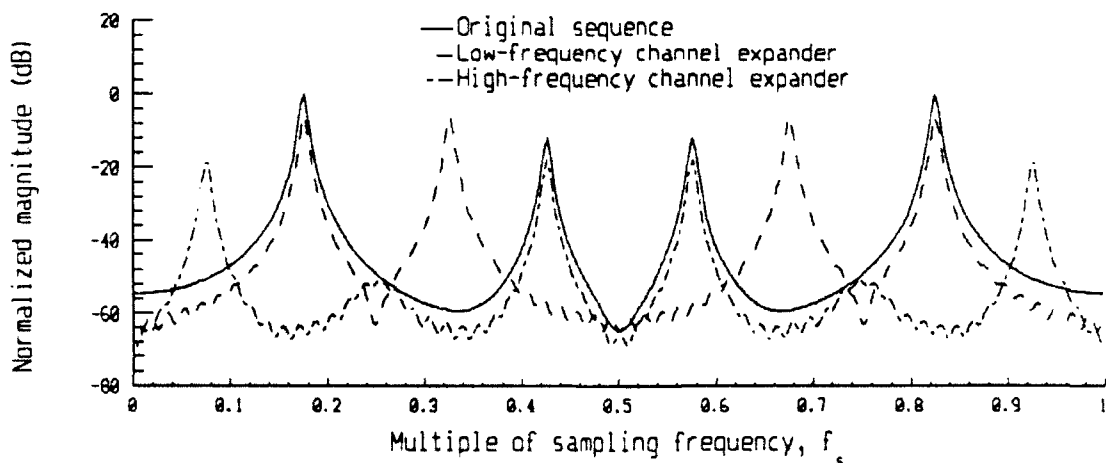


Figure 3.19--Superimposed power spectral density plots of the original 256-point test sequence generated by (3.30) and the high-frequency and low-frequency channel expander outputs.

Figure 3.19 includes spectral density plots of the original sequence and the output of each of the expanders. As indicated by (3.10b), the expander reintroduces the original sampling frequency at the expense of creation of aliasing terms. For the low-frequency channel, spectral peaks occur at the original location, $7\pi/20$ ($= 0.175 f_s$), and at $33\pi/20$ which, because of aliasing, appears as $13\pi/20$ ($= 0.325 f_s$). Similarly, for the high-frequency channel, in addition to the peak at its original position of $17\pi/20$ ($= 0.425 f_s$), an aliased peak is also present at $3\pi/20$ ($= 0.075 f_s$). Although, at the expander output, the width of each peak has been restored to that of the input, each peak is six decibels below the original since the signal energy has been divided between the original term and an aliasing term.

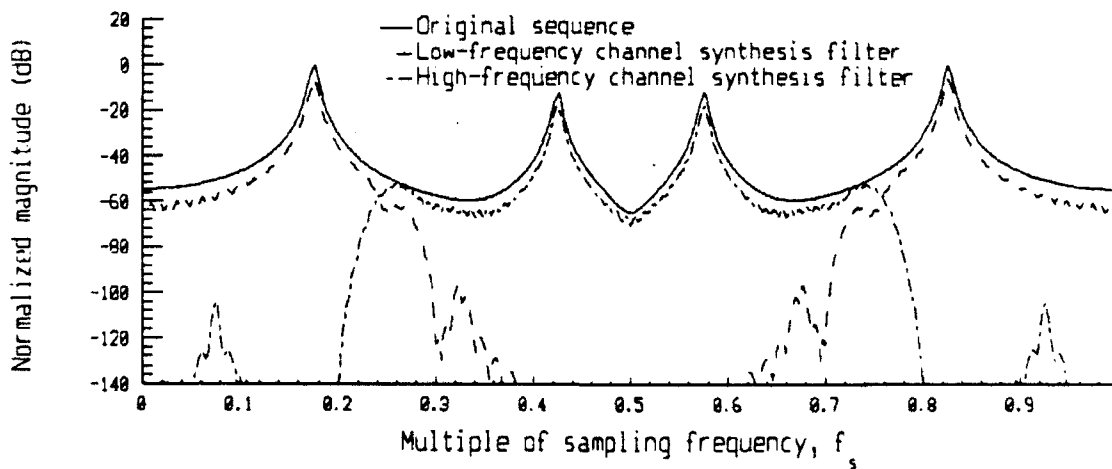


Figure 3.20--Superimposed plots of power spectral densities of original sequence $S(e^{j\omega})$ and of low-frequency QMF channel component and high-frequency QMF channel component.

Superimposed plots of the power spectral densities of the original 256-point test sequence, and of the sequences at the outputs of the low- and high-frequency channel synthesis filters are exhibited in Figure 3.20. For each channel, the effects of the synthesis filters are evident. The aliasing terms have not been completely eliminated, but the spectral peaks of the aliasing terms

have been reduced in magnitude by approximately 95 dB. The restored spectral peaks, still 3 dB below the original, track quite closely within the passbands of their respective filters. The time-domain of the reconstructed sequence, $\hat{s}(n) = \hat{s}_0(n) + \hat{s}_1(n)$, is plotted in Figure 3.21.

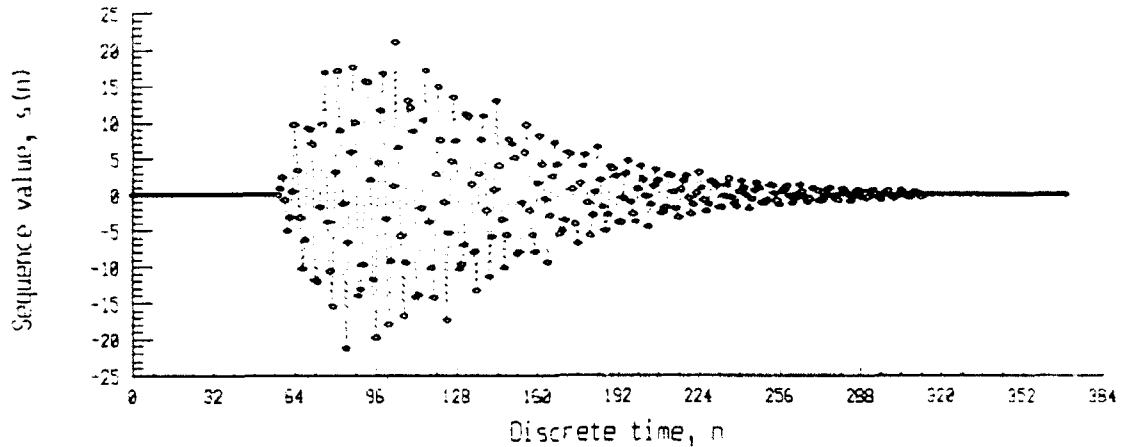


Figure 3.21--Plot of reconstructed version of 256-point test sequence applied to QMF bank input

In this plot, the resemblance of the reconstructed signal to the original is evident. The reconstructed sequence lags the original sequence by 57, the order of the filters from which the QMF bank was constructed. Furthermore, if the normalized, mean-squared error is defined as

$$\hat{\epsilon}_{dB} = \frac{\overline{|s(n) - \hat{s}(n)|^2}}{\overline{s^2(n)}} = \frac{\sum_{n=0}^{N-1} (s(n) - \hat{s}(n))^2}{\sum_{n=0}^{N-1} s^2(n)} \quad (3.32)$$

then for the sequences plotted in Figure 3.21, $\hat{\epsilon}_{dB} = -168.2$ dB.

D. M-CHANNEL FILTER BANKS

Having, in the previous section, discussed and demonstrated the implementation of a two-channel, quadrature mirror filter bank structure, it remains to extend the results to structures consisting of an arbitrary number of channels. With some simple modifications to relationships from sections B and C, M-channel filter banks can be shown to be largely analogous to QMF structures. Finally, it is worth observing that in literature [13], M-channel filter banks are

extensively referred to as *M-Channel Quadrature Mirror Filter Banks*. The use of the term quadrature represents, in this case, a misnomer. Nevertheless, the terminology has continued to be applied to these more complex systems.

The structure for an M-channel filter bank is illustrated in Figure 3.22. The structure is entirely analogous to the two-channel case. Each channel contains a factor-of-M decimator and an expander which, respectively, subsamples by a factor of M and inserts M-1 zeros between each sample. The filters are all M^{th} -band filters with, for the ideal case, frequency responses of

$$|H_k(e^{j\omega})| = \begin{cases} 1 & \forall \frac{\pi}{M} \cdot k \leq \omega \leq \frac{\pi}{M} \cdot (k+1) \\ 0 & \text{otherwise} \end{cases} \quad (3.33)$$

Furthermore, the concepts of perfect reconstruction and power symmetry also apply.

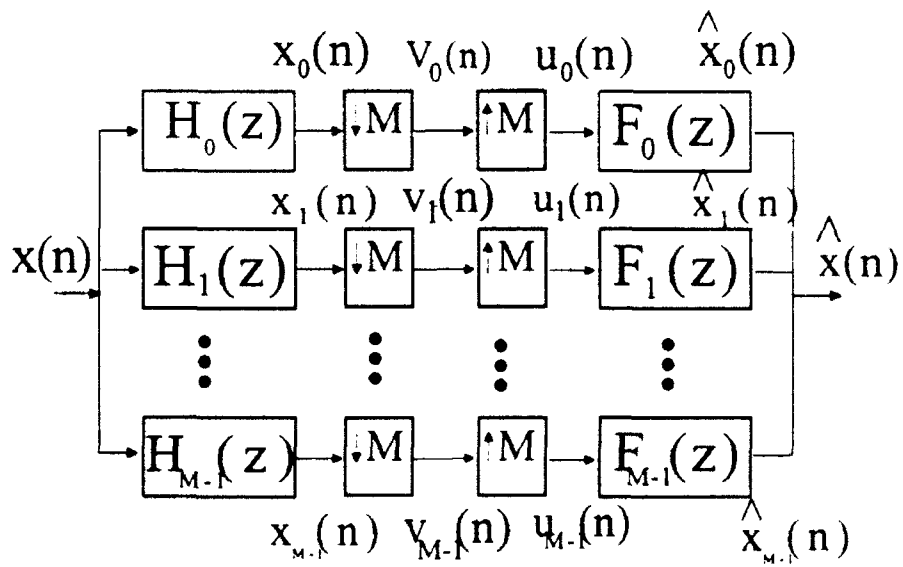


Figure 3.22--Structure of M-channel filter bank. After [11].

Beginning Z-transform analysis, transformation of a decimated sequence requires the construction of a "sifting" function equivalent to that defined in (3.5). For M channels this function is defined as [12]

$$\eta_M(n) = \frac{1}{M} \sum_{k=0}^{M-1} W_M^{-nk} \quad (3.34)$$

where $W_M = e^{j2\pi/M}$. Employing 3.34 produces $s_{\downarrow M}(n) = s(M \cdot n) \cdot \eta_M(M \cdot n)$, thereby ensuring that $s_{\downarrow M}(n)$ is zero for non-integer values of n . For any integer n which is an integer multiple of M , $W_M^{nM} = 1$. Otherwise, the series term in (3.34) becomes a summation around the unit circle in the complex plane which is evaluated as zero. Evaluating the Z-transform of the factor-of-M decimated sequence $s(n)$ produces

$$\begin{aligned} S_{\downarrow M}(z) &= \sum_n s(M \cdot n) \cdot \eta_M(M \cdot n) \cdot z^{-n} \\ &= \frac{1}{M} \sum_{m=0}^{M-1} \sum_n s(n) \left(W_M^m z^{1/M} \right)^{-n} \\ &= \frac{1}{M} \sum_{m=0}^{M-1} S \left(W_M^m z^{1/M} \right) \end{aligned} \quad (3.35)$$

Furthermore, the Z-transform of the decimated sequence $s_{\downarrow M}(n)$ after expansion by a factor of M is evaluated as

$$\begin{aligned} [S_{\downarrow M}]_{\uparrow M}(z) &= \sum_n s_{\downarrow M}(n/M) z^{-n} \\ &= \frac{1}{M} \sum_{m=0}^{M-1} S \left(W_M^m z \right) \end{aligned} \quad (3.36)$$

Evaluating 3.35 on the unit circle produces

$$S_{\downarrow M}(e^{j\omega}) = \frac{1}{M} \sum_{m=0}^{M-1} S \left(e^{j2\pi m/M} e^{j\omega M} \right) \quad (3.37)$$

Consequently, decimation spreads, by a factor of M, the power spectral density of a sequence. Furthermore, the M-fold decimator produces, from a sequence with a $2 \cdot \pi$ -periodic frequency

response, a sequence with a $2 \cdot M \cdot \pi$ -periodic sequence. Similarly, on the unit circle, (3.36)

becomes

$$\begin{aligned} [S_{\downarrow M}]_{\uparrow M}(e^{j\omega}) &= \frac{1}{M} \sum_{m=0}^{M-1} S(e^{j\omega} e^{j2\pi m/M}) \\ &= \frac{1}{M} \sum_{m=0}^{M-1} S(e^{j(\omega+2\pi m/M)}) \end{aligned} \quad (3.38)$$

By (3.38), it is apparent that expansion of a decimated sequence produces $M-1$ aliased terms in even intervals across the spectrum. Additionally, the frequency response of the sequence has been restored to its $2 \cdot \pi$ -periodicity.

Applying (3.35) and (3.36) to the M -channel structure in Figure 3.22 produces the following matrix formulation for the system output $\hat{X}(z)$ [12]:

$$\hat{X}(z) = \frac{1}{M} \begin{bmatrix} X(z) & X(W_M z) & \cdots & X(W_M^{M-1} z) \end{bmatrix} \begin{bmatrix} H_0(z) & H_1(z) & \cdots & H_{M-1}(z) \\ H_0(W_M z) & H_1(W_M z) & \cdots & H_{M-1}(W_M z) \\ \vdots & \vdots & \ddots & \vdots \\ H_0(W_M^{M-1} z) & H_1(W_M^{M-1} z) & \cdots & H_{M-1}(W_M^{M-1} z) \end{bmatrix} \begin{bmatrix} F_0(z) \\ F_1(z) \\ \vdots \\ F_{M-1}(z) \end{bmatrix} \quad (3.39)$$

The matrix $\mathbf{H}(z)$ in (3.39) is the M -channel analogy to the alias cancellation matrix. The column vector containing the synthesis filter characteristic polynomials can be represented as

$\mathbf{f}(z) = [F_0(z) \ F_1(z) \ \cdots \ F_{M-1}(z)]$. For alias cancellation, it is necessary that

$$\mathbf{t}(z) = \begin{bmatrix} t(z) \\ 0 \\ \vdots \\ 0 \end{bmatrix} = \mathbf{H}(z) \mathbf{f}(z). \quad (3.40)$$

Furthermore, analogous to (3.24), it is possible to define a polyphase representation of the characteristic polynomial $H_k(z)$:

$$\begin{aligned} H_k(z) &= \sum_n h_k(n) z^{-n} \\ &= \sum_n h_k(Mn) z^{-Mn} + z^{-1} \sum_n h_k(Mn+1) z^{-Mn} + \dots + z^{-(M-1)} \sum_n h_k(Mn+M-1) z^{-Mn} \\ &= \sum_{m=0}^{M-1} z^{-m} \sum_n h_k(Mn+m) z^{-Mn} \\ &= \sum_{m=0}^{M-1} z^{-m} E_{k,m}(z^M) \end{aligned} \quad (3.41)$$

where $E_{k,m}(z) \leftrightarrow e_{k,m}(n) \stackrel{\Delta}{=} h_k(Mn+m)$. From the definition of the polyphase representation, the polyphase representation follows that

$$\begin{aligned} \mathbf{h}(z) = \begin{bmatrix} H_0(z) \\ H_1(z) \\ \vdots \\ H_k(z) \end{bmatrix} &= \begin{bmatrix} E_{0,0}(z^M) & E_{0,1}(z^M) & \dots & E_{0,M-1}(z^M) \\ E_{1,0}(z^M) & E_{1,1}(z^M) & \dots & E_{1,M-1}(z^M) \\ \vdots & \vdots & \ddots & \vdots \\ E_{M-1,0}(z^M) & E_{M-1,1}(z^M) & \dots & E_{M-1,M-1}(z^M) \end{bmatrix} \begin{bmatrix} 1 \\ z^{-1} \\ \vdots \\ z^{-(M-1)} \end{bmatrix}, \quad (3.42) \\ &= \mathbf{E}(z^M) \mathbf{e}(z) \end{aligned}$$

where

$$\mathbf{E}(z^M) \stackrel{\Delta}{=} \begin{bmatrix} E_{0,0}(z^M) & E_{0,1}(z^M) & \dots & E_{0,M-1}(z^M) \\ E_{1,0}(z^M) & E_{1,1}(z^M) & \dots & E_{1,M-1}(z^M) \\ \vdots & \vdots & \ddots & \vdots \\ E_{M-1,0}(z^M) & E_{M-1,1}(z^M) & \dots & E_{M-1,M-1}(z^M) \end{bmatrix}$$

and $\mathbf{e}(z) = [1 \quad z^{-1} \quad \dots \quad z^{-(M-1)}]^T$.

Finally, the alias compensation matrix $\mathbf{H}(z)$ and the polyphase matrix $\mathbf{E}(z^M)$ are linked by a relationship analogous to (3.27). First,

$$\begin{aligned} \mathbf{H}(z) &= \begin{bmatrix} \mathbf{h}(z) & \mathbf{h}(W_M z) & \cdots & \mathbf{h}(W_M^{M-1} z) \end{bmatrix} \\ &= \begin{bmatrix} \mathbf{E}(z^M) \mathbf{e}(z) & \mathbf{E}\left((W_M z)^M\right) \mathbf{e}(W_M z) & \cdots & \mathbf{E}\left((W_M^{M-1} z)^M\right) \mathbf{e}(W_M^{M-1} z) \end{bmatrix} \end{aligned} \quad (3.43)$$

Now, since, for any integer k , $(W_M^k)^M = (e^{j2\pi k/M})^M = e^{j2\pi k} = 1$, (3.43) becomes:

$$\mathbf{H}^T(z) = \mathbf{E}(z^M) \begin{bmatrix} \mathbf{e}(z) & \mathbf{e}(W_M z) & \cdots & \mathbf{e}(W_M^{M-1} z) \end{bmatrix}. \quad (3.44)$$

The block matrix on the right-hand side of (3.44) is equivalent to

$$\begin{bmatrix} \mathbf{e}(z) & \mathbf{e}(W_M z) & \cdots & \mathbf{e}(W_M^{M-1} z) \end{bmatrix} = \begin{bmatrix} 1 & 0 & \cdots & 0 \\ 0 & z^{-1} & \cdots & 0 \\ \vdots & \vdots & \ddots & \vdots \\ 0 & 0 & \cdots & z^{-(M-1)} \end{bmatrix} \begin{bmatrix} W_M^0 & W_M^0 & \cdots & W_M^0 \\ W_M^0 & W_M^0 & \cdots & W_M^{M-1} \\ \vdots & \vdots & \ddots & \vdots \\ W_M^0 & W_M^{M-1} & \cdots & W_M^{(M-1)^2} \end{bmatrix} \quad (3.45)$$

Combining (3.44) and (3.45), therefore, produces a general relationship between the alias cancellation and polyphase matrices:

$$\mathbf{H}(z) = \mathbf{W}_M^H \mathbf{D}_M(z) \mathbf{E}^T(z^M) \quad (3.46)$$

where,

$$\mathbf{D}_M(z) \triangleq \begin{bmatrix} 1 & 0 & \cdots & 0 \\ 0 & z^{-1} & \cdots & 0 \\ \vdots & \vdots & \ddots & \vdots \\ 0 & 0 & \cdots & z^{-(M-1)} \end{bmatrix}.$$

Obviously, from (3.46), if $\mathbf{H}(z)$ is paraunitary, then $\mathbf{E}(z^M)$ is also paraunitary. Additionally, the properties expressed by (3.24), (3.25), and (3.29) are equally valid for the M -channel filter bank systems.

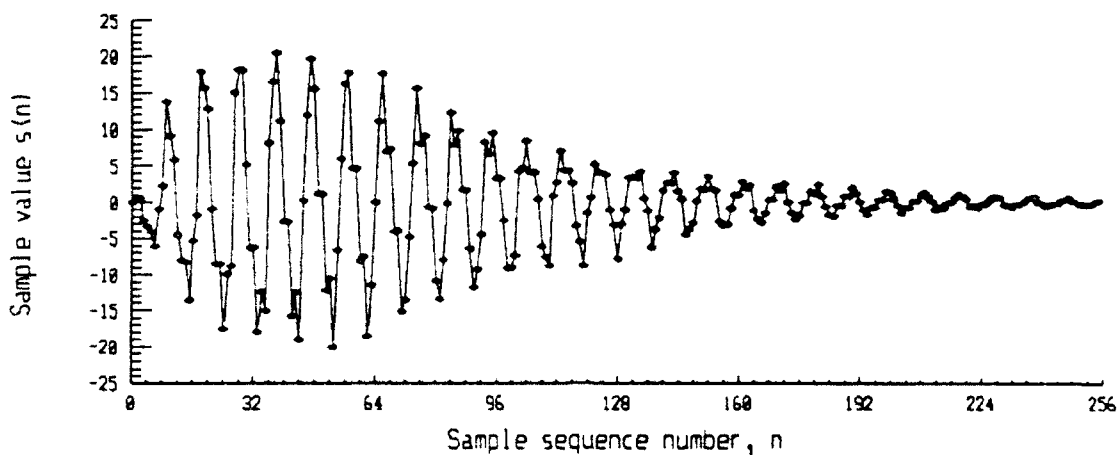


Figure 3.23--Time plot of 256-point test sequence generated using (3.47).

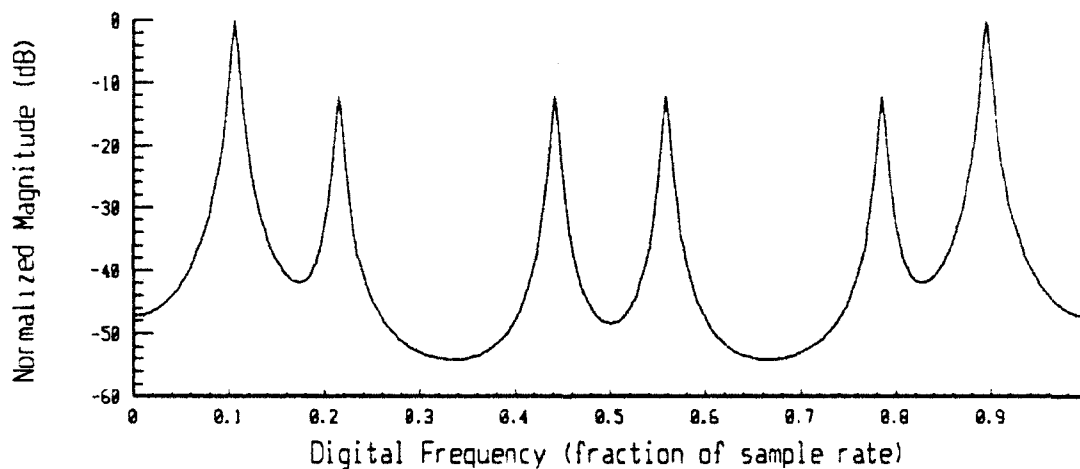


Figure 3.24--Power spectral density of 256-point test sequence generated using (3.47).

To demonstrate the operation of a three-channel filter bank system conforming to the structure of Figure 3.22, a 256-point test sequence similar to that of (3.30) was generated:

$$s(n) = \left(1 - e^{-n/64}\right) \cdot e^{-(n-94)/21} \cdot e^{2n/75} \cdot \left[\cos\left(\frac{2\pi}{256} 27 \cdot n\right) + \frac{1}{4} \cos\left(\frac{2\pi}{256} 55 \cdot n\right) + \frac{1}{4} \cos\left(\frac{2\pi}{256} 113 \cdot n\right)\right]. \quad (3.47)$$

Equation (3.47) employs the same envelope as (3.30) applied to the sum of three harmonic components. Spectral peaks in (3.47) are located at digital frequencies of $2 \cdot \pi \cdot 27/256$ ($\approx 0.027 \cdot f_s$),

$2 \cdot \pi \cdot 55/256$ ($\approx 0.215 \cdot f_s$) and $2 \cdot \pi \cdot 113/256$ ($\approx 0.44 \cdot f_s$). Consequently, spectral peaks occur within each third of the frequency spectrum below the Nyquist frequency. A time plot of the test sequence is displayed in Figure 3.23 while Figure 3.24 presents the power spectral density of the test sequence.

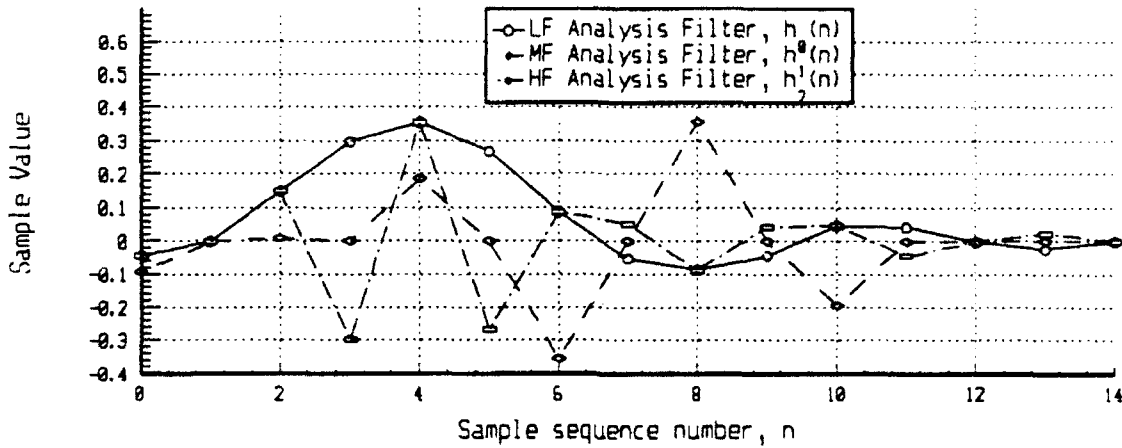


Figure 3.25--Superimposed plots of impulse responses of filters used to implement three-channel filter bank.

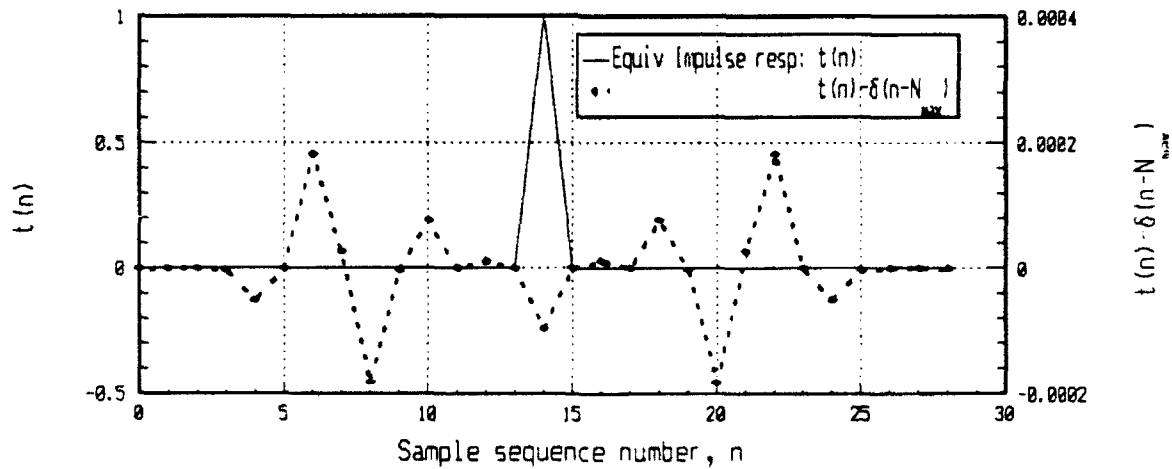


Figure 3.26--Equivalent impulse response for three-channel filter bank structure whose filter impulse responses are plotted in Figure 3.25.

The filter bank employed for the signal decomposition and reconstruction was implemented using 14-point third-band filters whose coefficients are tabulated in [11]. The filter impulse responses are plotted in Figure 3.25. Satisfying (3.34) for the M-channel case is significantly more difficult than for the two-channel case. Consequently, as illustrated in Figure 3.26, the deviation of the equivalent system impulse response deviates from the ideal case of (3.31) by an order of magnitude more than was observed for the two-channel structure demonstrated in Section C. For the two-channel structure, the root-mean-square deviation from (3.31) was 5.16×10^{-6} . For the three-channel system whose equivalent response is plotted in Figure 3.26, the root-mean-square deviation from (3.31) is 7.42×10^{-5} . Furthermore, the peak amplitude distortion is also greater. The peak amplitude distortion is approximately 4×10^{-3} dB from the power complementary case. This represents a noteworthy increase over the 1×10^{-3} dB peak distortion for the two-channel structure demonstrated in Section C.

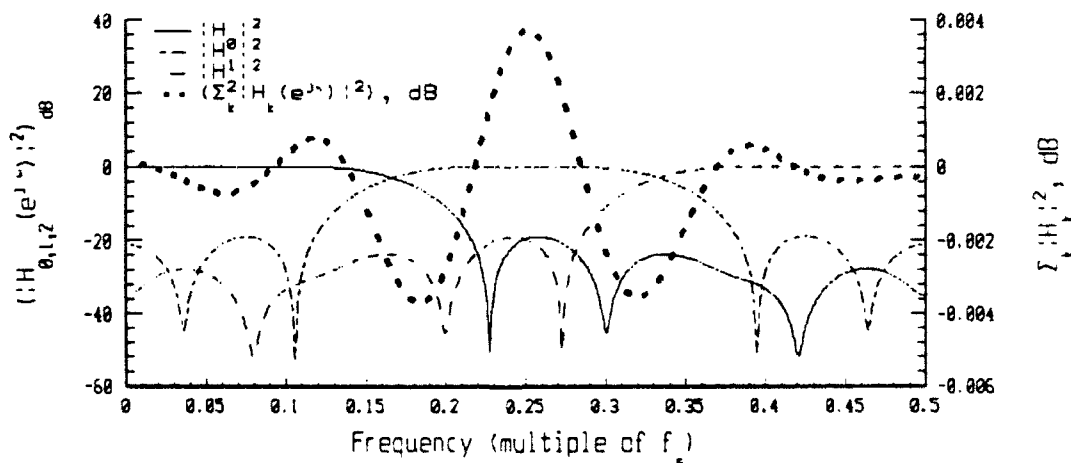


Figure 3.27--Superimposed plots of frequency responses for filters whose impulse responses are plotted in Figure 3.25 (right-hand axis) and amplitude distortion from three-channel filter bank constructed from filters of Figure (3.25) (left-hand axis).

Insight is obtained from considering the decimation operation from both the time and frequency domains. Time-domain plots for the output of each of the decimators appear in Figures 3.28a, b, and c. The power spectral densities of the decimator outputs are superimposed in a plot presented in Figure 3.29. As discussed previously, the decimation operator, in the case of a factor-of-three decimation, retains only one sample out of every three. Therefore, the length of the decimated sequences is one third of the length of the original sequence. Furthermore, the effective sampling frequency $f_{s\downarrow 3}$ for the sequence decimated by a factor of three is related to the sampling frequency f_s by

$$f_{s\downarrow 3} = f_s/3.$$

Additionally, decimation produces aliasing terms. However, these terms are of no consequence since they lie outside of the region $[0, 2\cdot\pi]$. Figure 3.29 displays the power spectral density of the content of each filter bank channel with respect to its post-decimation sampling frequency $f_{s\downarrow 3}$.

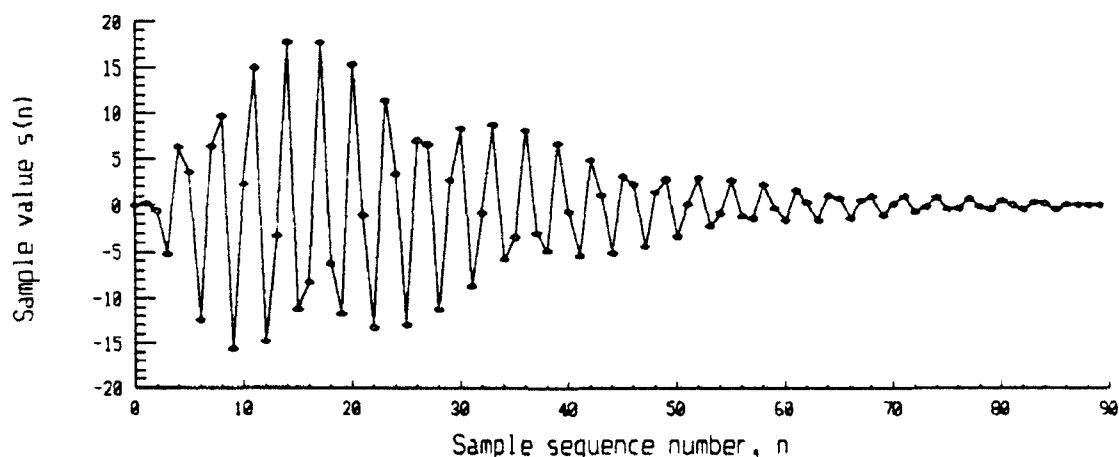


Figure 3.28a--Low-frequency channel decimator output for 256-point test sequence generated by (3.47) applied three-channel filter bank of Figure 3.25.

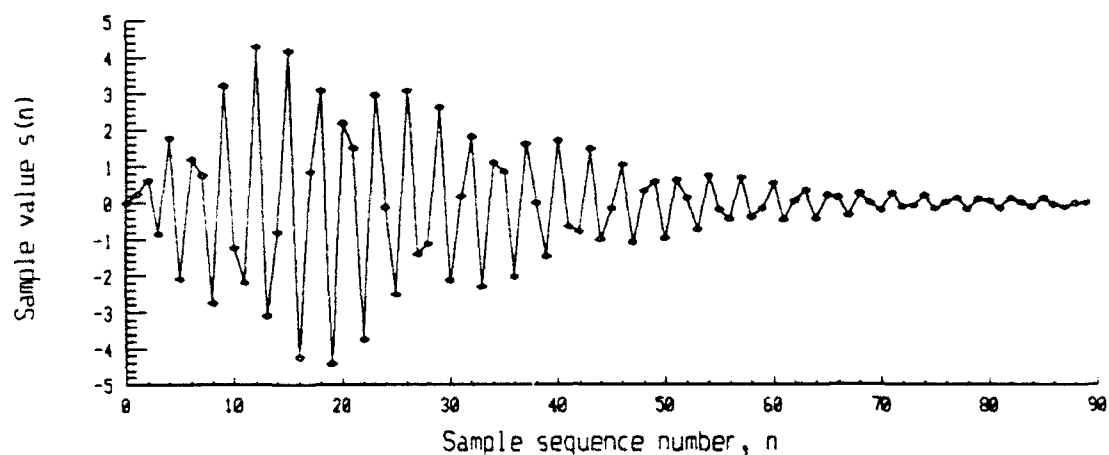


Figure 3.28b--Medium-frequency channel decimator output for 256-point test sequence generated by (3.47) applied to three-channel filter bank of Figure 3.25.

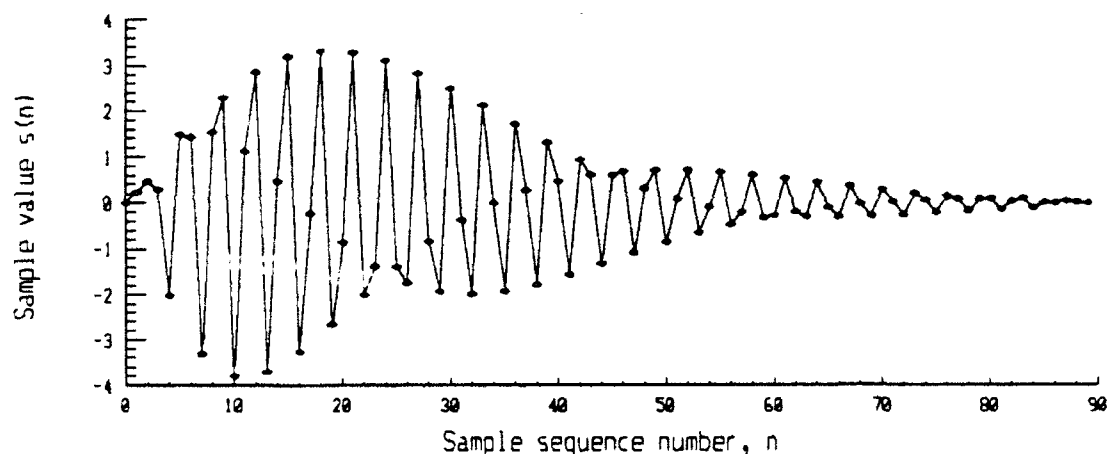


Figure 3.28c--High-frequency channel decimator output for 256-point test sequence generated by (3.47) applied to three-channel filter bank of Figure 3.25.

In the case of the low-frequency channel, the analysis filter transmits only that portion of the power spectral density of the test sequence which lies in the region $[0, \pi/3]$. As discussed during the development of (3.36) and (3.37), because of decimation, the content of the region $[0, \pi/3]$ will be linearly redistributed over the region $[0, \pi]$. The spectral peak passed through the low-frequency channel is, as a result, translated from its original location at $2\pi \cdot 27/256$

($\approx 0.105 \cdot f_s$) to an apparent, post-decimation location of $2 \cdot \pi \cdot 81/256$ ($\approx 0.316 \cdot f_{s\downarrow 3}$). Similarly, the spectral peak contained in the medium-frequency channel is translated from its original location at $2 \cdot \pi \cdot 55/256$ ($\approx 0.215 \cdot f_s$) to an apparent, post-decimation location of $2 \cdot \pi \cdot 165/256$ ($\approx 0.645 \cdot f_{s\downarrow 3}$). This expectation is confirmed in Figure 3.29 in which the spectral peak of the test-sequence component contained medium-frequency channel appears at the predicted location with an image appearing at $0.355 \cdot f_{s\downarrow 3}$. Finally, the test-sequence component passed through the high-frequency channel, originally appearing at a location of $2 \cdot \pi \cdot 113/256$ ($\approx 0.414 \cdot f_s$), after decimation, assumes an apparent position of $2 \cdot \pi \cdot 339/256$ ($\approx 1.324 \cdot f_{s\downarrow 3}$). Because of aliasing, this component, in Figure 3.29, is indicated at $2 \cdot \pi \cdot 339/256 - 2 \cdot \pi \cdot 256/256 = 2 \cdot \pi \cdot 83/256$ ($\approx 0.324 \cdot f_{s\downarrow 3}$).

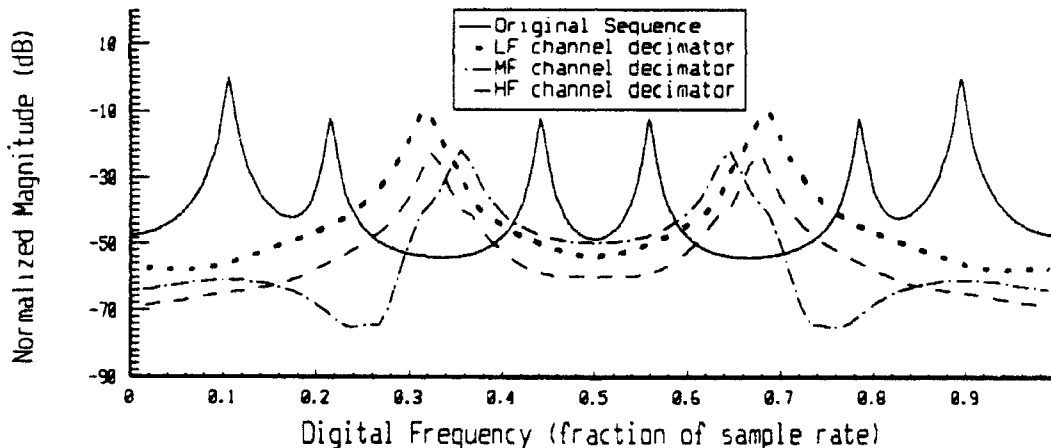


Figure 3.29--Superimposed plots of the power spectral densities of the original sequence and the outputs of each decimator for the 256-point test sequence of (3.47) applied to the three-channel filter bank of Figure 3.25.

In Figures 3.28a, b and c, the zero-crossings of the sequences appear to occur at similar frequencies. This observation is confirmed by plots of the decimator output spectral densities superimposed in Figure 3.29. In fact, for the case under consideration, the spectral peaks of the

decimator outputs are separated by a maximum of $0.5 \cdot f_s$. This example provides insight into the nature of the decimation operator. In general, decimation transforms a narrowband process such that the result "fills" the spectrum below the Nyquist frequency of the channel.

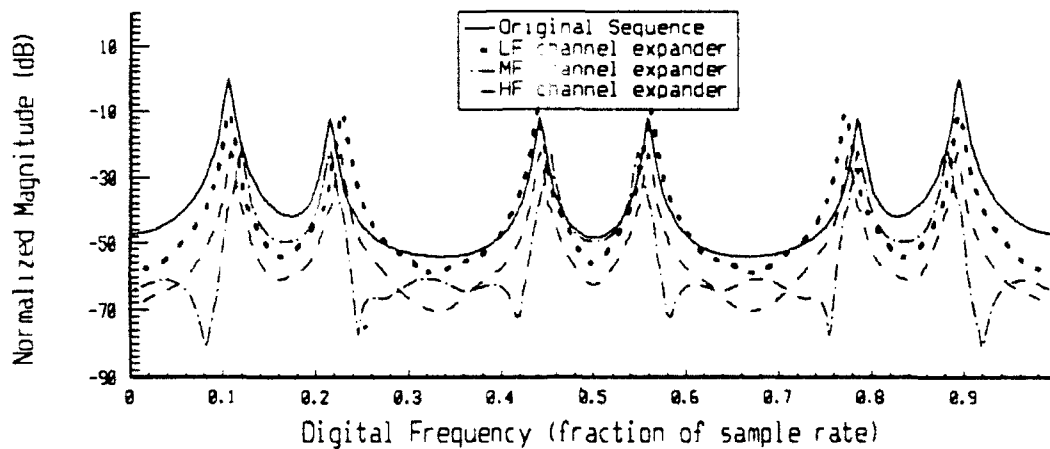


Figure 3.30--Superimposed plots of the power spectral densities of the original sequence and the expander outputs for each channel of the three-channel filter bank of Figure 3.25.

The power spectral densities for the expander outputs for each channel of the filter bank represented by Figure 3.25 are plotted in Figure 3.30 above. As predicted by (3.38), application of the expansion operator to a decimated sequence imposes two consequences. First, the effective sampling frequency of a decimated sequence is related to the sampling frequency of the original sequence by

$$[f_{s \downarrow 3}]_{\uparrow 3} = 3 \cdot f_{s \downarrow 3} = f_s,$$

in the case of expansion by a factor of three. Secondly, the aliasing terms generated by decimation, which are originally outside of the region $[0, 2 \cdot \pi]$, are translated to within the region $[0, 2 \cdot \pi]$.

In the case of the test sequence generated by (3.74), two aliasing components in addition to the desired component have appeared in each channel. For each channel, the aliasing components appear at integer translates of $2\cdot\pi/3$ with respect to the restored component of the original sequence. Because the spectral peaks of the original signal were separated from each other by roughly $\pi/3$, each aliasing term generated for each component coincides fairly closely with one of the other components. This occurrence is reflected in Figure 3.30.

In the low-frequency channel, the location of the peak of the spectral component has been restored to its original location of $2\cdot\pi\cdot 27/256=2\cdot\pi\cdot 81/768$. However it is accompanied by aliasing terms at $2\cdot\pi\cdot 337/768 (\approx 0.438\cdot f_s)$ and $2\cdot\pi\cdot 593/768 (\approx 0.772\cdot f_s)$ whose image appears at $2\cdot\pi - 2\cdot\pi\cdot 593/768 = 2\cdot\pi\cdot 175/768$. The restored medium-frequency-channel component, which reappears at $2\cdot\pi\cdot 55/256=2\cdot\pi\cdot 165/768$, is accompanied by aliasing terms at $2\cdot\pi\cdot 421/768 (\approx 0.548\cdot f_s)$ whose image is present at $2\cdot\pi\cdot 347/768 (\approx 0.452\cdot f_s)$ and at $2\cdot\pi\cdot 677/768 (\approx 0.882\cdot f_s)$ which has an image at $2\cdot\pi\cdot 91/768 (\approx 0.1185\cdot f_s)$. Finally, to the restored component for the high-frequency channel which is located at $2\cdot\pi\cdot 113/256=2\cdot\pi\cdot 339/768$, are added aliasing terms at $2\cdot\pi\cdot 595/768 (\approx 0.775\cdot f_s)$ for which an image appears at $2\cdot\pi\cdot 173/768 (\approx 0.225\cdot f_s)$ and at $2\cdot\pi\cdot 83/768 (\approx 0.1098\cdot f_s)$.

Figures 3.31a superimposes plots of the outputs of the synthesis filters for each channel of the filter bank of Figure 3.25. Each plot indicates the spectral content of the corresponding channel. The results of the recombination of the channels are plotted in Figure 3.31b. In Figure

3.31a, it is apparent that the aliasing components of the expander outputs have not been completely blocked by the synthesis filters. In the worst case, for the spectral region containing the medium-frequency channel, residual energy from an aliasing component is only approximately 20 dB below the desired spectral peak for that channel. However, upon examination of Figure 3.31b, it becomes apparent that *alias cancellation* does occur. The power spectral density of the reconstructed sequence very closely coincides with that of the original sequence.

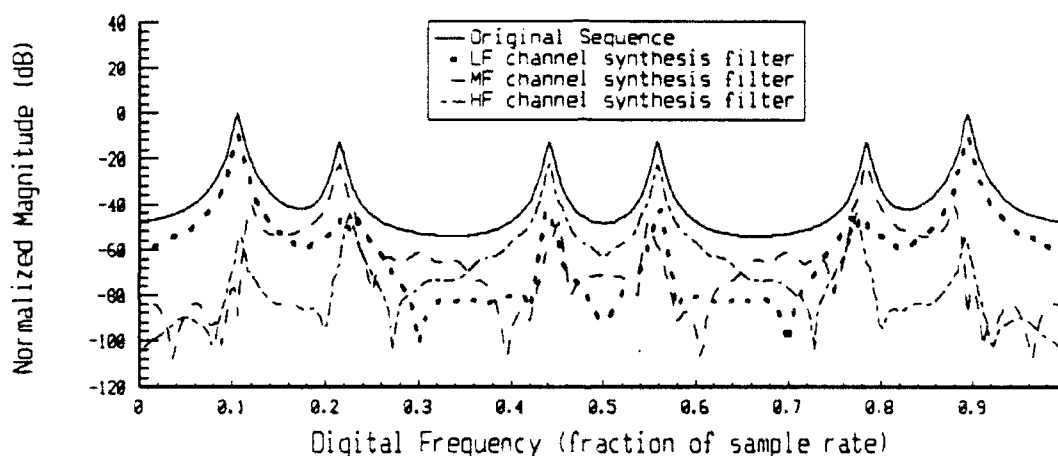


Figure 3.31a--Superimposed plots of the power spectral densities of the original sequence and of the expander outputs for each channel of the three-channel filter bank of Figure 3.25.

Figure 3.32 presents a time plot of the reconstructed sequence. Again, the reconstructed sequence appears to be an approximate delay of the original sequence. In fact, when the signals are synchronized, the normalized mean-square error (3.32) of the reconstructed signal is -66.94 dB. The the reconstruction error exceeds that of the two-channel demonstration of Section C because of the poorer quality of the filters with which the three-channel filter bank of Section D has been implemented. As indicated by Figure 3.26, the equivalent impulse response of the

three-channel filter bank deviates from a pure delay by a margin three orders of magnitude greater than the deviation for the two-channel filter bank.

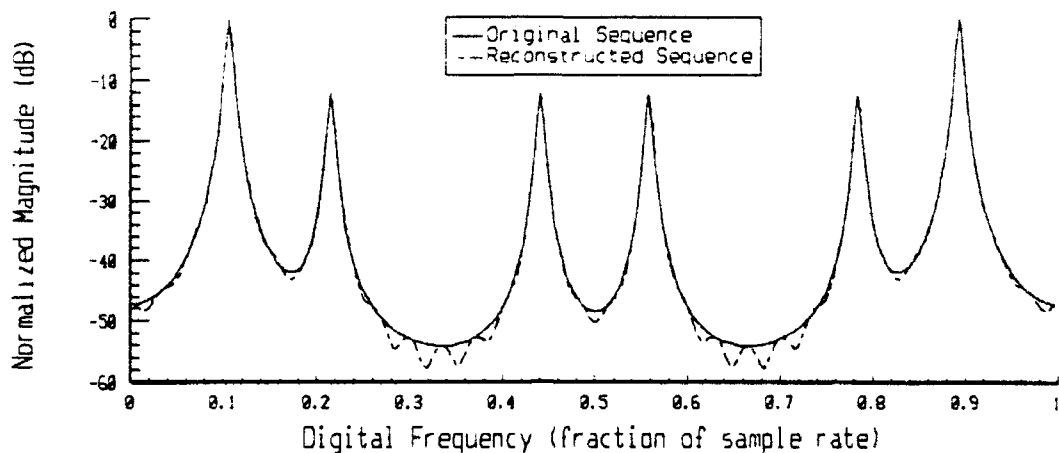


Figure 3.31b--Superimposed plots of power spectral densities of original sequence generated by (3.47) and of sequence reconstructed by three-channel filter bank of Figure 3.25.

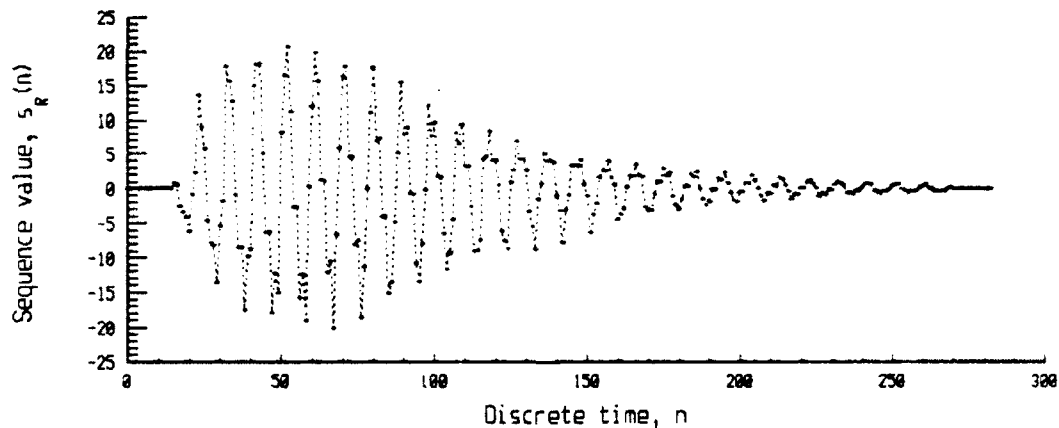


Figure 3.32--Time plot of reconstructed version of 256-point test sequence applied to three-channel filter bank of Figure 3.25.

IV. THE THEORY OF MULTIREOLUTION SIGNAL PROCESSING

A. INTRODUCTION

Having, in the preceding two chapters, laid the necessary groundwork, the theory of multiresolution signal processing will next be considered. In this chapter, Section B, presents the concept of multiresolution analysis. In Section C, Mallat's multiresolution algorithm will be developed from a projection operator perspective and the equivalence of multiresolution mathematical operations and two-channel QMF banks will be demonstrated. Section D will outline the development of the Laplacian pyramid and the À Trous algorithm, two of the earliest multiresolution decomposition techniques. In Section E, multiresolution structures comprised of cascades of filter banks will be constructed and demonstrated.

Signal processing techniques commonly entail decomposing a signal by representing it in terms of its projection on a vector space. The most common method, the Fourier Transform, defined in Chapter II:

$$\hat{f}(\omega) = \mathcal{F}\{f(t)\} = \int_{-\infty}^{\infty} f(t) e^{-j\omega t} dt . \quad (4.1)$$

In analyzing a time-varying signal, however, (4.1) presents an obvious disadvantage: Only one representation vector is used for all time. Consequently, time-varying aspects of $f(t)$ are averaged over all time and lost. To address this shortcoming, the concept of the *Short-Time Fourier Transform* (STFT) was developed [14]:

$$F(\omega, \tau) \triangleq \int_{-\infty}^{\infty} f(t) w(t - \tau) e^{-j\omega t} dt . \quad (4.2)$$

Equation (4.2), through the introduction of a window function $w(t)$, improves on (4.1).

Typically, the window a function is either strictly time-limited or possesses a rate of decay such that its value outside of a limited, contiguous region is negligible. Additionally, equation (4.2) can be interpreted as the projection of the signal of interest on modulations and translations of a vector $w(t)$. Employing concepts from Chapter II, (4.2) can be interpreted as a mapping from a one-dimensional space of real numbers to a two-dimensional space of real numbers, or,

$$F: \mathbb{R} \rightarrow \mathbb{R}^2.$$

Additionally, the representation vector $r(\omega, \tau)$ for the projection operator F , the operation of (4.2) is

$$r(\omega, \tau) = w(t - \tau) e^{-j\omega t} \quad (4.3)$$

In the branch of mathematics known as *group theory*, the operation (4.2) belongs to a particular class of operators known as the *Weyl-Heisenberg Group* [15]. A group is a set of transformations satisfying the properties of closure, associativity, identity and invertibility [16, 17]. The Weyl-Heisenberg Group consists of a family of transform operators characterized by modulation and translation of a single representation vector [18].

Although it is commonly employed, two shortcomings of the STFT have been asserted. The representation vectors for (4.2) represent a frame in the sense described in Chapter II [6]. Therefore, if it is necessary invert the transform in order to reconstruct a signal from its STFT decomposition, a dual operator must be constructed. Secondly, a sampled, discretized STFT operator partitions an analyzed function's two-dimensional conjugate space into uniform, rectangular partitions [19]. In the conjugate space, the spectral bin partition dimensions are

inflexibly dependent upon the window function $w(t)$ and to not vary with either translation or modulation. Many processes (for example, biological processes) can be characterized by components whose bandwidths increase with frequency. Consequently, (4.2) provides representation which is less than optimum processes comprised of spectral components of varying bandwidths [20].

For the reasons described above, alternative methods of signal decomposition have been suggested. Instead of a representation vector of the form (4.3), employment of a representation based on a family of functions [21]

$$\Psi_{a,b}(t) = |a|^{-1/2} \Psi\left(\frac{t-b}{a}\right) \quad (4.4)$$

produces a transformation $\mathcal{W}: \mathbb{R} \rightarrow \mathbb{R}^2$ such that

$$\mathcal{W}\{f(t)\} = W(a, b) = |a|^{-1/2} \int_{-\infty}^{\infty} f(t) \Psi^*\left(\frac{t-b}{a}\right) dt. \quad (4.5)$$

Similar to the STFT, transformations of the form of (4.5) also comprise a distinct class in the field of group theory. Transformations based on scaling and translation of a common representation vector comprise the *affine group* [18].

If, as in the case of digital signal processing, it is desired to restrict the transform to a lattice of discrete points, the representation vector becomes

$$\Psi_{m,n}(t) = a_0^{-m/2} \Psi(a_0^{-m} t - n b_0). \quad (4.6)$$

The representation (4.6) results in a transformation $\mathcal{W}: \mathbb{R} \rightarrow \mathbb{Z}^2$, where \mathbb{Z} is the set of all integers, such that

$$\mathcal{W}\{f(t)\} = w(m, n) = a_0^{-m/2} \int_{-\infty}^{\infty} f(t) \Psi^*(a_0^{-m} t - n b_0) dt. \quad (4.7)$$

Additionally, (4.6) constitutes a version of (4.4) sampled at $a = a_0^m$ for $a_0 > 1$ and at $b = n \cdot b_0 \cdot a_0^m$ for $b_0 \neq 0$. To conform to the conventions of octave-band filtering, a_0 is typically selected as $a_0=2$. The selection of b_0 determines whether $\{\psi_{m,n}\}_{n \in \mathbb{Z}}$ constitutes an incomplete set, a complete orthogonal set, or a frame. The representations of greatest interest to multiresolution signal processing are chosen such that $b_0 = 1$, providing unit translations with respect to sampled data.

The time-frequency properties of the representation vector $\psi_{m,n}$ address some of the shortcomings sometimes ascribed to the STFT representation. As the scaling integer m increases, the representation $\psi_{m,n}$ becomes more and more spread in the time domain, and, consequently, more concentrated in the frequency domain. Consequently, projection on a highly dilated vector function will provide poor time resolution but sharp frequency resolution. Decreasing m causes the reverse effect: Concentration in time and spreading in the frequency domain. In the case of a highly contracted representation vector, the transform operator provides sharp temporal resolution but poorer spectral resolution. Furthermore, the spreading effect of the representation $\psi_{m,n}$ occurs in a logarithmic manner. The bandwidth of the representation $\psi_{m,n}$ will be proportional to its center frequency.

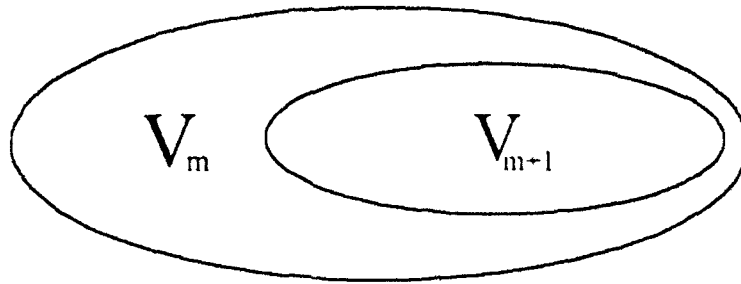


Figure 4.1--Venn diagram illustration of concept of embedded vector spaces. After [24].

B. THEORY OF MULTIREOLUTION ANALYSIS

In order to characterize the vector spaces consisting of the span of $\{\psi_{m,n}\}_{m,n \in \mathbb{Z}}$, it is first necessary to consider another set of basis functions $\{\phi_{m,n}\}_{n \in \mathbb{Z}}$ which spans another set of vector spaces $\{V_m\}_{m \in \mathbb{Z}} \in L^2(\mathbb{R})$. The operator A_{m-1} is defined as the projection of some function $f(t)$ on V_m :

$$A_{m-1}\{f(t)\} \triangleq \sum_n \left(f, \phi_{m,n} \right) \phi_{m,n}(t). \quad (4.8)$$

To be a *multiresolution analysis*, the set of operators $\{A_m\}$ must satisfy six properties [22,23]:

1. A_{m-1} is a linear operator which uniquely and completely approximates $f(t)$ at a resolution of 2^m . Consequently, the approximation

$$A_{m-1}\{A_{m-1}\{f(t)\}\} = A_{m-1}\{f(t)\}. \quad (4.9)$$

In words, $A_{m-1}\{f(t)\}$ contains all of the information about $f(t)$ which can be obtained at a resolution 2^m . Repeated projection upon V_m does not add or subtract any information to $A_{m-1}\{f(t)\}$.

2. Of all possible functions which exist at a resolution of 2^m , $A_{m-1}\{f(t)\}$ is the function which most closely resembles $f(t)$:

$$\forall g(t) \in V_m, \quad \|g(t) - f(t)\| \geq \|A_{m-1}\{f(t)\} - f(t)\|. \quad (4.10)$$

3. Approximation of some signal $f(t)$ at one resolution 2^m contains all information necessary to approximate it at the next resolution 2^{m-1} . This concept suggests a family of embedded, closed subspaces:

$$V_{m-1} \subset V_m \in L^2(\mathbb{R}) \quad \forall m \in \mathbb{Z}. \quad (4.11)$$

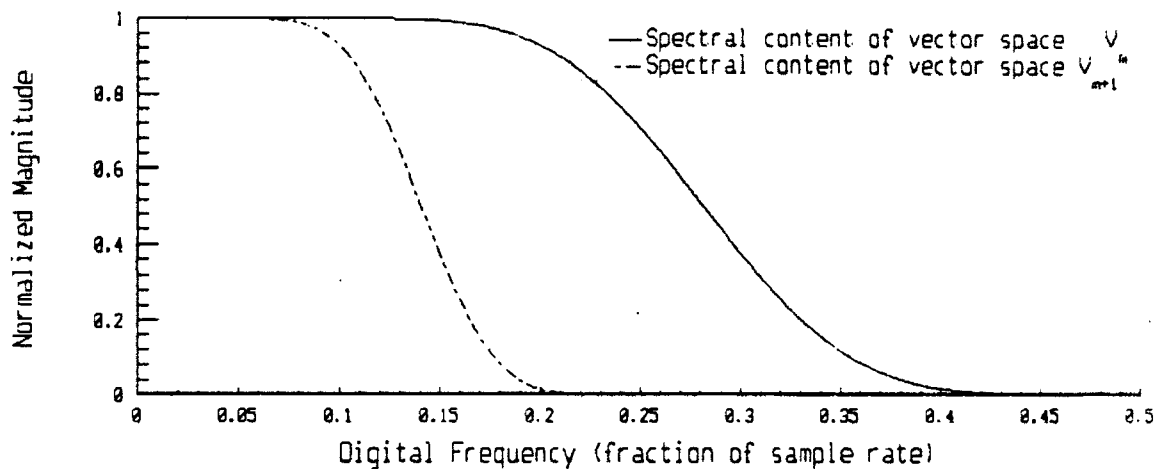


Figure 4.2--Spectral illustration of concept of embedded vector spaces. The vector spaces represented are based on Daubechies' orthonormal scaling function on $[0, 11]$. After [25].

Illustration of the concept of embedded spaces can be accomplished by either of two methods. The first illustration is via Venn diagram. In Figure 4.1, the embedded ellipses illustrate two related vector spaces. The outer ellipse represents the span of the vector space V_m and the inner ellipse the span of vector space V_{m-1} . As indicated by the diagram, the information which can be extracted from projection on vector space V_{m-1} is less than what can be extracted

from projection on vector space V_m . The two spaces differ by the information lost when some function $f(t)$ is approximated at 2^{m+1} instead of at 2^m . The vector space V_m possesses a greater density than the vector space V_{m+1} . Consequently, the approximation at 2^m will contain a greater quantity of information about the original function than the approximation at 2^{m+1} .

Figure 4.2 provides an illustration of the concept of embedded subspaces from the perspective of partitioning of the frequency spectrum. The lower half-band represents the vector space V_m while the lower fourth-band represents V_{m+1} . Approximation $A_{m+1}\{f(t)\}$ at resolution 2^m , therefore, entails an approximation based on the spectral components of $f(t)$ contained in the lower half of the frequency spectrum below the Nyquist frequency. Similarly, approximation at a resolution 2^{m+1} entails a representation based on the lower fourth of the frequency spectrum below the Nyquist frequency. Consequently, an approximation of $f(t)$ based on Figure 4.2 at resolution 2^m contains only the spectral content of $f(t)$ in the range $[0, \pi/2]$. An approximation of $f(t)$ at resolution 2^{m+1} contains only the spectral content of $f(t)$ in the range $[0, \pi/4]$.

4. The approximation operation is similar at all resolutions. The spaces of approximated functions can, therefore, be derived from one another by scaling each approximated function:

$$\forall m \in \mathbb{Z}, f(t) \in V_m \Leftrightarrow f(2 \cdot t) \in V_{m+1}. \quad (4.12)$$

5. The approximation $A_{m+1}\{f(t)\}$ of a signal can be characterized by 2^m samples per unit interval. When $f(t)$ is translated by an amount proportional to 2^{-m} , $A_{m+1}\{f(t)\}$ is translated

by the same amount and is characterized by translations of the vector space projections.

More simply,

$$\forall n \in \mathbb{Z}, f(t) \in V_m \Leftrightarrow f(t-2^{-m}n) \in V_m. \quad (4.13)$$

Equations (4.12) and (4.13) suggest a family of basis functions $\phi_{m,n}(t)$ similar to that characterized by (4.6):

$$\phi_{m,n}(t) = 2^{-m/2} \phi(2^{-m}t - n) \quad \forall m, n \in \mathbb{Z}^2. \quad (4.14)$$

The vector space $\{\phi_{m,n}\}_{n \in \mathbb{Z}} \in V_m$ consists of integer translates of $\phi_{m,n}$. (The t-dependence has been suppressed for compactness of notation.) The approximation operator $A_{m-1}\{f(t)\}$ is simply a projection of $f(t)$ in the space of the vectors $\{\phi_{m,n}\}$. Additionally, (4.12) reinforces the concept illustrated in Figure 4.2. Equation (3.7) indicates that a time-domain contraction of a signal causes a dilation--or spreading--of that signal's frequency spectrum. The frequency spectrum of V_{m-1} , therefore, occupies half of the bandwidth of the frequency spectrum of V_m . Furthermore, if the space spanned by V_m coincides with a lowpass region of the frequency spectrum, V_{m-1} will also coincide with a lowpass region.

Finally, one additional property remains to complete the definition of a multiresolution analysis:

6. A continuous function $f(t)$ can be initially considered to be represented with infinite resolution. Regardless of the scale, all information regarding $f(t)$ is originally assumed to be known. Applying the approximation $A_m\{f(t)\}$ results in some loss of information.

Increasing the degree of coarseness of A_m increases the amount of lost information.

Consequently,

$$\lim_{m \rightarrow -\infty} V_m = \bigcup_{k=-\infty}^{\infty} V_k = L^2(\mathbb{R}) \quad (4.15a)$$

and

$$\lim_{m \rightarrow \infty} V_m = \bigcap_{k=-\infty}^{\infty} V_k = \{ 0 \}. \quad (4.15b)$$

Equations (4.15a) and (4.15b) follow, by induction, directly as consequences of (4.11).

Equation (4.15a) states that, because of (4.11), the manner in which $\{V_m\}_{m \in \mathbb{Z}}$ are related to each other, $\lim_{m \rightarrow -\infty} V_m$ consists of the union of the spans of all $\{V_m\}_{m \in \mathbb{Z}}$. By induction from (4.11), all vector spaces $\{V_m\}_{m \in \mathbb{Z}}$ are subsets of $\lim_{m \rightarrow -\infty} V_m$. Using the notation of set theory, the concept behind (4.15a) is expressed as

$$\{V_m\}_{m \in \mathbb{Z}} \subset \lim_{m \rightarrow -\infty} V_m.$$

Consequently, adding to (4.15a) the concept expressed by (4.12), as the resolution of an approximation A_{m-1} , the projection on vector space V_m , becomes infinite, it is possible to represent $f(t)$ with arbitrary precision. Furthermore, employing a concept from Chapter II, $\lim_{m \rightarrow -\infty} V_m$ is *dense* in $L^2(\mathbb{R})$. In other words, given any vector $\phi_{m,n}$, it is possible to find another vector $\phi_{m,k \neq n}$ which is arbitrarily close to $\phi_{m,n}$. Contained within the union of all definable vector spaces $\{V_m\}$ is all the information which is known about a function.

The indication of equation (4.15b) exactly opposite of that of (4.15a). By induction from (4.11), $\lim_{m \rightarrow \infty} V_m$ constitutes the *least common subset* of all of the vector spaces

$\{V_m\}_{m \in \mathbb{Z}}$. Consequently, as the coarseness of the approximation $A_{m-1}(t)$ becomes infinite, all

information about $f(t)$ is lost. From the perspective of Figure 4.2, the portion of the frequency spectrum spanned by $\lim_{m \rightarrow \infty} V_m$ is contained in the closed interval $\left[0, \lim_{m \rightarrow \infty} \frac{\pi}{2^m} \right]$.

Consequently, at the limit, the approximation of $f(t)$ is characterized by only its DC component, or equivalently, $\lim_{m \rightarrow \infty} A_m\{f(t)\}$ becomes a constant-valued function.

Regarding multiresolution analyses, Mallat [22] proved a theorem which provides the theoretical foundation for all further development. The theorem states that, given a multiresolution approximation of $L^2(\mathbb{R})$ by projection on vector space V_m , there exists a unique function $\phi(x) \in L^2(\mathbb{R})$, called a *scaling function*, such that $\{\phi_{m,n}(x)\}_{n \in \mathbb{Z}}$ as defined by (4.14) constitutes an orthonormal basis of V_m . That is,

$$\left(\phi_{m,n}, \phi_{m,k} \right) = \delta_{k,n} \quad \forall n, k \in \mathbb{Z}. \quad (4.16)$$

Furthermore, V_m consists of the closed, linear span of $\{\phi_{m,n}\}_{n \in \mathbb{Z}}$.

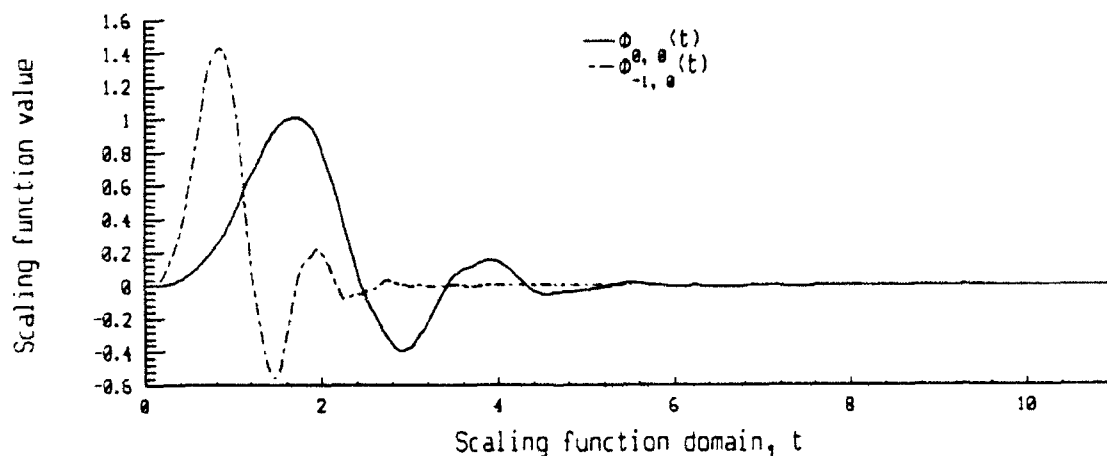


Figure 4.3--Superimposed plots of Daubechies' orthonormal scaling function $\phi_{0,0}(t)$ supported on $[0, 11]$ and of $\phi_{1,0}(t)$.

To characterize the relationship between the scaling function spaces $\{V_m\}$, it is useful to examine the projections of their vectors onto each other. From (4.11), (4.12) and (4.13), it is evident that

$$\phi_{m-1,n}(t) \in V_{m-1} \Leftrightarrow \phi_{m-1,n}(t) \in V_m \quad (4.17)$$

or equivalently, $\phi_{m-1,n}$ lies within the span of $\{\phi_{m,n}\}$. Figure 4.3 provides an illustration of a scaling function at two adjacent scales. The example presented is based on Daubechies' orthonormal scaling function supported on $[0, 11]$. $\phi_{1,0}(t)$ is obviously a contracted version of $\phi_{0,0}(t)$ with its amplitude increased by a factor of $\sqrt{2}$. Because of (4.17), the Fourier series theorem (2.17) can be applied to obtain

$$\phi_{m+1,n}(t) = \sum_k \left(\phi_{m+1,n}, \phi_{m,k} \right) \phi_{m,k}(t). \quad (4.18)$$

Substituting (4.14), the definition of $\phi_{m,n}$, into the inner product term of the summation (4.18) and applying a change of variables to evaluate the resulting integral produces [22]

$$\left(\phi_{m+1,n}, \phi_{m,k} \right) = \frac{1}{\sqrt{2}} \cdot \left(\phi_{1,0}, \phi_{0,k-2n} \right). \quad (4.19)$$

Equation (4.19) clearly indicates that the coefficients of the series (4.18) are independent of scale m . The summation (4.18), therefore, becomes

$$\phi_{m+1,n}(t) = \frac{1}{\sqrt{2}} \sum_k \left(\phi_{1,0}, \phi_{0,k-2n} \right) \cdot \phi_{m,k}(t). \quad (4.20)$$

Next, substituting (4.14) for the appropriate terms on each side of (4.20) results in

$$2^{-(m+1)/2} \phi(2^{-(m+1)}t - n) = \frac{1}{\sqrt{2}} \cdot 2^{-m/2} \sum_k \left(\phi_{1,0}, \phi_{0,k-2n} \right) \cdot \phi(2^{-m}t - k). \quad (4.21)$$

Applying the change of variables $u = 2^{-m} \cdot t - 2 \cdot n$ and the translation of indices $k = k' - 2 \cdot n$ to (4.21)

finally yields

$$\phi(u) = \sum_k \left(\phi_{1,0}, \phi_{0,k-2n} \right) \phi(2u - k). \quad (4.22)$$

For later convenience, (4.22) can be rewritten as

$$\frac{1}{2} \phi\left(\frac{u}{2}\right) = \sum_k h(k) \phi(u - k) \quad \text{where} \quad h(k) \triangleq \frac{1}{2} \left(\phi_{1,0}, \phi_{0,k} \right). \quad (4.23)$$

Selecting this normalization for $h(k)$ forces $\sum_k h(k) = 1$. As a result,

$$\left| \sum_k h(k) e^{j\omega} \right|_{\omega=0} = \left| H(e^{j\omega}) \right|_{\omega=0} = 1.$$

Furthermore, since $\phi(u)$ is real, $\{h(k)\}_{k \in \mathbb{Z}}$ is real. And finally, if $\phi(u)$ is compactly supported, then the filter $h(k)$ is a FIR filter. This occurs since, for compactly supported ϕ , in the inner product term of (4.23), there will be only a finite number of translations which will be evaluated as non-zero. The details of the development of (4.19) - (4.23) are presented in Appendix A.

Equations of the form (4.23) comprise in literature a class of equations referred to as *two-scale difference equations* [26] or as *dilation equations* [27]. This class of equations will be considered in greater detail in Chapter V within the context of basis functions for multiresolution analyses. From the preceding development it may be concluded that the functions ϕ which satisfy the properties for a multiresolution analysis consist of solutions to two-scale difference equations.

To obtain a multiresolution transform it is necessary to combine (4.20) with (4.23) to obtain

$$\phi_{m+1,n}(t) = \sqrt{2} \sum_k h(k-2n) \phi_{m,k}(t). \quad (4.24)$$

Applying Parseval's equality (2.18) to (4.24) results in a relationship between the projections of some function $f(t)$ onto V_m and V_{m+1} [22]:

$$(f, \phi_{m+1,n}) = \sqrt{2} \sum_k h(k-2n) (f, \phi_{m,k}). \quad (4.25)$$

By (4.25), given $A_{m+1}\{f\}$, the determination of the coefficient $(f, \phi_{m+1,n})$ for each term of the series for $A_{m+1}\{f\}$, requires *filtering and decimation* of the sequence $\{(f, \phi_{m,n})\}_{n \in \mathbb{Z}}$. The block diagram for the operation (4.25) is depicted in Figure 4.4. The similarity between Figure 4.4 and a channel of a QMF analysis bank is evident.

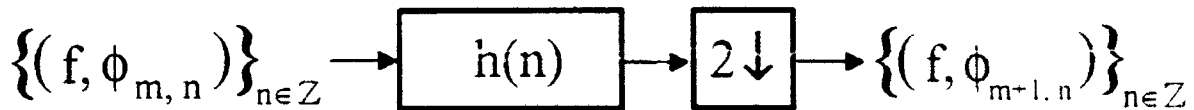


Figure 4.4--Block diagram of multiresolution transform characterized by (4.25).

Now, to complete the development of the concept of multiresolution analysis it is first necessary to consider some of the consequences of the preceding development. First, consider the concept of embedded subspaces characterized by (4.11). Let W_m be the orthogonal complement of V_m such that

$$V_m \cap W_m = \emptyset \quad (4.26a)$$

and

$$V_m \oplus W_m = V_{m+1}. \quad (4.26b)$$

From (2.26b), by induction, any scaling function vector space V_J can be decomposed as [23]

$$V_J = \bigoplus_{m=J+1}^{\infty} W_m. \quad (4.27)$$

And finally, the direct sum of all definable $\{W_m\}_{m \in \mathbb{Z}}$ is dense in $L^2(\mathbb{R})$ [21]:

$$\bigoplus_{m=-\infty}^{\infty} W_m = L^2(\mathbb{R}). \quad (4.28)$$

Figure 4.5 presents a two-scale example of (4.26b) from the perspective of spectral contents of V_m and W_m . The complementary subspace W_m is defined such that it is closed and is spanned by a set of vectors $\{\psi_{m,n}\}_{n \in \mathbb{Z}}$. Members of the set of vectors $\{\psi_{m,n}\}$ are related to each other in a manner similar to (4.14):

$$\psi_{m,n}(t) = 2^{-m/2} \psi(2^{-m} t - n) \quad \forall m, n \in \mathbb{Z}^2 \quad (4.29)$$

Overlap exists between the spectral regions characterizing V_{m-1} and W_{m-1} . This overlap occurs since the plots consist of frequency plots of FIR filters. However the FIR filters represented are related to orthogonal basis function and consequently, the filters for V_{m-1} and W_{m-1} are themselves orthogonal to each other in the time domain.

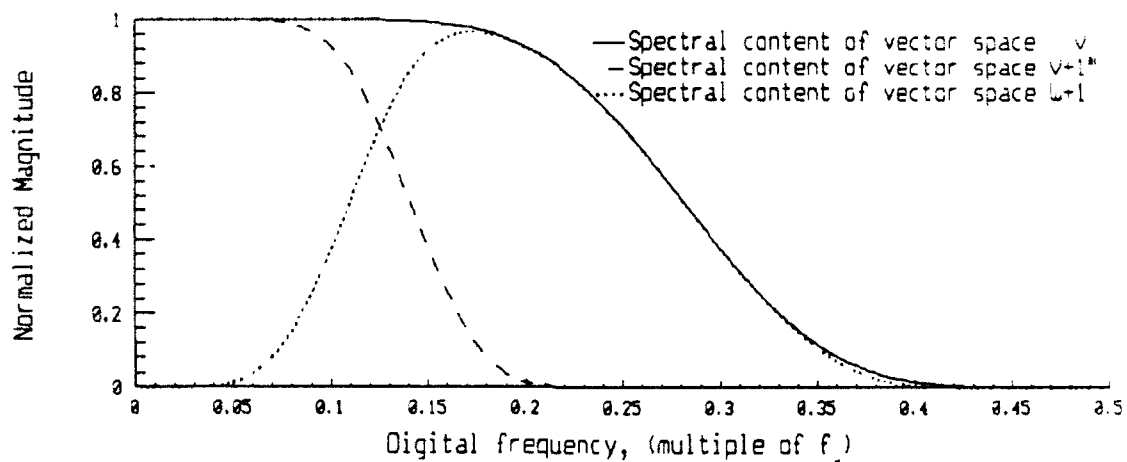


Figure 4.5--Spectral content of example of concept of orthogonally complementary, embedded subspaces. The example is based upon Daubechies' wavelet and scaling function on $[0, 11]$. The lowpass processes are $\phi_{m,n}$ and $\phi_{m-1,n}$ and the bandpass process is $\psi_{m-1,n}$

The set of vectors $\{\psi_{m,n}\}_{n \in \mathbb{Z}}$ constitutes the set of *wavelet functions* for the multiresolution analysis. From the relationships between the spaces W_m of wavelet vectors $\psi_{m,n}$ and the spaces V_m of scaling function vectors $\phi_{m,n}$ a number of relationships between the sets of vectors $\phi_{m,n}$ and $\psi_{m,n}$ may be deduced. Between the scaling and wavelet function vectors, follows from (4.26a), the relationship exists:

$$(\phi_{m,n}, \psi_{m,k}) \equiv 0. \quad (4.30)$$

Within a common scale, therefore, wavelets and scaling functions are orthogonal to each other. Furthermore, as a consequence of (4.11) and (4.26b),

$$(\psi_{m,n}, \psi_{j,k}) = \delta_{j,m} \delta_{k,n}. \quad (4.31)$$

In words, unlike scaling functions which are only orthogonal to each other with respect to translation within a common vector space V_m , wavelets are orthogonal to each other with respect to translation and scale. Wavelets not contained within the same vector space W_m are by definition orthogonal to each other. Finally, because $\psi_{m,n} \in W_m \subset V_{m-1}$,

$$(\phi_{m,n}, \psi_{k,n}) \neq 0, \quad \forall k \leq m-1.$$

More generally, if the wavelet $\psi_{k,j}$ is supported on the interval $[0, L] \in \mathbb{R}$, then,

$$(\phi_{m,n}, \psi_{k,j}) \neq 0, \quad \forall k \leq m-1, \quad |n-j| < L. \quad (4.32)$$

Wavelet vectors lie within the span of higher resolution spaces of scaling functions.

The projection of some signal $f(t)$ on the wavelet space W_m constitutes the *detail signal* [22] and contains the difference of the information contained in $A_{m-1}\{f\}$ and that in $A_m\{f\}$. The detail signal at resolution m is denoted by

$$D_{m-1}\{f(t)\} \triangleq \sum_k \left(f, \psi_{m,n} \right) \psi_{m,n}(t). \quad (4.33)$$

Equation (4.26b) implies that [21]

$$D_m\{f\} = A_{m-1}\{f\} - A_m\{f\}, \quad (4.34a)$$

or equivalently,

$$\sum_n \left(\psi_{m+1,n}, f \right) \psi_{m+1,n} = \sum_n \left(\phi_{m,n}, f \right) \phi_{m,n} - \sum_n \left(\phi_{m,n}, f \right) \phi_{m+1,n}. \quad (4.34b)$$

Substituting (4.24) into (4.34b) and expanding the result produces a time-domain form for the wavelet decomposition:

$$\sum_n \left(\psi_{m+1,n}, f \right) \psi_{m+1,n} = \sum_n \left[\left(\phi_{m,n}, f \right) \phi_{m,n} - 2 \sum_{j,k} h(k-2n) h(j-2n) \left(\phi_{m,k}, f \right) \phi_{m,j} \right]. \quad (4.35)$$

Obviously, except for simple cases such as the Haar basis (demonstrated in [21]), (4.35) is not easily separable. In order to obtain a relationship between scaling and wavelet functions it therefore becomes necessary to examine their Fourier-domain properties.

Equation (4.22) represents the starting point for considering the frequency-domain properties of the scaling function ϕ . If the Fourier transform of ϕ is defined as in (4.1)

$$\hat{\phi}(\omega) = \int_{-\infty}^{\infty} \phi(t) e^{-j\omega t} dt,$$

evaluating the Fourier transform of each side of (4.23) produces [23]

$$\hat{\phi}(2\omega) = H(e^{j\omega}) \hat{\phi}(\omega) \quad (4.36b)$$

where the Fourier series $H(e^{j\omega})$ of $h(k)$ is defined as

$$H(e^{j\omega}) = \sum_k h(k) e^{-j\omega k}. \quad (4.37)$$

Next, Poisson's summation can be employed to present an alternative expression for the orthogonality of ϕ with respect to translation [23]. This development begins with the complex Fourier series expansion for a train of Dirac impulse functions $\delta(\omega)$ [28]:

$$\sum_k \delta(\omega - 2\pi k) = \frac{1}{2\pi} \sum_k e^{jk\omega}. \quad (4.38)$$

Poisson's summation involves convolving a function with each side of (4.38). Convolving the expression $|\hat{\phi}(\omega)|^2$ with the right-hand side of (4.38) produces

$$|\hat{\phi}(\omega)|^2 * \sum_k \delta(\omega - 2\pi k) = \sum_k |\hat{\phi}(\omega - 2\pi k)|^2. \quad (4.39)$$

Furthermore, convolving $|\hat{\phi}(\omega)|^2$ with the right-hand side of (4.38) results in the expression

$$\begin{aligned} |\hat{\phi}(\omega)|^2 * \sum_k e^{jk\omega} &= \sum_k \int |\hat{\phi}(\xi)|^2 e^{jk(\omega-\xi)} d\xi \\ &= \sum_k e^{jk\omega} \iiint \phi(u)\phi(v) e^{j(v-u)\xi} du dv e^{-jk\xi} d\xi \end{aligned} \quad (4.40)$$

Applying the change of variables of integration $w = v - u$ and regrouping the terms contained in the second line of (4.40) produces

$$|\hat{\phi}(\omega)|^2 * \sum_k e^{jk\omega} = \sum_k e^{jk\omega} \iint \phi(u)\phi(u+w) \int e^{j(w-k)\xi} d\xi du dw. \quad (4.41)$$

Now, since

$$\int e^{j(w-k)\xi} d\xi = 2\pi \delta(w-k),$$

by the integral sifting property of the Dirac delta function $\delta(w)$, (4.41) becomes

$$\begin{aligned} |\hat{\phi}(\omega)|^2 * \sum_k e^{jk\omega} &= 2\pi \sum_k e^{jk\omega} \iint \phi(u)\phi(u+w) du \delta(w-k) dw \\ &= 2\pi \sum_k e^{jk\omega} \int \phi(u)\phi(u+k) du \end{aligned} \quad (4.42)$$

Finally, by (4.16), the integral in the final line of (4.42) is simply $(\phi_{0,0}, \phi_{0,k}) = \delta_{0,k}$ where $\delta_{m,n}$ is Kronecker's delta function. Consequently, the series in the final line of (4.42) contains only one non-zero term: when the index $k = 0$. Therefore,

$$\left| \hat{\phi}(\omega) \right|^2 * \sum_k e^{jk\omega} = 2\pi. \quad (4.43)$$

Substitution of (4.39) and (4.43) back into (4.38) produces

$$\sum_k \left| \hat{\phi}(\omega - 2\pi k) \right|^2 = 1. \quad (4.44)$$

Applying the results of (4.44) to (4.36) yields

$$\sum_k \left| \hat{\phi}(2\omega - 2\pi k) \right|^2 = \sum_k \left| H(e^{j(\omega - \pi k)}) \right|^2 \left| \hat{\phi}(\omega - \pi k) \right|^2 = 1. \quad (4.45)$$

The right-hand side of (4.45) can be expressed as

$$\sum_k \left| H(e^{j(\omega - 2k\pi)}) \right|^2 \left| \hat{\phi}(\omega - 2k\pi) \right|^2 + \sum_k \left| H(e^{j(\omega - (2k+1)\pi)}) \right|^2 \left| \hat{\phi}(\omega - (2k+1)\pi) \right|^2 = 1. \quad (4.46)$$

Since, as a consequence of its definition, $H(e^{j\omega})$ is periodic with respect to 2π , the terms of

$\left| H(e^{j(\omega - 2k\pi)}) \right|^2$ and $\left| H(e^{j(\omega - (2k+1)\pi)}) \right|^2$ can be factored out of the series on the left-hand side of (4.46) producing

$$\left| H(e^{j\omega}) \right|^2 \sum_k \left| \hat{\phi}(\omega - 2k\pi) \right|^2 + \left| H(e^{j(\omega - \pi)}) \right|^2 \sum_k \left| \hat{\phi}(\omega - (2k+1)\pi) \right|^2 = 1. \quad (4.47)$$

The remaining two sums in (4.47) are identical to (4.44) and are evaluated as unity. Therefore,

(4.47) becomes

$$\left| H(e^{j\omega}) \right|^2 + \left| H(e^{j(\omega - \pi)}) \right|^2 = 1. \quad (4.48)$$

Comparing (4.48) with (3.20b) reveals that the frequency response $H(e^{j\omega})$ for the approximation filter defined by (4.23) is power-complementary with a version of itself shifted in the frequency domain by π . Therefore, $H(e^{j\omega})$ either is constant or possesses a half-band frequency response. Furthermore, if the scaling function ϕ is normalized such that

$|\hat{\phi}(0)|^2 = 1$, then, as a consequence of (4.36b),

$$|H(e^{j\omega})|^2 = 1. \quad (4.49)$$

C. MALLAT'S ALGORITHM FOR MULTIREOLUTION ANALYSIS

It remains to characterize the wavelet functions. This can be accomplished by completing the development of the multiresolution decomposition begun in the previous section. The first true multiresolution algorithm was developed by Mallat [22]. Two other techniques will be considered in the next section which were not directly derived from the mathematical definition of a multiresolution analysis (4.8)-(4.13).

The multiresolution decomposition process begins with the projection of a function $f(t)$ on the scaling function space of finest resolution $\{\phi_{0,n}\}_{n \in \mathbb{Z}}$ [21]. The functional expansion appears as

$$f(t) = A_{-1}\{f(t)\} = \sum_n c_{0,n} \phi(t-n) \quad \text{where} \quad c_{0,n} \triangleq \left(f, \phi_{0,n} \right). \quad (4.50)$$

Generally, the decomposition is performed on a sampled data sequence and the scale of the initial approximation is defined such that the first equality in (4.50) holds. Since the basis

vectors $\phi_{0,n} \in V_0$, the original approximation (4.50) is also clearly contained within the span of V_0 .

The next step in the multiresolution decomposition requires the division of the scaling function space V_0 into orthogonally complementary subspaces $V_1 \oplus W_1 = V_0$. Re-arranging (4.34a) leads to

$$A_{-1}\{f(t)\} = A_0\{f(t)\} + D_0\{f(t)\}.$$

Consistent with the definition (4.8) of the approximation transform A_m and the definition (4.33) for the detail transform D_m ,

$$\begin{aligned} A_0\{f\} &\approx \sum_k c_{1,k} \phi_{1,k} \\ &\text{and} \\ D_0\{f\} &\approx \sum_k b_{1,k} \psi_{1,k} \end{aligned}$$

where $c_{1,k} = (f, \phi_{1,k})$ and $b_{1,k} = (f, \psi_{1,k})$. A relationship between $\phi_{1,k}$ and $\phi_{0,n}$ was presented in (4.23). Furthermore, (4.32) showed that $\psi_{1,k}$ lies within the span of V_0 . Consequently, following development analogous to that for (4.23), the Fourier series expression for wavelet function becomes,

$$\frac{1}{2} \psi\left(\frac{u}{2}\right) = \sum_k g(k) \phi(u-k) \quad \text{where} \quad g(k) \stackrel{\Delta}{=} \frac{1}{2} \left(\psi_{1,0}, \phi_{0,k} \right), \quad (4.51a)$$

since

$$\left(\psi_{m+1,n}, \phi_{m,k} \right) = \frac{1}{\sqrt{2}} \left(\psi_{1,0}, \phi_{0,k-2n} \right). \quad (4.51b)$$

Since, if $\psi_{m,n}$ is real, the filter coefficients $\{g(k)\}_{k \in \mathbb{Z}}$ are strictly real. Additionally, Fourier

transformation of (4.51a) produces a relationship analogous to (4.36):

$$\hat{\psi}(2\omega) = G(e^{j\omega}) \hat{\phi}(\omega). \quad (4.51c)$$

Finally, the form of (4.24) for the wavelet function appears as

$$\psi_{m+1,n}(t) = \sqrt{2} \sum_k g(k-2n) \phi_{m,k}(t). \quad (4.52)$$

Applying Parseval's equality (2.18) to (4.24) and (4.52) in order to calculate $c_{1,n}$ and $b_{1,n}$ in terms of $c_{0,n}$ produces

$$c_{1,n} = \sqrt{2} \cdot \sum_k h(k-2n) c_{0,k}$$

and

$$b_{1,n} = \sqrt{2} \cdot \sum_k g(k-2n) c_{0,k}.$$

The approximation based on the expansion of the terms $\{c_{1,n} \cdot \phi_{1,n}\}$ constitutes a "blurred" version of the expansion of the terms $\{c_{0,n} \cdot \phi_{0,n}\}$. The detail which is lost in the approximation $A_0\{f\}$ is contained in an expansion of the terms $\{b_{1,n} \cdot \psi_{1,n}\}$. This process can be repeated as many times as desired. The resultant general expression becomes

$$\begin{aligned} c_{m+1,n} &= \sqrt{2} \cdot \sum_k h(k-2n) c_{m,k} \\ &\text{and} \\ b_{m+1,n} &= \sqrt{2} \cdot \sum_k g(k-2n) c_{m,k} \end{aligned} \quad (4.53)$$

where each successive iteration generates in an approximation of $f(t)$ containing half the resolution of the previous approximation. At each iteration, the approximation and detail of the signal are related to the previous approximation by

$$A_{m+1}\{f\} = A_m\{f\} + D_m\{f\}. \quad (4.54)$$

Furthermore, the operations described by (4.53) closely resemble the analysis bank for the QMF bank structure investigated in the previous chapter. The approximation and detail operations at each resolution consist of filtering a common sequence with two different filters. The output of each filter is then decimated. The resemblance of QMF structure to the operation characterized by (4.53) cannot yet be asserted to be exact since the appropriate relationship between the filters whose impulse responses are $h(k)$ and $g(k)$ yet to be established.

To reconstruct a signal from its decomposition, the definition (4.8) of the approximation operator is employed. The expansion coefficient $c_{m,k}$ is, by definition,

$$c_{m,k} = (A_{m-1}\{f\}, \phi_{m,k}) = (A_m\{f\}, \phi_{m,k}) + (D_m\{f\}, \phi_{m,k}). \quad (4.55)$$

Substituting into (4.55) the expressions for the series A_m and D_m produces

$$c_{m,n} = \sum_k c_{m+1,k} (\phi_{m,n}, \phi_{m+1,k}) + \sum_k b_{m+1,k} (\phi_{m,n}, \psi_{m+1,k}). \quad (4.56)$$

The inner product terms in (4.56) are precisely those encountered in (4.19) and in (4.51b) except that the positions of the translation indices n and k have been reversed. Consequently, (4.56) is equivalent to

$$c_{m,n} = \frac{1}{\sqrt{2}} \cdot \sum_k h(n-2k) c_{m+1,k} + \frac{1}{\sqrt{2}} \cdot \sum_k g(n-2k) b_{m+1,k} \quad (4.57)$$

The operation in (4.57) entails expansion of the detail and approximation series coefficients followed by the application of filters whose impulse responses are the time reversals of those used in (4.53) for signal decomposition. Again, a resemblance to the QMF bank synthesis structure is noteworthy.

Examining the decomposition operation in the frequency domain provides further insight

into the nature of the wavelet functions [23]. First the Fourier transform $\hat{A}_0(\omega)$ of the approximation

$A_{-1}(t)=A_{-1}\{f(t)\}=f(t)$ is expressed by

$$\begin{aligned}\hat{A}_{-1}(\omega) &= \sum_n c_{0,n} \int_{-\infty}^{\infty} \phi_{0,n}(t) e^{-j\omega t} dt \\ &= \sum_n c_{0,n} e^{-j\omega n} \int_{-\infty}^{\infty} \phi(t) e^{-j\omega t} dt \\ &= C_0(e^{j\omega}) \hat{\phi}(\omega)\end{aligned}\quad (4.58)$$

where $C_m(e^{j\omega}) \triangleq \sum_k c_{m,k} e^{-j\omega k}$. Applying similar analysis, $\hat{A}_0(\omega)$ and $\hat{D}_0(\omega)$, the Fourier transforms of the approximation $A_0(t)=A_0\{f(t)\}$ and $D_0(t)=D_0\{f(t)\}$, respectively, appear as

$$\begin{aligned}\hat{A}_0(\omega) &= \sum_k c_{1,k} \int_{-\infty}^{\infty} \phi_{1,k}(t) e^{-j\omega t} dt \\ &= \frac{1}{\sqrt{2}} \sum_k c_{1,k} \int_{-\infty}^{\infty} \phi\left(\frac{t}{2} - k\right) e^{-j\omega t} dt \\ &= \sqrt{2} \sum_k c_{1,k} e^{-j2\omega k} \int_{-\infty}^{\infty} \phi(u) e^{-j\omega 2u} du\end{aligned}\quad (4.59a)$$

$$\hat{A}_0(\omega) = \sqrt{2} C_1(e^{j2\omega}) \hat{\phi}(2\omega)$$

and

$$\hat{D}_0(\omega) = \sqrt{2} B_1(e^{j2\omega}) \hat{\psi}(2\omega) \quad (4.59b)$$

where $B_m(e^{j\omega}) \triangleq \sum_k b_{m,k} e^{-j\omega k}$. By (4.54) therefore, it follows that,

$$\hat{A}_{-1}(\omega) = \hat{A}_0(\omega) + \hat{D}_0(\omega),$$

or equivalently

$$\hat{f}(\omega) = C_0(e^{j\omega}) \hat{\phi}(\omega) = \sqrt{2} C_1(e^{j2\omega}) \hat{\phi}(2\omega) + \sqrt{2} B_1(e^{j2\omega}) \hat{\psi}(2\omega). \quad (4.60)$$

Substitution of (4.36) and (4.51c) into (4.60) produces

$$C_0(e^{j\omega}) \hat{\phi}(\omega) = \sqrt{2} C_1(e^{j2\omega}) H(e^{j\omega}) \hat{\phi}(\omega) + \sqrt{2} B_1(e^{j2\omega}) G(e^{j\omega}) \hat{\phi}(\omega),$$

or, after dropping the common factor of $\hat{\phi}(\omega)$,

$$C_0(e^{j\omega}) = \sqrt{2} C_1(e^{j2\omega}) H(e^{j\omega}) + \sqrt{2} B_1(e^{j2\omega}) G(e^{j\omega}). \quad (4.61a)$$

From their definitions, $C_0(e^{j\omega}) \in L^2([0, 2\pi])$ and is periodic with respect to 2π while $C_1(e^{j2\omega}), B_1(e^{j2\omega}) \in L^2([0, \pi])$ and are periodic with respect to π . Therefore, it follows from (4.61a) that

$$\begin{bmatrix} C_0(e^{j\omega}) \\ C_0(e^{j(\omega+\pi)}) \end{bmatrix} = \sqrt{2} \begin{bmatrix} H(e^{j\omega}) & G(e^{j\omega}) \\ H(e^{j(\omega+\pi)}) & G(e^{j(\omega+\pi)}) \end{bmatrix} \begin{bmatrix} C_1(e^{j2\omega}) \\ B_1(e^{j2\omega}) \end{bmatrix}. \quad (4.61b)$$

From (4.61b), define

$$\mathbf{H}(e^{j\omega}) \triangleq \begin{bmatrix} H(e^{j\omega}) & G(e^{j\omega}) \\ H(e^{j(\omega+\pi)}) & G(e^{j(\omega+\pi)}) \end{bmatrix}.$$

Now, if the $\mathbf{H}(e^{j\omega})$ is unitary in the sense described in Chapter III, then multiplication of each side of (4.61) with its Hermitian transpose yields

$$\left| C_0(e^{j\omega}) \right|^2 + \left| C_0(e^{j(\omega+\pi)}) \right|^2 = 2 \left[\left| C_1(e^{j2\omega}) \right|^2 + \left| B_1(e^{j2\omega}) \right|^2 \right]. \quad (4.62)$$

Integrating (4.62) over the interval $[0, \pi]$ produces

$$\int_0^\pi \left| C_0(e^{j\omega}) \right|^2 + \left| C_0(e^{j(\omega+\pi)}) \right|^2 d\omega = 2 \int_0^\pi \left| C_1(e^{j2\omega}) \right|^2 + \left| B_1(e^{j2\omega}) \right|^2 d\omega$$

which is equivalent to

$$\int_0^{2\pi} \left| C_0(e^{j\omega}) \right|^2 d\omega = 2 \int_0^\pi \left| C_1(e^{j2\omega}) \right|^2 d\omega + 2 \int_0^\pi \left| B_1(e^{j2\omega}) \right|^2 d\omega. \quad (4.63)$$

Equation (4.63) is an expression of the orthogonality of the decomposition: The energy in the approximation $A_0\{f(t)\}$ is simply equal to the sum of the energies in the approximation $A_1\{f(t)\}$ and the detail $D_1\{f(t)\}$. No energy is present in terms comprised of the cross-product

$\left| C_1(e^{j2\omega}) \right| \cdot \left| B_1(e^{j2\omega}) \right|$. Furthermore, the specification of $\mathbf{H}(e^{j\omega})$ as unitary is exactly

equivalent to the specification that the alias compensation matrix for the two-channel QMF bank

is exactly equivalent to the specification that the alias compensation matrix for the two-channel QMF bank be paraunitary. Consequently, a single-stage decomposition followed by a single-stage reconstruction employing Mallat's algorithm is exactly equivalent to a QMF bank. Moreover, the paraunitary nature of $H(e^{j\omega})$ implies

$$\begin{aligned} |H(e^{j\omega})|^2 + |G(e^{j\omega})|^2 &= 1 \\ H(e^{j\omega})G(e^{-j\omega}) + H(e^{j(\omega-\pi)})G(e^{-j(\omega-\pi)}) &= 0 \end{aligned} \quad (4.64)$$

One solution for $G(e^{j\omega})$ as constrained by (4.64) is given by

$$G(e^{j\omega}) = e^{-j\omega L} H(e^{j(\omega-\pi)}) \quad (4.65)$$

where L represents the length of the FIR filter $h(n)$. Selection of (4.65) dictates that the filter whose impulse response is $g(n)$ will be a FIR filter of length L and that, by (4.51c), the wavelet function $\psi(t)$ will have exactly the region of support of the scaling function $\phi(t)$.

D. EARLY MULTIREOLUTION ALGORITHMS

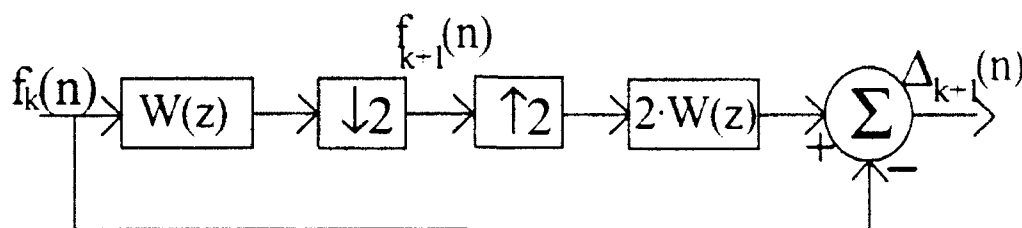


Figure 4.6--Block diagram of process by which detail is extracted from signal through the use of the Laplacian pyramid algorithm. After [29].

In this section, two early multiresolution techniques--the Laplacian pyramid and the à trous algorithm--will be considered. The first, the Laplacian pyramid, represents an algorithm developed in the early 1980's for the purposes of image coding. Conceptually, the Laplacian pyramid very closely resembles Mallat's multiresolution algorithm presented in the previous

section. In fact, Daubechies credits the Laplacian pyramid with providing Mallat with significant for the development of his own multiresolution algorithm [21].

The Laplacian pyramid, as with Mallat's multiresolution algorithm, entails iterative filtering of a sequence to progressively smooth out the rapidly varying components [29]. At any stage, the next coarser approximation is obtained from

$$f_{k+1}(n) = \sum_m w(2n - 1n) f_k(m). \quad (4.66)$$

Unlike Mallat's algorithm, however, where the detail is extracted through filtering, the Laplacian pyramid extracts the detail through re-expanding and filtering the approximation and subtracting the result from the previous approximation. This process is illustrated in Figure 4.6.

Mathematically, extraction of the detail lost $\Delta_{k+1}(n)$ when $f_k(n)$ is approximated as $f_{k+1}(n)$ is expressed as

$$\Delta_{k+1}(n) = f_k(n) - 2 \sum_m w(n - 2m) f_{k+1}(m). \quad (4.67)$$

The series expression on the right-hand side of (4.67) is recognizable as the same form of equation as appeared in (4.57). The form represents expansion of a sequence followed by FIR filtering. The factor of two is introduced to cancel the factor of 1/2 introduced by the decimation operation as indicated by (3.6). As with Mallat's algorithm, iteratively repeating, results in the cascaded tree structure of Figure 4.7a. Reconstruction of a decomposed signal is

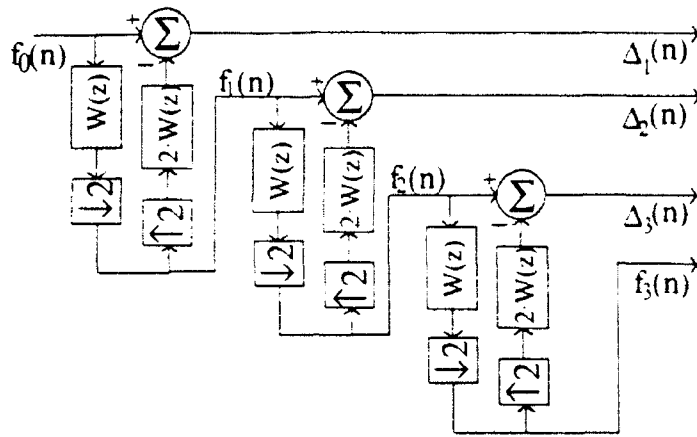


Figure 4.7a--Block diagram illustrating three-stage decomposition by Laplacian pyramid.

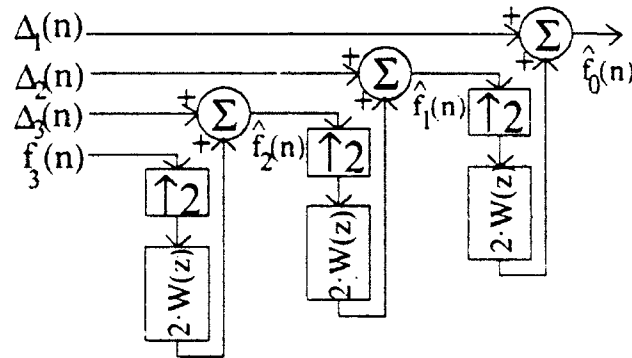


Figure 4.7b--Block diagram of structure for reconstructing sequence decomposed by three-level decomposition depicted by block diagram of Figure 4.7.

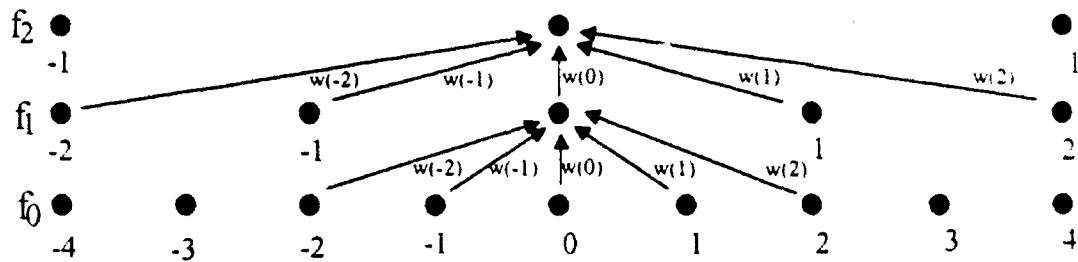


Figure 4.8--Lattice illustrating concept behind generation of kernel $w(n)$ used for Laplacian pyramid decomposition and reconstruction. After [30].

accomplished by simply reversing (4.67) and reintroducing to $f_{k-1}(n)$ the detail $\Delta_{k-1}(n)$ removed during decomposition:

$$f_k(n) = \Delta_{k+1}(n) + 2 \cdot \sum_m w(n - 2 \cdot m) f_{k+1}(m). \quad (4.68)$$

Figure 4.7b illustrates the process by which a sequence decomposed by Figure 4.7a is reconstructed.

Figure 4.8 provides a graphical illustration of the averaging process employed in the Laplacian pyramid. The Laplacian pyramid decomposition involves the approximation of some sequence $f_0(n)$ by an averaged version $f_1(n)$. The technique developed by Burt and Adelson [30], in calculating the values of the nodes in $f_1(n)$, endeavors to consider each node in $f_0(n)$ with an equal weight. In the case of a five-point weighting sequence $w(n)$, each node in $f_1(n)$ is calculated from an average of its five nearest neighbors in $f_0(n)$. For example, the value of node $f_0(n)$ in Figure 4.18 is evaluated as

$$f_1(0) = w(-2) \cdot f_0(-2) + w(-1) \cdot f_0(-1) + w(0) \cdot f_0(0) + w(1) \cdot f_0(1) + w(2) \cdot f_0(2).$$

Additionally, obtaining $f_1(-1)$ and $f_1(1)$, requires evaluation of

$$f_1(-1) = w(-2) \cdot f_0(-4) + w(-1) \cdot f_0(-3) + w(0) \cdot f_0(-2) + w(1) \cdot f_0(-1) + w(2) \cdot f_0(0)$$

and

$$f_1(1) = w(-2) \cdot f_0(0) + w(-1) \cdot f_0(1) + w(0) \cdot f_0(2) + w(1) \cdot f_0(3) + w(2) \cdot f_0(4).$$

Now $f_0(0)$, an even-numbered node, contributes to the computation of three nodes in $f_1(n)$: to $f_1(0)$, to which it is directly adjacent across scale, and to $f_1(-1)$ and $f_1(1)$. However, $f_0(1)$, an

odd-numbered node, only contributes to the contribution of two-nodes in $f_1(n)$: to $f_1(0)$ and to $f_1(1)$.

As stated previously, the objective is to define $\{w(n)\}_n$ such that the total weighted contribution by each node in $f_0(n)$ to the computation of nodes in $f_1(n)$ is equal. Therefore, the requirement that the total weighting factor for all contributions by $f_0(0)$ to equals the total weighting factor for all contributions by $f_0(1)$ implies that

$$w(-1) + w(1) = w(0) + 2 \cdot w(2). \quad (4.69a)$$

The left-hand side of (4.69a) represents the sum of the weighting factors for all contributions by $f_0(1)$ to all nodes to which it contributes in $f_1(n)$. Similarly, the right-hand side of (4.69a) indicates the sum of the weighting factors for all contributions by $f_0(0)$ to all nodes to which it contributes in $f_1(n)$. Inductively, for a five-point weighting sequence the sum of the weights for all contributions by any even-numbered node in $f_0(n)$ will equal the right-hand side of (4.69a) while the sum of the weights for all contributions by any odd-numbered node in $f_0(n)$ will equal the left-hand side of (4.69a).

An additional constraint was imposed on the selection of the weighting sequence $w(n)$:

$$\sum_{k=-2}^2 w(k) = 1. \quad (4.69b)$$

The constraint imposed by (4.69b) ensures that, for any node in $f_1(n)$, the sum of the weights by all contributing nodes in $f_0(n)$ will be unity. Consequently, the average energy in $f_0(n)$ is preserved by the approximation $f_1(n)$.

To satisfy (4.69a) and (4.69b), Burt and Adelson selected

$$\mathbf{w} = \left[\frac{1}{4} - \frac{a}{2} \quad \frac{1}{4} \quad a \quad \frac{1}{4} \quad \frac{1}{4} - \frac{a}{2} \right]^T. \quad (4.70)$$

Each odd-numbered node contributes twice, each time with a weighting of $1/4$. The even-numbered nodes contribute with a weighting of "a" when directly adjacent across scale while contributing twice with a weighting of $1/4 - a/2$ when separated by scale and translation. Consequently, each node contributes with a total weight of $1/2$.

Considering the top branch of the structure in Figure 4.6 from a two-sided Z-transform perspective provides insight into the frequency-domain character of the Laplacian pyramid. The transform of the weighting sequence can be expressed as

$$W(z) = \left(\frac{1}{4} - \frac{a}{2} \right) (z^2 + z^{-2}) + \frac{1}{4} (z + z^{-1}) + a. \quad (4.71)$$

Applying (3.6), decimating (4.71) produces

$$\begin{aligned} W_{\downarrow 2}(z) &= \frac{1}{2} [W(z^{1/2}) + W(-z^{1/2})] \\ &= \left(\frac{1}{4} - \frac{a}{2} \right) (z + z^{-1}) + a \end{aligned}$$

which after expansion becomes

$$[W_{\downarrow 2}]_{\uparrow 2}(z) = \left(\frac{1}{4} - \frac{a}{2} \right) (z^2 + z^{-2}) + a. \quad (4.72)$$

The effective transfer function $T(z)$ of the top branch of the structure in Figure 4.6 can be expressed as

$$T(z) = 2 \cdot [W_{\downarrow 2}]_{\uparrow 2}(z) \cdot W(z). \quad (4.73)$$

Through trial and error, Burt and Adelson observed that for the choice of $a = 3/10$, repeated applications of the transfer function (4.73) produced an impulse response with approximately the

same shape with each iteration and which ultimately, approached a Gaussian shape. For this choice of "a", the system transfer function becomes

$$T(z) = \frac{\frac{1}{50}z^8 + \frac{1}{20}z^7 + \frac{3}{25}z^6 + \frac{1}{5}z^5 + \frac{11}{50}z^4 + \frac{1}{5}z^3 + \frac{3}{25}z^2 + \frac{1}{20}z + \frac{1}{50}}{z^4}$$

Furthermore, from Figure 4.6, by inspection, the expression for the detail sequence $\Delta_{k+1}(n)$ is, in terms of $f_k(n)$ and $t(n)$,

$$\Delta_{k+1}(n) = \sum_k t(n-k) f_k(k) - f_k(n)$$

Equivalently, if the transfer function for the entire structure of Figure 4.6 is defined such that its impulse response is $d(n)$, then $d(n) = t(n) - \delta(n)$ where $\delta(n)$ is Kronecker's delta function.

Consequently, the transfer function $D(z)$ becomes

$$D(z) = \frac{\frac{1}{50}z^8 + \frac{1}{20}z^7 + \frac{3}{25}z^6 + \frac{1}{5}z^5 - \frac{39}{50}z^4 + \frac{1}{5}z^3 + \frac{3}{25}z^2 + \frac{1}{20}z + \frac{1}{50}}{z^4}$$

From this analysis follows a conceptually clearer but computationally less efficient structural equivalent for Figure 4.6. This equivalent structure is indicated in Figure 4.9.

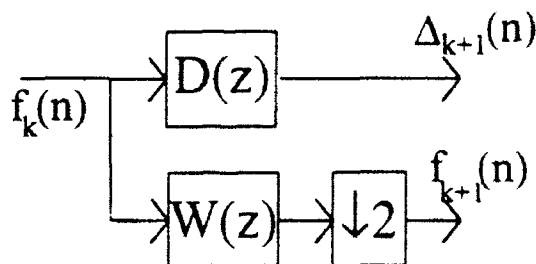


Figure 4.9--Equivalent structure to that shown in Figure 4.6.

As a method of time-frequency decomposition, the Laplacian pyramid provides performance for processes containing high-frequency components which inferior to that which shall later be observed for Mallat's algorithm. Figure 4.10 illustrates the partitioning of the

frequency spectrum which occurs when a signal is decomposed by the Laplacian pyramid. The spectral bins which are formed do not follow the pattern of an even division of the frequency

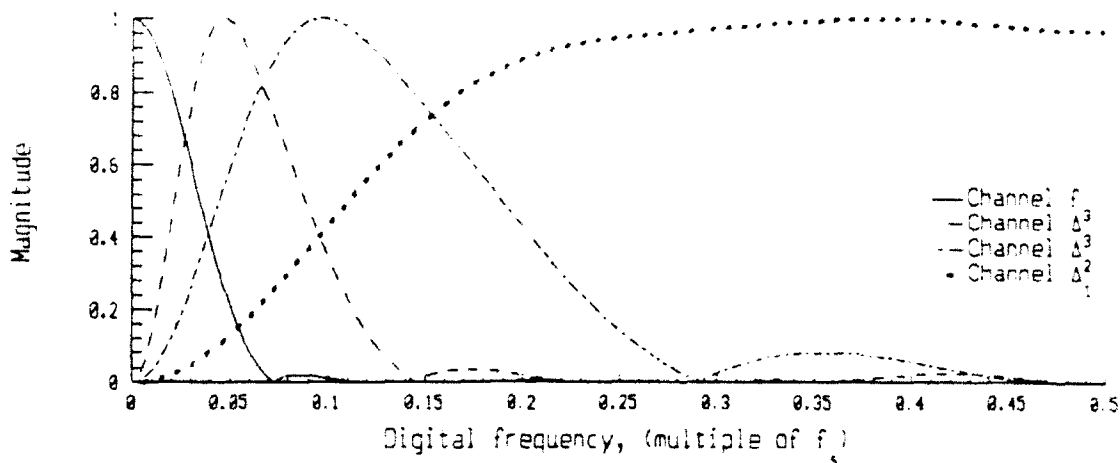


Figure 4.10--Partitioning of frequency spectrum performed by three-stage Laplacian pyramid of Figure 4.7.

spectrum at each stage as would be anticipated by operations involving factor-of-two decimation and expansion. In fact, approximately three fifths of the frequency spectrum below the Nyquist frequency is contained within the highest frequency bin. Consequently, for classification applications, a Laplacian pyramid-based analyzer would provide poor localization of frequencies above approximately $0.2 f_s$. However, for an over-sampled sequence comprised primarily of lower frequency components, a Laplacian pyramid detector would likely provide slightly better spectral resolution than would be afforded by a multiresolution detector which divides the spectrum evenly at each stage. For a three-stage, even-division multiresolution scheme, the region in the frequency domain from 0 to $0.125 \cdot f_s$ would be divided into two spectral bins. For the scheme of Figure 4.10, the region in the frequency domain from 0 to approximately $0.15 \cdot f_s$ is divided into three spectral bins.

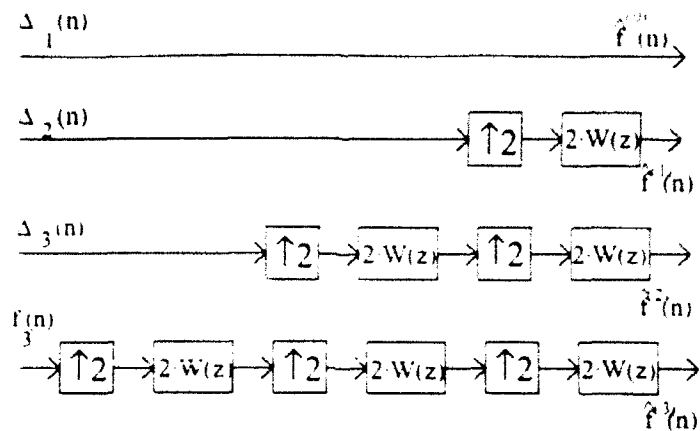


Figure 4.11--Block diagram for full expansion by channel approach for reconstruction of a sequence decomposed by the Laplacian pyramid. Structure is equivalent to that of Figure 4.7b.

In general, multiresolution decomposition schemes which involve factor-of-two decimation generate lattices which resemble Figure 4.8. At each stage, the approximation density is reduced by a factor of two. For information transmission systems, this represents the primary advantage of such systems. However, for display of time-scale decompositions involving mesh or contour plots, most computer graphical routines require the insertion of zeros in order to create a lattice of points of constant density. For mesh plots, such as those provided by *Matlab*, a lattice of the form of Figure 4.8 will appear as rows of fin-like structures of varying density. Because of the rapid transition to zero at each lattice node, contour plots essentially provide binary indications of a sequence's time-scale content: Indication of the presence of energy at a node is given, without indication of the relative magnitude of the sequence at that node.

Figure 4.11 provides a block diagram of a full expansion by channel scheme for preparing the lattice similar to that of Figure 4.8 for plotting. The structure of Figure 4.11

represents the result of separating each branch of Figure 4.7b at its summation points. The consequence of implementing a structure like that in Figure 4.11 is that sparse rows in a lattice like that in Figure 4.8 will be interpolated resulting in a uniform density of lattice nodes.

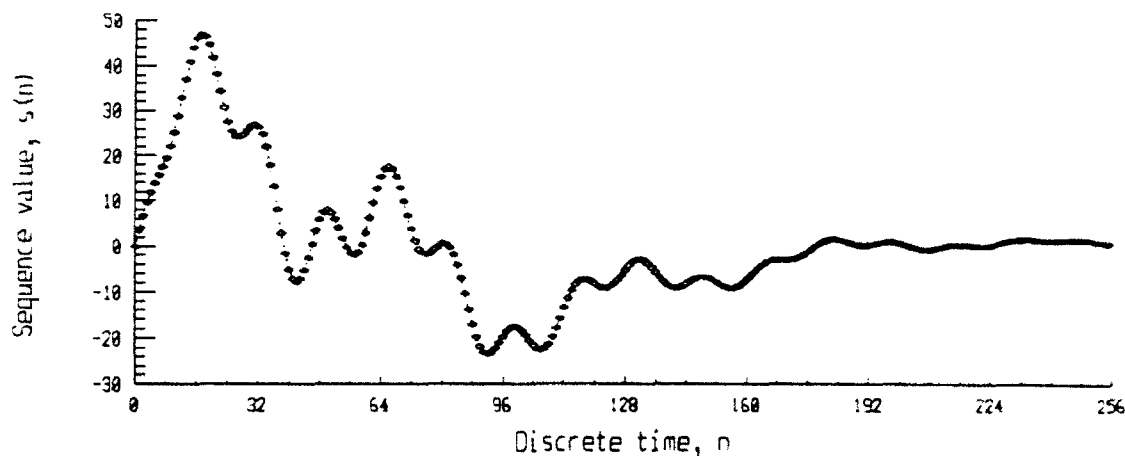


Figure 4.12--Time plot of 256-point test sequence generated by (4.74a) for demonstration of Laplacian Pyramid.

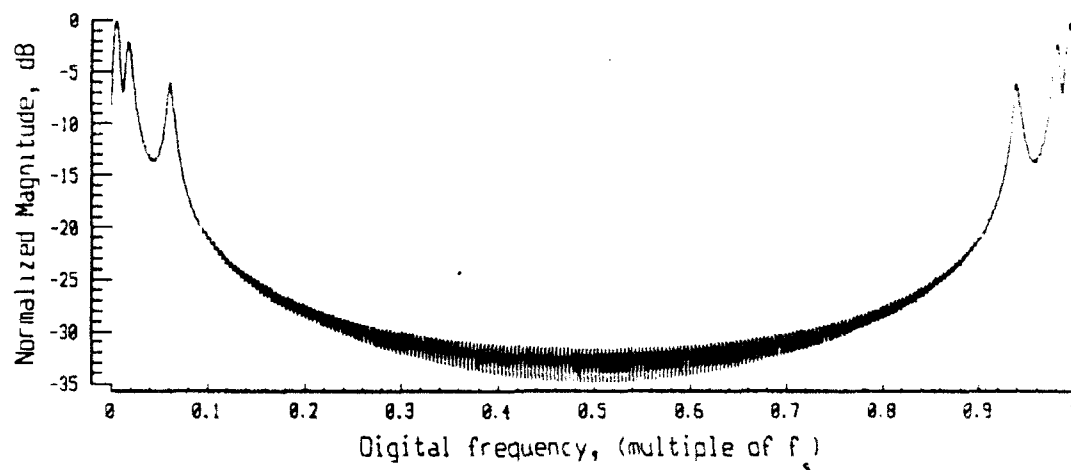


Figure 4.13--Plot of power spectral density of 256-point test sequence generated by (4.74a).

Furthermore, the reconstructed sequence from the structure in Figure 4.7b is accomplished by

$$\hat{f}_0(n) = \sum_m \hat{f}^{(m)}(n).$$

In other words, the reconstructed sequence $\hat{f}_0(n)$ consists of the sum of the content of all the channels $\hat{f}^{(m)}(n)$ obtained from Figure 4.11.

To demonstrate the operation of the Laplacian pyramid, two test sequences were employed. The first sequence was constructed from low-frequency components:

$$s_{LF}(n) = \left(1 - e^{-n/64}\right) \cdot e^{-(n-94)/21} \cdot e^{2n/75} \left[2 \cdot \cos\left(2 \cdot \pi \cdot \frac{2}{512} n\right) + \sin\left(2 \cdot \pi \cdot \frac{9}{512} n\right) + \frac{1}{2} \cos\left(2 \cdot \pi \cdot \frac{31}{512} n\right)\right]. \quad (4.74a)$$

A time plot of the sequence is presented in Figure 4.12 and a power spectral density plot appears in Figure 4.13. The test sequence was chosen such that the spectral content would lie predominantly in the lower portions of the frequency spectrum. Test sequence (4.74a) contained one spectral component, which completes only one complete oscillation during the duration of the sequence, at $\pi/128$ ($\approx 0.004 \cdot f_s$). Additional components are present at $9 \cdot \pi/256$ ($\approx 0.018 \cdot f_s$) and at $31 \cdot \pi/256$ ($\approx 0.06 \cdot f_s$).

The second sequence, identical to (3.47) employed in Chapter III, Section C is repeated here for convenience:

$$s_{HF}(n) = \left(1 - e^{-n/64}\right) \cdot e^{-(n-94)/21} \cdot e^{2n/75} \cdot \left[\cos\left(2 \cdot \pi \cdot \frac{27}{256} \cdot n\right) + \frac{1}{4} \cos\left(2 \cdot \pi \cdot \frac{55}{256} \cdot n\right) + \frac{1}{4} \cos\left(2 \cdot \pi \cdot \frac{113}{256} \cdot n\right)\right] \quad (4.74b)$$

A time plot of (4.74b) is presented in Figure 3.23 and its power spectral density is plotted in Figure 3.24. Test sequence (4.74b) contains spectral components at $2 \cdot \pi \cdot 27/256$ ($\approx 0.105 \cdot f_s$), $2 \cdot \pi \cdot 55 \cdot \pi/256$ ($\approx 0.215 \cdot f_s$) and at $2 \cdot \pi \cdot 113 \cdot \pi/256$ ($\approx 0.44 \cdot f_s$).

Figure 4.14a presents a surface plot depicting the eight-scale, full expansion by channel of the Laplacian pyramid decomposition of the test sequence generated by (4.74a). Despite the fact that the spectral components of the lowpass test sequence (4.74a) are quite close together, the Laplacian pyramid is able to distinguish between the three separate components. One peak is evident at around sample 32 at a scale of five to six, a series of approximately four peaks are evident at a scale of three to four from samples 10 to 60 and a series of peaks corresponding to the high-frequency components are apparent at scales one to two from samples 20 to 120.

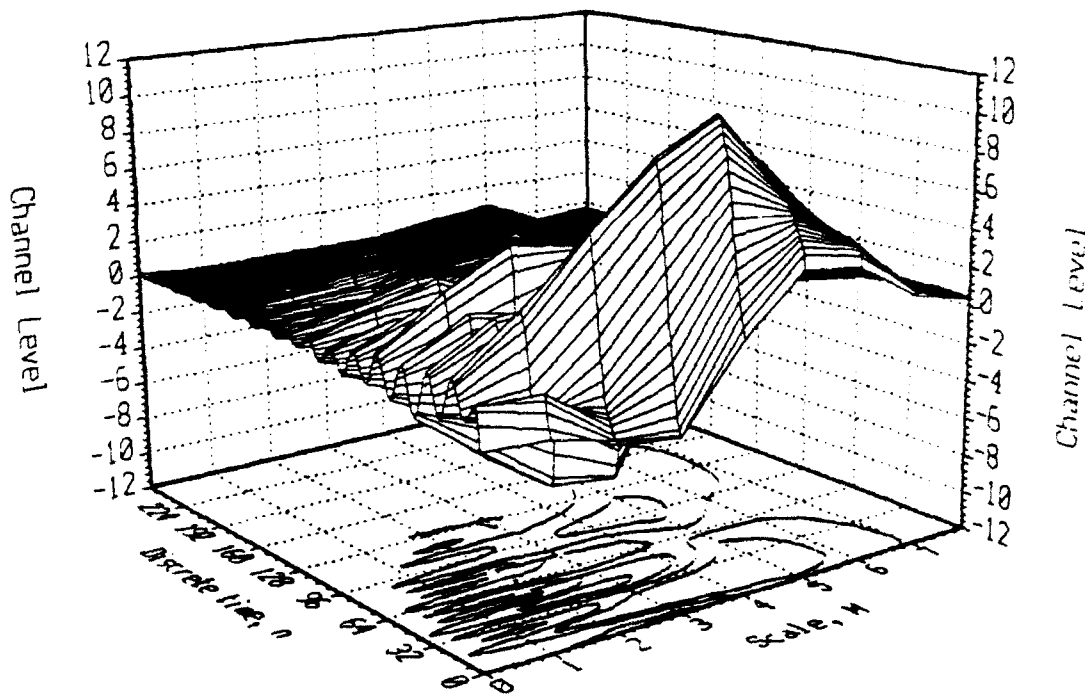


Figure 4.14a--Surface plot of full expansion by channel of Laplacian pyramid decomposition of 256-point, lowpass test sequence generated by (4.74a).

Figure 4.14b illustrates the Laplacian pyramid decomposition of the highpass 256-point test sequence (4.74b). As discussed within the context of the frequency partition diagram,

Figure 4.10, the Laplacian pyramid produces significantly poorer resolution for sequences comprised of high-frequency components. In fact, for the highpass test sequence (4.74b), the two spectral components with the highest frequencies fall within a single spectral bin. Consequently, as Figure 4.14b indicates, it is very difficult using the Laplacian pyramid to resolve spectral components residing in the upper two thirds of the frequency spectrum below the Nyquist frequency.

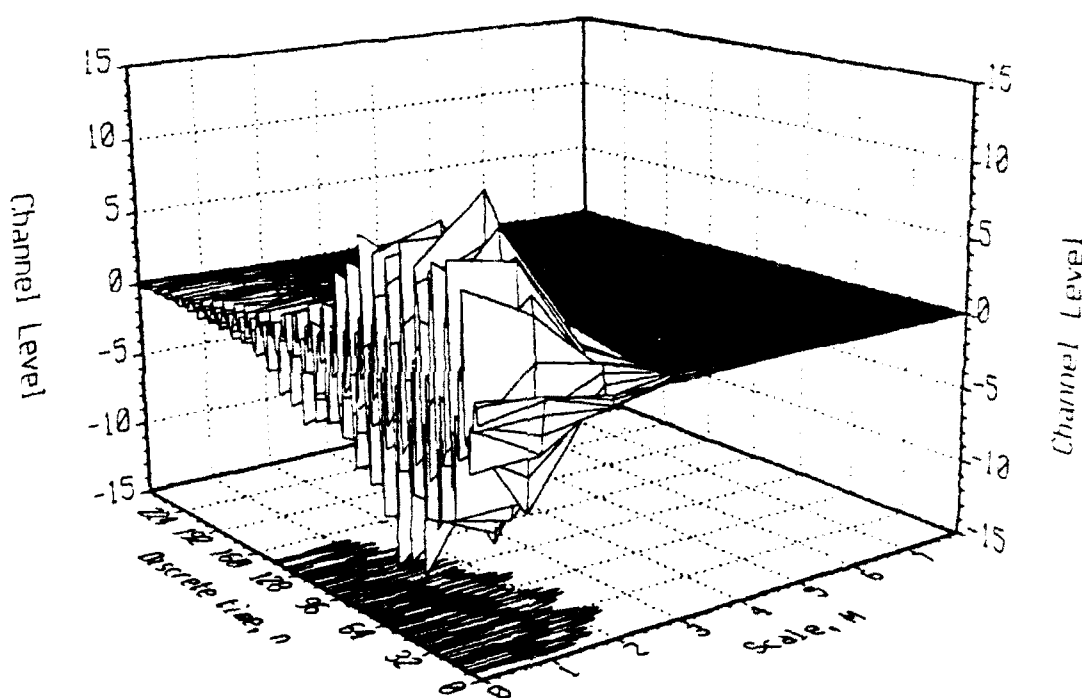


Figure 4.14b--Surface plot of full expansion by channel of Laplacian pyramid decomposition of 256-point, highpass test sequence generated by (4.74b).

The reconstruction error for the Laplacian pyramid operation on the test sequence was consistently outstanding. The mean square reconstruction error as defined by (3.32) is plotted in Figure 4.15. As indicated by Figure 4.15, the reconstruction error never rose above -317 dB.

This accuracy roughly corresponds to the numerical precision of *Matlab* which was used for this demonstration.

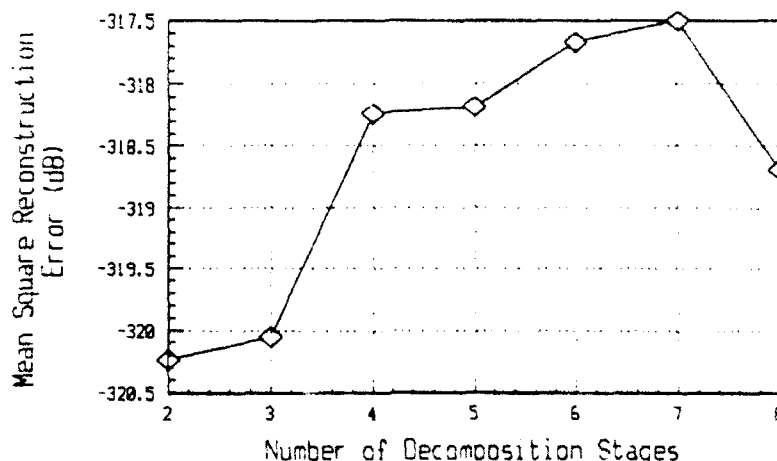


Figure 4.15--Trend of mean square reconstruction error for Laplacian pyramid operating on 256-point lowpass test sequence of (4.74a).

The à trous algorithm represents the first multiresolution analysis technique explicitly based on an affine-type representation vector. This technique consists of evaluating a discretized approximation of the continuous wavelet transform. Specifically, the starting point for the à trous method is the *discrete wavelet series* [31]:

$$w(m, n) = 2^{-m^2} \sum_k \psi^*(2^{-m}k - n) s(k). \quad (4.75)$$

Essentially, the discrete wavelet series consists of the discrete correlation between some sequence $s(n)$ and translations of a sampled wavelet function $2^{-m^2} \psi(2^{-m}k - n)$ at scale m .

Evaluating (4.75) for $w(1, n)$ produces

$$w(1, n) = \frac{1}{\sqrt{2}} \sum_k \psi^*\left(\frac{k}{2} - n\right) s(k). \quad (4.76)$$

In (4.76), it is obvious that $\psi\left(\frac{k}{2} - n\right) = \psi\left(\frac{k-2n}{2}\right)$. Consequently, (4.76) becomes

$$w(1, n) = \frac{1}{\sqrt{2}} \sum_k \psi^*\left(\frac{k-2n}{2}\right) s(k).$$

Now, if $\psi(k)$ is known for integer-valued arguments, its values at half-integer arguments can be approximated through interpolation. If $f(k)$ represents the impulse response for an interpolation filter, then $\psi(k)$ at half-integers is approximately

$$\psi\left(\frac{n}{2}\right) = \sqrt{2} \sum_k f^*(2k - n) \psi(k), \quad (4.77)$$

where the conjugation and time-reversal of the filter and the factor of $\sqrt{2}$ have been introduced for later convenience. The form of the summation term on the right-hand side of (4.77) is recognizable as expansion of a sequence $\psi(k)$ followed by convolution with a filter whose impulse response is $f(-k)$.

To obtain the best approximation, special conditions are imposed on the filter represented by $f(k)$. Shensa [31] applies the term *à trous* filter and employs the notation

$$f(2 \cdot k) = \frac{1}{\sqrt{2}} \delta_{0,k},$$

where $\delta_{0,k}$ is Kronecker's delta function. Perhaps a slightly more illuminating manner in which to express this concept is to use the notation

$$f_{\downarrow 2}(k) = \frac{1}{\sqrt{2}} \delta_{0,k}. \quad (4.78)$$

In other words, the decimated impulse response $f(k)$ is non-zero only for $k = 0$. Equivalently, the only non-zero, even-numbered coefficient for the filter $f(k)$ corresponds to $k = 0$. The condition (4.78) is necessary in order to ensure that known values for the interpolated sequence $\psi(k)$ are unaffected by the interpolation process. When evaluating $f^*(2k - n) \psi(k)$, if n is an even integer, an argument for which $\psi(n/2)$ is known, $2k - n$ will also be an even integer, and

the series (4.77) will contain only one non-zero term, for $n = 2k$. Consequently, (4.77) will be evaluated as

$$\psi\left(\frac{n}{2}\right) = \sqrt{2} f^*(0) \psi\left(\frac{n}{2}\right).$$

Hence, the factor of $1/\sqrt{2}$ in (4.78). On the other hand, if n is an odd integer, an argument value for which the interpolation must be calculated, the series (4.77) will be evaluated as a weighted sum of the function values for $\psi(n/2)$ for surrounding even values of n . The à trous condition (4.78) assumes a position of importance in the theory of FIR filters. The condition (4.78) is equivalent to the half-band condition. A *half-band filter* is a symmetric, FIR digital filter whose impulse response satisfies (4.78). Mitzner [32] showed that filters satisfying (4.78), of necessity, also satisfy

$$F(e^{j\omega}) + F(e^{j(\omega-\pi)}) = 2f(0) \quad \text{where} \quad F(e^{j\omega}) = \sum_k f(k) e^{j\omega k}. \quad (4.79)$$

Consequently, the interpolation filter whose impulse response is $f(k)$ is also a half-band filter. Furthermore, Shensa showed that the filters for Daubechies' orthonormal scaling functions belong to a special class of filters satisfying (4.78) known as *Lagrangian interpolation filters*. Specifically, if $c(n)$ is the impulse response for the filter producing one of Daubechies' orthonormal scaling functions, the corresponding Lagrangian interpolation filter is obtained from

$$f(n) = \frac{1}{\sqrt{2}} \cdot \sum_k c(k) c(k-n).$$

Continuing the development of the à trous algorithm, substitution of (4.77) into (4.76) produces

$$w(1, n) = \sum_j \sum_k f(2j + 2n - k) \psi^*(j) s(k). \quad (4.80)$$

Now, if a filter $g(n)$ is defined such that

$$g(n) = \psi^*(-n), \quad (4.81)$$

and a change of indices $m = j + n$ is applied to (4.80), it follows that

$$w(l, n) = \sum_m g(n - m) \sum_k f(2m - k) s(k). \quad (4.82)$$

Equation (4.82) simply describes decimation of $s(k)$ followed by filtering with a FIR filter whose impulse response is $f(k)$. The result is then further filtered by an additional FIR filter whose impulse response is $g(n)$. Furthermore, the second FIR filter is the conjugated time-reversal of the sampled wavelet function. Therefore, filtering with $g(n)$ is equivalent to evaluating the correlation with $\psi(n)$.

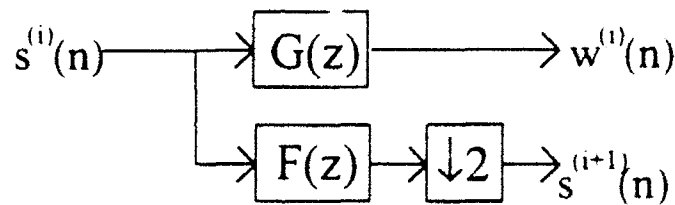


Figure 4.16--Block diagram of one-stage decomposition by à trous algorithm.

Now, the operation of decimation and then filtering $s(n)$ resembles the portion of Mallat's algorithm, (4.53), where successively coarser approximations of $s(n)$ were obtained by decimating and filtering each preceding approximation. For the signal detail is extracted merely by filtering the upper half of the spectrum below the Nyquist frequency. If the notation $s^{(i)}(n)$ is adopted for the i^{th} -level approximation of $s(n)$ and $w^{(i)}(n)$ for $w(i, n)$, by induction, from (4.82) it follows that

$$\begin{aligned} s^{(i+1)}(n) &= f * s^{(i)}(n) \\ w^{(i)}(n) &= g * s^{(i)}(n) \end{aligned} \quad (4.83)$$

The block diagram for (4.83) is shown in Figure 4.16.

Earlier wavelet transform techniques resemble Gabor transforms in which sequences were decomposed by projection on representation vectors consisting of modulated Gaussian windows. Consequently, the wavelet function used by Shensa in his study of wavelets was a modulated Gaussian, also known as a *Morlet window*:

$$\psi(t) = e^{j\nu t} e^{-\beta^2 t^2} \quad (4.84a)$$

Fourier transformation of (4.84a) produces

$$\hat{\psi}(\omega) = \frac{1}{\beta} \sqrt{2\pi} e^{-\frac{(\omega-\nu)^2}{2\beta^2}} \quad (4.84b)$$

In order to specify a wavelet function, it is, therefore, necessary to specify its center frequency ν and its window rolloff factor β .

Furthermore, in order to increase resolution in the Fourier domain it is possible to employ a wavelet function consisting of superimposed Gaussian envelopes modulated at different frequencies. In this case, the wavelet $\psi(t)$ and its Fourier transform become

$$\begin{aligned} \psi(t) &= \sum_{k=0}^{M-1} e^{-\frac{\beta^2}{2} \left(\frac{t}{2^k M}\right)^2} e^{j\nu \frac{t}{2^k M}} \\ \hat{\psi}(\omega) &= \frac{1}{\beta} \sqrt{2\pi} \sum_{k=0}^{M-1} 2^{-\frac{k}{M}} e^{-\frac{1}{2\beta^2} \left(\frac{\omega}{2^k M} - \nu\right)^2} \end{aligned} \quad (4.85)$$

Multiple frequency-domain translations of the Gaussian window are referred to as *voices*.

Through the use of voices, the upper half of the frequency spectrum below the Nyquist frequency is partitioned into multiple spectral bins. Shensa listed a series of guidelines for designing a wavelet function with multiple voices:

1. The center frequency must lie in the upper half of the frequency spectrum below the Nyquist frequency. Consequently,

$$\pi/2 \leq \nu. \quad (4.86)$$

2. In order for $\psi(t)$ to be an analytic function,

$$\beta \leq \frac{\nu}{2\pi}. \quad (4.87)$$

Obviously, (4.84b) has an infinite region of support. However, if, for (4.87), the equality is selected,

$$\hat{\psi}(0) = \sqrt{2\pi} e^{-2\pi^2} \approx 6.71 \times 10^{-9}.$$

Consequently, the spectral content in regions of negative frequency will be negligible.

3. To exclude aliasing,

$$\nu \leq \pi - \sqrt{2} \beta. \quad (4.88)$$

The quantity $\sqrt{2} \beta$ is equal to one half of the Gaussian window where, at the edge of the passband, the frequency response of the filter is less than its maximum by a factor of e^{-1} . Condition (4.88) ensures that the high-frequency edge of the passband is located below the Nyquist frequency.

4. The fourth condition for designing wavelets employs the concept of relative bandwidth.

The *relative bandwidth* B_R of the window is defined to be the ratio of the window bandwidth to its center frequency, or

$$B_R = \frac{2\sqrt{2}\beta}{\nu}.$$

Since, from (4.86) and (4.88), $\pi/2 \leq \nu \leq \pi$, it follows that

$$\frac{2\sqrt{2}}{\pi} \beta = \beta \leq B_R \leq 2\beta = \frac{4\sqrt{2}}{\pi}. \quad (4.89)$$

This condition is essentially a combination of previous conditions.

5. Furthermore, if multiple voices are desired, it follows that the number of voices M required to completely cover the upper half of the spectrum is

$$M = \frac{\pi^2}{2 \cdot 2 \beta} \approx \frac{1}{2\beta}.$$

As a result, an approximate choice for β is

$$\beta = \frac{1}{2M}. \quad (4.90)$$

6. To construct the separate voices, the *mother wavelet* $\psi(t)$ is scaled by various factors $2^{k/M}$ where M indicates the number voices. Specifically, the k^{th} voice $v_k(t)$ for $k = 0, \dots, M-1$, is given by

$$v_k(t) = \psi\left(\frac{t}{2^{k/M}}\right) \quad (4.91a)$$

from which it follows by the scaling property of the Fourier transform,

$$\hat{v}_k(\omega) = \frac{1}{\beta} 2^{k/M} \sqrt{2\pi} e^{-(2^{k/M} \omega - \nu)^2 / 2\beta^2}. \quad (4.91b)$$

This scaling produces the combined affects of increasing the Gaussian window decay factor by a multiple of $2^{2 \cdot k/M}$ and of translating the location of the window's maximum value to $\omega = 2^{-2 \cdot k/M} \nu$. Selection of this scheme also maintains the affine nature of the transform.

7. Then, to select the filter length, it is appropriate to consider the decay of the Gaussian window in the time domain. The filter will consist of a discretely sampled version of the continuous wavelet function. The DFT of the wavelet is, by definition,

$$V_k(z^j \omega) = \sum_m v_k(k) e^{-j\omega m}.$$

Due to the rapid decay of the window function $\psi(t)$, the series can be truncated for values of the summation index k such that $v_{k,j}(k)$, the voice with the slowest time-domain rate of decay, will be negligible. If a negligibility threshold T_n is specified, then a filter half-length K must be selected such that

$$|v_{k,j}(K)| \leq T_n$$

Inverting the envelope portion of (4.91a) produces for the filter half-length K

$$K \geq \frac{1}{\beta} 2^{(M-1)/M} \sqrt{-2 \ln(T_n)} \quad (4.92)$$

Consequently, the analyzing wavelet filter $g(n)$ from (4.81) is defined to be

$$g(n) = \begin{cases} \psi^*(-n) & \forall n = -K, \dots, K \\ 0 & \text{otherwise} \end{cases} \quad (4.93a)$$

and the filter $g_k(n)$ corresponding to the k^{th} voice $v_k(t)$ becomes

$$g_k(n) = \begin{cases} \psi^*(-n/2^{kM}) & \forall n = -K, \dots, K \\ 0 & \text{otherwise} \end{cases} \quad (4.93b)$$

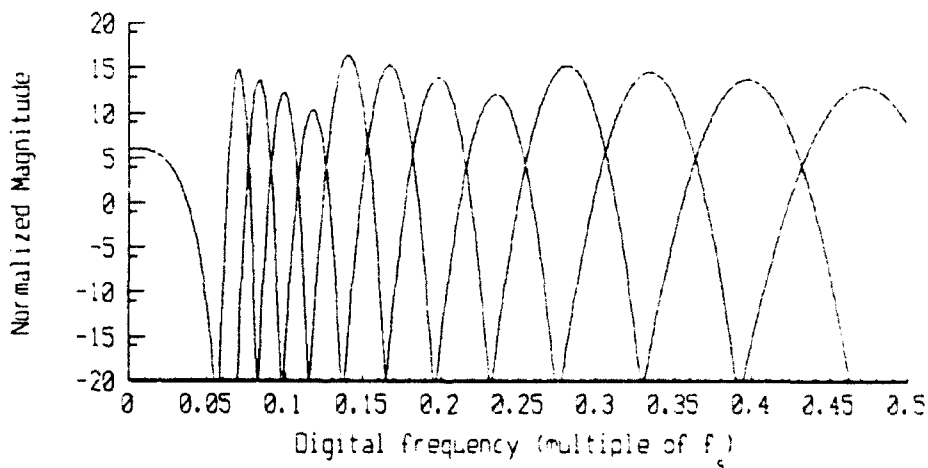


Figure 4.17--Spectral partitioning performed by three-stage decomposition by a trous method using four-voice Morlet window as analyzing wavelet. The interpolation filter, plotted as the lowpass filter represents a Lagrangian filter calculated from Daubechies' orthonormal scaling function on $[0, 3]$

To illustrate the spectral behavior of the à trous method, Figure 4.17 plots the frequency decomposition performed by a three-stage structure employing a four-voice Morlet window. The spectral bin density increases in a logarithmic manner as digital frequency approaches zero and the width of each bin decreases similarly. The relatively large bandwidth of the lowest frequency bin occurs because of the relatively small number of stages. Additional stages would result in the continued trend of logarithmically increasing spectral bin density and bin width. The logarithmic trend must, however, be ultimately broken by the final spectral bin which will be defined by a half-band, lowpass filter.

Figures 4.18a and 4.18b demonstrate the performance of the à trous algorithm for identification of the spectral components comprising a sequence. Figure 4.18a presents the decomposition of the lowpass test sequence (4.74a). Examining Figure 4.18a, the three harmonic components can be observed. At a scale of approximately 2.5 to 3, the band corresponding to the highest frequency component is evident. The middle frequency component is apparent in the range from three to four. The lowest frequency constituent is indicated by the sparse group of fins at scales of five to seven. The shape of the envelope is evident from the relative heights of the peaks of the two components possessing higher frequencies. However the lower frequency component appears relatively constant across the entire range of samples. This occurs because the integration time of the final scale extends the duration of the sequence.

The à trous decomposition of the highpass test sequence (4.74b) is plotted in Figure 4.18b. Unlike the Laplacian pyramid, the à trous method displays no difficulty in resolving the spectral components of (4.74b). Figure 4.18 provides an opportunity to understand the

relationship between the location of spectral components in the time-scale plane and their location in the frequency spectrum. The regions contained within each spectral bin are, again, indicated in Figure 4.17. The spectral component of the test sequence at $0.44 f_c$ falls into the right-most spectral bin of Figure 4.17. This component is indicated with in Figure 4.18b at a scale of zero from approximately samples zero to 160. The location of the spectral component at $0.21 f_c$ approximately coincides with the location of the boundary of the fifth and six spectral bins from the right-hand side of Figure 4.17. Since the analyzing wavelet contains four voices

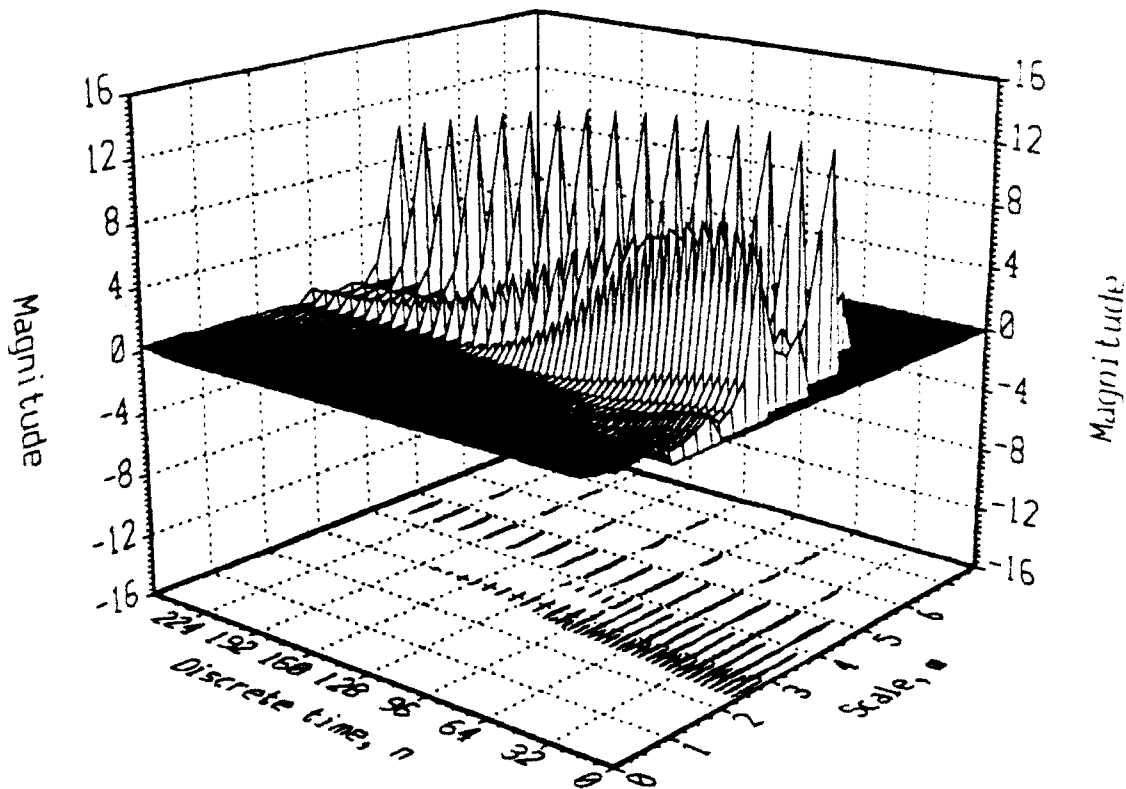


Figure 4.18a--Surface plot of a trous wavelet transform decomposition of 256-point, lowpass test sequence generated by (4.7-4a). Plot represents eight-stage decomposition using four-voice Morlet analyzing wavelet and Lagrangian interpolation filter calculated from filter for Daubechies' orthonormal scaling function supported on $[0, 3]$.

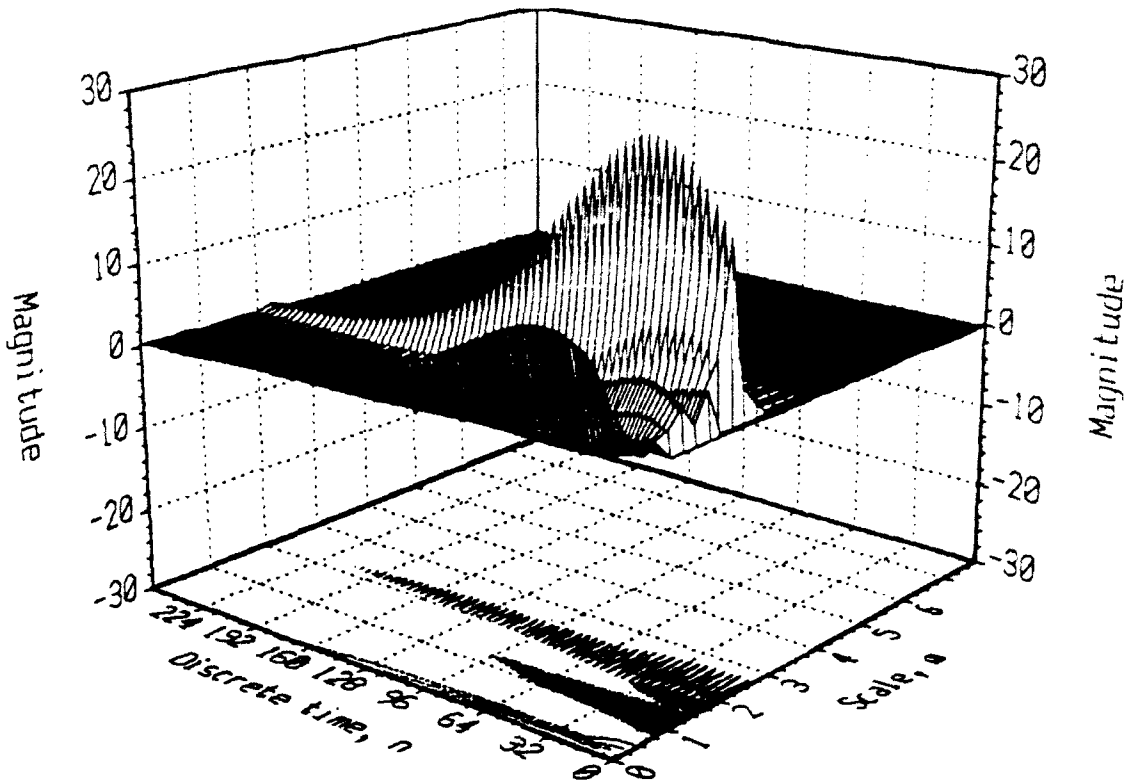


Figure 4.18b--Surface plot of a trous wavelet transform decomposition of 256-point, highpass test sequence generated by (4.74b). Plot represents eight-stage decomposition using four-voice Morlet analyzing wavelet and Lagrangian interpolation filter calculated from filter for Daubechies' orthonormal scaling function supported in $[0, 3]$.

(therefore there are four spectral bins per scale), the fifth and sixth spectral bins coincide with scales of 1.0 and 1.25, respectively. These scales coincide with an indication on 4.18b from samples zero to 96. Finally, the spectral component at $0.105 \cdot f_s$ is located in the 10th spectral bin of Figure 4.17. This bin coincides with a scale of 2.25. Therefore, this final component, possessing the greatest power, provides an indication in Figure 4.18b throughout the entire range of samples.

In working with the a trous algorithm, one significant disadvantage arises. Specifically, reconstruction of a sequence decomposed by the a trous method is extremely difficult. The

wavelet basis functions used in the à trous decomposition comprise frames in the sense described in Chapter II. Consequently, in order to reconstruct a sequence decomposed by the à trous method, it is necessary to construct biorthogonal set of bases. Daubechies outlined the details of construction the dual of a specified basis in [6].

Apart from the difficult of inversion, the à trous algorithm, as implemented by Shensa, suffers from the disadvantage of long filter lengths. In the example under consideration, in order to satisfy a negligibility threshold (4.92) of 5×10^{-3} , a filter length of 81 was necessary. Each of the four voices was implemented with a filter of equal length. Furthermore, the wavelet filter coefficients are complex. Complex filter coefficients increase the computational burden. Furthermore, from Figure 4.17 it is evident that the spectral decomposition resulting from the à trous method is anything but power complementary. Partitioning in a manner similar to that of Figure 4.17 results in exaggeration of spectral content near the peaks of the voices and subdued indications between the peaks. In favor of the à trous algorithm, however, is the attainability of arbitrarily high resolution with smooth, regular filters. (It will be observed in the next section that filters sometimes suffer from lack of regularity.)

E. MULTIRESOLUTION ALGORITHMS FROM CASCADED FILTER BANKS

Section C of this chapter outlined the equivalence between Mallat's multiresolution analysis and a structure constructed from cascaded, two-channel, perfect reconstruction QMF banks. This section explores, in a more general manner, implementation of multiresolution analysis structures constructed from cascades of filter banks of arbitrary numbers of channels. For each method, the issues of division of the frequency spectrum and invertibility will be

considered. Spectral properties of the structures are of interest to obtain an understanding of the frequency resolution attainable with techniques under consideration. Invertibility is important because, in general, one good test of a decomposition technique is the accuracy of its reconstruction.

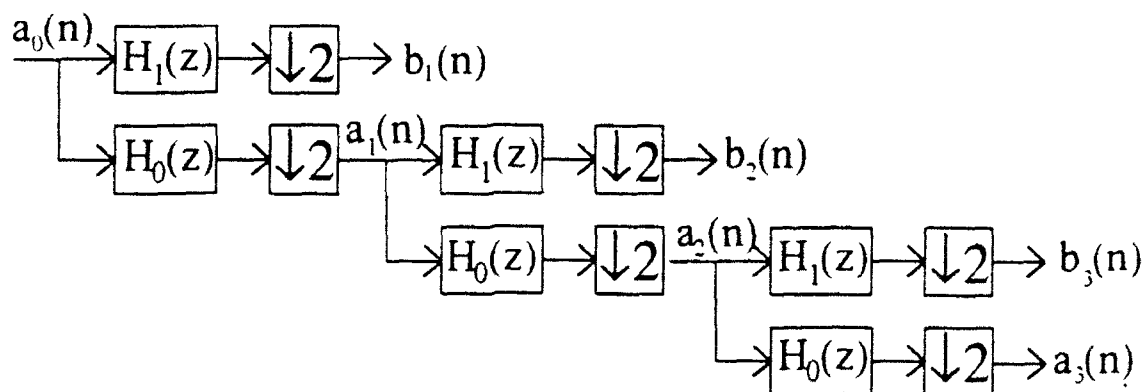


Figure 4.19--Block diagram of three-stage, two-channel multiresolution structure constructed from cascaded QMF analysis banks. Algorithm represented is equivalent to Mallat's algorithm (4.53).

A block diagram of the most basic multiresolution algorithm is depicted in Figure 4.19. The process of Figure 4.19 is exactly equivalent to that of (4.53), Mallat's multiresolution decomposition. At each stage, the approximation sequence $a_k(n)$ is filtered with high-pass and low-pass half-band filters. The output of each filter is then dilated. The low-frequency channel decimator output--or the approximation channel, conforming to the terminology of multiresolution theory is then applied to another stage. The high-frequency, or detail, channel is employed for transmission, in the case of a communication system, or is applied to a detector in one possible case of a digital signal processing application.

If, hypothetically, the filter for each channel in the structure depicted in Figure 4.9 is an ideal filter, the DFT filter output sequence for the approximation sequence bandlimited to $L^2([-\pi/2, \pi/2])$, applying concepts from Chapter III. The DFT of the detail sequence is likewise bandlimited to $L^2([\pi/2, 3\pi/2])$. Decimation of each sequence dilates its spectrum so that the approximation and detail sequence spectra are members of $L^2([-\pi, \pi])$ and $L^2([\pi, 2\pi])$, respectively. Consequently, the time-domain decimation and resultant frequency-domain dilation result, at each stage, in the examination of a smaller segment of the frequency spectrum.

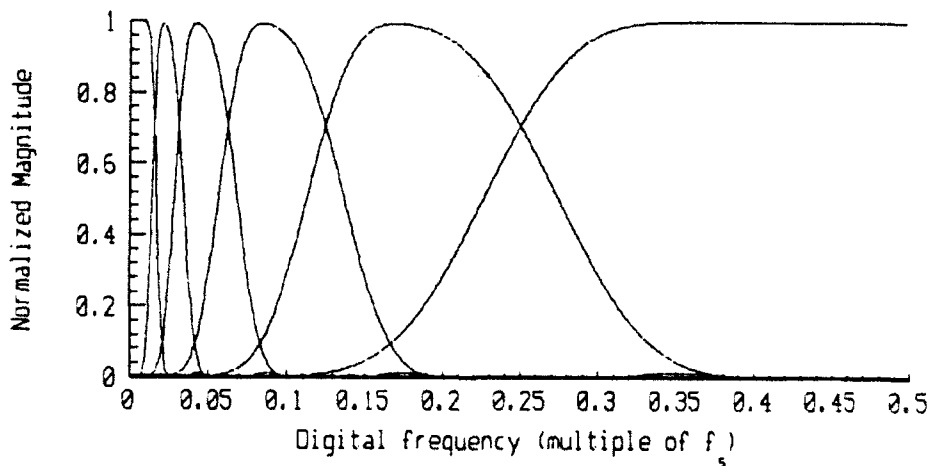


Figure 4-20--Partitioning of the frequency spectrum resulting from five-stage decomposition structure of Figure 4.19. Structure was implemented using, for the approximation and detail channels, the filters corresponding to Daubechies' orthonormal scaling function and wavelet, respectively, supported on $[0, 13]$.

Figure 4.20 plots the spectral partitions resulting from a five-stage decomposition structured as in Figure 4.19. The spectral divisions indicated represent those obtained using the filters for Daubechies' orthonormal scaling function and wavelet on $[0, 13]$. The logarithmic contraction of succeeding spectral bins constitute the multiresolution analysis. The spectral partitioning of Figure 4.20 compares favorably to that obtained by the Laplacian pyramid in

Figure 4.10. However, the localization provided by the partitioning of the frequency spectrum plotted in Figure 4.17 obtained by the à trous is obviously vastly superior to that of 4.20. For some applications, the resolution of Figure 4.20 may be inadequate while the computational burden necessary to obtain the results of Figure 4.17 is excessive.

Brooks [33], in experimentation with signal processing techniques for ultra-wideband radar systems, observed that a dichotomous spectral decomposition, as is performed by the structure of Figure 4.19, provided poorer results than the à trous algorithm. One possible reason for the disparity between the performance of the two techniques considered was the inadequacy of the spectral resolution provided by Mallat's algorithm. Consequently, consideration of a way in which to improve the spectral resolution of multiresolution techniques without incurring the disadvantages of the à trous algorithm is justified.

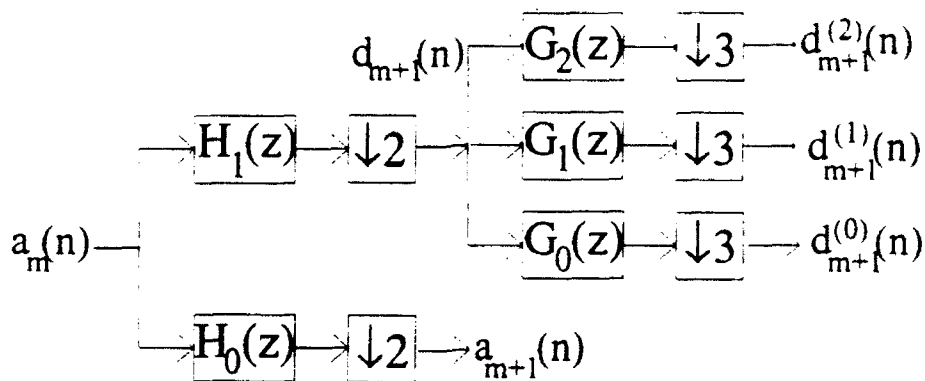


Figure 4.21--Multiresolution structure obtained by cascading detail channel of Figure 4.20 with a three-channel QMF-type filter bank.

Figure 4.21 represents one possible approach to improving the results of Figure 4.20. Applying, at each stage, the detail channel to the input of the analysis bank of another filter bank produces a signal decomposition method capable of obtaining arbitrary precision. The study of

filter bank design is an advanced field and techniques for the design of perfect reconstruction filter banks of an arbitrary number of channels are available employing lattice structures [11] or through cosine modulation of a properly designed prototype filter [34].

Figure 4.21 presents one example of a single stage of a structure using subchannel decomposition of the detail channel at each stage. In Figure 4.21, at each stage, the spectral bin corresponding to the detail sequence is further subdivided into three subchannels. Figure 4.22 illustrates the spectral partitioning which results from a four-stage structure constructed from stages indicated by Figure 4.21. The improvement in spectral resolution is obvious. The density of groups of subchannels increases as digital frequency approaches zero. However, the overall structure does not provide the logarithmic spacing of spectral bins observed for the à trous decomposition as indicated in Figure 4.17.

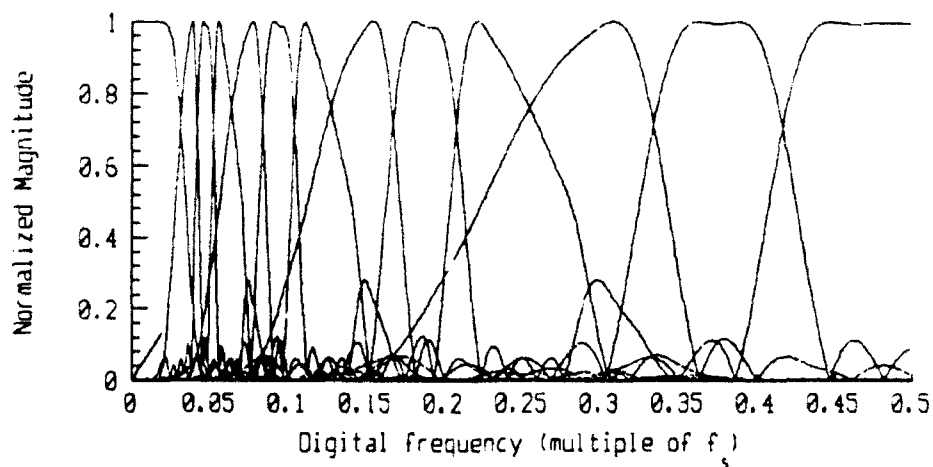


Figure 4.22--Partitioning of frequency spectrum resulting from four-stage multiresolution structure constructed from stages appearing in Figure 4.21. Structure was implemented using, for the approximation and detail channels, the filters corresponding to Daubechies' orthonormal scaling function and wavelet, respectively, supported on $[0, 13]$. Subchannel filter banks were implemented with three-channel filter bank coefficients are presented in [11].

Subchannel decomposition can be performed using either perfect reconstruction QMF banks or pseudo-QMF banks--filter banks which do not strictly satisfy the perfect reconstruction criteria. Similarly, to the extent in which the pseudo-QMF bank deviates from the power complementary property, accurate representation in scale will be forfeited.

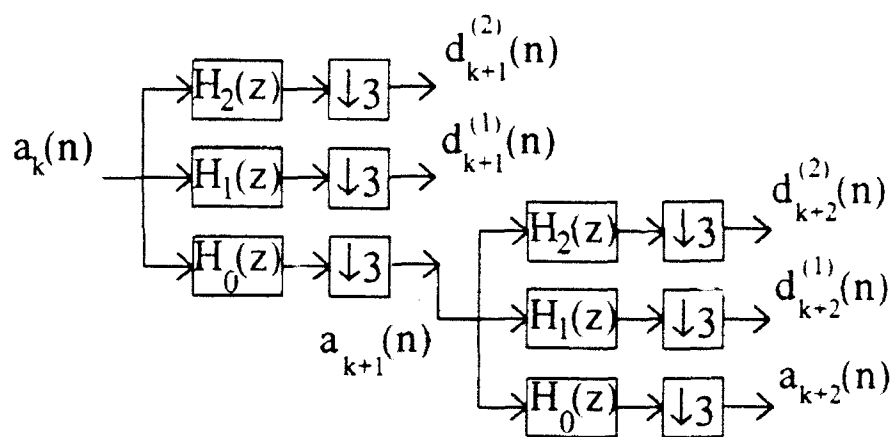


Figure 4.23--Structure constructed from cascade of three-channel filter banks.

An additional method to improve spectral resolution of multiresolution techniques was suggested by Gopinath and Burrus [35]. Employing the term *multiplicity M wavelet transform*, Gopinath and Burrus suggested the concept illustrated in Figure 4.23 as a generalization of the dichotomous structure proposed by Mallat. In the frequency domain, spectral resolution increases as a base three logarithm instead of the base two logarithmic contraction observed in frequency spectra resulting from Mallat-type structures. Furthermore, structures similar to those of Figure 4.3 can be cascaded from filter banks of any number of channels.

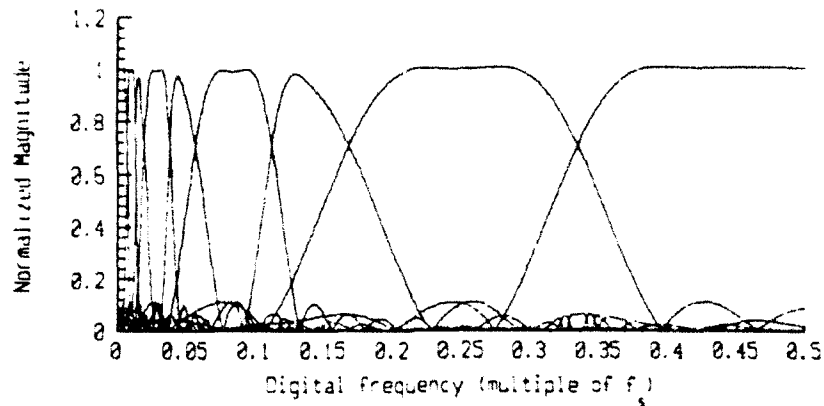


Figure 4.24--Spectral partitioning resulting from four-stage decomposition constructed of structures as in Figure 4.23. The filters indicated are 14-point pseudo-QMF filters designed in [11].

Figure 4.24 illustrates the partitioning of the frequency spectrum which results from a

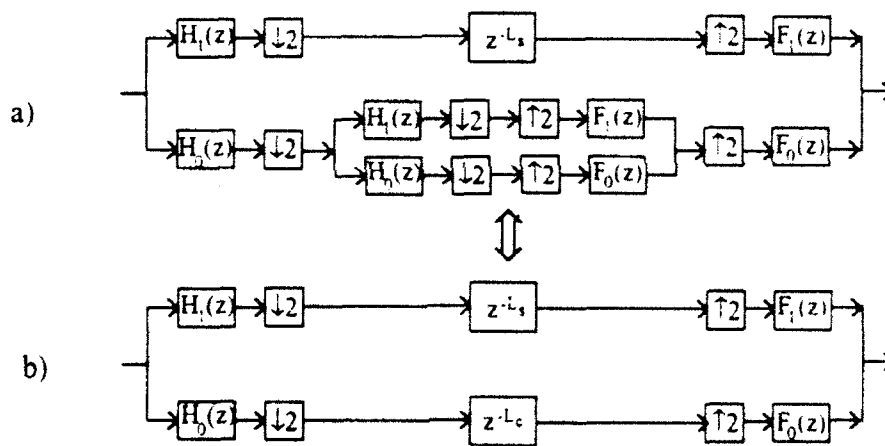


Figure 4.25--Illustration of equivalence of two-stage decomposition-reconstruction structure with one-stage structure with delays in each channel.

In reconstructing sequences decomposed by cascaded filter banks, the issue of delay must be addressed. As was discussed within the context of multirate system theory in Chapter II, a perfect reconstruction filter bank possesses an equivalent system transfer function which is equal to a delay. In decomposition-reconstruction structure "a" of Figure 4.25, the detail channel contains a delay L_c representing, for example, a reconstruction filter bank used, as in Figure

4.21, to decompose the detail sequence into subchannels. The lower branch, the approximation channel, contains a two-channel bank corresponding to the next stage of decomposition. In the equivalent structure in structure "b" of Figure 4.25, the follow-on stage filter bank has been converted to the delay L_c with which it is equivalent if it is a perfect reconstruction filter bank. Obviously, the delay in each channel must be equal. Otherwise, the approximation and detail sequences will be shifted with respect to each other and accurate reconstruction will not occur. Consequently, although a subchannel decomposition filter bank is not indicated in the detail channel of the final decomposition stage in Figure 4.25, if one were installed, an artificial delay in the approximation channel would be necessary.

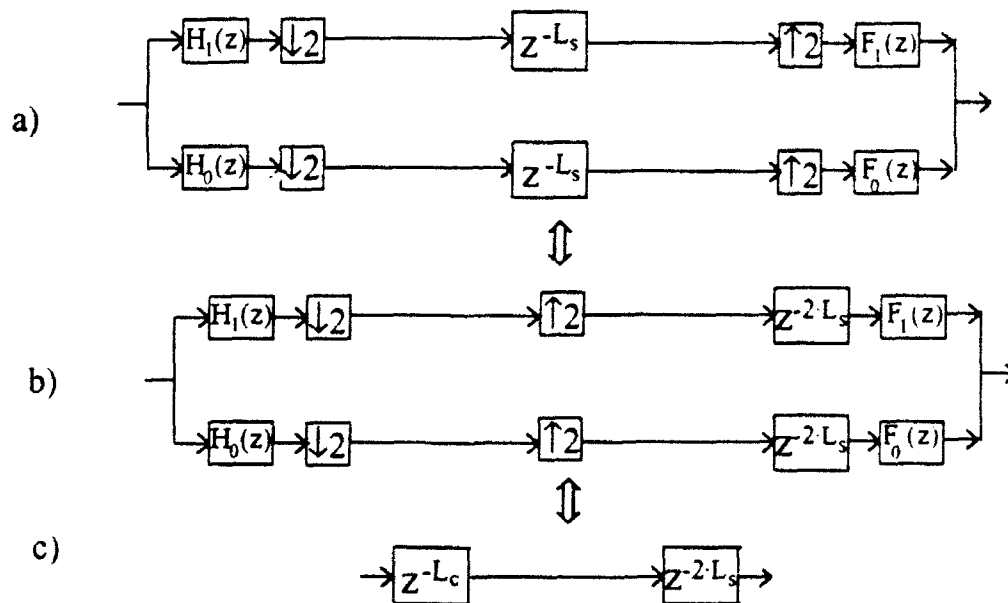


Figure 4.26--Illustration of equivalent structures resulting from transmission of delay occurring in approximation and detail channels of a filter bank multiresolution structure.

Figure 4.26 illustrates the total equivalent delay of a QMF decomposition-reconstructure containing a delay in each channel. In each channel a delay L_s (equal to the order of the filters

used for decomposition into subchannels) is indicated which could include combinations of delays of subchannel decomposition-reconstruction structures, delays from subsequent decomposition-reconstruction stages and artificial delays introduced to resynchronize channel sequences. Since, by (3.9), $[z^{-L_s}]_{\uparrow 2} = z^{-2L_s}$, the total effective delay after the expander in each channel will be twice the delay of the channel prior to the expander. This equivalence is indicated by the transition from structure "a" of Figure 4.26 to structure "b." Furthermore, since the application of FIR filter and application of a delay represent linear operations, the two operations are also commutative. Consequently, as indicated in structure "c" of Figure 4.26b, the total, effective delay of the channel after the decimator can be moved beyond the summation point. Since a sequence reconstructed by a perfect reconstruction QMF bank is simply a delayed version of the original sequence, the total equivalent delay of structure "a" in Figure 4.26 is simply the sum of L_c (the order of the filters used for decomposition into primary channels), the delay of the decomposition-reconstruction QMF bank structure itself, and $2 \cdot L_s$, the contribution from all of the delays introduced into the decomposed channels.

To obtain a characterization of the total delay introduced into each channel of a multiresolution analysis constructed from cascaded filter banks, consider again structure "a" in Figure 4.25 as it would be implemented to reconstruct a sequence decomposed by M stages of the structure depicted in Figure 4.21. First, if a delay of L_s , resulting from a subchannel decomposition-reconstruction structure, is introduced into the detail channel at stage M , of the final stage of decomposition, then an artificial delay of L_s must be introduced into the approximation channel of the same stage to resynchronize the detail and approximation channel

sequences. Consequently, the total delay introduced into the detail and approximation stages consists of the sum of two contributions. The first source includes the delay L_s resulting from decomposition-reconstruction structure corresponding to the decomposition of the detail sequence into subchannels and its corresponding equal delay in the approximation channel. Secondly, a delay L_c corresponding to the primary channel decomposition-reconstructure at stage M must be considered.

Continuing to the next stage, recombining the approximation and detail sequences from stage $M-1$ to form the stage $M-2$ approximation sequence adds a delay of L_c to the doubled equivalent delay present into the approximation sequence of stage $M-1$. As a result, the total delay present in the approximation sequence at stage $M - 2$ is equal to $4 \cdot L_s + 2 \cdot L_c + L_c$. It is therefore necessary to introduce a delay of $4 \cdot L_s + L_c + L_c$ to the detail sequence of stage $M - 2$ to resynchronize that stages approximation and detail sequences.

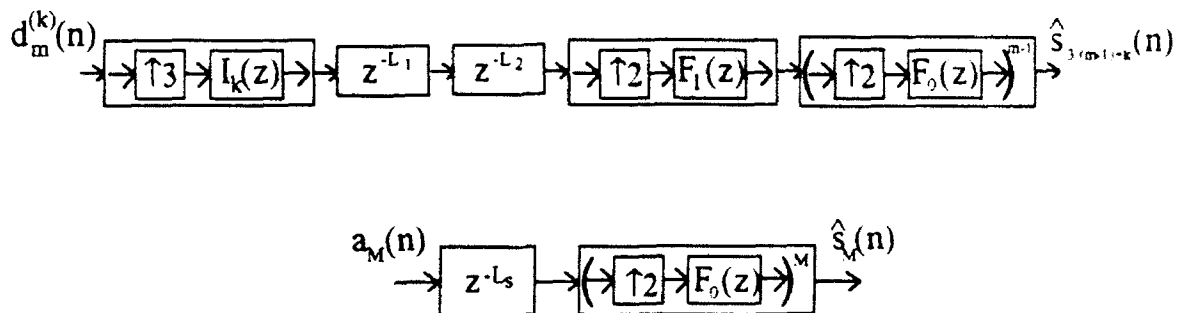


Figure 4.27--Block diagram indicating structure necessary to obtain full expansion by channel from a sequence decomposed by M stages of the structure depicted in Figure 4.23. The values for L_1 and L_2 are defined in (4.94a) and (4.94b), respectively.

To obtain the structure required to obtain a full expansion by channel of the decomposed sequence by M stages of the structure presented in Figure 4.21, inductively the line of reasoning begun in Figures 4.25 and 4.26 must be pursued. The consequences of this induction appear in Figure 4.27. First, some arbitrary stage m , the subchannel sequence $d_m^{(k)}(n)$ must first be expanded and then filtered by the synthesis filter $I_k(z)$ corresponding to its subchannel. Artificial delays from two sources must then be introduced in order to re-synchronize the resultant stage m detail sequence component with its corresponding approximation sequence. The first delay L_1 compensates for the artificial delay of L_c introduced into the approximation sequence at stage M and is evaluated as

$$L_1 = (2^{M \cdot m} - 1) \cdot L_c. \quad (4.94a)$$

The second artificial delay contribution results from the primary approximation channel decomposition-reconstruction performed at all subsequent stages $m+1$ through M and is represented by a geometric series:

$$L_2 = L_c \cdot \sum_{p=0}^{M-m-1} 2^p. \quad (4.94b)$$

Next, the detail sequence component must be expanded and passed once through the primary detail channel synthesis filter. To complete the re-expansion, the sequence is subjected to $m-1$ iterations of expansion followed by filtering with the primary approximation channel synthesis filter. The final stage approximation sequence is fully expanded--as indicated by the second structure of Figure 4.27--by M iterations of expansion followed by filtering with the primary approximation channel synthesis filter. Application of the steps described by Figure

4.27 provides for a decomposed sequence a representation analogous to that depicted in Figure 4.11 for the Laplacian pyramid. The reconstructed sequence is simply the sum of all of the expanded channels or, if applicable, subchannels.

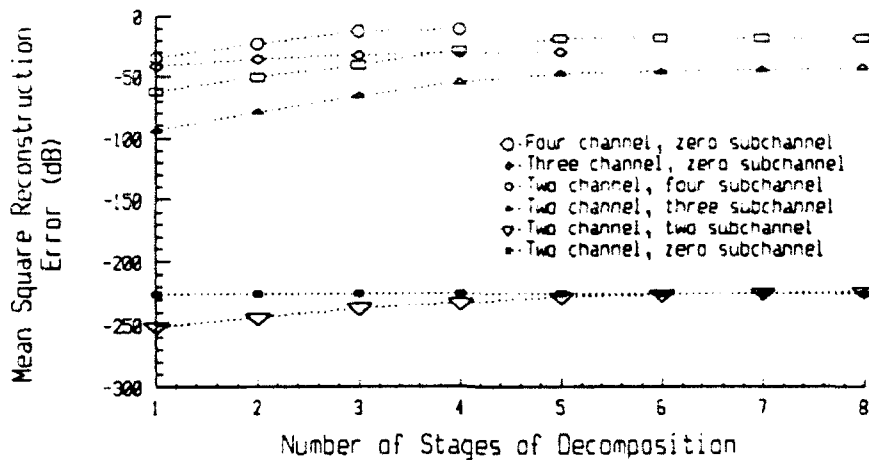


Figure 4.28a--Plots of reconstruction error versus number of decomposition stages for various decomposition stages applied to 256-point, lowpass test sequence produced by (4.74a).

The accuracy of sequence reconstruction is dependent on the number of stages of decomposition performed and on the quality of the filter bank. For several stages of decomposition, small errors resulting from filter imperfections, such as roundoff error, accumulate and corrupt the reconstruction process. To obtain optimum results, filter banks which strictly satisfy the perfect reconstruction criteria should be used. In using pseudo-QMF filter banks which do not satisfy the perfect reconstruction, poorer results will be obtained. These concepts are illustrated by Figures 4.28a and 4.28b. Figure 4.28a indicates reconstruction errors for multiresolution structures applied to the test sequence generated using (4.74a).

The lowpass test sequence from (4.74a) was constructed from low-frequency harmonics. From the spectral partition diagrams presented for the various multiresolution structures

considered, the spectral resolution of the multiresolution structures was greatest in the lower regions of the frequency spectrum. In Figure 4.28b, the reconstruction error for the highpass test sequence (4.74b) is presented. Illustrating results for the test sequence generated by (4.74b), Figure 4.28b illustrates multiresolution technique performance for signals constructed from frequency components located in the upper half of the frequency spectrum below the Nyquist frequency.

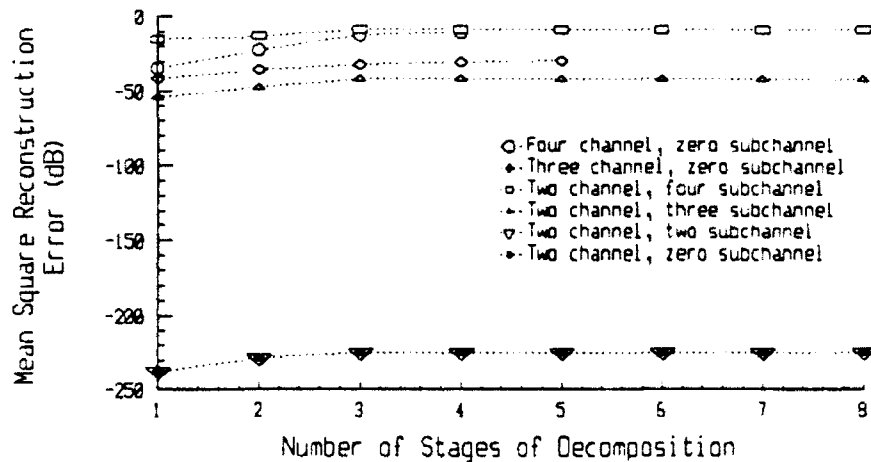


Figure 4.28b--Plots of reconstruction error versus number of decomposition stages for various decomposition stages applied to 256-point test sequence produced by (4.74b).

In the case of both test sequences, the lowest reconstruction errors resulted from multiresolution structures comprised strictly of perfect reconstruction filter banks. In two-channel, zero-subchannel and two-channel, two-subchannel structures, the filters used were all obtained from Daubechies' orthonormal wavelet and scaling function supported on $[0, 13]$. Consequently, the multiresolution analyses obtained were equivalent to true, orthogonal decompositions.

For the two-channel, three-subchannel, the two-channel, four-subchannel and the three-channel, zero-subchannel cases, the structures all entailed the use of pseudo-QMF banks which did not strictly satisfy the perfect reconstruction criteria. The structures constructed using the three-channel filter banks employed the set of filters designed by Vaidyanathan in [11]. The four-channel filter bank used a set of 30-point, fourth-band filters designed by spectral factorization of filters obtained by the McClellan Parks algorithm. The design process for the four-channel filter bank will be outlined in Chapter V. Because of failure to satisfy the perfect reconstruction property, structures using these methods consistently produced greater reconstruction error.

TABLE 4.1--PARTITION OF SPECTRUM RESULTING FROM EIGHT-STAGE, TWO-CHANNEL, ZERO-SUBCHANNEL MULTIREOLUTION DECOMPOSITION.

Decomposition stage	Scale	Spectral bin lower bound	Spectral bin Upper bound
Stage 1 Detail	0	$2^{-2} \cdot f_s$	$2^{-1} \cdot f_s$
Stage 2 Detail	1	$2^{-3} \cdot f_s$	$2^{-2} \cdot f_s$
Stage 3 Detail	2	$2^{-4} \cdot f_s$	$2^{-3} \cdot f_s$
Stage 4 Detail	3	$2^{-5} \cdot f_s$	$2^{-4} \cdot f_s$
Stage 5 Detail	4	$2^{-6} \cdot f_s$	$2^{-5} \cdot f_s$
Stage 6 Detail	5	$2^{-7} \cdot f_s$	$2^{-6} \cdot f_s$
Stage 7 Detail	6	$2^{-8} \cdot f_s$	$2^{-7} \cdot f_s$
Stage 8 Detail	7	$2^{-9} \cdot f_s$	$2^{-8} \cdot f_s$
Stage 8 Approximation	8	0	$2^{-9} \cdot f_s$

Inductively extending the results of the spectral partition diagram (4.20) corresponding to this structure provides insight into the relationship between scale and frequency. The first spectral bin, which coincides with scale zero in Figure 4.29a, constrains the region of the frequency spectrum from $0.5 \cdot f_s$ to $0.25 \cdot f_s$. A scale of unity coincides with the region of the

frequency spectrum from $0.25 \cdot f_s$ to $0.125 \cdot f_s$, the region corresponding to the signal detail extracted during the first stage of decomposition.. Inductively, therefore, a scale of m , corresponding to the signal detail extracted at the m^{th} stage of decomposition, coincides with the spectral bin partitioning the region from $2^{-(m-1)} \cdot f_s$ to $2^{-(m-2)} \cdot f_s$. This subdivision is tabulated in Table 4.1.

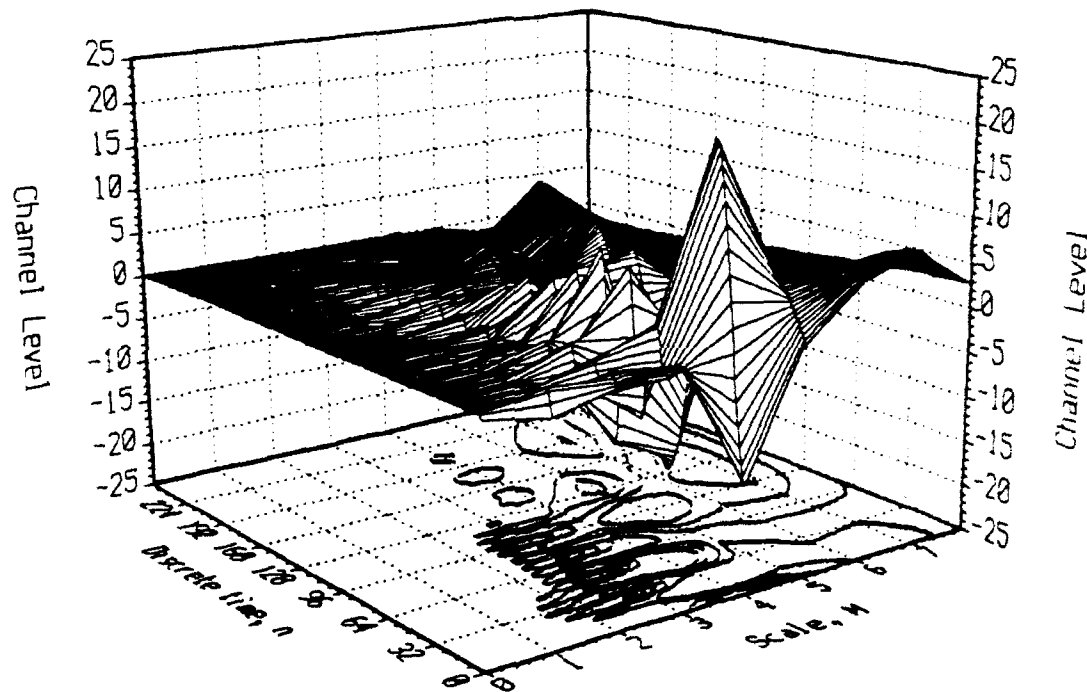


Figure 4.29a--Surface plot of decomposition of lowpass test sequence (4.74a) using eight-stage, two-channel, zero-subchannel multiresolution structure constructed from cascaded QMF banks. The filters were obtained from Daubechies' orthonormal wavelet and scaling function supported on $[0, 13]$.

Figures 4.29a and 4.29b demonstrate the full expansion by channel of decomposition of sequences (4.74a) and (4.74b), respectively. In Figure 4.29a, the depiction of the lowpass sequence (4.74a), the resolution of scale of the decomposition at low-frequencies is apparent. The component of sequence (4.74a) located at digital frequency $2 \cdot \pi \cdot 9/512 (\approx 0.018 \cdot f_s)$ falls in

the range of $2^{-5} \cdot f_s$ to $2^{-6} \cdot f_s$ which corresponds to a scale of four. In Figure 4.29a, a series of circular contours centered on the scale axis for $m = 4$ can be observed from approximately samples 32 to 216. Similarly, the spectral component located at digital frequency $2 \cdot \pi \cdot 31/512$ ($\approx 0.06 \cdot f_s$) lies in the region $2^{-5} \cdot f_s$ to $2^{-4} \cdot f_s$ corresponding to a scale of $m = 3$. As a non-integer power of two, the location $0.06 \cdot f_s \approx 2^{-4.05}$ which is very near the boundary between adjacent scales two and three. Consequently, much of the component's energy appears spread between scales two and three. The component at digital frequency $\pi/256$ ($\approx 0.002 \cdot f_s$) exists at the boundary between scales six and seven. The indication of this component, which completes only a single oscillation during the duration of the test sequence, appears spread between the two scales.

Figure 4.29b presents the two-channel, zero-subchannel decomposition of highpass test sequence (4.74b). The relative coarseness of the multiresolution decomposition in the higher regions of the frequency spectrum becomes apparent in Figure 4.29b. Because of the rapid variations with respect to time, the contour plot in Figure 4.29b is difficult to read. However, information can be gained from examining the surface plot. Again, comparing the plot with the spectral partition diagram, the spectral component of (4.74b) which lies at a digital frequency of $2 \cdot \pi \cdot 27/512$ ($\approx 0.105 \cdot f_s$) falls within the region of 2^{-3} to 2^{-4} corresponding to a scale of $m = 2$ as plotted in Figure 4.29b. The scale of $m = 2$ corresponds to the range of peaks with highest amplitude. The spectral component located at $2 \cdot \pi \cdot 55/256$ ($\approx 0.215 \cdot f_s$) is contained within the region 2^{-2} to 2^{-3} which corresponds to a scale of $m = 1$ as plotted in Figure 4.29b. The

indication of this component is recognizable in the second range of peaks between the highest at $m = 2$ and the range that runs along the edge of the surface plot. Finally, the spectral component at digital frequency $2 \cdot \pi \cdot 113/256 (= 0.44 \cdot f_s)$ lies within the region of 2^{-1} to 2^{-2} and is indicated in the range of peaks at scale $m = 0$ which runs along the edge of the surface plot. For the highpass test sequence, each of the harmonic components can be resolved. However, in the case of the highest frequency components, the spectral separation is approximately $0.2 \cdot f_s$. Furthermore, each of the three spectral components fell within adjacent spectral bins. Consequently, the example demonstrates the maximum resolution for a two-channel, zero-subchannel multiresolution structure.

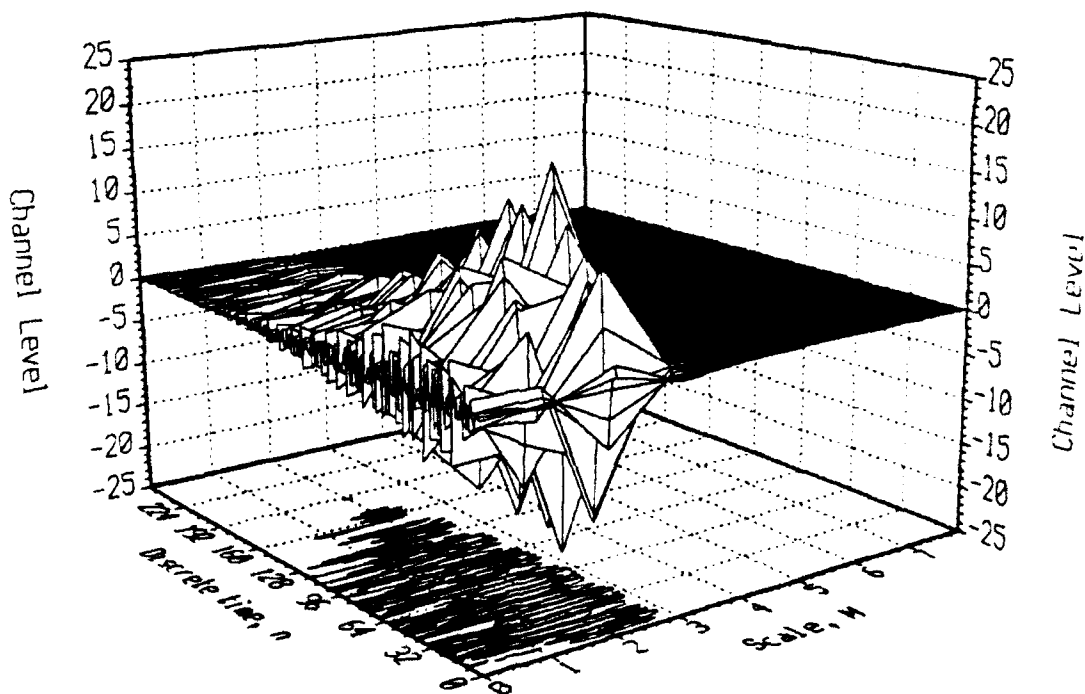


Figure 4.29b--Surface plot of decomposition of highpass test sequence (4.74b) using eight-stage, two-channel, zero-subchannel multiresolution structure constructed from cascaded QMF banks. The filters were obtained from Daubechies' orthonormal wavelet and scaling function supported on $[0, 13]$.

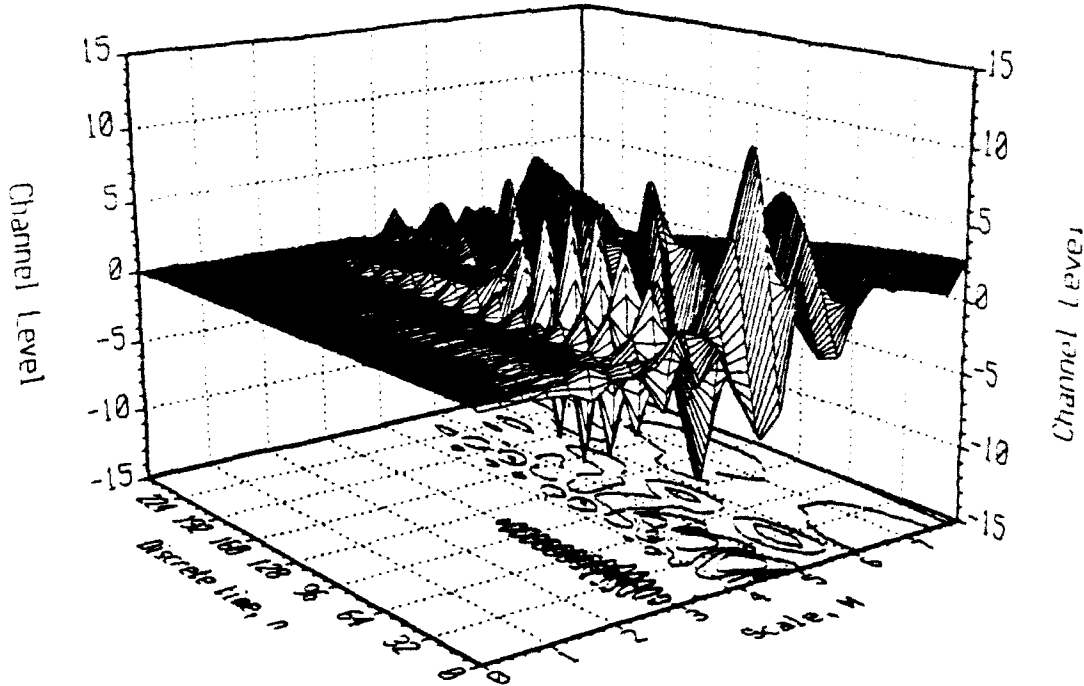


Figure 4.30a--Surface plot of decomposition of lowpass test sequence (4.74a) using eight-stage, two-channel, three-subchannel multiresolution structure constructed from cascaded QMF banks. The filters were obtained from Daubechies' orthonormal wavelet and scaling function supported on $[0, 13]$. The subchannel decomposition was performed with pseudo-QMF filters designed in [11].

Figures 4.30a and 4.30b provide two-channel, three-channel decompositions of the lowpass test sequence (4.74a) and the highpass test sequence (4.74b), respectively. From the spectral partition diagram for this structure, Figure 4.22, each spectral region $2^{-(m-2)}$ to $2^{-(m-1)}$ is further subdivided into three subregions. For the general case, a multiresolution structure constructed to divide, at each stage, the detail sequence into M subchannels, at the m^{th} stage of decomposition, the k^{th} subchannel corresponds to the region of spectrum contained in the interval

$$\left[\left(2^{-(m+2)} + \frac{k-1}{M} \cdot (2^{-(m+1)} - 2^{-(m+2)}) \right) \cdot f_s, \left(2^{-(m+2)} + \frac{k}{M} \cdot (2^{-(m+1)} - 2^{-(m+2)}) \right) \cdot f_s \right].$$

Because of the increase in the density of spectral subdivision afforded by decomposition of the lowpass test sequence into subchannels, the time-scale localization presented in Figure

4.30a provides time-scale localization which is improved over results presented in Figure 4.29a. In particular, the component at digital frequency $2 \cdot \pi \cdot 31/512$ clearly localized at a scale of three instead of being partially spread over adjacent scales as occurred in Figure 4.29a. Similarly, the component at digital frequency $2 \cdot \pi \cdot 9/512$, which roughly corresponds to a digital frequency of $2^{5.8} \cdot f_s$, can be recognized to exist primarily between scales of four and five. The component characterized by the lowest frequency is still recognizable in the vicinity of scales six and seven. However, an indication appears between scales of five and six which cannot be accounted for based on the components known to exist in the test sequence. This unaccounted for component may have appeared as a result of spreading from the component at scale six.

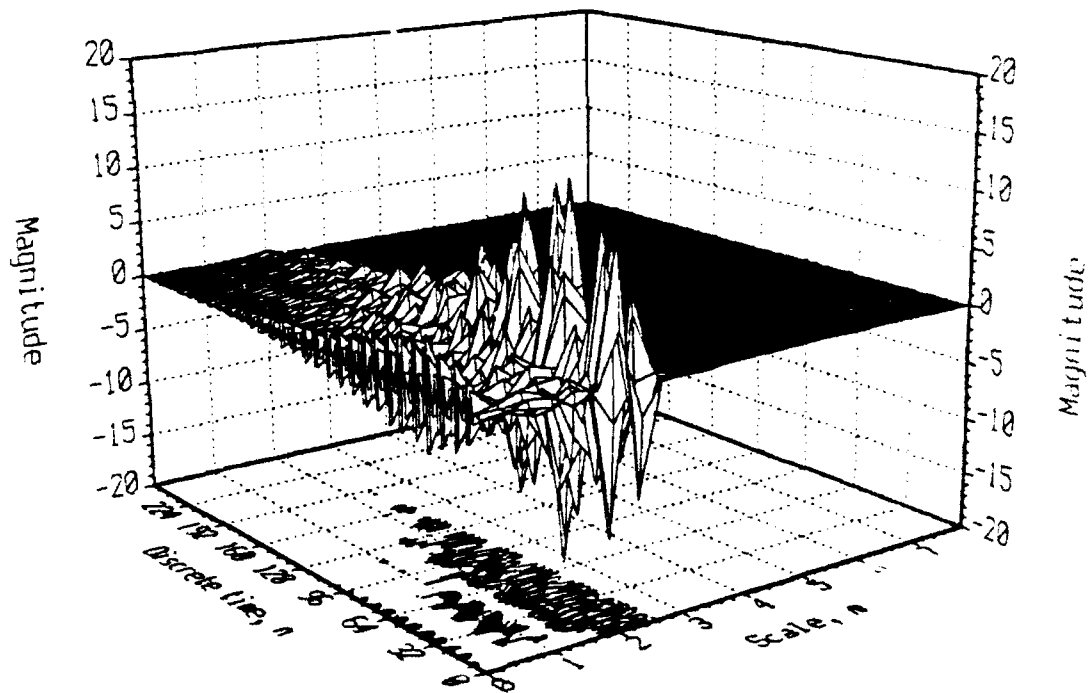


Figure 4.30b--Surface plot of decomposition of highpass test sequence (4.74b) using eight-stage, two-channel, three-subchannel multiresolution structure constructed from cascaded QMF banks. The filters were obtained from Daubechies' orthonormal wavelet and scaling function supported on $[0, 13]$. The subchannel decomposition was performed with pseudo-QMF filters designed in [11].

In the case of two-channel, three-subchannel decomposition, the spectral components of the highpass test sequence (4.74b) have also become more distinct. In the plot of Figure 4.30b, because the spectral content of the test sequence has been localized in specific subchannels and excluded from others, resulting in an indication of three separate components. Consequently, the indication provided by the contour plot constitutes a more useful display than the contour plot for Figure 4.29a.

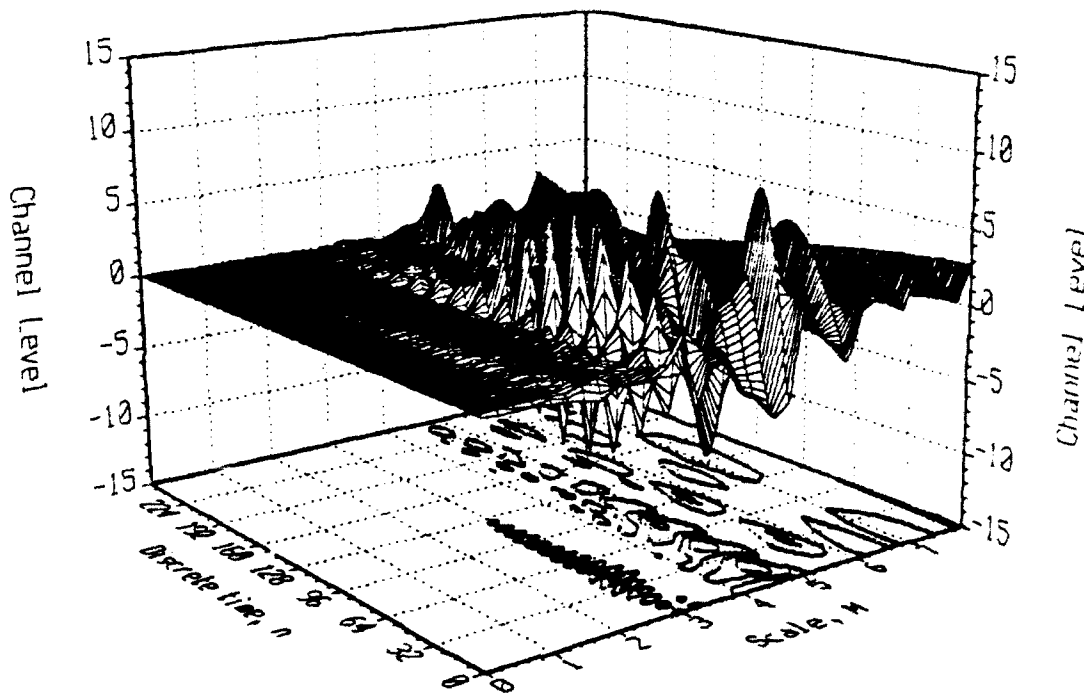


Figure 4.31a--Surface plot of decomposition of lowpass test sequence (4.74a) using eight-stage, two-channel, four-subchannel multiresolution structure constructed from cascaded QMF banks. The filters were obtained from Daubechies' orthonormal wavelet and scaling function supported on $[0, 13]$. The subchannel decomposition was performed with pseudo-QMF filters obtained from spectral factorization of fourth-band filters designed by the McClellan-Parks method.

Examining Figure 4.31a, a plot of a two-channel, four-subchannel decomposition of lowpass test sequence (4.74a), increasing structural complexity from three to four subchannels provides some improvement in localization for the test sequence presented. The component of

digital frequency $2\pi \cdot 9/512$ appearing between scales four and five have become distinct from the indication unaccounted for between scales five and six. Consequently, it is likely that the false indication resulted from spillover of energy from the component at $2\pi \cdot 2/512$. Between scales five and six, the resolution of the decomposition using four subchannels becomes $0.25 \cdot 2^{-6} \cdot f_s (=f_s/512)$. Beneath those scales the resolution continues to increase logarithmically in base two. It appears, therefore, as though the four-subchannel decomposition may provide excessive resolution for the test sequence demonstrated. In general, the principal benefits of decomposing sequence into subchannels occurs in the higher regions of the frequency spectrum.

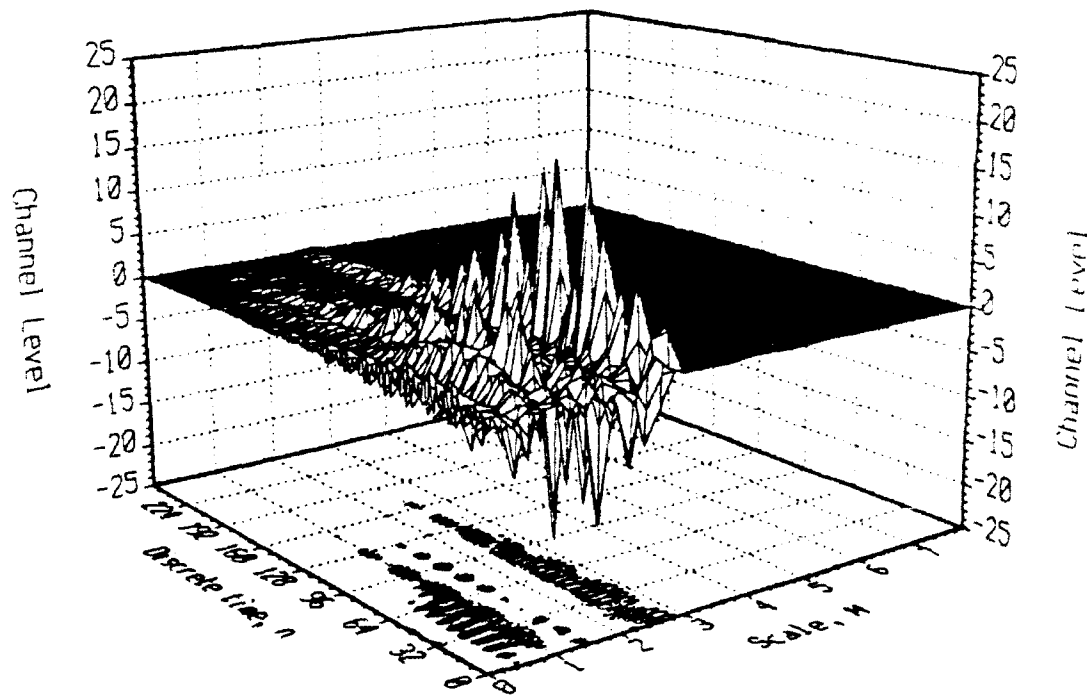


Figure 4.31b--Surface plot of decomposition of highpass test sequence (4.74b) using eight-stage, two-channel, four-subchannel multiresolution structure constructed from cascaded QMF banks. The filters were obtained from Daubechies' orthonormal wavelet and scaling function supported on $[0, 13]$. The subchannel decomposition was performed with pseudo-QMF filters obtained from spectral factorization of fourth-band filters designed by the McClellan-Parks method.

Figure 4.31b further illustrates the principal afforded by subchannel decomposition. Specifically, in Figure 4.31b, an improvement in the resolution of the upper regions of the frequency spectrum is evident. In Figure 4.31b, a plot of the two-channel, four-subchannel decomposition of highpass test sequence (4.74b), the sequence component at digital frequency $2\pi \cdot 113/256$ has been localized as distinct from scale zero. Furthermore, as compared with the two-channel, three-subchannel plot of figure 4.30b, the test sequence component at digital frequency $2\pi \cdot 27/256$ exhibits improved localization.

TABLE 4.2--PARTITION OF SPECTRUM RESULTING FROM FIVE-STAGE, THREE-CHANNEL, ZERO-SUBCHANNEL MULTIREOLUTION DECOMPOSITION.

Decomposition stage	Multiresolution scale	Spectral bin lower bound	Spectral bin upper bound
Stage 1	Scale 0.0	$f_s/3$	$f_s/2$
	Scale 0.5	$f_s/6$	$f_s/3$
Stage 2	Scale 1.0	$f_s/9$	$f_s/6$
	Scale 1.5	$f_s/18$	$f_s/9$
Stage 3	Scale 2.0	$f_s/27$	$f_s/18$
	Scale 2.5	$f_s/54$	$f_s/27$
Stage 4	Scale 3.0	$f_s/81$	$f_s/54$
	Scale 3.5	$f_s/162$	$f_s/81$
Stage 5	Scale 4.0	$f_s/243$	$f_s/162$
	Scale 4.5	$f_s/486$	$f_s/243$
	Scale 5.0	0	$f_s/486$

As indicated previously, decomposition into three primary channels provides base three logarithmic partition of the frequency spectrum. Specifically, the first stage of decomposition divides the frequency spectrum into spectral bins covering the regions $f_s/6$ to $2 \cdot f_s/6$ and $2 \cdot f_s/6$ to $3 \cdot f_s/6$. During the second stage of decomposition, the lower third of the frequency spectrum is

partitioned along intervals $f_s/18$ to $2 \cdot f_s/18$ and from $2 \cdot f_s/18$ to $3 \cdot f_s/18$. At stage m , the signal detail extracted will occupy the spectral regions $f_s/(2 \cdot 3^m)$ to $2 \cdot f_s/(2 \cdot 3^m)$ and from $2 \cdot f_s/(2 \cdot 3^m)$ to $3 \cdot f_s/(2 \cdot 3^m)$. Table 4.2 presents tabulated information regarding the spectral subdivision occurring from a three-channel, zero-subchannel multiresolution decomposition.

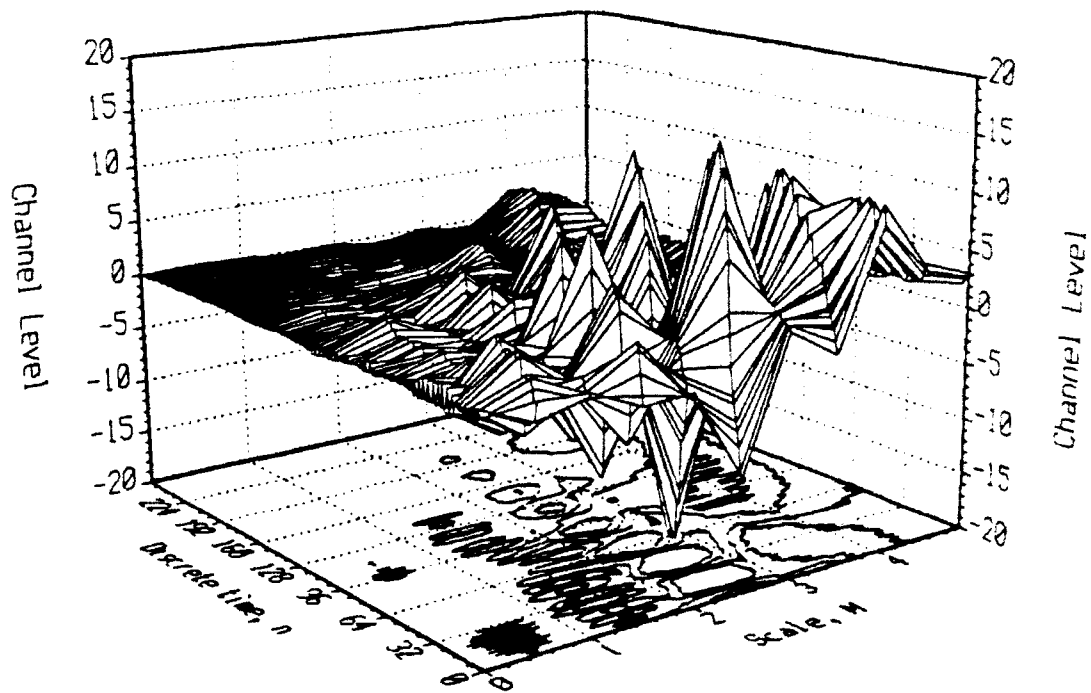


Figure 4.32a--Surface plot of decomposition of sequence (4.74a) using five-stage, three-channel, zero-subchannel multiresolution structure constructed from cascaded QMF banks. The decomposition was performed with pseudo-QMF filters designed in [11].

Finally, Figures 4.32a and 4.32b present the results of three-channel, zero-subchannel decomposition of the lowpass test sequence (4.74a) and highpass test sequence (4.74b), respectively. Because of the base three logarithmic partitioning of the frequency spectrum, localization of sequence spectral components in the lower portion of the frequency spectrum will be improved over the localization resulting from a two-channel decomposition. Specifically, for

sequence (4.74a), component at digital frequency $2\pi \cdot 2/512$ is located, according to Table 4.2, in the vicinity of the boundary between scales 4.0 and 4.5. In fact, most of the energy of this component appears in the channel corresponding to scale 4.0. Similarly, the component at $2\pi \cdot 9/512$ is located in the vicinity of the boundary between scales 2.5 and 3. The energy of the appears mostly at scale 2.5. Finally, the energy of the component at digital frequency $2\pi \cdot 31/512$ is indicated at scale 1.5. An unexplainable indication appears at a scale of 0.5 between samples zero and 32 and also at approximately sample 96. From Figure 4.24, the filters from which the three-channel filter bank was constructed produced greater stopband error than the two-channel filter bank. Consequently, energy from the sequence appears to leak, producing less precise localization of components of the test sequence.

With regard to Figure 4.32b which presents the three-channel, zero-subchannel of the highpass test sequence (4.74b), the structure appears to localize sequence components approximately as well as the two-channel, zero subchannel. Comparing the two-channel, zero-subchannel frequency partition diagram Figure 4.20 with the corresponding diagram Figure 4.24 for the three-channel, zero-subchannel structure, the two methods provide very similar resolution in the upper regions of the frequency spectrum. Specifically, the three-channel structure divides the spectral region between $f_s/2$ and $f_s/6$ into two channels while the two-channel structure divides the region between $f_s/2$ and $f_s/4$ into two channels. This similarity is reflected in the Figure 4.32b. The component at digital frequency $2\pi \cdot 27/256$ appears as the largest range of peaks at a scale of two. The component at digital frequency $2\pi \cdot 113/256$ is

indicated at a scale of zero along the edge of the surface. The indication of the component at $2\pi \cdot 55/256$, however, is less well localized. Indications of this final component appear to be present at scales of 0.5 and 1.0.

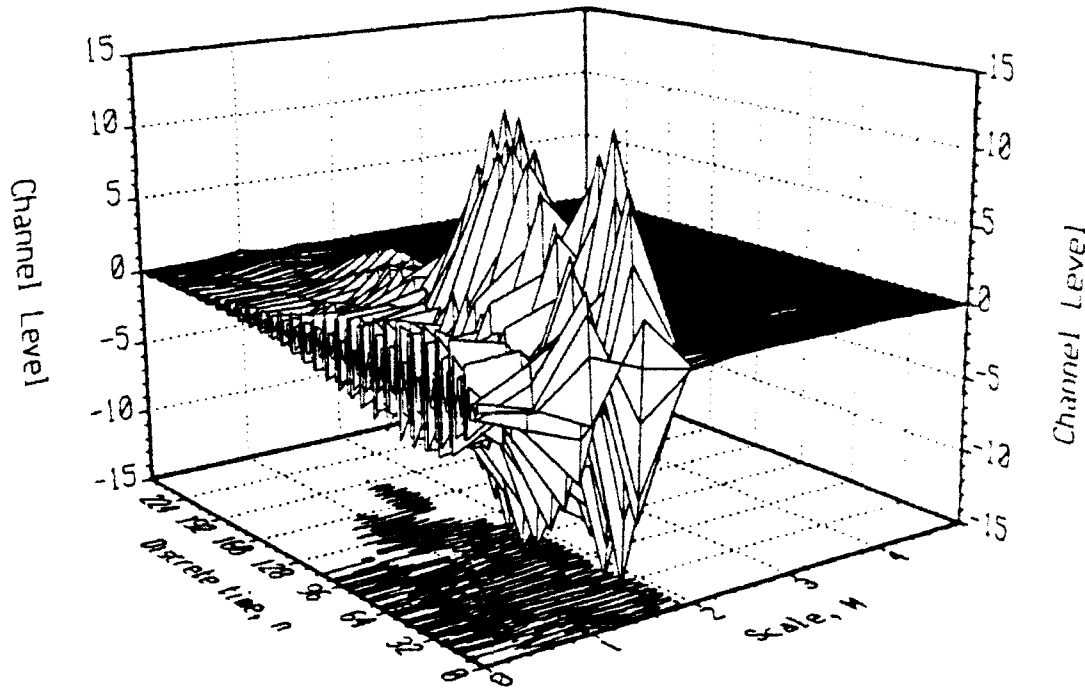


Figure 4.32b--Surface plot of decomposition of highpass test sequence (4.74b) using five-stage, three-channel, zero-subchannel multiresolution structure constructed from cascaded QMF banks. The decomposition was performed with pseudo-QMF filters designed in [11].

Finally, the three-channel structure demonstrated in Figure 4.32a presents a noteworthy phenomenon. The surface in the higher scale (lower frequency) regions possesses a jagged texture. When the surface resulting from expansion by a filter is characterized by rapid variations such as are shown in Figure 4.32a, the filter is said to lack *regularity*. The appearance of this jagged quality is noteworthy because it occurs in the high-scale channels containing the slowly varying components. For the the two-channel structures, the surfaces in the regions of

higher scales presented relatively smooth appearances. The non-regular surface observed in Figure 4.32a increases the difficulty in reading of the surface plot. The issue of regularity will be addressed again in Chapter V.

To provide an overall assessment of the three-channel structure, it affords greater resolution at higher scales (lower frequencies) without incurring the increase in structure complexity involved in performing decomposition into subchannels. Compared to the two-channel, zero-subchannel structure, the structure provided somewhat improved resolution. However, the performance in the high-frequency regions is not as great. Consequently, included among the issues in deciding whether to employ three channels or two-channels with subchannels is whether resolution at higher frequencies is critical.

V. BASIS FUNCTIONS AND FILTERS FOR MULTIREOLUTION DECOMPOSITION

A. INTRODUCTION

Chapter IV developed the theory of multiresolution decomposition and demonstrated its equivalence to the cascading of QMF bank structures described in Chapter III. In Chapter IV, the wavelets and scaling functions used for multiresolution signal decomposition were addressed only in the most abstract sense. In the present chapter the nature of these functions will be addressed in greater detail. Section B outlines some of the basic concepts of the theory of two-scale difference equations, the class of equations from which wavelets and scaling functions were, in Chapter IV, shown to be derived. In Section C, some of the properties of Daubechies' orthonormal wavelets and scaling functions will be considered. Finally, Section D will return to a filter bank perspective for the study of multiresolution decompositions. Some basics of the theory of perfect reconstruction and pseudo-QMF bank filters will be addressed.

It must be noted that a number of approaches exist for the construction of wavelets and scaling functions which will not be addressed in the present study. One of the earliest methods which has subsequently become relatively well-developed is to construct wavelet and scaling function filters from polynomial splines [36, 37]. In the construction of wavelets from splines, a polynomial spline is used for the scaling function. Since polynomial splines of non-zero order are not orthogonal with respect to integer translation, the scaling function family constitutes a frame in the sense described in Chapter 2. The biorthogonal basis functions which complement the polynomial splines to complete the frame can be constructed from, among other methods,

using recursive (IIR) filtering techniques. Finally, the design of wavelets has been approached from an optimization theory perspective, as well [38].

B. TWO-SCALE DIFFERENCE EQUATIONS

In equation (4.23) (repeated here for convenience), it was shown that scaling functions represent the solutions to two-scale difference equations:

$$\frac{1}{2} \cdot \phi\left(\frac{u}{2}\right) = \sum_k h(k) \cdot \phi(u - k). \quad (5.1)$$

Before attempting to solve (5.1), it is first useful to consider some of its properties. The development which follows makes the assumption that ϕ is a real function. However, the results can easily be generalized to complex functions as well. First, integrating each side of (5.1) over its region of support produces [27]

$$\frac{1}{2} \cdot \int \phi\left(\frac{u}{2}\right) du = \sum_k h(k) \cdot \int \phi(u - k) du. \quad (5.2)$$

Applying the changes of variables $v = u/2$ and $w = u - k$ to the appropriate sides of (5.2) results in

$$\int \phi(v) dv = \sum_k h(k) \cdot \int \phi(w) dw. \quad (5.3)$$

Now, each side of (5.3) contains a common factor of $\int \phi(u) du$, which, if it is non-zero, can be cancelled on both sides of the equation resulting in

$$\sum_k h(k) = 1. \quad (5.4)$$

Two properties have now been specified for the families of scaling functions which represent solutions to two-scale equations. The first is (5.4) which indicates that the filter whose

impulse response is $h(k)$ possess a DC gain of unity. The second, which was necessary to obtain (5.4) requires that

$$\int \phi(u) du \neq 0. \quad (5.5)$$

In fact, if the objective is to construct orthonormal basis functions, it is desirable to specify that $\int \phi(u) du \equiv 1$.

If the condition is imposed that the family $\{\phi(u - k)\}_{k \in \mathbb{Z}}$ constitutes an orthonormal basis, then another interesting property for $h(k)$ can be obtained. First, the change of variables $t = 2 \cdot u$ is made for (5.1) resulting in

$$\phi(t) = 2 \cdot \sum_k h(k) \cdot \phi(2 \cdot t - k). \quad (5.6)$$

Now, if ϕ is orthonormal with respect to integer translation, then $\int \phi(t - k) \phi(t - j) dt = \delta_{j,k}$ where δ is Kronecker's delta function. Furthermore, $\int \phi(2 \cdot t - k) \phi(2 \cdot t - j) dt = \delta_{j,k} / 2$ also holds.

Consequently, evaluation of the projection of integer translates of ϕ onto each other yields

$$\int \phi(t - m) \cdot \phi(t - n) dt = 4 \cdot \sum_k \sum_j h(k) \cdot h(j) \cdot \int \phi(2 \cdot (t - m) - j) \cdot \phi(2 \cdot (t - n) - k) dt. \quad (5.7)$$

Applying the change of variables $u = 2 \cdot (t - m)$ to (5.7) produces

$$\int \phi(t - m) \cdot \phi(t - n) dt = 2 \cdot \sum_k \sum_j h(k) \cdot h(j) \cdot \int \phi(2 \cdot u - j) \cdot \phi(u + 2 \cdot (m - n) - k) dt. \quad (5.8)$$

Next, applying the consequences of the assumption of orthonormality to both sides of (5.8), results in

$$\delta_{m,n} = 2 \cdot \sum_k \sum_j h(k) \cdot h(j) \cdot \delta_{j, k - 2(m - n)}. \quad (5.9)$$

Finally, by the summation sifting property of the Kronecker delta function,

$$\delta_{m,n} = 2 \cdot \sum_k h(k) \cdot h(k - 2 \cdot (m - n)). \quad (5.10)$$

Equation (5.10) provides the basis for at least two conclusions. First, for the case when $m = n$,

$$\sum_k h^2(k) = \frac{1}{2}. \quad (5.11)$$

In other words, if the two-scale difference equation solution ϕ is orthonormal with respect to integer translation, then the sum of the squares of the coefficients of the corresponding generating filter is one half.

A second interpretation, made by Vetterli [25], state that the impulse response $h(k)$ of the generating filter is orthogonal respect to even translates of itself. This is equivalent to another interpretation. Define the sequence $g(n)$ from the convolution of $h(n)$ with its own time reversal $\tilde{h}(n)$:

$$g(n) = 2 \cdot \sum_k h(k) \cdot \tilde{h}(n - k). \quad (5.12)$$

If $g(n)$ is defined in this manner, then (5.10) is equivalent to the expression

$$g_{\downarrow 2}(n) = g(2 \cdot n) = \delta_{0,n}. \quad (5.13)$$

Now, (5.13) is equivalent to (4.78). Therefore, the filter $g(n)$ is an à trous filter in the sense described by Shensa [31] or a half-band filter in the sense described by Mintzer [32].

Furthermore, (5.13) requires that the length of $h(k)$ be an even integer [25]. If the length of h were an odd integer L , then $g(L - 1) = 2 \cdot h(0) \cdot h(L-1) \neq 0$, and (5.13) would not hold. Finally, the evaluating the Z-transform of (5.12) results in

$$G(z) = H(z) \cdot \tilde{H}(z) = H(z) \cdot H(1/z). \quad (5.14)$$

By (5.14), $H(z)$ is simply a spectral factor of a half-band filter. This concept will be employed later in Section D of this chapter within the context of designing filters for QMF banks.

Solving for scaling equations given an appropriate filter can be performed in either the time domain or in the Fourier domain. The Fourier-domain solution begins with Fourier transformation of (5.1), which was shown in (4.36b) to produce an expression equivalent to

$$\hat{\phi}(\omega) = H(e^{j\frac{\omega}{2}}) \cdot \hat{\phi}\left(\frac{\omega}{2}\right). \quad (5.15)$$

By induction, (5.15) produces [27]

$$\hat{\phi}(\omega) = \hat{\phi}(0) \cdot \prod_{k=1}^{\infty} H(e^{j\omega 2^k}). \quad (5.16a)$$

Now, if the family of scaling functions ϕ is orthonormal, then $\int \phi(u) du = 1$ which is equivalent to $\hat{\phi}(0) = 1$. Therefore, (5.16a) becomes

$$\hat{\phi}(\omega) = \prod_{k=1}^{\infty} H(e^{j\omega 2^k}). \quad (5.16b)$$

The Fourier transform of the scaling function ϕ is simply the infinite product of progressively more dilated versions of the Discrete Fourier Transform (DFT) of the generating filter $h(k)$. Moreover, as the product index k tends towards infinity, the DFT term $H(e^{j\omega 2^k})$ on the right-hand side of (5.16b) becomes infinitely spread out in the Fourier domain. The Fourier transform of ϕ , therefore, has an infinite region of support which indicates the possibility of finite support in the time domain. Compact support of the scaling function ϕ is highly desirable since, because of how $h(k)$ was defined in equation (4.23), only a compactly supported scaling function will produce a finite impulse response filter.

To solve the scaling function in the time domain, it is first convenient to absorb the factor of two on the right hand side of (5.6) into the filter coefficients by defining $h_{(2)}(k) = 2 \cdot h(k)$. Consequently, an equivalent form for (5.6) becomes

$$\phi(t) = \sum_k h_{(2)}(k) \cdot \phi(2 \cdot t - k). \quad (5.17a)$$

The time-domain solution of (5.17) begins by solving for values of the function ϕ at integer points in its domain [39]. Consequently, the equation to be solved becomes

$$\phi(n) = \sum_k h_{(2)}(k) \cdot \phi(2 \cdot n - k). \quad (5.17b)$$

Now, if the scaling function ϕ is strictly supported on the region $[0, 2 \cdot L - 1]$ and its generating filter $h(k)$ is of length $2 \cdot L - 1$ for some inter L , then (5.17b) can be expressed in matrix form as

$$\begin{pmatrix} \phi(0) \\ \phi(1) \\ \vdots \\ \phi(2 \cdot L - 1) \end{pmatrix} = \begin{pmatrix} h_{(2)}(0) & 0 & 0 & \cdots & 0 \\ h_{(2)}(2) & h_{(2)}(1) & h_{(2)}(0) & \cdots & 0 \\ \vdots & \ddots & \ddots & \ddots & \vdots \\ 0 & \cdots & h_{(2)}(2 \cdot L - 1) & h_{(2)}(2 \cdot L - 2) & h_{(2)}(2 \cdot L - 3) \\ 0 & \cdots & 0 & 0 & h_{(2)}(2 \cdot L - 1) \end{pmatrix} \begin{pmatrix} \phi(0) \\ \phi(1) \\ \vdots \\ \phi(2 \cdot L - 1) \end{pmatrix} \quad (5.18)$$

It is obvious that (5.18) is simply an eigenvalue problem. The vector containing the values of the scaling function ϕ for integer arguments is simply the eigenvector of a unit eigenvalue for the double-right-shift matrix of filter coefficients in (5.18).

Now that the value of the scaling function ϕ has been solved for integer arguments, the next step is to rewrite (5.17b) in a form that will yield half-integer values.

$$\phi\left(\frac{n}{2}\right) = \sum_k h_{(2)}(k) \cdot \phi(n - k). \quad (5.18)$$

Equation (5.18) is obviously a simple convolution, nevertheless, insight is gained from expressing it in matrix form:

$$\begin{pmatrix} \phi(\frac{0}{2}) \\ \phi(\frac{1}{2}) \\ \vdots \\ \phi(\frac{2 \cdot L - 1}{2}) \end{pmatrix} = \begin{pmatrix} \phi(0) & 0 & \dots & 0 \\ \phi(1) & 0 & \dots & 0 \\ \phi(2) & \phi(0) & \ddots & \vdots \\ \vdots & \vdots & \ddots & \vdots \\ \phi(2 \cdot L - 1) & \phi(2 \cdot L - 3) & \ddots & \phi(0) \\ 0 & \phi(2 \cdot L - 2) & \ddots & \phi(1) \\ \vdots & \vdots & \ddots & \vdots \\ 0 & 0 & \dots & \phi(2 \cdot L - 1) \end{pmatrix} \begin{pmatrix} h_{(2)}(0) \\ h_{(2)}(0) \\ \vdots \\ h_{(2)}(2 \cdot L - 1) \end{pmatrix} \quad (5.19)$$

From (5.19), a pattern begins to emerge. Extended (5.18) to the general dyadic case produces

$$\phi(\frac{n}{2^{m+1}}) = \sum_k h_{(2)}(k) \cdot \phi(\frac{n}{2^m} - k). \quad (5.20)$$

Finally, adopting the vector notation

$$\begin{aligned} \Phi^{(m)} &= \left(\frac{0}{2^m} \quad \frac{1}{2^m} \quad \dots \quad \frac{2^m(2 \cdot L - 1)}{2^m} \right)^T, \\ \mathbf{h} &= \left(h_{(2)}(0) \quad h_{(2)}(1) \quad \dots \quad h_{(2)}(2 \cdot L - 1) \right)^T \end{aligned}$$

and

$$\Phi^{(m)} = \begin{pmatrix} \phi(\frac{0}{2^m}) & 0 & \dots & 0 \\ \phi(\frac{1}{2^m}) & 0 & \dots & 0 \\ \vdots & \vdots & \ddots & \vdots \\ \phi(\frac{1 \cdot 2^m}{2^m}) & \phi(\frac{0}{2^m}) & \ddots & 0 \\ \phi(\frac{1 \cdot 2^m + 1}{2^m}) & \phi(\frac{1}{2^m}) & \ddots & 0 \\ \vdots & \vdots & \ddots & \vdots \\ \phi(\frac{(2 \cdot L - 1) \cdot 2^m}{2^m}) & \phi(\frac{(2 \cdot L - 2) \cdot 2^m}{2^m}) & \ddots & \phi(\frac{0}{2^m}) \\ 0 & \phi(\frac{(2 \cdot L - 2) \cdot 2^m + 1}{2^m}) & \ddots & \phi(\frac{1}{2^m}) \\ \vdots & \vdots & \ddots & \vdots \\ 0 & 0 & \dots & \phi(\frac{(2 \cdot L - 1) \cdot 2^m}{2^m}) \end{pmatrix}.$$

equation (5.20) can be expressed in a more compact form:

$$\phi^{(m+1)} = \Phi^{(m)} \mathbf{h}. \quad (5.21a)$$

Similarly, if the vector $\psi^{(m)}$ for the wavelet function $\psi(t)$ is defined in a manner analogous to $\phi^{(m)}$ for the scaling function $\phi(t)$ and the wavelet generating filter \mathbf{g} in a manner analogous to the scaling function generating filter \mathbf{h} , then, as a consequence of (4.51c), the values of $\psi(t)$ can be obtained at dyadic points from

$$\psi^{(m+1)} = \Phi^{(m)} \mathbf{g}. \quad (5.21b)$$

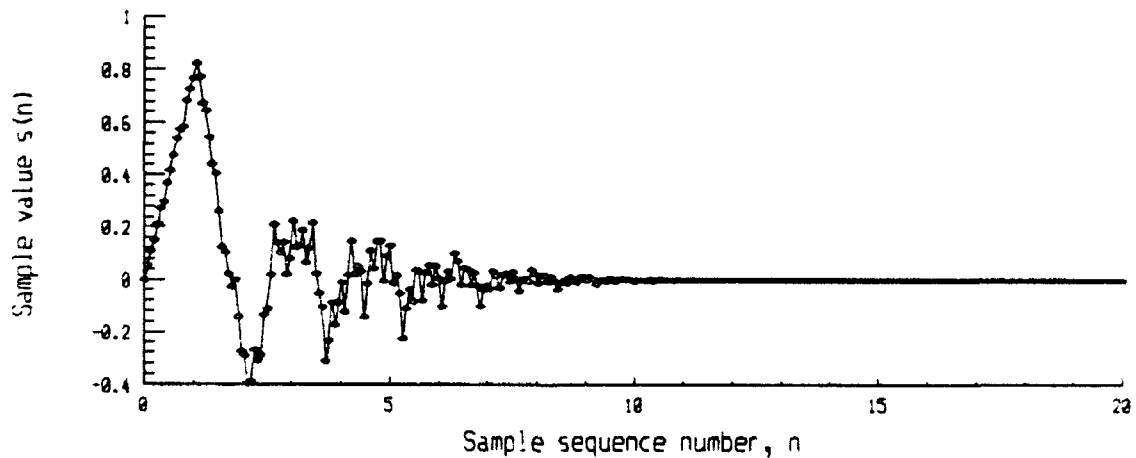


Figure 5.1a--Function generated by four-stage dyadic expansion of a 20-point lowpass filter with cutoff frequency of $0.375 \cdot f_c$. The function represents an example of a function which lacks regularity.

The recursive operations described by (5.21a) and (5.21b) represent *dyadic expansions* of the functions $\phi(t)$ and $\psi(t)$. At each iteration the discrete sequences characterized by the vectors $\phi^{(m)}$ and $\psi^{(m)}$ are expanded by a factor of two and then convolved with filters $\mathbf{h}(n)$ and $\mathbf{g}(n)$, respectively, whose coefficients are contained in \mathbf{h} and \mathbf{g} . After m iterations, the values of the

of the scaling function $\phi(t)$ and wavelet $\psi(t)$ will be known at all points t_n in region of support such that $t_n = n \cdot 2^m$.

A final issue which must be addressed within the scope of two-scale difference equations is the topic of regularity. *Regularity* is defined to be the degree to which a recursively expanded function, such as a two-scale difference equation, converges to a continuous smooth function [26]. The conditions under which the regularity of a function can be guaranteed of themselves constitute grounds for an extensive study. However, one apparent example of a requirement for regularity was observed during experimentation performed during the course of the present study. For regularity, it is necessary that, for the filter to be expanded, the DFT exist primarily within the lower half of the frequency spectrum below the Nyquist frequency. Figures 5.1a and 5.1b show two examples of the dyadic expansion of two candidate filters for the generation of a scaling function. Both filters were designed by performing spectral factorization of lowpass filters designed using the window method [12]. For the first filter the cutoff frequency was selected as $0.375 \cdot f_s$ and the second filter was assigned a cutoff frequency of $0.25 \cdot f_s$. As can be seen in Figure 5.1a, the function possesses an erratic appearance. As the bandwidth of the candidate function generating filter increases, the generated function becomes less smooth and more and more erratic.

On the other hand, Figure 5.1b shows a function generated through dyadic expansion of a filter designed with exactly the same specifications except that the cutoff frequency was specified as $0.25 \cdot f_s$. The plot of the function generated by the second filter displays significantly

greater smoothness. Figure 5.1b represents an example of a function which, as far as can be determined from the plot, possesses the quality of regularity.

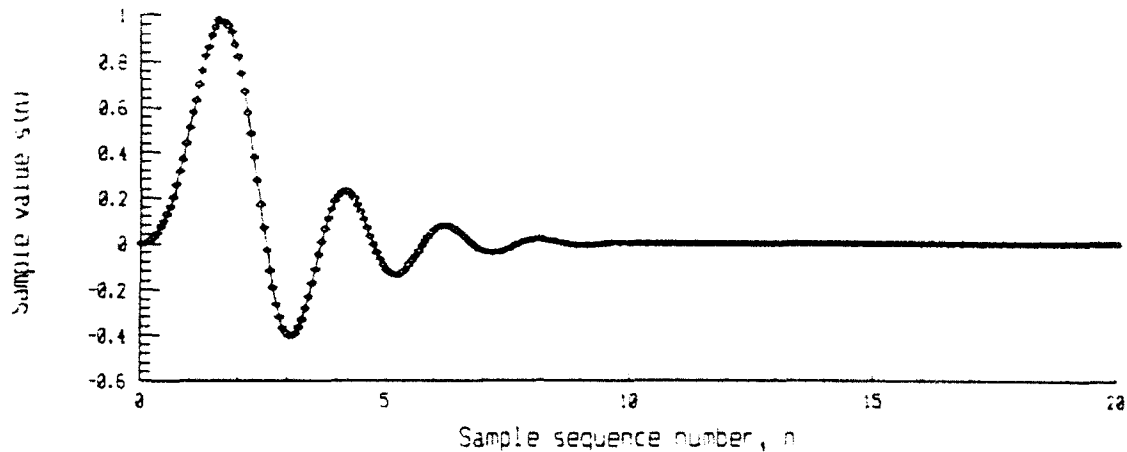


Figure 5.1b--Function generated by four-stage dyadic expansion of a 20-point lowpass filter with cutoff frequency of $0.5 \cdot f_s$. The function represents an example of a function which possesses regularity

C. DAUBECHIES' FAMILY OF ORTHONORMAL WAVELETS

Ingrid Daubechies of Bell Laboratories made a landmark contribution to the field of multiresolution analysis when, in 1988, she published a mathematical paper on orthonormal wavelets [21]. Aside from providing a general overview of the progress which during recent years had occurred within the field of wavelets, Daubechies' paper described the construction of a class of functions which possessed many of the most desirable aspects of wavelet functions. The functions were specified in terms of their generating filters. Even-length filters from length four to 20 were tabulated in the paper. Each of the filters satisfied (5.4) and (5.11). Furthermore, they each maximized the number of zeros on the unit circle at $z = -1$, a condition which ensures maximum regularity [26]. In this section plots of two wavelet-scaling function

pairs will be presented, and one will be examined more thoroughly from the perspective of implementation of the multiresolution structures from Chapter IV.

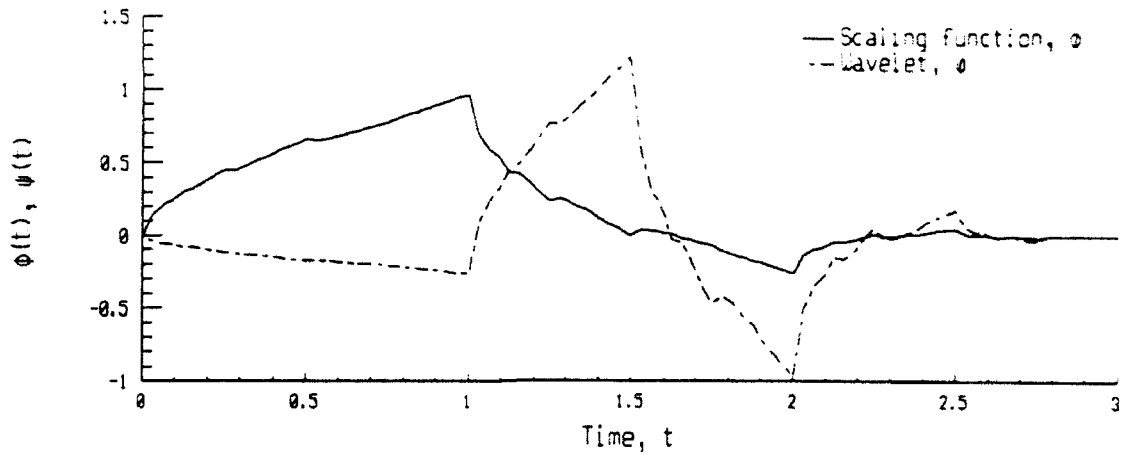


Figure 5.2a--Superimposed plots of Daubechies' orthonormal wavelet and scaling function on $[0, 3]$. Plots were generated by four-stage dyadic expansion of corresponding filter listed in [21].

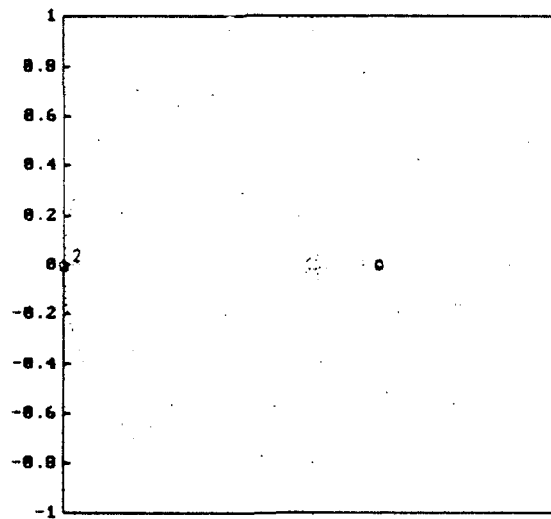


Figure 5.2b--Polar plot of zero locations for generating filter for Daubechies' orthonormal wavelet and scaling function supported on $[0, 3]$.

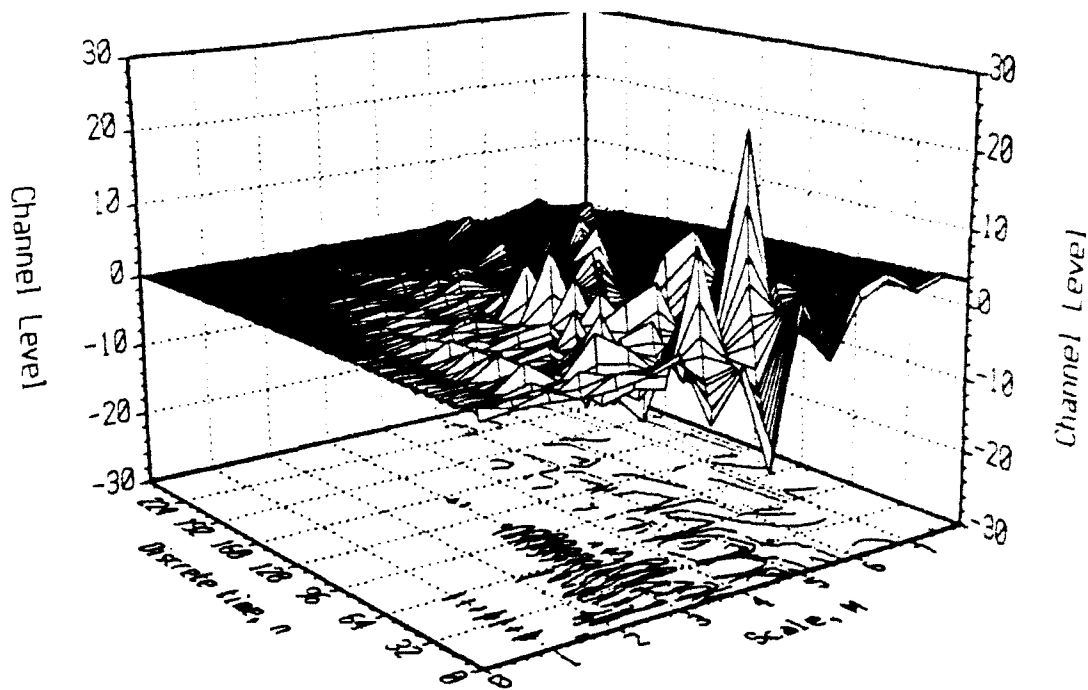


Figure 5.3--Two-channel, two-subchannel multiresolution decomposition of 256-point lowpass test sequence (4.74a). Decomposition was performed using generating filter for Daubechies' orthonormal basis function supported on $[0, 3]$.

Perhaps the most famous of Daubechies' orthonormal scaling function-wavelet pair is plotted in Figure 5.2a. The functions are generated from a four-point filter and are supported on $[0, 3]$. As can be inferred from viewing the plots, the smoothness of these functions is marginal. Figure 5.2b provides a polar plot of the zeros of the generating filter. Of its three poles, two fall on the unit circle. Finally, as indicated in Chapter IV, the wavelet transform, which essentially consists of the detail function (4.33), is comprised of a plot of weighted, shifted versions of the wavelet. Consequently, it is expected that the texture of a surface plot of a wavelet decomposition should reflect the shape of the wavelet from which it is constructed. Figure 5.3 supports this expectation. In particular, the peaks in the which appear at higher scales reflect the shape of the wavelet function plotted in Figure 5.2.

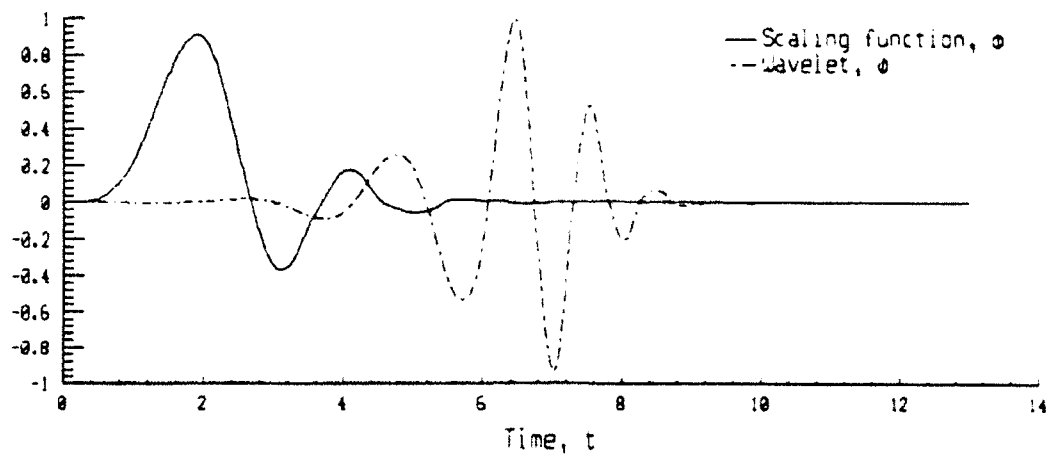


Figure 5.4--Superimposed plots of Daubechies' orthonormal wavelet and scaling function on $[0, 13]$. Plots were generated by four-stage dyadic expansion of corresponding filter listed in [21].

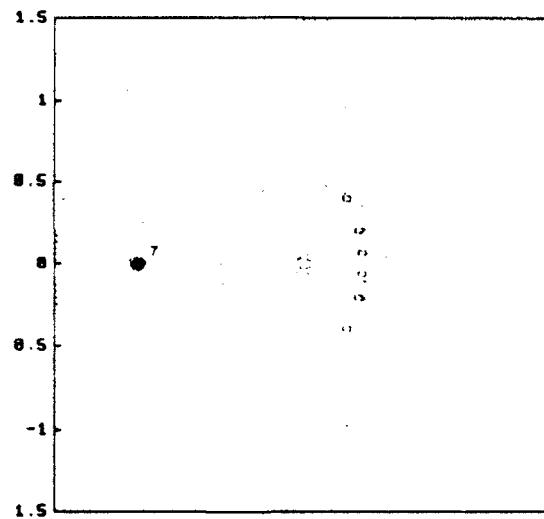


Figure 5.5--Polar plot of zero locations for generating filter for Daubechies' orthonormal wavelet and scaling function supported on $[0, 13]$.

Figure 5.4 presents superimposed plots of Daubechies' orthonormal basis function and scaling function supported on $[0, 13]$. This pair was used extensively throughout Section IV.E to illustrate the performance of multiresolution decomposition techniques. The zeros of the

generating filter are plotted in Figure 5.5. Of the 13 zeros of the generating filter's characteristic polynomial, seven occur at the location $z = -1$.

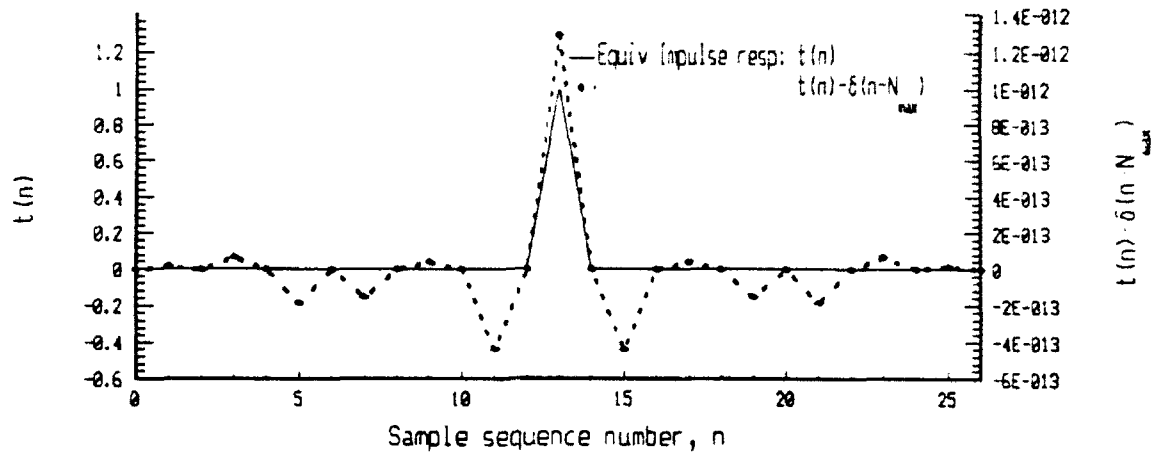


Figure 5.6--Time-domain demonstration of performance of QMF bank constructed from generating filter for Daubechies' orthonormal wavelet and scaling function on $[0, 13]$. Left-hand axis indicates equivalent impulse response while right-hand axis indicates deviation $t(n) - \delta(n - N_{\max})$ from ideal perfect reconstruction performance.

In Section IV.E, multiresolution decomposition techniques were addressed from the filter bank perspective. In Chapter III, the degree to which specific examples of filter banks satisfied the perfect reconstruction criterion and the power complementary property was demonstrated. The question, therefore, arises as to the degree to which the generating filters for Daubechies' orthonormal wavelets and scaling functions satisfy the perfect reconstruction and power complementary properties. Figures 5.6 and 5.7 illustrate the performance of these functions employing the same plots used in Chapter III. Figure 5.6 presents a plot analogous to Figure 3.14. Upon comparing Figure 5.7 with Figure 3.14, it is apparent that Daubechies' generating function provides vastly superior performance for filter bank applications. The filter bank demonstrated in Figure 3.14 deviated from the ideal response of a perfect delay by 2×10^{-5} .

Daubechies' 14-point generating filter deviates from an perfect delay by 1.4×10^{-11} . This represents six orders of magnitude in performance improvement over the time-domain performance of the QMF bank considered in Section III.C.

Figure 5.7 indicates similar results for the frequency-domain performance of a QMF bank constructed from Daubechies' 14-point generating filter. The desirability of a power-complementary pair of analysis and synthesis filters was addressed in Chapter III. The QMF bank of Figure 3.15 deviates from being a perfectly power complementary pair by 10^{-3} dB. A QMF bank constructed from Daubechies' 14-point generating function deviates from being a perfect power complementary pair by 1.2×10^{-11} dB. This represents eight orders of magnitude in improvement. Consequently, Daubechies' generating function for wavelets and scaling functions supported on $[0, 14]$ provide for outstanding QMF bank performance conforming very closely to the power complimentary and perfect reconstruction properties.

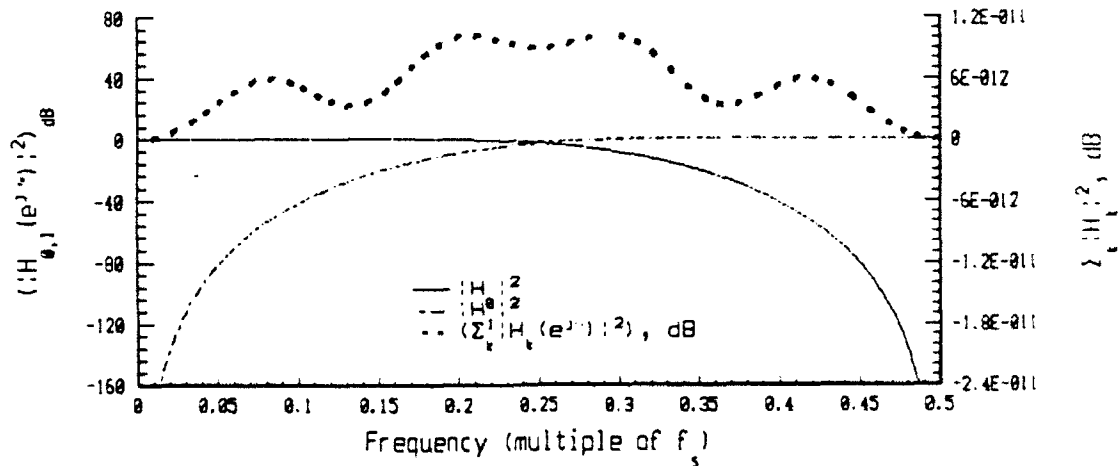


Figure 5.7--Demonstration of the degree to which generating filter for Daubechies' orthonormal wavelet and scaling function on $[0, 13]$ produces a power complementary pair for QMF bank purposes. The left-hand axis indicates the frequency responses for the filter and its modulated complement. The right-hand axis indicates the degree to which the filter pair forms a power complementary set.

D. DESIGN OF FILTERS FOR QMF BANKS

In the final Section of this chapter, procedures for the design of filters for filter bank applications will be examined. The steps for the design of a filter set for a two-channel QMF bank will be outlined. After that, the process of a filter design for a four-channel pseudo-QMF bank--a filter bank which only approximately satisfies the perfect reconstruction and power complementary properties--will be outlined. Procedures for the design of perfect reconstruction banks of an arbitrary number of channels exist [11, 34], but will not be addressed in the present study.

To construct a two-channel filter bank with real-coefficient filters which possesses the perfect reconstruction property, it is necessary, as was shown by (3.20a), that the Z-transforms of the synthesis and analysis filters, both of order N, for a given channel k be related by [13]

$$F_k(z) = z^{-N} \cdot H_k^*(1/z^*). \quad (5.22)$$

Equation (5.22) is equivalent to the notion that impulse response of the synthesis filter is equal to the time reversal of the impulse response for the analysis filter. Additionally, from (3.19), the equivalent transfer response T(z) of the filter bank structure must, to satisfy the perfect reconstruction criterion, be of the form

$$T(z) = \frac{1}{2} \cdot [F_0(z) \cdot H_0(z) + F_1(z) \cdot H_1(z)] = z^{-N}. \quad (5.23)$$

For convenience, an equivalent transfer response $G_k(z)$ for the branch of the filter bank corresponding to each channel can be defined:

$$G_k(z) = \frac{1}{2} \cdot H_k(z) \cdot F_k(z). \quad (5.24)$$

Now, assume that $G_k(z)$ represents the transfer function for a half-band filter. If $G_k(z)$ satisfies the half-band filter property in the sense described by Mintzer [32], then the impulse response $g_k(n)$ corresponding to $G_k(z)$ satisfies [13]

$$(g_k)_{\downarrow 2}(n) = \delta_{N, n} \quad (5.25)$$

where N represents the orders of the filters $h_k(n)$ and $f_k(n)$. Therefore, by (5.25), the only non-zero, even-numbered element of the impulse response of $g_k(n)$ is the sample $g_k(N)$.

Continuing, the objective is to satisfy (5.23), or equivalently,

$$T(z) = G_0(z) + G_1(z) = z^{-N}. \quad (5.26)$$

One way to satisfy (5.26) is to specify that the odd-numbered elements of $g_1(n)$ each be of the opposite sign, or

$$g_1(2 \cdot n + 1) = -g_0(2 \cdot n + 1). \quad (5.27a)$$

Because of (5.25), (5.27a) is equivalent to

$$g_1(n) = (-1)^n \cdot g_0(n). \quad (5.27b)$$

But, (5.27b) is equivalent to

$$G_1(z) = G_0(-z). \quad (5.27c)$$

From the preceding development, it may be inferred that $H_k(z)$ and $F_k(z)$ are equal-ordered spectral factors of a halfband filter $G_k(z)$. Furthermore, $g_1(n)$ is simply a modulated version of $g_0(n)$. Therefore, the frequency response $G_1(e^{j\omega})$ consists simply of the frequency response of $G_0(e^{j\omega})$ shifted in the frequency domain by π . Finally, since $G_k(z)$ is a

polynomial with two equal-ordered spectral factors which are simply the reversals of each other, certain constraints on the locations of the zeros of $G_k(z)$ arise. First, for each zero z_q of $G_k(z)$ on the real axis corresponding to $H_k(z)$, there must be a reciprocal zero $1/z_q$ on the real axis corresponding to $F_k(z)$. Secondly, since it has been specified that the filter impulse responses $h_k(n)$ and $f_k(n)$ be strictly real, the zeros of $G_k(z)$ must occur in complex-conjugate pairs. Furthermore, for every zero z_q located inside the unit circle corresponding to $H_k(z)$, there must be a corresponding reciprocal zero $1/z_q$ corresponding to $F_k(z)$ located outside the unit circle. Consequently, all zeros not on the unit circle or the real axis must occur in complex conjugate quadruples. Finally, in order for $H_k(z)$ and $F_k(z)$ to be of equal order, for each complex-conjugate pair of zeros z_p and z_q^* located on the unit circle corresponding to $H_k(z)$, an identical set corresponding to $F_k(z)$ must occur in the exact same location. In other words, the zeros on the unit circle for $G_k(z)$ must occur as double zeros. Consequently, $G_k(z)$ must be a filter with a strictly real, non-zero, symmetric, zero-phase filter.

The requirements for the locations of the zeros for $G_k(z)$ suggest a design technique for filters for perfect reconstruction filter banks. The first step is to design a zero-phase, symmetric half-band, lowpass filter $G_0(z)$. This may be accomplished by any standard method such as the McClellan-Parks routine or by the window method [12]. Such a filter will be symmetric and will satisfy the half-band filter criterion (5.25). In order for $G_0(z)$ to be strictly non-zero, the maximum stopband ripple ϵ_R must next be measured. If this ripple ϵ_R is added to the central

element of the filter impulse response $g_0(n)$, the result will be an impulse response of a modified filter

$$g_{0R}(n) = g_0(n) + \epsilon_R \cdot \delta(n - N) \quad (5.28a)$$

with a corresponding transfer function

$$G_{0R}(Z) = G_0(z) + \epsilon_R. \quad (5.28b)$$

Because of the addition of the term ϵ_R the frequency response of $G_{0R}(z)$ will be strictly non-zero.

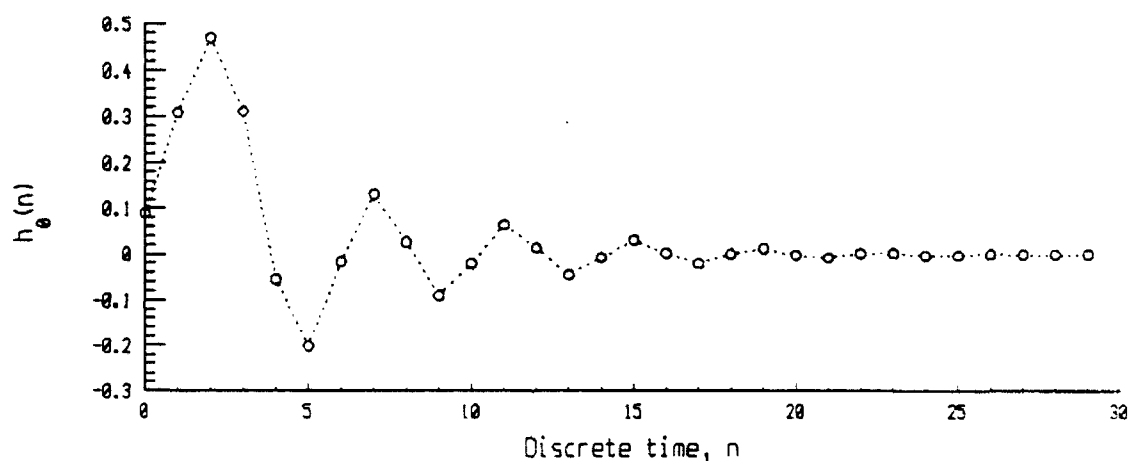


Figure 5.8--Impulse response of 30-point, lowpass filter designed for QMF bank.

The next step requires the rooting of $G_{0R}(z)$. The zeros of $G_{0R}(z)$ must be grouped into three subsets: zeros located inside of the unit circle, zeros located on the unit circle, and zeros located outside of the unit circle. The zeros inside of the unit circle belong strictly to $H_0(z)$ and the zeros outside of the unit circle belong strictly to $F_0(z)$. The zeros on the unit circle should all be double zeros occurring in sets of complex conjugate pairs. One set of each double complex conjugate pairs belongs to $H_0(z)$ while the other belongs to $F_0(z)$. If the zeros corresponding to

$H_0(z)$ are re-expanded into a polynomial, the coefficients of the result should be strictly real and belong to $h_0(n)$.

As an example, a 30-point QMF filter was designed whose impulse response is plotted in Figure 5.8. The halfband filter was generated from applying a Kaiser window to a 59-point sinc function

$$g_0(n) = \frac{\sin\left(\frac{\pi}{2}(n-N)\right)}{\pi(n-N)}$$

After adding the peak stopband error ϵ_R to impulse response element $g_0(30)$, the corresponding polynomial was rooted and zeros grouped as was described above, resulting in a polynomial whose coefficients represent the impulse response $h_0(n)$ of a QMF-bank lowpass analysis filter.

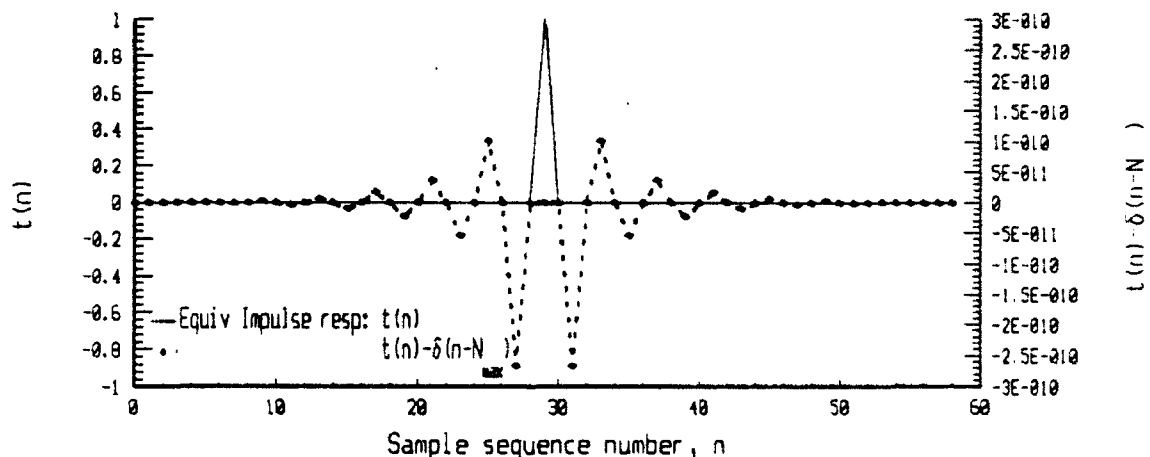


Figure 5.9--Time-domain demonstration of performance of QMF bank constructed from the 30-point lowpass filter designed by spectral factorization of a half-band filter produced by the window method. Left-hand axis indicates equivalent impulse response while right-hand axis indicates deviation $t(n) - \delta(n - N_{\max})$ from ideal perfect reconstruction performance.

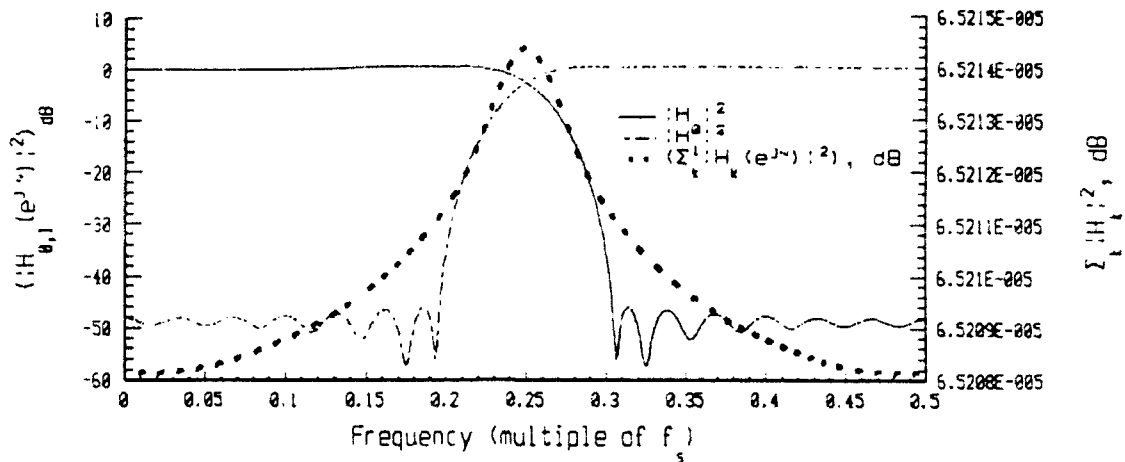


Figure 5.10--Demonstration of the degree to which 30-point lowpass filter designed by spectral factorization of a half-band filter produced by the window method produces a power complementary pair for QMF bank purposes. The left-hand axis indicates the frequency responses for the filter and its modulated complement. The right-hand axis indicates the degree to which the filter pair deviates from a power complementary set.

Figures 5.9 and 5.10 indicate the results of application to the filter the analysis methods demonstrated in Chapter III for filter banks. Figure 5.9 plots the equivalent transfer response of a filter bank constructed from $h_0(n)$, and its deviation from the ideal response of an ideal delay. As can be seen from Figure 5.9, this method works quite effectively. The peak deviation from an ideal delay was less than 3×10^{-10} . This result compares favorably with the response for the generating filter for Daubechies' wavelets examined earlier. The power complementary properties are demonstrated in Figure 5.10. This filter did not quite perform as well as the Daubechies' wavelet generating filter performed. The peak deviation from a response for a power complementary pair was approximately 6×10^{-9} compared with 1.2×10^{-11} for the Daubechies filter. This result is also slightly inferior to the performance of Daubechies' wavelet generating function by roughly two orders of magnitude, but still significantly superior to the QMF bank filters considered in Chapter III.

Finally, within the context of a study addressing wavelet transforms the question arises as to the use of perfect reconstruction QMF filters for generating wavelets. First of all, the filter impulse response $h_0(n)$ does not strictly satisfy (5.11). Specifically,

$$\sum_k h^2(k) \approx \frac{1}{2} + 7.5 \times 10^{-6}.$$

Consequently, any scaling functions or wavelets generated by $h_0(n)$ would not be orthonormal. Additionally, if a two-scale difference equation for $h_0(n)$ is set up in the form of (5.18), the nearest eigenvalue to unity for the double-right-shift matrix of coefficients of $h_0(n)$ is 1.0052. As a result, only an approximate system of a two-scale difference equation can be constructed from $h_0(n)$. Based on the preceding two measures it may be concluded that although, as was

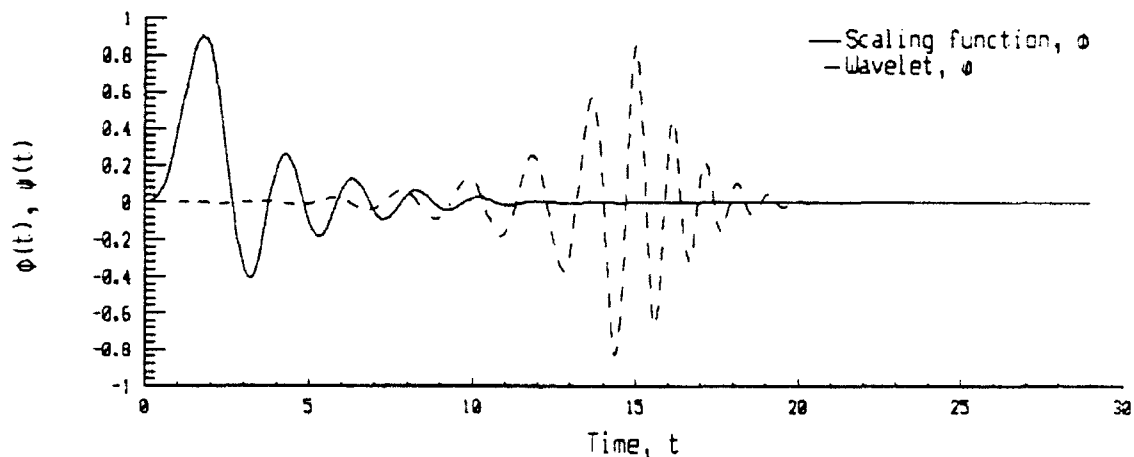


Figure 5.11--Plots of "pseudo-scaling function" and "pseudo-wavelet" generated from four-stage dyadic expansion of 30-point filter designed from spectral factorization of a half-band filter.

shown in Chapter IV, wavelet decompositions are exactly equivalent to structures of cascaded, perfect reconstruction QMF banks, the converse is not true. In fact, in the present example, the perfect reconstruction filter bank only approximately satisfies the properties described for

orthonormal wavelet decompositions. Nevertheless, if these issues are ignored and a dyadic expansion of $h_0(n)$ is performed, the resultant functions, after four iterations, appear as plotted in 5.11. The functions possess obvious smoothness and present appearances similar to those of Daubechies' wavelets.

To generate a filter bank for a four-subchannel multiresolution decomposition, a pseudo-QMF bank was designed using a spectral factorization technique similar to that used for the preceding example. The strategy was to approximate the power complementary property. Using the McClellan-Parks algorithm, two filters $h_0(n)$ and $h_1(n)$ were designed whose passbands covered the regions $[0, \pi/4]$ and $[\pi/4, \pi/2]$, respectively. The upper half of the frequency spectrum below the Nyquist frequency was covered by modulating the first two filters:

$$h_2(n) = (-1)^n \cdot h_1(n)$$

and

$$h_3(n) = (-1)^n \cdot h_0(n).$$

The design of the first two filters involved an iterative process in which, at each stage, the closeness of the filter set to the power complementary process was checked. At each step, the sum of the frequency responses was adjusted by modifying the boundaries to the passband and stopband for each filter. Tables 5.1a-c document the iterations. Each column of Tables 5.1a and 5.1b indicates the frequency at which the desired gain in the top row is to be met for the filter to be factorized spectrally. Table 5.1c indicates, at each iteration, the peak deviation in the transition bands between each filter. Based on the deviation in the transition bands between

$h_0(n)$ and $h_1(n)$ and between $h_2(n)$ and $h_3(n)$, the filter indicated by $h_0(n)$ was not modified after the third iteration. Eight iterations were necessary to obtain acceptable results for the transition band between $h_1(n)$ and $h_2(n)$.

TABLE 5.1A--RECORD OF ITERATIVE ADJUSTMENTS TO PASSBAND AND STOPBAND FREQUENCY BOUNDARIES IN DESIGN OF FIRST FILTER $H_1(N)$ FOR FOUR-CHANNEL, PSEUDO-QMF BANK

Target Gain	1	1	10^{-8}	10^{-8}
Frequency				
Iteration 1	0	$\pi/8$	$5\pi/16$	π
Iteration 2	0	$3\pi/16$	$5\pi/16$	π
Iteration 3	0	$21\pi/128$	$5\pi/16$	π

TABLE 5.1B--RECORD OF ITERATIVE ADJUSTMENTS TO PASSBAND AND STOPBAND FREQUENCY BOUNDARIES IN DESIGN OF SECOND FILTER $H_2(N)$ FOR FOUR-CHANNEL, PSEUDO-QMF BANK.

Target Gain	10^{-8}	10^{-8}	1	1	10^{-8}	10^{-8}
Frequency						
Iteration 1	0	$3\pi/16$	$5\pi/16$	$7\pi/16$	$9\pi/16$	π
Iteration 2	0	$5\pi/32$	$5\pi/16$	$7\pi/16$	$19\pi/32$	π
Iteration 3	0	$19\pi/128$	$21\pi/64$	$27\pi/64$	$19\pi/32$	π
Iteration 4	0	$39\pi/256$	$41\pi/128$	$26\pi/64$	$37\pi/64$	π
Iteration 5	0	$39\pi/256$	$83\pi/256$	$53\pi/128$	$75\pi/128$	π
Iteration 6	0	$39\pi/256$	$83\pi/256$	$105\pi/256$	$151\pi/256$	π
Iteration 7	0	$39\pi/256$	$83\pi/256$	$52\pi/128$	$151\pi/256$	π
Iteration 8	0	$39\pi/256$	$83\pi/256$	$103\pi/256$	$151\pi/256$	π

Upon review of Table 5.1c and of Figures 5.13 and 5.14 it becomes obvious that the performance obtained from the four-channel filter bank is nowhere near what was obtained by any filterbank considered at any other time during this study. The peak delay of the equivalent impulse response for the filter bank was of the order of magnitude 5×10^{-3} . Furthermore, the

peak deviation from the power complementary standard could only be reduced to tenths of decibels.

TABLE 5.1C--TRANSITION BAND DEVIATION FROM POWER COMPLEMENTARY, BY ITERATION, FOR DESIGN OF FOUR-CHANNEL PSEUDO-QMF FILTER BANK.

	Peak deviation in transition bands between $h_0(n)$ and $h_1(n)$ and between $h_2(n)$ and $h_3(n)$	Peak deviation in transition band between $h_1(n)$ and $h_2(n)$
Iteration 1	Excessive	Excessive
Iteration 2	0.22	0.38
Iteration 3	0.07	0.23
Iteration 4	0.08	0.2
Iteration 5	0.02	0.2
Iteration 6	0.02	0.08
Iteration 7	0.02	0.06
Iteration 8	0.02	0.03

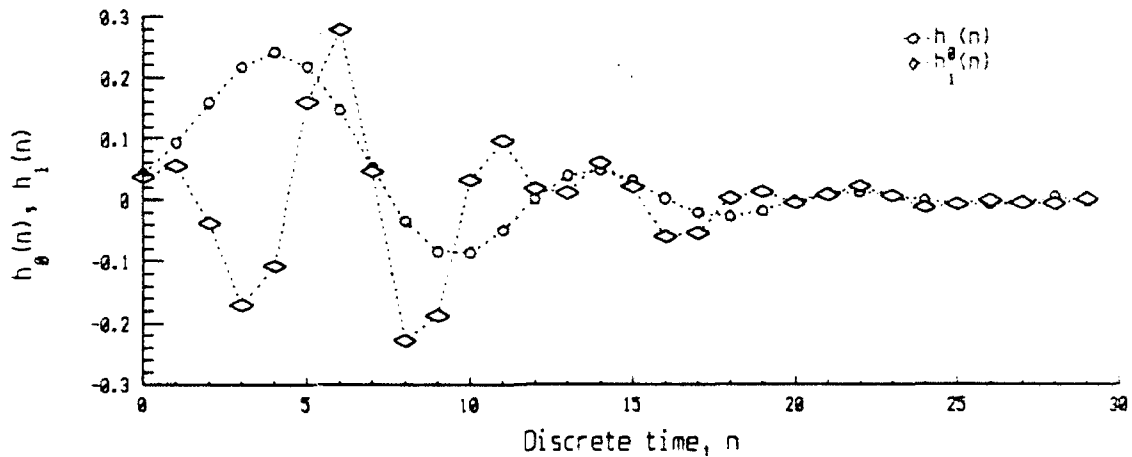


Figure 5.12--Impulse responses $h_0(n)$ and $h_1(n)$ of filters designed by spectral factorization of fourth-band filters designed using McClellan-Parks algorithm.

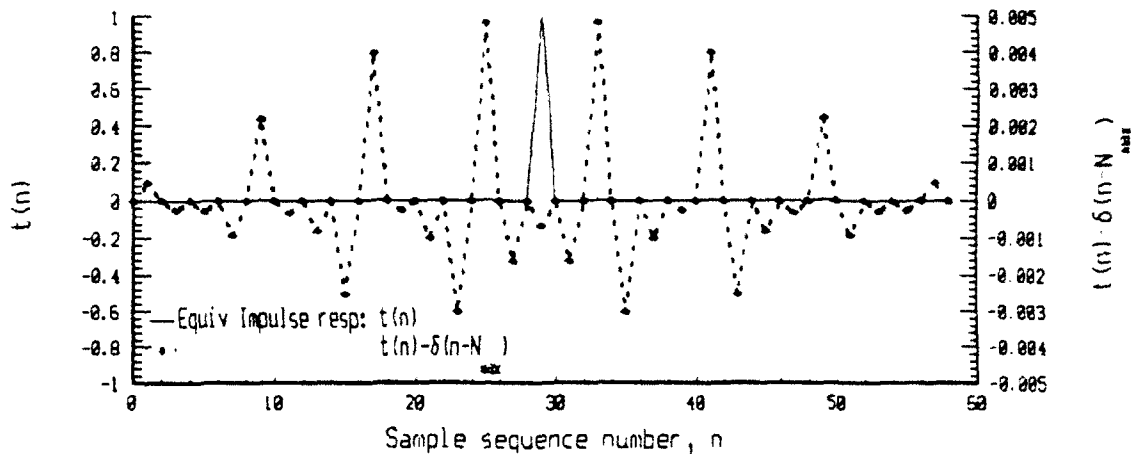


Figure 5.13--Time-domain demonstration of performance of four-channel QMF bank constructed from filters designed from spectral factorization of fourth-band McClellan-Parks filters. Left-hand axis indicates equivalent impulse response while right-hand axis indicates deviation $t(n) - \delta(n - N_{Max})$ from ideal perfect reconstruction performance.

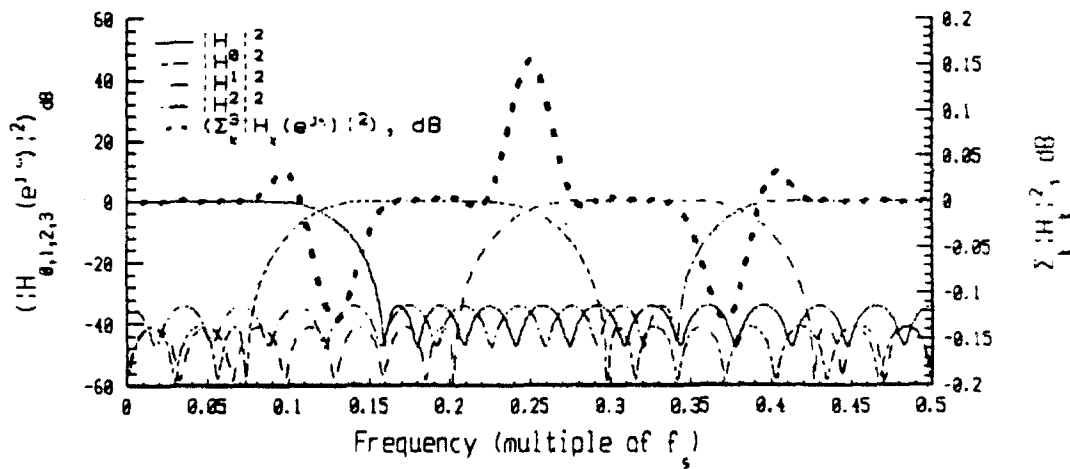


Figure 5.14--Demonstration of the degree to which four-channel, pseudo-QMF bank designed by spectral factorization of a McClellan-Parks fourth-band filters produces a power complementary pair for QMF bank purposes. The left-hand axis indicates the frequency responses for the filter and its modulated complement. The right-hand axis indicates the degree to which the filter pair deviates from a power complementary set.

VI. EVALUATION OF MULTIREOLUTION TECHNIQUES FOR DETECTION APPLICATIONS

A. INTRODUCTION

In this chapter, additional performance characteristics of the multiresolution structures developed in Chapter IV will be examined within the context of evaluation of suitability for detection applications. In Section B, the computational efficiency of multiresolution structures will be considered. In the Section C, receiver operating characteristics will be plotted for various multiresolution structures applied to the test sequences generated by (4.74b) and (4.74a). Finally, Section D will demonstrate resolution of scale within the context of steady-state harmonics and chirped signals.

The basis for evaluation of multiresolution performance will be the spectrogram, one of the most commonly used techniques for detection and spectral estimation. Figures 6.1a and 6.1b present the spectrogram decomposition of the two 256-point test sequences generated by (4.74a) and (4.74b), respectively. The plots were generated by plotting the frequency spectrum below the Nyquist frequency for a sequence windowed with a 128-point Hanning window shifted in increments of two samples. This representation was selected because of its frequency resolution and because it presents a similar number of points compared to the multiresolution decompositions presented in Chapter IV.

In Figure 6.1a, the lack of frequency resolution in the extreme lower range of the frequency spectrum is apparent. For lowpass test sequence (4.74a), the spectral components at

digital frequencies $2\pi \cdot 2/512$ and $2\pi \cdot 9/512$ are not clearly resolved. The component at $2\pi \cdot 2/512$, which appears at spectral bin location 0.5, because of its relatively greater power, spreads into adjacent spectral bins. Consequently the component at $2\pi \cdot 9/512$, which coincides with spectrogram bin 2.25, is partially masked by leakage from the component at $2\pi \cdot 2/512$. The only indication of the component at $2\pi \cdot 9/512$ is evident on the leading edge of the surface plot.

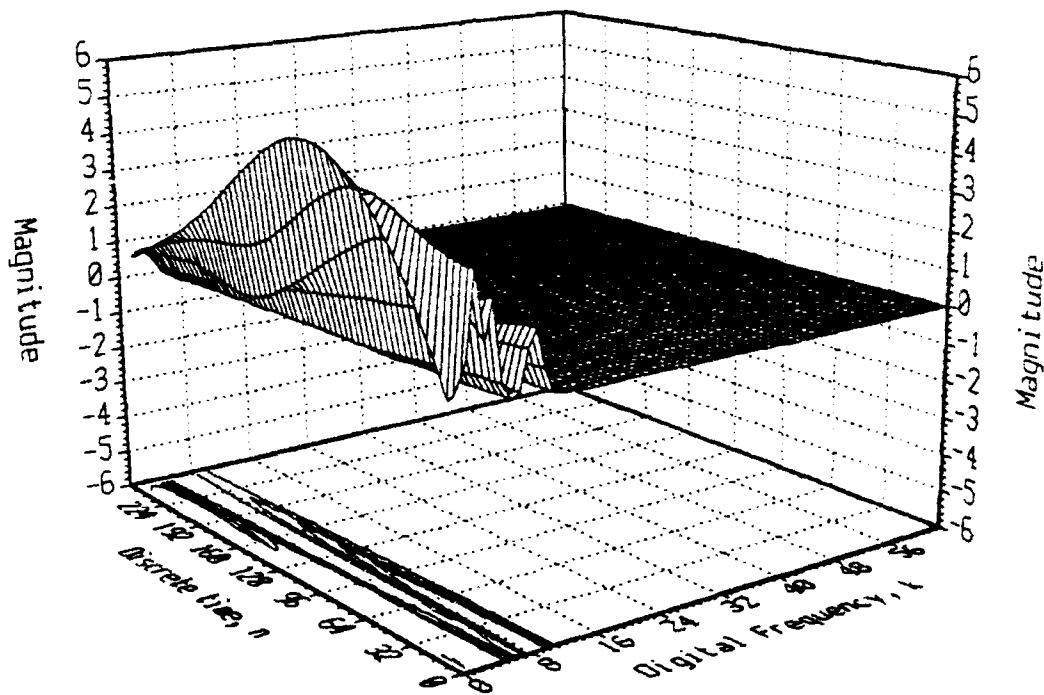


Figure 6.1a--Spectrogram representation of lowpass test sequence (4.74a). The plot was generated using a 128-point Hanning window shifted in increments of two samples. Only the half of the frequency spectrum below the Nyquist frequency is plotted.

On the other hand, Figure 6.1b provides an obvious indication of the advantages of constant spectral bin density: The three harmonics of (4.74a) are quite easily resolved. The plots have the additional advantage of a smoother presentation. Spectrogram decompositions

smooth out the phase information while multiresolution presentations indicate individual oscillation cycles of the sequences decomposed.

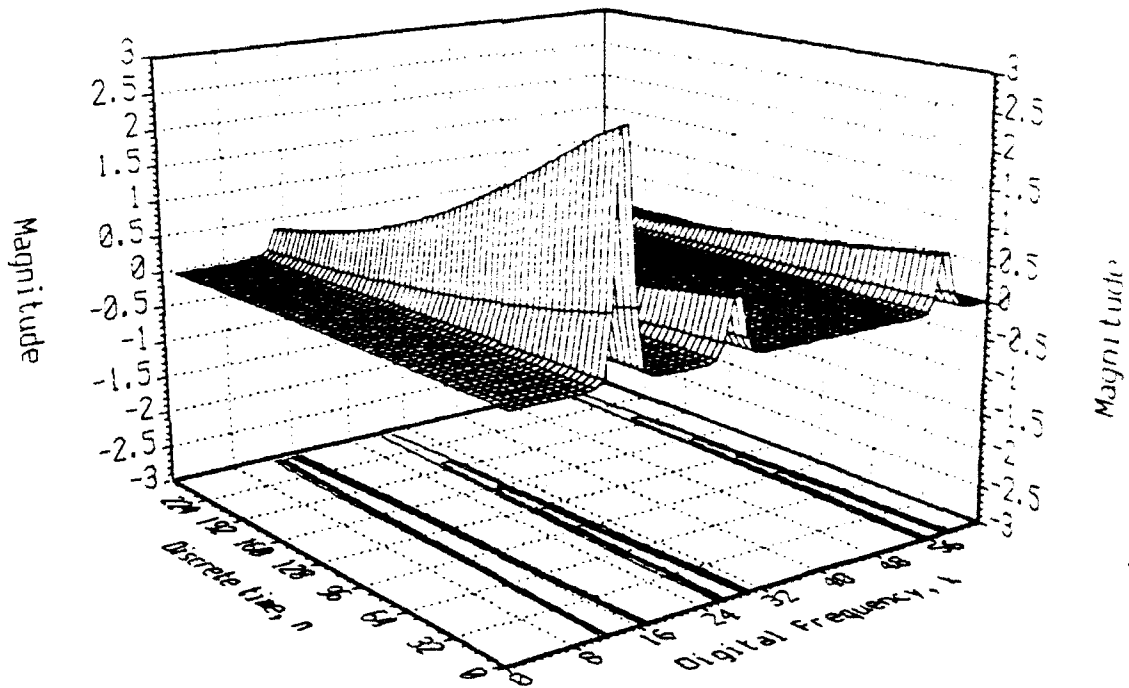


Figure 6.1b--Spectrogram representation of highpass test sequence (4.74b). The plot was generated using a 128-point Hanning window shifted in increments of two samples. Only the half of the frequency spectrum below the Nyquist frequency is plotted.

B. COMPUTATIONAL EFFICIENCY OF SIGNAL ANALYSIS TECHNIQUES

Computational efficiency comprises one of the principal advantages ascribed to Fast Fourier Transform (FFT) methods of digital signal processing. The required number of multiplications provides a common number for evaluating digital processing techniques. In the case of FFT decomposition of a sequence of length M , the required number of complex multiplications N_x is expressed by

$$N_x = \frac{M}{2} \log_2(M). \quad (6.1)$$

Furthermore, application of the window sequence to each segment of a sequence of length L requires M multiplications. Finally, if the window is shifted in increments of k , then the FFT will be applied to $\frac{L-M}{k} + 1$ sequences. Therefore, the total number of multiplications necessary to generate a windowed FFT decomposition is

$$N_x = \left(\frac{L-M}{k} + 1 \right) \frac{M^2}{2} \log_2(M). \quad (6.2a)$$

In general, the multiplications performed in FFT decomposition represent complex multiplications. Evaluation of a complex multiplication requires four real multiplications and two additions. Consequently, assuming that real data and window sequences are used, the number of multiplications for the FFT decomposition is actually

$$N_x = 2 \left(\frac{L-M}{k} + 1 \right) M^2 \log_2(M). \quad (6.2b)$$

For each of the decompositions plotted in Figures 6.1a and 6.1b, the sequence length $L = 256$, and the window length $M = 128$. Furthermore, the window was shifted in increments of $k = 2$ samples. Consequently, using (6.2b), the number of real multiplications N_x required to perform the decomposition was $N_x = 14,909,0440$.

For the multiresolution decompositions of Chapter IV, Section E, FFT-type radix-2 algorithms are not available. Consequently, each stage of decomposition requires the convolution of two real sequences. Therefore, for decomposition of sequences of length L_0 , using filters of length M_c for decomposition into two primary channels, the required number of real multiplications for the first stage is

$$N_x = 2 \cdot M_c \cdot L_0.$$

After convolution by the analysis filters of each stage, the approximation and detail sequences are both decimated, providing sequences of length

$$L_1 = \frac{L_0 + M_c - 1}{2}.$$

By induction, the length L_p of the approximation and detail sequences at stage p is given by the geometric series

$$\begin{aligned} L_p &= \frac{L_0}{2^p} + (M_c - 1) \cdot \sum_{q=1}^p \frac{1}{2^q} \\ &= \frac{L_0}{2^p} + (M_c - 1) \cdot \left(1 - \frac{1}{2^p}\right) \\ &= \frac{1}{2^p} \cdot \left(L_0 - (M_c - 1)\right) + (M_c - 1) \end{aligned} \quad (6.3)$$

Since, at each stage, each of two sequences is convolved with a filter of length M_c , the total number of multiplications N_c necessary to perform a K -stage multiresolution decomposition into primary channels

$$N_c = 2 \cdot M_c \cdot \sum_{p=0}^{K-1} L_p. \quad (6.4)$$

Substitution of (6.3) into (6.4) produces

$$N_c = 2 \cdot K \cdot (M_c - 1) + 2 \cdot M_c \cdot \left(L_0 - (M_c - 1)\right) \cdot \sum_{p=0}^{K-1} \frac{1}{2^p}. \quad (6.5)$$

Finally, evaluating the geometric series in (6.5) produces

$$N_c = 2 \cdot K \cdot (M_c - 1) + 4 \cdot M_c \cdot \left(L_0 - (M_c - 1)\right) \cdot \left(1 - \frac{1}{2^K}\right). \quad (6.6)$$

Equation (6.6) covers all of the multiplications necessary to perform the decomposition into primary channels in accordance with block diagram 4.19.

If the primary detail channels are each to be decomposed into J subchannels using a subchannel filter bank constructed from filter of length M_s , additional computation is necessary.

First, if a sequence of length L_p is convolved with a filter of length M_s and subsequently decimated by a factor of J , the length $L_r^{(p)}$ of the resultant sequence will be

$$L_r^{(p)} = \frac{1}{J} (L_p + M_s - 1).$$

The number of multiplications $N_r^{(p)}$ to perform this signal reduction at stage p is expressed by

$$N_r^{(p)} = M_s \cdot L_p,$$

which by substitution of (6.3) becomes

$$N_r^{(p)} = M_s \cdot \left(\frac{1}{2^p} \cdot (L_0 - (M_c - 1)) + (M_c - 1) \right).$$

If there are a total of J subchannels per stage and a total of K stages, then the total number of multiplications N_r required to perform all subchannel decomposition operations is evaluated as

$$\begin{aligned} N_r &= J \cdot \sum_{p=1}^K N_r^{(p)} \\ &= J \cdot K \cdot M_s \cdot (M_c - 1) + J \cdot M_s \cdot (L_0 - (M_c - 1)) \cdot \sum_{p=1}^K \frac{1}{2^p} \\ &= J \cdot K \cdot M_s \cdot (M_c - 1) + J \cdot M_s \cdot (L_0 - (M_c - 1)) \cdot \left(1 - \frac{1}{2^K}\right) \end{aligned} \quad (6.7)$$

If the decomposed sequence of length $L_r^{(p)}$ is expanded by a factor of J and subsequently convolved with a filter of length M_c , the length $L_e^{(p)}$ of the resultant sequence is expressed by

$$L_e^{(p)} = J \cdot L_r^{(p)} + M_s - 1 = L_p + 2 \cdot (M_s - 1).$$

The number of multiplications $N_e^{(p)}$ necessary to perform this operation for J subchannels at decomposition stage p is therefore

$$N_e^{(p)} = J \cdot M_s \cdot L_e^{(p)} = J \cdot M_s \cdot (L_p + 2 \cdot (M_s - 1)).$$

Furthermore, the total number of multiplications necessary to expand all subchannel decompositions is expressed as

$$N_e = J \cdot M_s \cdot \sum_{p=1}^K L_e^{(p)} = J \cdot M_s \cdot \sum_{p=1}^K \left[\frac{1}{2^p} \cdot (L_0 - (M_c - 1)) + (M_c - 1) \right]. \quad (6.8)$$

Substituting (6.3) into (6.8) and evaluating the series produces

$$\begin{aligned} N_e &= J \cdot M_s \cdot \sum_{p=1}^K \left[\frac{1}{2^p} \cdot (L_0 - (M_c - 1)) + (M_c - 1) + 2 \cdot (M_s - 1) \right] \\ &= J \cdot K \cdot M_s \cdot \left((M_c - 1) + 2 \cdot (M_s - 1) \right) + J \cdot M_s \cdot (L_0 - (M_c - 1)) \cdot \sum_{p=1}^K \frac{1}{2^p} \\ &= J \cdot K \cdot M_s \cdot \left((M_c - 1) + 2 \cdot (M_s - 1) \right) + J \cdot M_s \cdot (L_0 - (M_c - 1)) \cdot \left(1 - \frac{1}{2^K} \right) \end{aligned} \quad (6.9)$$

To calculate the number of multiplications necessary to re-expand a detail component sequence reconstructed from decomposition into subchannels, the notation $L_q^{(p)}$ will be employed to indicate the length of the sequence at a stage of interest. The superscript $^{(p)}$ indicates the number of the stage of decomposition at which the detail component sequence was extracted. The subscript $_q$ denotes the stage of reconstruction. The stages of reconstruction are labeled in decreasing order from $p-1$ to 0 for a component extracted at the p^{th} stage of decomposition. At stage p , the length of the detail sequence, after reconstruction from subchannel decomposition, is given by $L_e^{(p)} = L_p^{(p)}$. Now, upon expanding the detail sequence of length $L_p^{(p)}$ and convolving it with the channel synthesis filter of length M_c , at stage $p-1$, the expanded sequence which is obtained has length

$$L_{p-1}^{(p)} = 2 \cdot L_p^{(p)} + M_c - 1 = 2 \cdot L_p + 4 \cdot (M_s - 1) + M_c - 1. \quad (6.10)$$

Inductively, after q stages of decimation followed by convolution with the appropriate channel's synthesis filters, (6.10) becomes

$$\begin{aligned}
 L_{p-q}^{(p)} &= 2^q \cdot \left(L_p + 2 \cdot (M_s - 1) \right) + (M_c - 1) \cdot \sum_{r=0}^{q-1} 2^r \\
 &= 2^q \cdot \left(L_p + 2 \cdot (M_s - 1) \right) + (M_c - 1) \cdot (2^q - 1) \quad (6.11) \\
 &= 2^q \cdot \left(L_p + 2 \cdot (M_s - 1) + (M_c - 1) \right) - (M_c - 1)
 \end{aligned}$$

Now, substituting L_p from (6.3) into (6.11) produces

$$L_{p-q} = 2^q \cdot \left(\frac{1}{2^p} \cdot \left(L_0 - (M_c - 1) \right) + (M_c - 1) + 2 \cdot (M_s - 1) + (M_c - 1) \right) - (M_c - 1) \quad (6.12)$$

Consequently, the total number of multiplications required for a full expansion by channel of a decomposed sequence can be evaluated by summing up the contributions from each convolution performed in each channel. It stands to reason, that the number of multiplications $N_{p-1}^{(p)}$ involved in expansion of J detail component sequences (one detail component sequence for each of J subchannels) of length $L_p^{(p)}$, at stage p , to obtain a sequence of length $L_{p-1}^{(p)}$, at stage $p - 1$, is indicated by

$$N_{p-1}^{(p)} = J \cdot M_c \cdot L_{p-1}^{(p)}.$$

Inductively, therefore, the total number of multiplications $N_0^{(p)}$ necessary to completely expand the J decomposed sequences in channel p is obtained from

$$N_0^{(p)} = J \cdot M_c \cdot \sum_{q=1}^p L_{p-q}^{(p)}. \quad (6.13)$$

Therefore, to obtain $N_0^{(p)}$, it is necessary to substitute (6.12) into (6.13) and evaluate the series, which produces

$$\begin{aligned}
 N_0^{(p)} &= J \cdot M_c \cdot \left[\frac{1}{2^p} \cdot (L_0 - (M_c - 1)) + 2 \cdot (M_c - 1) + 2 \cdot (M_s - 1) \right] \sum_{q=1}^p (2^q) - p \cdot J \cdot M_c \cdot (M_c - 1) \\
 &= 2 \cdot J \cdot M_c \cdot \left[\frac{1}{2^p} \cdot (L_0 - (M_c - 1)) + 2 \cdot (M_c - 1) + 2 \cdot (M_s - 1) \right] \cdot (2^p - 1) - p \cdot J \cdot M_c \cdot (M_c - 1) \\
 &= 2 \cdot J \cdot M_c \cdot (L_0 - 3 \cdot (M_c - 1) - 2 \cdot (M_s - 1)) + 2 \cdot J \cdot M_c \cdot (2 \cdot (M_c - 1) + 2 \cdot (M_s - 1)) \cdot 2^p \\
 &\quad - 2 \cdot J \cdot M_c \cdot (L_0 - (M_c - 1)) \cdot \frac{1}{2^p} - p \cdot J \cdot M_c \cdot (M_c - 1)
 \end{aligned} \tag{6.14}$$

And lastly, to obtain N_0 , the total number of multiplications to compute the full expansion by channel, it is necessary to sum the contributions $N_0^{(p)}$ from each channel. This sum appears as

$$\begin{aligned}
 N_0 &= 2 \cdot J \cdot K \cdot M_c \cdot (L_0 - 3 \cdot (M_c - 1) - 2 \cdot (M_s - 1)) \\
 &\quad + 2 \cdot J \cdot M_c \cdot (2 \cdot (M_c - 1) + 2 \cdot (M_s - 1)) \cdot \sum_{p=1}^K 2^p \\
 &\quad - 2 \cdot J \cdot M_c \cdot (L_0 - (M_c - 1)) \cdot \sum_{p=1}^K \frac{1}{2^p} \\
 &\quad - J \cdot M_c \cdot (M_c - 1) \cdot \sum_{p=1}^K p
 \end{aligned} \tag{6.15}$$

The first series in (6.15) are simply the geometric series evaluated previously in this development. The last series can be solved using Bernoulli polynomials [40] which produce

$$\sum_{p=1}^K p = \frac{1}{2} \cdot (K^2 + K).$$

Substituting each of the evaluated series into (6.15) and collecting similar terms produces, for N_0 ,

$$\begin{aligned}
N_0 = & 2 \cdot K \cdot J \cdot M_c \cdot \left(L_0 - 3 \cdot (M_c - 1) - 2 \cdot (M_s - 1) \right) \\
& + 4 \cdot J \cdot M_c \cdot \left(2 \cdot (M_c - 1) + 2 \cdot (M_s - 1) \right) \cdot (2^K - 1) \\
& - 2 \cdot J \cdot M_c \cdot \left(L_0 - (M_c - 1) \right) \cdot \left(1 - \frac{1}{2^K} \right) \\
& - \frac{1}{2} \cdot J \cdot M_c \cdot (M_c - 1) \cdot (K^2 + K)
\end{aligned} \tag{6.16}$$

Equation (6.16) applies whether or not subchannel decomposition is performed. If subchannel is not performed, then the detail sequence at each stage is decomposed into $J = 1$ subchannels and the filter $g_0(n)$ used for subchannel decomposition possesses as its impulse response $g_0(n) = \delta_{0,n}$ where $\delta_{0,n}$ is Kronecker's delta function. Consequently, because of how $g_0(n)$ is defined, $M_s=1$ and, in (6.16), each of the terms in involving $M_s - 1$ become zero.

TABLE 6.1--COMPARISON OF NUMBER OF MULTIPLICATIONS NECESSARY FOR MULTIREOLUTION AND SPECTROGRAM SIGNAL REPRESENTATIONS.

	Primary Channel Decomposition	Primary Channel Re-expansion	Subchannel Decomposition	Subchannel Re-expansion	Total
Two-Channel, Zero-Subchannel	13,762	406,558	0	0	420,321
Two-Channel, Two-Subchannel	13,762	1,544,028	9,689	15,513	1,582,902
Two-Channel, Three-Subchannel	13,762	2,400,378	15,572	25,625	2,455,274
Two-Channel, Four-Subchannel	13,762	4,887,224	41,526	97,206	5,039,634
Spectrogram	-----	-----	-----	-----	14,909,440

Summarizing, there are four contributors which must be evaluated to calculate the number of multiplications N_0 necessary for a full channel by expansion of a decomposed sequence. The basic decomposition, N_c , is provided by (6.6). The decomposition into

subchannels, N_p is calculated using (6.7). To re-expand subchannel decompositions, the number of multiplications is indicated by (6.9). And finally, for the full expansion by channel, the number of calculations is provided by (6.15). For some of the multiresolution structures demonstrated in Section IV.E, the number of multiplications is tabulated in Table 6.1.

In considering Table 6.1, it must be noted that the decompositions listed do not represent the optimum representation. In the case of the multiresolution decompositions, the essential information about the decomposed signal is contained in the primary channel and subchannel. The re-expansion by channel merely provides a manner of displaying the information which is more convenient than plotting coefficients in a non-uniform lattice of the type of Figure 4.8.

In the case of the spectrogram, shifting a 128-point window by increments of two samples provides what is likely excessive overlap. This degree of overlap was used in an attempt to capture, to the greatest extent possible, the time-varying features of the test sequences on which decomposition was performed. If, for instance, the 128-point window was shifted in increments of 64 samples to provide for a 50% overlap, the number of multiplications N_p would be $N_p=688,128$. This overlap, however, would provide poorer indication of the non-stationary features of the sequences for which decomposition was performed. A 50% overlap with a window length of 128 used to decompose a sequence of length 256 would provide for three time shifts.

With regard to the multiresolution decompositions, excluding the calculation used to re-expand the components of decomposition, a significant advantage in computational efficiency

is evident. Because of the factor-of-two decimation performed at each stage of decomposition, the sequence length at each stage is one half the length of the sequence of the previous stage. Consequently, the number of calculations necessary to perform the calculation is related to a geometric series in one half.

C. PERFORMANCE OF DECOMPOSITIONS IN THE PRESENCE OF NOISE

Many signal processing techniques are employed with the intent of extracting a signal from noise in which it is embedded. The spectrogram, one of the most commonly used signal processing tools, represents an attempt to localize spectral components of a signal. If the noise in which the signal is imbedded can be characterized as "white," possessing a flat power spectral density, a signal which can be localized in a spectral sense will be detectable in greater noise intensity than a signal which is not spectrally localized. Consequently, when attempting to detect a signal by means of spectral localization, the effective signal-noise ratio can be reduced to the ratio of signal power to the power of only the noise contained within the spectral region of interest.

To detect a time-varying process, the detection process becomes a two-dimensional problem, requiring localization in both frequency and time. Within the context of time-frequency localization, multiresolution techniques present the potential for an alternative method of detection. Many of the advantages of multiresolution transforms which lend those decompositions to signal decomposition also provide the basis for extraction of embedded signals from noise. Multiresolution transforms provide good time resolution at high frequencies and frequency resolution at lower frequencies. Furthermore, if it is sought to detect a class of

processes for which bandwidth is proportional to the center frequency of the process, multiresolution techniques may provide the optimum detection technique.

If a sequence $s(n)$ is embedded in additive, white, Gaussian noise $\eta(n)$, the resultant sequence

$$x(n) = s(n) + \eta(n) \quad (6.17)$$

will also be a Gaussian random variable. If the noise process has $\eta(n)$ a mean of zero then the mean of the signal plus noise $x(n)$ is indicated by

$$\overline{x(n)} = s(n). \quad (6.18)$$

Furthermore, the variance of $x(n)$ equals the variance of $\eta(n)$:

$$\sigma_x^2 = \sigma_\eta^2. \quad (6.19)$$

In Chapter IV it was demonstrated that decomposition of a sequence by multiresolution structures constructed from cascaded perfect reconstruction quadrature mirror filter banks is equivalent to projection of the sequence to be decomposed upon a space of orthonormal vectors. Decomposition by perfect reconstruction filter banks into subchannels, furthermore, can be interpreted as subdivision of the detail vector space W_m , using the notation from Chapter IV, into another set of complementary set of subspaces $\{W_m^{(k)}\}_k$. If, however, the filter banks do not satisfy the perfect reconstruction criteria, orthonormality of the equivalent projection operation is not guaranteed.

The the wavelet coefficients $\{b_{m,n}\}_{n \in \mathbb{Z}}$ obtained from decomposing a sequence $x(n)$ were defined in Section IV.C as

$$b_{m,n} = (x, \psi_{m,n}). \quad (6.20)$$

Now, if $x(n)$ is a Gaussian random variable, then $b_{m,n}$ will also be a Gaussian random variable.

Furthermore, if the set of basis functions $\{\psi_{m,n}\}$ is orthonormal, then the wavelet coefficients

$b_{m,n}$ will be linearly independent. To obtain the expected value of $b_{m,n}$, substitution of (6.17)

into (6.20) produces

$$b_{m,n} = (s, \psi_{m,n}) + (\eta, \psi_{m,n}). \quad (6.21)$$

Assuming the η has a mean of zero, then the mean of the wavelet coefficient $b_{m,n}$ for a signal

$s(n)$ embedded in noise is simply the value of the wavelet coefficient evaluated in the absence of noise.

To obtain the variance of $b_{m,n}$, the squared mean is first

$$\mathcal{E}\{b_{m,n}^2\} = (s, \psi_{m,n})^2 + \mathcal{E}\{(\eta, \psi_{m,n})^2\} \quad (6.22)$$

The expectation on the right-hand side of (6.22) is evaluated as

$$\mathcal{E}\{(\eta, \psi_{m,n})^2\} = \mathcal{E}\left\{\iint \eta(u)\eta(v)\psi_{m,n}(u)\psi_{m,n}(v) du dv\right\}. \quad (6.23)$$

The expectation operator on the right-hand side of (6.23) can be passed through the double

integral to operate on the terms $\eta(u)\eta(v)$ producing

$$\mathcal{E}\{\eta(u)\eta(v)\} = \sigma_\eta^2 \delta(u-v) \quad (6.24)$$

where $\delta(t)$ denotes the Dirac delta function. By the integral sifting property of the Dirac delta

function, (6.24) reduces to

$$\mathcal{E}\{(\eta, \psi_{m,n})^2\} = \sigma_\eta^2 (\psi_{m,n}, \psi_{m,n}) = \sigma_\eta^2. \quad (6.25)$$

The wavelet coefficients, therefore, simply comprise Gaussian random variables whose mean is $(s, \psi_{m,n})$ with a variance of σ_η^2 .

If detection of a *known sequence* in the presence of noise is required, one way to generate a decision statistic is to sum the squared magnitudes of all of the nodes in the transform space whose powers exceed a specified threshold. In performing multiresolution decomposition of a sequence, the essential information about a signal is contained in a linearly independent array $D_{j,k}$ of non-uniform density such as that in figure 4.8. In detecting a known sequence in the presence of noise, it is conveniently possible to consider only the decomposition nodes in which a significant portion of the signal energy is represented. Mathematically, given a multiresolution decomposition represented by a lattice of points $D_{j,k}$, the decision statistic can, equivalently, be constructed which excludes nodes contained in $D_{j,k}$ which are negligible in value. The subset of $D_{j,k}$ of which the decision statistic is comprised can be limited to those nodes whose addresses are indicated by κ :

$$\kappa = \left\{ (j, k) : \left| D_{j,k} \right|^2 \geq \rho \cdot \max_{j,k} \left| D_{j,k} \right|^2 \right\}. \quad (6.26)$$

Figures 6.2a, 6.2b, 6.3a and 6.3b present the results for statistics constructed from all nodes defined by (6.26) where $\rho = 1/100$. Table 6.2 indicates the mean square reconstruction error (3.32) which results from the value selected for ρ . The information in Table 6.2 is intended as an indication of the consequences incurred from considering only the nodes in D_κ .

where κ is defined by (6.26). The decision statistics for the periodogram were generated in the same manner as for the multiresolution decompositions.

TABLE 6.2--NORMALIZED MEAN-SQUARE RECONSTRUCTION ERROR RESULTING FROM TRUNCATED DECOMPOSITION. RECONSTRUCTION PERFORMED FROM SUBLATTICE DEFINED BY (6.26) WITH $\rho = 1/100$. EIGHT DECOMPOSITION STAGES WERE PERFORMED IN THE TWO-CHANNEL CASES WHILE FIVE-STAGE DECOMPOSITIONS ARE INDICATED FOR THE THREE-CHANNEL CASES

	Test sequence (4.74a)	Test Sequence (4.74b)
Two-channel, zero-subchannel	0.0065	0.0121
Two-channel, two-subchannel	0.0121	0.0244
Two-channel, three-subchannel	0.0046	0.0209
Two-channel, four-subchannel	0.0288	0.1578
Three-channel, zero-subchannel	0.01	0.01

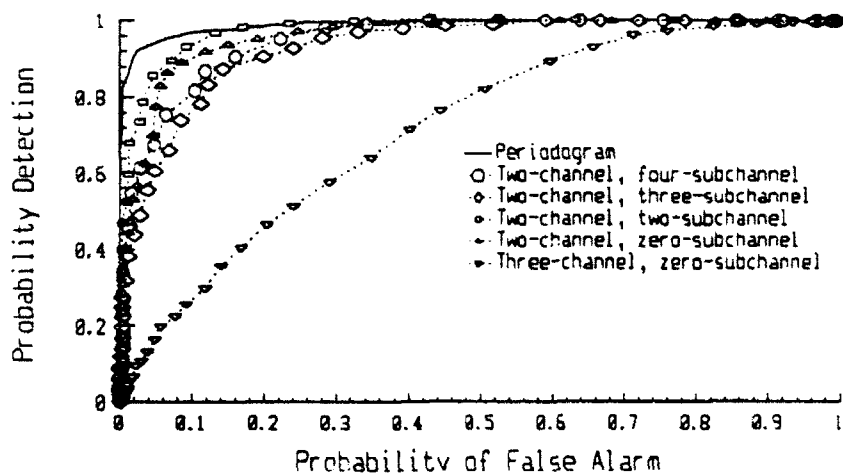


Figure 6.2a--Receiver operating characteristics for spectrogram and for various multiresolution decompositions of low-frequency transient (4.74a) embedded in noise with a -3 dB signal-noise ratio. Characteristics generated from 500-realizations of 256-point random noise vector.

For each technique indicated, 500 realizations of a 256-point, Gaussian random vector were generated. For each multiresolution technique reflected in Figures 6.2a and 6.2b, prior

generating the receiver operating characteristics, decision statistics were generated for separate noise realizations alone. The receiver operator characteristics for noise alone consisted of unity-slope straight lines. The decompositions were then performed for the test sequences (4.74a) and (4.74b) with additive noise and then for the noise vector alone. The decision statistics for the receiver operator characteristics consisted of all nodes in the composition whose magnitudes were greater than the one-percent threshold described above.

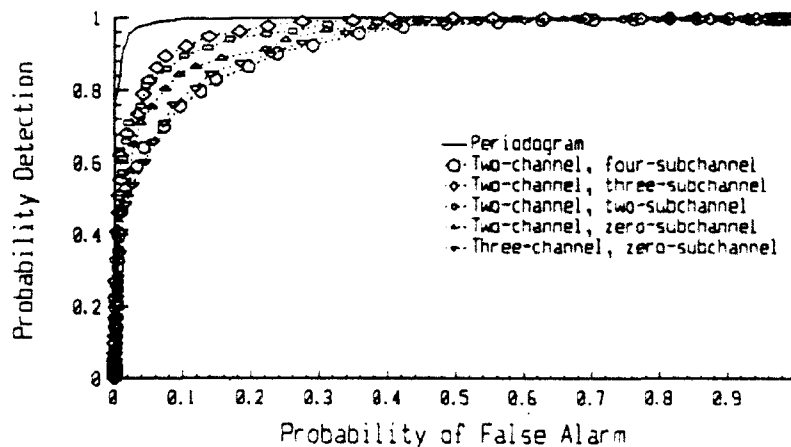


Figure 6.2b--Receiver operating characteristics for spectrogram and for various multiresolution decompositions of high-frequency transient (4.74b) embedded in noise with a -3 dB signal-noise ratio. Characteristics generated from 500-realizations of 256-point random noise vector.

The receiver operating characteristics were, therefore, constructed from central and non-central chi-square distributions. The sum of the squares of the selected nodes of the noise decomposition, since they were generated from zero-mean noise, constitutes a chi-square distribution. Summing the selected nodes of the decomposition of signal plus noise produces a non-central chi-square distribution.

In both Figures 6.2a and 6.2b, the spectrogram provided greater robustness than the multiresolution techniques. With the exception of the three-channel, zero-subchannel

decomposition applied to highpass test sequence (4.74b) in -3 dB signal-noise ratio, the differences were not, however, dramatic. Moreover, for test sequence (4.74b), the multiresolution curves were, with the named exception, closer to the performance of the spectrogram than for lowpass test sequence (4.74a). The greater disparity in the case of highpass test sequence (4.74b) may be attributable to the difference in resolution between the multiresolution and spectrogram techniques in the high-frequency regions of the spectrum.

It is interesting to observe that, in Figure 6.2a, the best results among the multiresolution decompositions were obtained from the two-channel, zero-subchannel and two-channel, two-subchannel algorithms. Those two algorithms were constructed strictly from perfect-reconstruction filter banks and, therefore, produced the lowest reconstruction error. Additionally, in the case of highpass test sequence (4.74b), the best performance was obtained from the two-channel, three-subchannel decomposition. The two-channel, four-subchannel decomposition provided, by a small margin, the worst of all results.

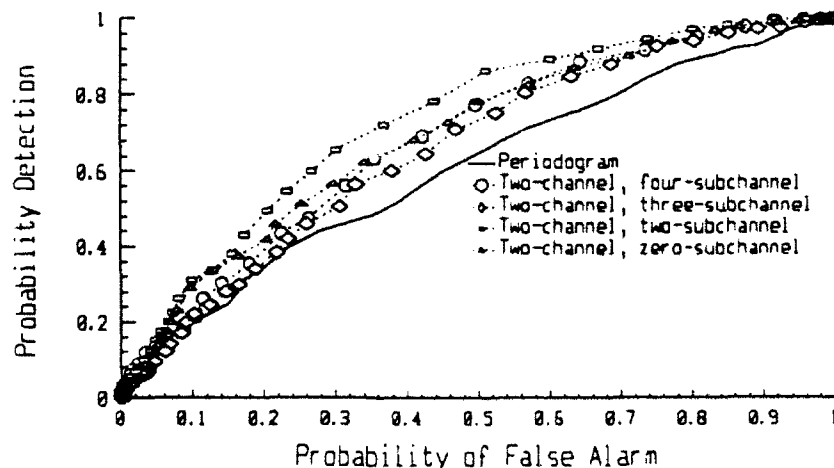


Figure 6.3a--Receiver operating characteristics for spectrogram and for various multiresolution decompositions of low-frequency transient (4.74b) embedded in noise with a -6 dB signal-noise ratio. Characteristics generated from 500-realizations of 256-point random noise vector.

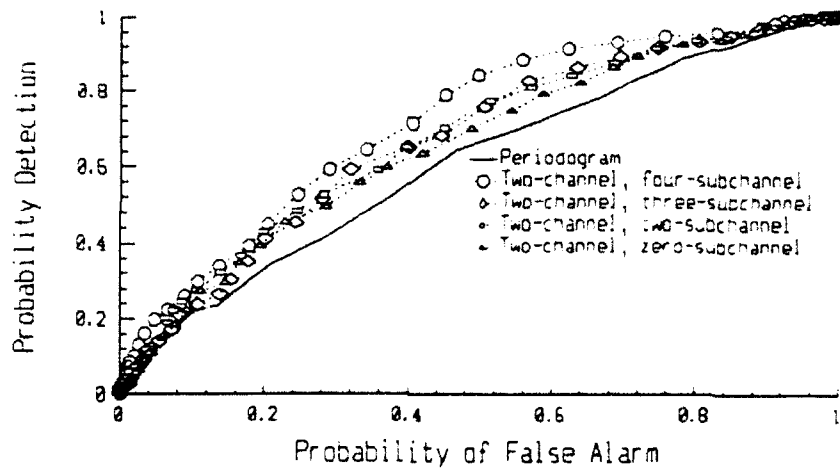


Figure 6.3b--Receiver operating characteristics for spectrogram and for various multiresolution decompositions of high-frequency transient (4.74a) embedded in noise with a -6 dB signal-noise ratio. Characteristics generated from 500-realizations of 256-point random noise vector.

Results for a signal-noise ratio of -6 dB are presented in Figures 6.3a and 6.3b. In the case of the lower signal-noise ratio, all of the multiresolution methods outperformed the spectrogram by a small measure. In the case of lowpass test sequence (4.74a) the best results were provided, as with the -3 dB signal-noise ratio test, by the two-channel, two-subchannel and the two-channel, zero-subchannel, respectively. This trend may be related to the superior reconstruction error provided by these techniques. In the case of highpass test signal (4.74b), on the other hand, the best results came from the four-subchannel and three-subchannel decompositions. This may have occurred as a result of the resolution of the decompositions. For the low-frequency transient, (4.74a), the three-subchannel and four-subchannel may have over-resolved the signal. For the high-frequency transient, (4.74b), the two-subchannel and zero-subchannel decompositions may have under-resolved the signal. Consequently, in the first case, the signal energy, for the higher resolution decompositions, may have been distributed over a greater-than-optimum number of time-scale bins. In the second case, the lower resolution,

decomposition may not have sufficiently localized the signal to isolate it from the effects of the noise.

D. DECOMPOSITION OF STEADY-STATE HARMONICS AND FM CHIRPS

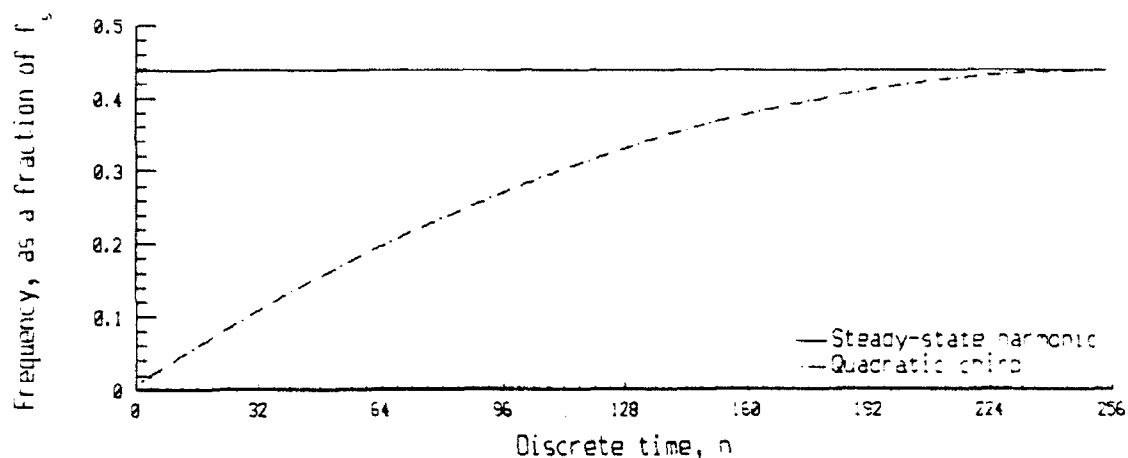


Figure 6.4a--Time-frequency plot of evolution of constituents of first 256-point test signal constructed from one steady-state harmonic and a quadratically chirped component.

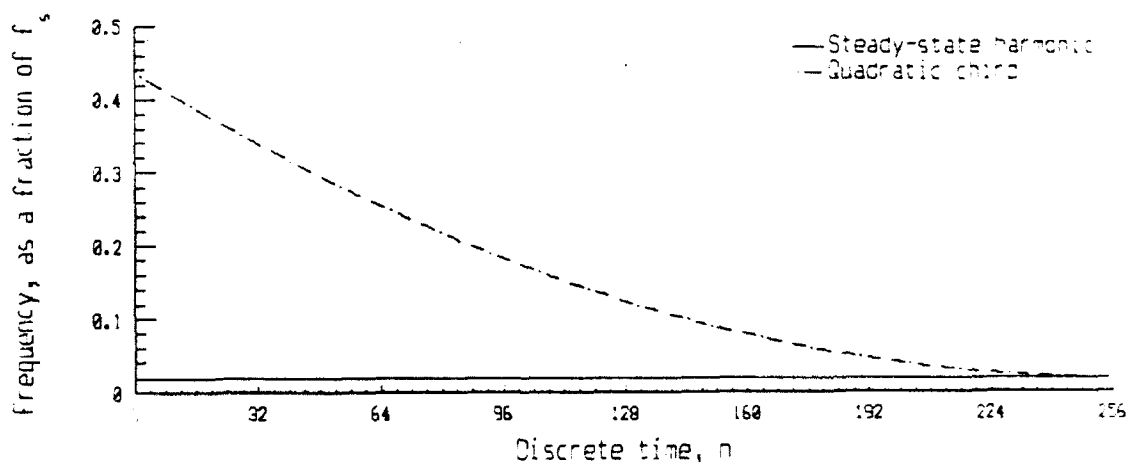


Figure 6.4b--Time-frequency plot of evolution of constituents of second 256-point test signal constructed from one steady-state harmonic and a quadratically chirped component.

The time-scale resolutions of multiresolution decomposition techniques were somewhat addressed in Section IV.E. However, in order to better understand the performance of these methods, a more controlled demonstration is desirable. In this section, results will be

demonstrated for a frequency-modulated, quadratic chirp converging to a steady-state harmonic component. The performance of the spectrogram method will first be illustrated. Then the results will be considered for two multiresolution techniques--the two-channel, four-subchannel and the two-channel, three-subchannel decompositions.

Two test signals were generated for this demonstration. To illustrate the variations of resolution of scale provided by multiresolution decompositions in different regions of the frequency spectrum, it was desired to demonstrate the case in which the quadratic FM chirp converges from above to a steady-state harmonic in the lower half of the frequency spectrum and the case in which the FM chirp converges from below to a steady-state harmonic in the upper half of the frequency spectrum. Based on the experience of Chapter IV, it is expected that, for the first case, better resolution will be provided by the multiresolution techniques.

The form for dynamic component of the test sequences is given by

$$s(t) = \cos(2 \cdot \pi \cdot \int_0^n f(t) dt) + \cos(2 \cdot \pi \cdot f_r \cdot n) \quad (6.27)$$

where the instantaneous frequency $f(t)$ possesses the form of a parabola whose vertex is, in the time-frequency plane, located at (t_f, f_f) , the coordinates of the final time and frequency in the test region. The time-frequency parabola satisfying this criterion assumes the form of

$$f(t) = \alpha \cdot (t - t_f)^2 + f_f. \quad (6.28)$$

Evaluating the integral in the argument of the first cosine term on the right-hand side of (6.26) produces for the phase of the chirped component

$$F(n) = \frac{\alpha}{3} \cdot \left((n - t_f)^3 - t_f^3 \right) + f_r \cdot n. \quad (6.29)$$

To uniquely define $f(t)$, it is necessary to specify the location of (t_f, f_f) , the vertex of the parabola, and the location of some other point on the curve in the time-frequency plane. If the time $t_0 = 0$ and frequency f_0 of the chirp at the beginning of the test sequence are specified, the coefficient α from (6.28) becomes

$$\alpha = \frac{f_0 - f_f}{t_f^2} \quad (6.30)$$

Since 256-point test sequences are to be used, the final time $t_f = 256$. It therefore remains to specify beginning and ending frequencies.

For the first test sequence, a chirp which converges from below to a steady-state harmonic in the upper half of the frequency spectrum below the Nyquist frequency. The beginning and ending frequencies selected for the chirp were

$$\begin{aligned} f_0 &= \frac{1}{128} \cdot f_s \\ \text{and} & \\ f_f &= \frac{7}{16} \cdot f_s \end{aligned} \quad (6.31a)$$

For the second test sequence in which the quadratic chirp converged from above to a steady-state harmonic in the lower half of the frequency spectrum, the frequencies selected were

$$\begin{aligned} f_0 &= \frac{7}{16} \cdot f_s \\ \text{and} & \\ f_f &= \frac{5}{256} \cdot f_s \end{aligned} \quad (6.31b)$$

The ideal, time-frequency evolution of the two test signals are plotted in Figures 4.6a and 4.6b, respectively.

The spectrogram decompositions of the two test signals are plotted in Figures 6.5a and 6.5b for two purposes. The first reason is to verify that the desired affects were obtained in

construction of the test sequences. The second reason for the periodograms is to provide a standard with which the performance of the multiresolution decompositions can be compared. The spectrogram plots were generated in a manner identical to that used in Section A of the present chapter. The data sequences were windowed by a 128-point Hanning window which was shifted in two-sample increments. Only the half of the frequency spectrum below the Nyquist frequency was plotted.

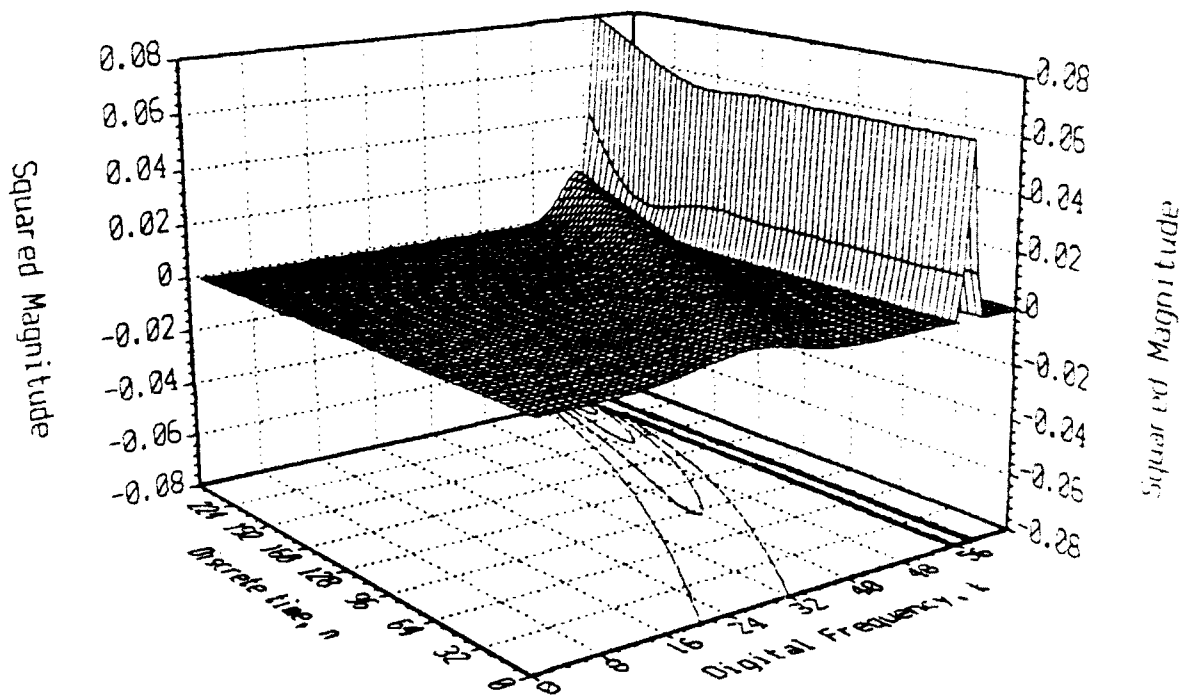


Figure 6.5a--Spectrogram decomposition of first 256-point test sequence constructed from a steady-state harmonic component and a frequency-modulated quadratic chirp. The decomposition was obtained by windowing the data sequence with a 128-point Hanning window shifted in increments of two samples. Only the half of the frequency spectrum below the Nyquist frequency is plotted.

Examining Figures 6.5a and 6.5b, the two components of each test sequence can be seen to converge as expected. The steady-state harmonic produces a much better resolved indication than the chirped component. This occurs because of the smearing of the chirp which results

from the frequency shift occurring during the integration time of each FFT. Both decompositions represent the data with uniform resolution throughout the frequency spectrum. Consequently, the time, for both sequences, at which the components cannot be resolved is the same for both sequences at approximately the 230th sample. Consequently, from (6.28), the spectral resolution of the spectrogram decomposition is approximately $0.0043 \cdot f_s$. No attempt was made to optimize the window length with respect to resolution of the test signal components. The 128-point window provides good frequency resolution, however, because of the long integration time, the frequency of the chirped component has shifted significantly during each transform.

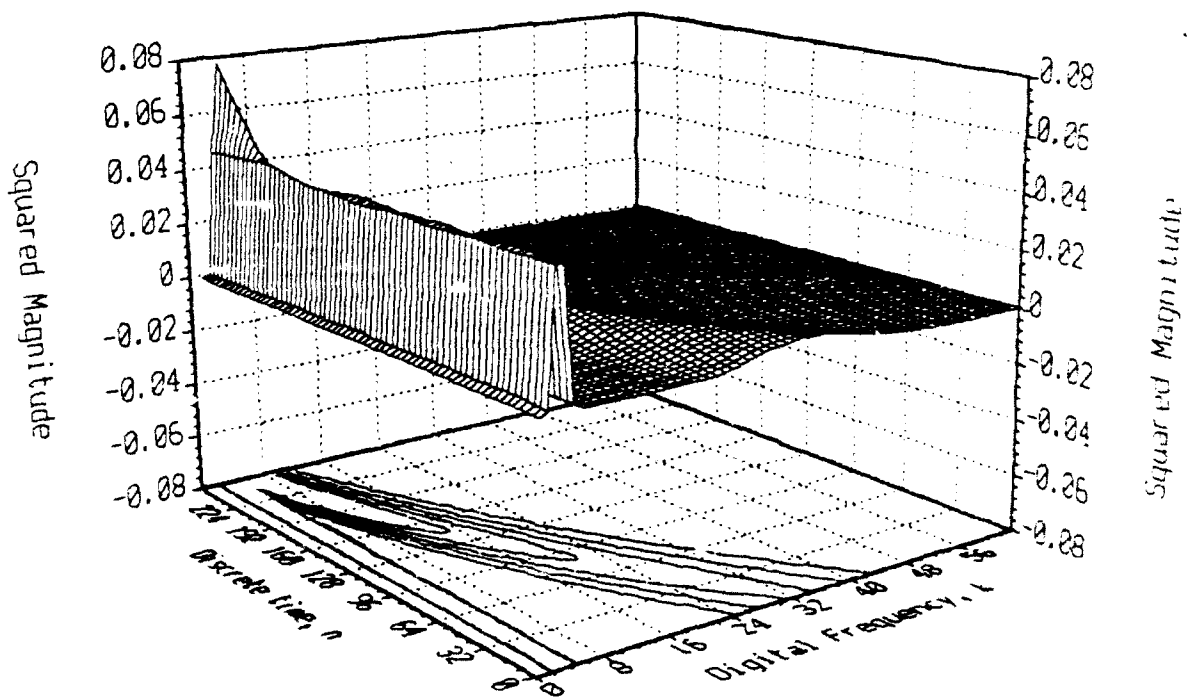


Figure 6.5b--Spectrogram decomposition of second 256-point test sequence constructed from a steady-state harmonic component and a frequency-modulated quadratic chirp. The decomposition was obtained by windowing the data sequence with a 128-point Hanning window shifted in increments of two samples. Only the half of the frequency spectrum below the Nyquist frequency is plotted.

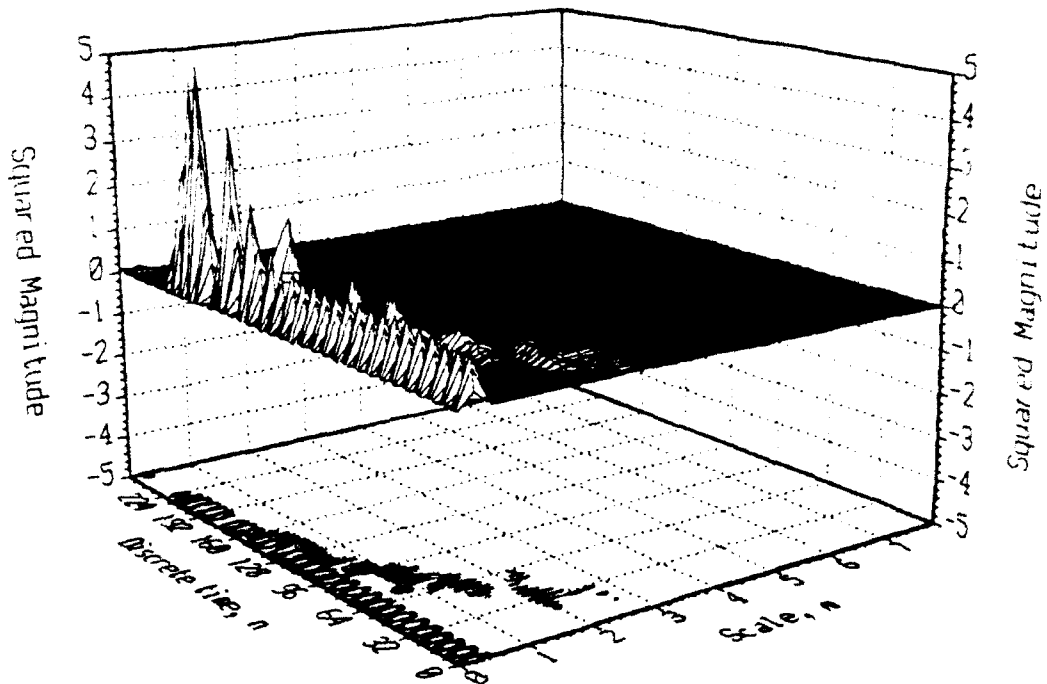


Figure 6.6a--Two-channel, three-subchannel multiresolution decomposition of first 256-point test sequence constructed from steady-state harmonic component and quadratic chirp. Primary channel filters were based on Daubechies' orthonormal wavelet and scaling function on $[0, 13]$. Subchannel decomposition was performed with pseudo-QMF filter bank designed in [11].

Examining Figures 6.5a and 6.5b, the two components of each test sequence can be seen to converge as expected. The steady-state harmonic produces a much better resolved indication than the chirped component. This occurs because of the smearing of the chirp which results from the frequency shift occurring during the integration time of each FFT. Both decompositions represent the data with uniform resolution throughout the frequency spectrum. Consequently, the time, for both sequences, at which the components cannot be resolved is the same for both sequences at approximately the 230th sample. Consequently, from (6.28), the spectral resolution of the spectrogram decomposition is approximately $0.0043 \cdot f_c$. No attempt was made to optimize the window length with respect to resolution of the test signal

components. The 128-point window provides good frequency resolution, however, because of the long integration time, the frequency of the chirped component has shifted significantly during each transform.

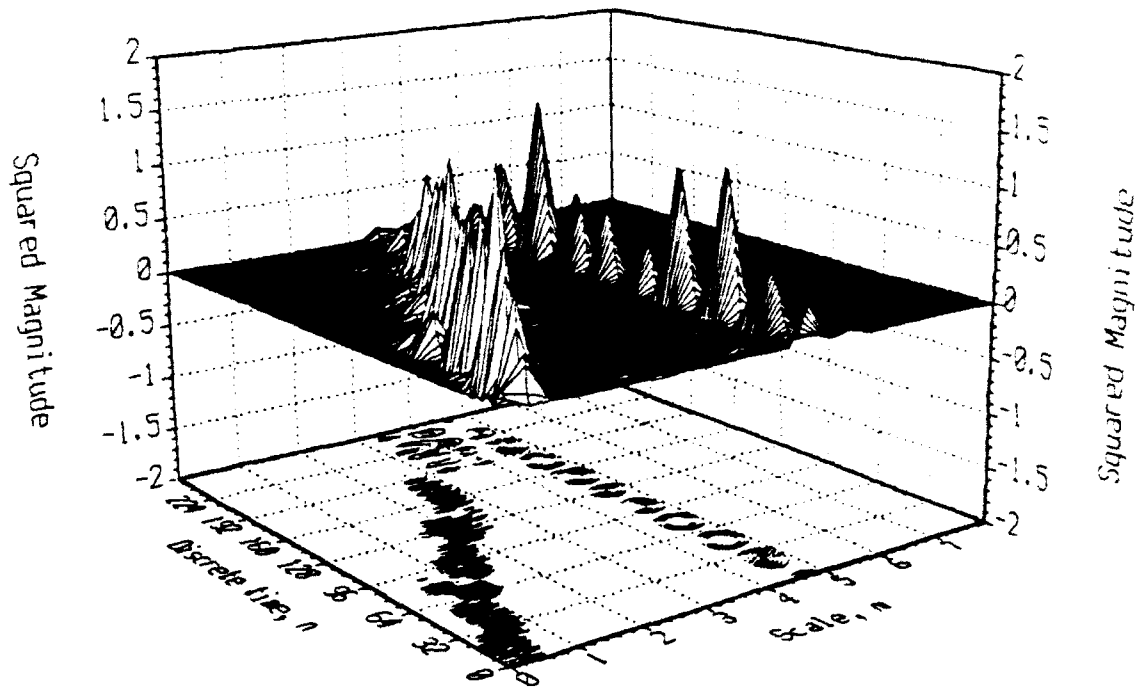


Figure 6.6b--Two-channel, three-subchannel multiresolution decomposition of second 256-point test sequence constructed from steady-state harmonic component and quadratic chirp. Primary channel filters were based on Daubechies' orthonormal wavelet and scaling function on $[0, 13]$. Subchannel decomposition was performed with pseudo-QMF filter bank designed in [11].

The two-channel, three-subchannel decomposition of the second test sequence is plotted in Figure 6.6b. In the case of this plot, the chirp becomes unresolvable from the steady-state harmonic at approximately the 230th sample. By (6.28), therefore, the frequency resolution is approximately $0.0043 \cdot f_s$. This number is quite close to the figure for the spectrogram decomposition. Furthermore, the two test sequence components become unresolvable around a scale of four which coincides detail subchannels obtained from the fourth stage of

decomposition. If the final frequency f_f had occurred at a lower frequency, the convergence point between the two components would have occurred in the detail subchannels of a later decomposition stage resulting in even greater resolution.

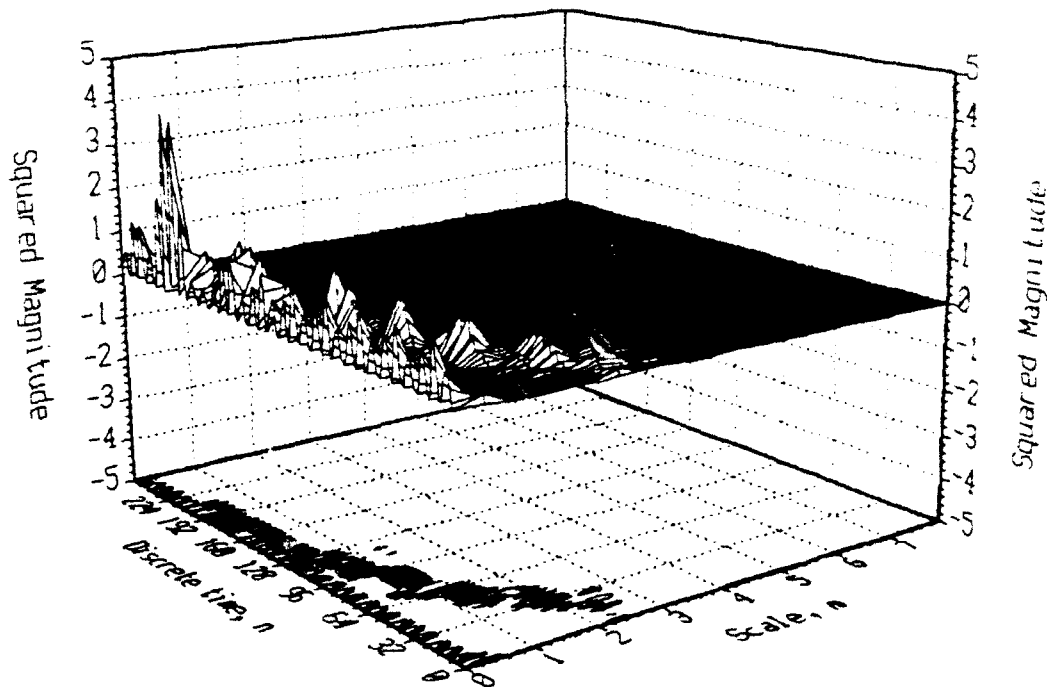


Figure 6.7a--Two-channel, four-subchannel multiresolution decomposition of first 256-point test sequence constructed from steady-state harmonic component and quadratic chirp. Primary channel filters were based on Daubechies' orthonormal wavelet and scaling function on $[0, 13]$. Subchannel decomposition was performed with pseudo-QMF filter designed in Chapter V.

Figures 6.6a and 6.6b present results of three-channel, four-subchannel multiresolution decomposition of the two test sequences. In Section IV.E, within the context of considering the decomposition of transients constructed from components of varying frequencies, the performance of the three-channel decomposition proved quite similar to that of the four-channel decomposition. This similarity appears in the case of decomposition of the present set of test sequences. In Figure 6.7a, the chirp and the harmonic become indistinguishable at

approximately sample number 108. This represents a slight improvement over the three-subchannel decomposition. In the case of Figure 6.7a, again using (6.28), the frequency resolution appears to be approximately $0.140 \cdot f_s$. This represents a subtle improvement over the performance of the three-channel decomposition. Nevertheless, in this region of the frequency spectrum, the spectrogram continues to provide performance which is superior by a significant margin.

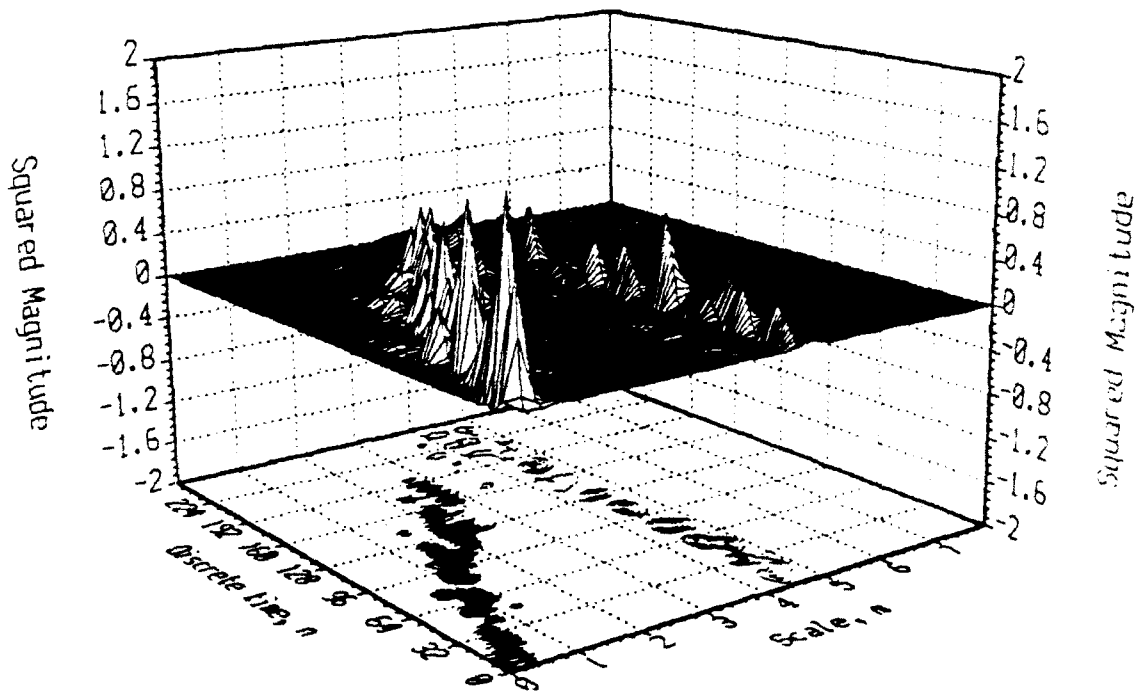


Figure 6.7b--Two-channel, four-subchannel multiresolution decomposition of second 256-point test sequence constructed from steady-state harmonic component and quadratic chirp. Primary channel filters were based on Daubechies' orthonormal wavelet and scaling function on $[0, 13]$. Subchannel decomposition was performed with pseudo-QMF filter designed in Chapter V.

Finally, the performance decomposition of the second test sequence is plotted in Figure 6.7b. The chirp and the harmonic converge at approximately the same location. This result is also consistent the observations of Section IV.E. When decomposing transient test signals, it

was observed that increasing from three to four subchannels does not dramatically improve resolution of scale at large scales. The primary from the increase is realized in the smaller scale--or higher frequency--regions.

VII. CONCLUSION

A. SUMMARY OF RESULTS

When compared with conventional periodogram techniques, the multiresolution techniques considered provided mixed results. In resolving signals at the extreme low end of the frequency spectrum below the Nyquist frequency, the multiresolution structures achieved their best results. In higher frequency regions, the multiresolution proved to be on par with or inferior to the periodogram. Overall, wavelet-like methods should be optimum for proportional bandwidth processes. The test signals employed performed marginally at demonstrating this strength in the upper regions of the frequency spectrum.

With respect to other performance measures, the multiresolution techniques achieved, even when expanding fully by channel, decomposition of the test sequences with fewer calculations than the periodogram decomposition. In fairness to the latter method, the implementation demonstrated did not reflect any attempts to optimize the technique for the applications shown. However, in determining the number of calculations, the computational burden necessary to convert the resulting complex decomposition into a real representation was not considered either.

The most interesting results were perhaps obtained from generation of the receiver operating characteristics. In the relatively high (-3 dB) signal-noise ratio demonstration the periodogram outperformed the multiresolution decomposition techniques by a small margin. However when the signal-noise ratio was decreased (-6 dB), the multiresolution decomposition achieved

superior results. Among the multiresolution structures, the results varied with the number of subchannels implemented and the region of the spectrum considered.

Finally, in examining the application of multiresolution decomposition to dynamic signals, the results were entirely dependent on the region of the frequency spectrum in which the process being detected occurred. In the higher regions of the spectrum, the ability of the multiresolution techniques to resolve proximate narrowband components was poor at best. In the lower end of the spectrum, however, good results were achieved.

B. RECOMMENDATIONS FOR FURTHER STUDY

The most obvious direction in which to continue the study of multiresolution decomposition techniques is to improve the quality of the filter banks used for subchannel decomposition. In the structures implemented, decomposition into more than two subchannels was accomplished with pseudo-QMF banks. As indicated, methods for the design of perfect reconstruction filter banks of an arbitrary number of channels exist. The question arises as to whether results might not improve through the use of perfect reconstruction filter banks for decomposition into subchannels.

Further study directed toward the determination of the optimum decomposition structure may also be warranted. In section 6.C, within the context of generation of comparing receiver operator characteristics for different structures, it was suggested that structures involving the decomposition of detail sequences into multiple subchannels may result in excessive resolution at low frequencies. As an alternative to decomposing the detail sequence into subchannels at each stage, limiting the performance of subchannel decomposition to the first two to three stages

may improve results. Alternatively, varying at each stage the number of subchannels into which the detail sequence is decomposed may also provide an option. For instance, a possible scheme would involve decomposition of the first stage detail sequence into three subchannels, the second stage detail sequence into two subchannels and performing no subchannel decomposition for the detail sequence at all subsequent stages.

Additionally, the performance of multiresolution techniques for detecting dynamic signals in the presence of noise was not addressed. The periodogram decompositions of the quadratically chirped signals produced, through a spreading over multiple spectral bins, a significant reduction in the level of signal indication for the dynamic signal component. The steady-state harmonic component of the test sequence remained confined to one or two spectral bins while the dynamic component appeared spread over 12-16 spectral bins. Consequently, the signal levels of equal-power dynamic and steady-state components of the signal varied by several decibels. This did not occur in the case of the multiresolution decomposition. Since, for the multiresolution decomposition the dynamic signal and the steady-state components remained equally well localized, the peaks of the dynamic signal component maintained the same approximate height as the steady-state component. It stands to reason, therefore, that the multiresolution detector may be less susceptible to noise when applied to the problem of a dynamic signal.

Finally, further work is merited in the determination of the optimum manner in which to present multiresolution decompositions. For, a given signal, the essential information provided by multiresolution techniques is contained in a non-uniform lattice of nodes representing signal components spread, in varying degrees, over time. The method demonstrated in the present

work was to decompose the channel into channels and subchannels and then re-expand each channel individually in such a manner that the sum of the contents of each channel provides the reconstructed signal. This process of presentation introduces a significant computational burden. As was indicated in the section 6.B, the number of multiplications necessary to re-expand the signal always exceeded the number of computations for the actual decomposition by a significant margin. Brooks [33], on the other had presented only the coefficients of expansion in a surface plot with varying numbers of zeros inserted between nodes of information at different scales. This approach resulted in plots such as were presented in the present study for the à trous algorithm. Not only does this approach provide plots from which information is relatively difficult to extract, but as addressed in chapter 4, the issue of delays which are disparate among channels arises. Further consideration regarding the best manner in which to present the results of multiresolution decomposition is, therefore, merited.

APPENDIX A DETAILS OF DEVELOPMENT OF MALLAT'S ALGORITHM

In chapter 4, it was demonstrated that, since the scaling function vector $\phi_{m-1, n}$ lies within the span of the set of scaling function vectors, $\{\phi_{m, n}\}_{n \in \mathbb{Z}}$, any vector $\phi_{m-1, n}$ can be represented as a Fourier series expansion in $\phi_{m, n}$:

$$\phi_{m+1, n}(t) = \sum_k \left(\phi_{m+1, n}, \phi_{m, k} \right) \phi_{m, k}(t). \quad (\text{A.1})$$

Now the series coefficient, the inner product term contained in the summation (A.1), equals, by definition

$$\left(\phi_{m+1, n}, \phi_{m, k} \right) = \int \phi_{m+1, n}(t) \cdot \phi_{m, k}(t) dt. \quad (\text{A.2})$$

Substituting (4.14) into the right-hand side of (A.2) produces

$$\begin{aligned} \int \phi_{m+1, n}(t) \cdot \phi_{m, k}(t) dt &= 2^{-(m+1)/2} 2^{-m/2} \int \phi(2^{-(m+1)} \cdot t - n) \cdot \phi(2^{-m} \cdot t - k) dt \\ &= \frac{1}{\sqrt{2}} 2^{-m} \int \phi(2^{-(m+1)} \cdot t - n) \cdot \phi(2^{-m} \cdot t - k) dt \\ &= \frac{1}{\sqrt{2}} 2^{-m} \int \phi\left(\frac{2^{-m}t - 2n}{2}\right) \cdot \phi(2^{-m} \cdot t - k) dt \end{aligned} \quad (\text{A.3})$$

Now, (A.1) will become much simpler if the series coefficients can be expressed independent of the scale index m . Application of the change of variable of integration $u = 2^{-m} \cdot t - 2 \cdot n$ to the final line of (A.3) produces this result:

$$\begin{aligned} \int \phi_{m+1, n}(t) \cdot \phi_{m, k}(t) dt &= \frac{1}{\sqrt{2}} 2^{-m} \int \phi\left(\frac{2^{-m}t - 2n}{2}\right) \cdot \phi(2^{-m} \cdot t - k) dt \\ &= \frac{1}{\sqrt{2}} \int \phi\left(\frac{u}{2}\right) \cdot \phi\left((u + 2 \cdot n) - k\right) du \\ &= \frac{1}{\sqrt{2}} \int \phi\left(\frac{u}{2}\right) \cdot \phi\left(u - (k - 2 \cdot n)\right) du \end{aligned} \quad (\text{A.4})$$

Since, therefore, by (4.14), $\phi_{m,n}(t) \triangleq 2^{-m/2} \cdot \phi(2^{-m} \cdot t - n)$, (A.4) becomes

$$\begin{aligned} \frac{1}{\sqrt{2}} \int \phi\left(\frac{u}{2}\right) \cdot \phi(u - (k - 2 \cdot n)) \, du &= \frac{1}{\sqrt{2}} \int \phi_{1,0}(u) \cdot \phi_{0,k-2n}(u) \, du \\ &= \frac{1}{\sqrt{2}} \left(\phi_{1,0}, \phi_{0,k-2n} \right) \end{aligned} \quad (\text{A.5})$$

Consequently, (4.19) is proved. From (A.5) and (4.19), (4.20) follows:

$$\phi_{m+1,n}(t) = \frac{1}{\sqrt{2}} \sum_k \left(\phi_{1,0}, \phi_{0,k-2n} \right) \phi_{m,k}(t).$$

Developing (4.23) from (4.20) involves, first, substitution of the definition (4.14):

$$2^{-(m+1)/2} \phi(2^{-(m+1)} \cdot t - n) = 2^{-m/2} \frac{1}{\sqrt{2}} \sum_k \left(\phi_{1,0}, \phi_{0,k-2n} \right) \phi(2^{-m} \cdot t - k). \quad (\text{A.6})$$

Now, contained on each side of (A.6) are factors of 2^{-m} and $2^{-1/2}$. Cancellation of those common factors produces

$$\phi(2^{-(m+1)} \cdot t - n) = \sum_k \left(\phi_{1,0}, \phi_{0,k-2n} \right) \phi(2^{-m} \cdot t - k). \quad (\text{A.7})$$

Next, again introducing the change of variables $u = 2^{-m} \cdot t - 2 \cdot n$ results in

$$\phi\left(\frac{u}{2}\right) = \sum_k \left(\phi_{1,0}, \phi_{0,k-2n} \right) \phi(u - (k - 2 \cdot n)). \quad (\text{A.8})$$

Finally, translation of the index of summation $k = k' - 2 \cdot n$ in (A.8) yields

$$\phi\left(\frac{u}{2}\right) = \sum_k \left(\phi_{1,0}, \phi_{0,k} \right) \phi(u - k). \quad (\text{A.9})$$

To generate the FIR filter defined in (4.23), it must first be specified that the scaling functions ϕ are compactly supported. Then, integrating both sides of (A.9) over their domains results in

$$\int \phi\left(\frac{u}{2}\right) \, du = \sum_k \left(\phi_{1,0}, \phi_{0,k} \right) \int \phi(u - k) \, du. \quad (\text{A.10})$$

Application of the changes in variables of integration $v = u - 2$ and $w = u - k$ to (A.10) produces

$$2 \cdot \int \phi(v) dv = \sum_k \left(\phi_{1,0}, \phi_{0,k} \right) \int \phi(w) dw \quad (\text{A.11})$$

If the common factors of $\int \phi(v) dv$ are removed from each side of (A.11), the result becomes

$$2 = \sum_k \left(\phi_{1,0}, \phi_{0,k} \right). \quad (\text{A.12})$$

If $h(k) \triangleq \frac{1}{2} \left(\phi_{1,0}, \phi_{0,k} \right)$, then

$$\sum_k h(k) = 1.$$

APPENDIX B MATLAB SOURCE CODE

The source *Matlab* code for primary algorithms employed during this study are provided in this appendix.

A. LAPLACIAN PYRAMID

```
%
% This MATLAB function performs FULL-CHANNEL DECOMPOSITION
% OF A SEQUENCE IN ACCORDANCE WITH THE LAPLACIAN PYRAMID.
% The Laplacian Pyramid algorithm is described in Michael
% Unser, "An improved least squares Laplacian pyramid ... ",
% Signal Processing 27 (1992) 187-203.
%
% The function syntax is:
%       P=lappmd(s, N)
% where: "s"   is a vector containing the sequence
%           to be decomposed.
%       "N"   is an integer indicating the number
%           of levels of decomposition to be
%           performed.
%       "P"   is an array whose rows contain the
%           sequence component corresponding
%           to that channel.
% The array "P" is computed such that summing along each
% column produces the reconstructed sequence.
%
function P=lappmd(s, N)
%
% The decomposition kernel is defined as "w."
%
w=[1/4-.2 1/4 .4 1/4 1/4-.2];
%
% The input sequence "s" is reshaped as a row vector.
%
s=reshape(s,1,length(s));
%
% The content of "s" is assigned to vector "pk1." The array
% "D" is initialized as a zero vector.
%
pk1=s;
%
% Decomposition of the sequence is performed.
```

```

%
for k=1:N
%
%   "pk" is reinitialized for next iteration.
%
pk=pk1;
%   The sequence is reduced using user-defined function REDUCE.
%
pk1=reduce(pk,w);
%
%   "pk1" is symmetrically windowed to one-half the length of "pk."
%
pk1=pk1(2:length(pk1)-1);
%
%   The sequence "pk1" is expanded and the result assigned to "dk."
%
dk=expand(pk1,2*w);
%
%   "dk" is symmetrically windowed to the length of "pk."
%
dk=dk(3:length(dk)-2);
%
%   The sequence "dk" is assigned to the kth row of array "D." The
%   length of "dk" is stored in the kth element of "L."
%
L(k)=min(length(dk),length(pk));
D(k,1:L(k))=pk(1:L(k))-dk(1:L(k));
%
end
%
%   The final approximation is assigned to the "k+1'th" row
%   of "D."
%
L(length(L)+1)=length(pk1);
D(length(L),1:L(length(L)))=pk1;
%
%   The full-channel expansion is calculated from the
%   rows of array "D" and the results assigned to the rows
%   of "P." The first row of "P" is equal to the first row
%   of "D."
%
P(1,:)=D(1,:);
%
for k=2:N+1

```

```

%
% The detail from channel "k" is assigned to vector "dk."
%
% dk=D(k,1:L(k));
%
% The channel content is expanded.
%
% for j=2:k
%     dk=expand(dk,2*w);
%     dk=dk(3:length(dk)-2);
% end
%
% The expanded channel content is assigned to row "k" of
% array "P."
%
% P(k,1:length(dk))=dk;
%
end

```

A TROUS ALGORITHM

```

%
% This MATLAB function calculates an approximation of the
% DISCRETE WAVELET TRANSFORM of a function
% using SHENSA'S ATROUS ALGORITHM discribed in "The
% Discrete Wavelet Transform: Wedding the A Troues and
% Mallat Algorithms," IEEE Transactions on Signal
% Processing, Vol. 40, No. 10, Oct. 1992.
%
% The function syntax is:
% W=shendwt(s, M, P_i, P_f)
% where: "s" represents a vector of data to be transformed
% "M" is an integer indicating the number of "voices"
% tu be used to cover the frequency spectrum
% "W" is an array containing the coefficients of
% the magnitude-squared wavelet transform
% of "s."
% "P_i" represents the first wavelet transform scale
% to be calculated
% "P_f" represents the final wavelet transform scale
% The transform is calculated using a madulated Gaussian
% window as an analyzing wavelet. If multiple voices are
% specified, the projection of "s" on each voice will be
% represented separately. The Lagrange, a trous interpolation

```

```

% filter used is obtained from convolving a four-point
% Daubechies scaling filter with itself.
function W=shendwt(s, M, P_i, P_f)
%
% First, the argument vector "s" is conditioned. If "s" is
% defined as a column vector, it is converted to a row vector.
% Secondly, "s" is zeropadded to the next integer power of "2."
%
[rows,cols]=size(s);
%
if cols == 1
    s=s.';
end
clear rows;clear cols;
%
s=zeropad(s,1,2^ceil(log(length(s))/log(2)));
%
% Default values are imposed for starting and ending scales if
% none are specified.
%
if exist('P_i') == 0
    P_i=1;
end
if exist('P_f') == 0
    P_f=floor(log(length(s))/log(2));
end
%
% If the number of voices is not specified, a default value of
% M=2 is imposed.
%
if exist('M') == 0
    M=2;
end
%
% Next the analyzing wavelet must be calculated. The starting
% point of this process is to specify the Gaussian window rolloff
% factor "beta" in accordance with the specified number of
% voices. (Shensa (6.31)). If M=1, the value of "beta" is defined
% as "pi/(4*sqrt(2))."
%
if M == 1
%
    beta=pi/(4*sqrt(2));
%

```

```

else
%
    beta=1/(2*M);
%
end
%
% The location of the center frequency "nu" is assigned in accordance
% with Shensa (6.27).
%
nu=pi-sqrt(2)*beta;
%
% The voice scaling factor "a" is calculated using Shensa (6.32).
%
a=2^(1/M);
%
% The region of support for the analyzing wavelet filter "g" is
% approximated as the region for which the Gaussian window
% is greater than 10^-3. Consequently, the filter impulse
% response domain is [-a^(M-1)*sqrt(14)/beta, a^(M-1)*sqrt(14)/beta].
% The length of "g" is represented by an odd integer.
%
n=-ceil(a^(M-1)*sqrt(14)/beta):ceil(a^(M-1)*sqrt(14)/beta);
%
% The analyzing wavelet is calculated for each voice in accordance
% with Shensa (6.32). It is then normalized such that its peak
% passband frequency response is unity.
%
for k=1:M
%
    g(k,:)=exp(j*nu*(n/(a^(k-1))))*exp(-(beta^2*(n/a^(k-1)).^2)/2);
%
end
clear n;
%
% A variable "G" indicating the half-length of filter "g" is
% defined.
%
G=ceil(length(g)/2);
%
% Next, the Lagrange interpolation filter is calculated. The filter
% is obtained from "auto-convolution" of a Daubechie four-point
% DWT filter.
%
f=[1+sqrt(3) 3+sqrt(3) 3-sqrt(3) 1-sqrt(3)]/(4*sqrt(2));

```

```

%
f=conv(f,flipr(f));
f=f/sqrt(2);
%
%   A variable "F" indicating the half-length of "f" is defined.
%
F=ceil(length(f)/2);
%
%   The recursion is next executed according to Shensa (2.12a & b).
%   The sequence is filtered and decimated the first "P_i" times.
%
for k=1:P_i-1
%
    s=conv(s,f);
%
    s=s(F:2:length(s)-F);
%
end
%
%   The output matrix "W" is initialized as a zero vector of
%   dimensions identical to those of "s."
%
W=zeros(s);
%
for k=P_i:P_f
%
%   The data vector "s" is first filtered with each voice of "g."
%   The squared magnitude of the result is assigned to the appropriate
%   column of "W."
%
    for n=(k-P_i)*M+1:(k-P_i+1)*M
%
%   The row of "W" to be evaluated is initialized as zero.
%
        W(n,:)=zeros(W(1,:));
%
%   The squared magnitude of the filter output is calculated
%   and assigned to "Wk."
%
        Wk=sqrt(abs(conv(s,g(n-(k-P_i)*M,:))).^2);
%
%   The elements of "Wk" are assigned to the corresponding
%   columns of the row of "W" being calculated.
%

```

```

W(n,2^(k-P_i):2^(k-P_i):length(W))=Wk(G:length(Wk)-G+1);
%
end
%
%
% "s" is filtered with the lagrange interpolation filter and then
% decimated.
%
s=conv(s,f);
%
s=s(F:2:length(s)-F);
%
end

```

C. MULTIREOLUTION DECOMPOSITIONS FROM CASCADES OF FILTER BANKS

```

%
%
% This MATLAB function performs WAVELET-LIKE DECOMPOSITION
% of a sequence using CASCADES OF QMF-TYPE FILTER BANKS
% and then performs FULL EXPANSION BY CHANNEL
% for each channel of decomposition. At each stage, the
% sequence is decomposed into an approximation channel and
% one or more detail channels. The detail channels can then
% be further decomposed into subchannels.
% The function syntax is:
%     D=wavebank(s,h,N,g)
% where: "s" is a vector representing the sequence to
%        be decomposed
%        "h" is an array whose rows contain the filter
%        coefficients for the primary analysis filter
%        bank in order of increasing center frequency.
%        "N" is an integer indicating the number of stages
%        of decomposition to perform.
%        "g" is an array whose rows contain the filter
%        coefficients for the analysis filter for the
%        subchannel decomposition in order of
%        increasing center frequency. (OPTIONAL)
% If "g" is not specified, the function, by default, does not
% decompose the detail channel into subchannels.
%

```

```

function D=wavebank(s,h,N,g)
%
%   The dimensions of "h" and "g" (if defined) are stored in
%   variables Rc, Cc, Rs, Cs, indicating the array dimensions for
%   channel and subchannel decompositions, respectively. The number
%   of rows will be used as the decimation and expansion factors.
%   Then, the analysis filter banks are defined and stored in
%   "f" for the primary channels and "i" for the subchannels.
%   Because of the effects of decimation, the synthesis filters
%   must be scaled by a the decimation factor.
%
[Rc,Cc]=size(h);
f=Rc*fliplr(h);
Lc=length(h)-1;
%
Ls=0;
Rs=1;
if exist('g') == 1
%
    [Rs, Cs]=size(g);
    i=Rs*fliplr(g);
    Ls=length(g)-1;
%
end %if
%
%   The sequence "s" is reshaped as a row vector.
%
s=reshape(s,1,length(s));
%
%   The sequence is decomposed. At each stage, the
%   approximation of "s" is stored in a vector "sk."
%   The next stage of decomposition is stored in "sk1."
%
sk1(Rc,:)=s;
%
for k=0:N-1
%
%   Sequence vector s is reinitialized for next iteration.
%
    sk=sk1;
%
%   The sequence "s" is decomposed into primary channels by
%   the function REDUCE and the result is assigned to "sk1."
%

```

```

for p=1:Rc
%
    dp=reduce(sk(Rc,:),h(Rc-p+1,:),Rc);
    skl(p,1:length(dp))=dp;
%
end %p
%
% "skl" is truncated to its proper post-"REDUCE" length.
%
    skl=skl(:,1:length(dp));
%
% If "g" is defined, the sequence "dkl" is reduced into Rc
% subchannels. The lengths of the subchannel sequences for
% each channel are stored in a vector "L."
%
    for p=1:Rc-1
        if exist('g') == 1
%
            for q=1:Rs
%
                dq=reduce(skl(p,:),g(Rs-q+1,:),Rs);
                L(k+1)=length(dq);
                D((Rc-1)*Rs*k+Rs*(p-1)+q,1:L(k+1))=dq;
%
            end %q
%
        else
%
            L(k+1)=length(dp);
            D((Rc-1)*k+p,1:L(k+1))=skl(p,:);
%
        end %if
    end %p
%
end %k
%
keyboard
%
% The sequence is reconstructed using full expansion by channel.
%
for k=1:N
%
% If "g" is defined, the detail "d" for each subchannel is
% extracted from the corresponding row of "D."

```

```

%
if exist('g') == 1
%
    for p=1:Rc-1
        for q=1:Rs
%
            d=D(Rs*(Rc-1)*(k-1)+Rs*(p-1)+q,1:L(k));
%
            % The detail is expanded with the corresponding subchannel
            % synthesis filter.
%
            d=expand(d,i(Rs-q+1,:),Rs);
%
            % The subchannel component is expanded with the primary detail
            % channel synthesis filter "f(@,:)" and then by the approximation
            % channel synthesis filter "f(1,:)" the number of times
            % appropriate for the number of stages of decomposition performed.
%
            d=expand(d,f(Rc+1-p,:),Rc);
%
            for m=1:k-1
%
                d=expand(d,f(1,:),Rc);
%
            end %m
%
            % The total delay resulting from transmission through
            % the system is calculated and assigned to "delay." It
            % is then removed and the expanded sequence "d" is
            % reintroduced to the corresponding row of array "D."
%
            delay=sum((Rc).^[0:k-1])*Lc+Rc^k*Ls;
            d=d(delay+1:delay+length(s));
            M(k)=length(d);
            D(Rs*(Rc-1)*(k-1)+Rs*(p-1)+q,1:M(k))=d;
%
        end %q
    end %p
%
    % If "g" is not defined, the subchannel reconstruction steps
    % are bypassed. Reconstruction of the primary detail channel
    % is performed.
%
else

```

```

%
    for p=1:Rc-1
        d=D((Rc-1)*(k-1)+p,1:L(k));
    %
    % The detail sequence is expanded by the primary detail channel
    % synthesis filter "f(Rc+1-p,:)" and then by the approximation
    % channel synthesis filter "f(1,:)" as many times as
    % appropriate for the number of stages of decomposition performed.
    %
        d=expand(d,f(Rc+1-p,:),Rc);
    %
        for m=1:k-1
            %
                d=expand(d,f(1,:),Rc);
            %
        end %m
    %
    % The total delay resulting from transmission through
    % the system is calculated and assigned to "delay." It
    % is then removed and the expanded sequence "d" is
    % reintroduced to the corresponding row of array "D."
    %
        delay=sum((Rc).^[0:k-1])*Lc;
        d=d(delay+1:delay+length(s));
        M(k)=length(d);
        D((Rc-1)*(k-1)+p,1:M(k))=d;
    %
        end %p
    %
end %if
%
end %k
%
% The final approximation sequence is selected as the final
% row of "sk1."
%
sk1=sk1(Rc,:);
%
% The final approximation signal is expanded with primary
% approximation channel synthesis filter according to the
% number of decomposition stages.
%
for m=1:N
    %

```

```

    skl=expand(skl,f(1,:),Rc);
%
end %m
%
%   The expanded approximation sequence is added as the final row
%   of array "D."
%
%   The total delay resulting from transmission through
%   the system is calculated and assigned to "delay." It
%   is then compensated and the expanded sequence "skl" is
%   reintroduced to the final row of array "D."
%
delay=sum((Rc).^[0:N-1])*Lc;
skl=skl(delay+1:delay+length(s));
M(length(M)+1)=length(skl);
D(Rs*(Rc-1)*N+1,1:M(length(M)))=skl;

```

D. PERIODOGRAM DECOMPOSITION

```

%
%   This MATLAB function calculates the PERIODOGRAM SPECTRAL ESTIMATE
%   for a specified input data vector. The function syntax is
%
%       S=pgram(s,w, N);
%
%   where: "s" is the data vector to be analyzed.
%           "w" represents a window with which data will be windowed
%           "N" is an integer indicating the number of steps to
%               shift the window for each step
%               (default = length(w)/2)
%           "S" is a periodogram-type output matrix.
%
%   The argument data vector is subdivided with 50% overlap. Each
%   row of the output array represents the transform of a subdivision
%   of the original data vector.
%
function S=pgram(s,w,N);
%
%   Check to see if "w" is defined. If "w" is not defined,
%   a rectangular window of length "length(s)" is imposed as
%   a default.
%
if exist('w') == 0

```

```

%
    w=ones(s);
%
end
%
%   A default vale is imposed for "N"
%
if exist('N') == 0
%
    N=length(w)/2;
%
end
%
%   Convert column vector data vector arguments to row vector
%   format.
%
s=reshape(s,length(s),1);
w=reshape(w,length(w),1);
%
%   "s" is zeropadded to an integer number of window lengths.
%
for k=1:(length(s)-length(w))/N+1
%
    r=fft(w.*s((k-1)*N+1:(k-1)*N+length(w)));
%
    S(:,k)=r(1:length(w)/2);
%
end
%
%   In accordance with the definition of the periodogram, the
%   periodogram magnitude is divided by the window length.
%
S=S./length(w);

```

E. DYADIC EXPANSION OF TWO-SCALE DIFFERENCE EQUATIONS

```

%
%   This function expands a two-scale, difference equation of
%   the form
%       phi(x)=sum(c_k*phi(2*x-k)).
%   The function syntax is
%       [phi, psi]=twoscale(c,P,eigtol)
%   where the function arguements are:
%       "c" is a coefficient vector [c_0 c_1 ... c_{N-1}]
%       "P" is the number of dyadic points evaluated between

```

```

%           each integer in the domain.
%           "eigtol" is indicates the maximum deviation from unity
%           which will be tolerated in calculating the eigenvalue
%           corresponding to the eigenvector containing the
%           values of "phi" for integer arguments.
%           (DEFAULT = 1E-3)
%           The output variables are
%           "phi" represents the scaling function satisfying the
%           difference equation
%           "psi" is the corresponding wavelet.
%
function [phi,psi]=twoscale(c,P, eigtol)
%
%           If "eigtol" is not defined, a default vale is imposed.
%
if exist('eigtol') ~= 1
    eigtol=1e-3;
end
%           The argument vector "c" is reshaped as a column vector.
%
c=reshape(c,length(c),1);
%           The condition that the sum of the elements of "c" equals "2"
%           is imposed.
%
c=2*c/sum(c);
%           First the scale function is evaluated for integer points
%           on its domain. A zero-padded version "c_n" of the coefficient
%           vector "c" is created.
%
c_n=[zeros(1:length(c)-1)'; c; zeros(1:length(c)-1)'];
%           A matrix "C" containing values of the coefficient vector
%           "c" is generated.
%
for k=1:length(c)
%           C(k,:)=flipud(c_n(2*k-1:2*(k-1)+length(c)));
%
end
%
%           The matrix "C" is truncated to eliminate rows corresponding
%           to the trivial solutions corresponding to non-unity

```

```

%      "c_0" and "c_N-1".
%
if c(1) ~= 1
%
%      C=C(2:length(C),2:length(C));
%
end
%
if c(length(c)) ~= 1
%
%      C=C(1:length(C)-1,1:length(C)-1);
%
end
%
%      The resulting matrix is checked to ensure that it contains
%      at least one eigenvalue of unity. If one unity eigenvalue
%      is present, the function continues. Otherwise, it terminates
%      in an error message.
%
%      The eigenvectors and eigenvalues of "C" are calculated.
%      The diagonal matrix containing the eigenvalues is converted to
%      a column vector of eigenvalues.
%
[E,D]=eig(C);
D=diag(D);
%
if min(abs(D-ones(D))) <= eigtol
%
%      The address of the unit eigenvalue is determine. The
%      eigenector corresponding to that address is defined as "phi."
%      Values of "zero" are imposed on the endpoints for non-unity
%      "c_0" or "c_N-1".
%
K=find(abs(D-ones(D)) == min(abs(D-ones(D))));
K=K(1);
phi=E(:,K);
%
%      if c(1) ~= 1
%
%          phi=[0:phi];
%
%      end
%
%      if c(length(c)) ~= 1

```

```

%
    phi=[phi;0];
%
end
%
%
%
% The values of the scaling function are calculated recursively
% for dyadic values of "phi." The values of "phi" at half-integer
% domain points is merely the convolution of "phi" and "c."
%
N=length(c)-1;
for k=0:max(0,P-1)
%
% A circulant, convolution matrix "M" is created.
%
% The matrix "M" is cleared from memory for the next iteration.
%
    clear M
%
    for m=0:N
%
M(:,m+1)=[zeros(m*2^k,1);phi;zeros((N-m)*2^k,1)];
%
    end
%
%size(M)
% The convolution is evaluated.
%
    phi=M*c;
%
%
end
%
% The corresponding wavelet is calculated.
%
n=0:length(c)-1;
c=flipud(c).*((-1).^n);
psi=M*c;
%
% An error message is displayed in the event no
% eigenvalues of unity are present.
%
else

```

```

%
% 'Filter string produces no unity-value eigenvalues.'
%
end

```

H. GENERATION OF RECEIVER OPERATING CHARACTERISTICS

```

% This MATLAB script file generates receiver operating characteristics
% for various multiresolution decompositions, saves the results
% to files, and when complete, terminates MATLAB.
%
% Generate roc curve for two-channel, four-subchannel,
% SNR = - 3 dB, high-frequency transient
%
load slf
load pqmfb4
g4=h;
load wavebank
D=wbdec(s,h,8,g4);
K=find(D.^2 >= max(max(D.^2))/100);
rand('normal');
sig=sqrt(mean(s.^2));
%
'two-channel, four-subchannel'
for k=1:500
    n=4*sig*rand(s);
    D=wbdec(n,h,8,g4);
    H0(k)=sum(sum(D(K).^2));
    D=wbdec(n+s,h,8,g4);
    H1(k)=sum(sum(D(K).^2));
end
%
[PFA23lf,PD23lf]=roc(H0, H1, 50);
save roc23lf PFA23lf PD23lf
%
clear
%
clear
%
% Generate roc curve for two-channel, three-subchannel,
% SNR = - 3 dB, high-frequency transient
%

```

```

load slf
load wavebank
D=wbdec(s,h,8,g);
K=find(D.^2 >= max(max(D.^2))/100);
rand('normal');
sig=sqrt(mean(s.^2));
%
'two-channel, three-subchannel'
for k=1:500
    n=4*sig*rand(s);
    D=wbdec(n,h,8,g);
    H0(k)=sum(sum(D(K).^2));
    D=wbdec(n+s,h,8,g);
    H1(k)=sum(sum(D(K).^2));
end
%
[PFA23lf,PD23lf]=roc(H0, H1, 50);
save roc23lf PFA23lf PD23lf
%
clear
%
%   Generate roc curve for two-channel, two-subchannel,
%   SNR = - 3 dB, high-frequency transient
%
load slf
load wavebank
D=wbdec(s,h,8,h);
K=find(D.^2 >= max(max(D.^2))/100);
rand('normal');
sig=sqrt(mean(s.^2));
%
'two-channel, two-subchannel'
for k=1:500
    n=4*sig*rand(s);
    D=wbdec(n,h,8,h);
    H0(k)=sum(sum(D(K).^2));
    D=wbdec(n+s,h,8,h);
    H1(k)=sum(sum(D(K).^2));
end
%
[PFA22lf,PD22lf]=roc(H0, H1, 50);
save roc22lf PFA22lf PD22lf
%
```

```

clear
%
%
%   Generate roc curve for two-channel, zero-subchannel,
%   SNR = - 3 dB, high-frequency transient
%
load slf
load wavebank
D=wbdec(s,h,8);
K=find(D.^2 >= max(max(D.^2))/100);
rand('normal');
sig=sqrt(mean(s.^2));
%
'two-channel, zero-subchannel'
for k=1:500
    n=4*sig*rand(s);
    D=wbdec(n,h,8);
    H0(k)=sum(sum(D(K).^2));
    D=wbdec(n+s,h,8);
    H1(k)=sum(sum(D(K).^2));
end
%
[PFA20lf,PD20lf]=roc(H0, H1, 50);
save roc20lf PFA20lf PD20lf
%
clear
%
%
%   Generate roc curve for three-channel, zero-subchannel,
%   SNR = - 3 dB, high-frequency transient
%
load slf
load wavebank
D=wbdec(s,g,8);
K=find(D.^2 >= max(max(D.^2))/100);
rand('normal');
sig=sqrt(mean(s.^2));
%
'three-channel, zero-subchannel'
for k=1:500
    n=4*sig*rand(s);
    D=wbdec(n,g,8);
    H0(k)=sum(sum(D(K).^2));
    D=wbdec(n+s,g,8);

```

```

        H1(k)=sum(sum(D(K).^2));
    end
    %
    [PFA30lf,PD30lf]=roc(H0, H1,50);
    save roc30lf PFA30lf PD30lf
    %
    clear
    %
    clear
    %
    %
    %    Generate roc curve for two-channel, four-subchannel,
    %    SNR = - 3 dB, high-frequency transient
    %
    load shf
    load pqmfb4
    g4=h;
    load wavebank
    D=wbdec(s,h,8,g4);
    K=find(D.^2 >= max(max(D.^2))/100);
    rand('normal');
    sig=sqrt(mean(s.^2));
    %
    'two-channel, four-subchannel'
    for k=1:500
        n=4*sig*rand(s);
        D=wbdec(n,h,8,g4);
        H0(k)=sum(sum(D(K).^2));
        D=wbdec(n+s,h,8,g4);
        H1(k)=sum(sum(D(K).^2));
    end
    %
    [PFA23hf,PD23hf]=roc(H0, H1, 50);
    save roc23hf PFA23hf PD23hf
    %
    clear
    %    Generate roc curve for two-channel, two-subchannel,
    %    SNR = - 3 dB, high-frequency transient
    %
    load shf
    load wavebank
    D=wbdec(s,h,8,h);
    K=find(D.^2 >= max(max(D.^2))/100);
    rand('normal');

```

```

sig=sqrt(mean(s.^2));
%
'two-channel, two-subchannel'
for k=1:500
    n=4*sig*rand(s);
    D=wbdec(n,h,8,h);
    H0(k)=sum(sum(D(K).^2));
    D=wbdec(n+s,h,8,h);
    H1(k)=sum(sum(D(K).^2));
end
%
[PFA22hf,PD22hf]=roc(H0, H1, 50);
save roc22hf PFA22hf PD22hf
%
clear
%
%
%    Generate roc curve for two-channel, zero-subchannel,
%    SNR = - 3 dB, high-frequency transient
%
load shf
load wavebank
D=wbdec(s,h,8);
K=find(D.^2 >= max(max(D.^2))/100);
rand('normal');
sig=sqrt(mean(s.^2));
%
'two-channel, zero-subchannel'
for k=1:500
    n=4*sig*rand(s);
    D=wbdec(n,h,8);
    H0(k)=sum(sum(D(K).^2));
    D=wbdec(n+s,h,8);
    H1(k)=sum(sum(D(K).^2));
end
%
[PFA20hf,PD20hf]=roc(H0, H1, 50);
save roc20hf PFA20hf PD20hf
%
%
quit
%
```

G. GENERAL-PURPOSE ROUTINES CALLED BY OTHER ROUTINES

```
%  
% This function zero-pads an argument matrix forming  
% a new matrix of the specified size. The original matrix  
% will be in the upper left-hand corner the new matrix.  
%  
% The function syntax is:  
%  
%       X=zerospad(x,N1,N2)  
%  
% where:  
%       "x" is the initial argument matrix  
%       "N1" is the total number of rows for the new matrix  
%       "N2" is the total number of columns for the new matrix  
%  
function X=zerospad(x,N1,N2)  
%  
[M1,M2]=size(x);  
%  
X=[x zeros(M1,N2-M2)];  
%  
X=[X; zeros(N1-M1,N2)];  
  
%  
% This MATLAB function reduces A SEQUENCE IN THE SENSE OF  
% THE EXPAND OPERATION EMPLOYED IN LAPLACIAN PYRAMID  
% DECOMPOSITION. The operation entails FIR filtering  
% followed by decimation in time.  
%  
% The function syntax is  
%       fk1=reduce(fk, h, M)  
% where: fk   is a vector containing the sequence to be expanded  
%         h   is a vector containing the FIR filter coefficients  
%         M   is an integer indicating the decimation  
%           factor (default == 2)  
%  
% Regardless of the shape of the input vectors, output vectors  
% are returned as row vectors.  
%  
function fk1=reduce(fk, h, M);  
%  
% A default value of two is imposed on "M."  
%
```

```

if exist('M') ~= 1
    M=2;
end
%
%   The sequences "fk" and "h" are reshaped as row vectors.
%
fk=reshape(fk,1,length(fk));
h=reshape(h,1,length(h));
%
%   The sequence "fk" is filtered with "h" and the result is
%   assigned to "fk1."
%
fk1=conv(fk,h);
%
%   The sequence "fk1" is decimated by a factor of "M."
%
fk1=fk1(1:M:length(fk1));

%
%   This MATLAB function EXPANDS A SEQUENCE IN THE SENSE OF
%   THE EXPAND OPERATION EMPLOYED IN LAPLACIAN PYRAMID
%   DECOMPOSITION. The operation entails FIR filtering
%   followed by decimation in time.
%
%   The function syntax is
%       fk1=expand(fk, h, M)
%   where: fk   is a vector containing the sequence to be expanded
%           h   is a vector containing the FIR filter coefficients
%           M   is an integer indicating the decimation
%               factor (default == 2)
%
%   Regardless of the shape of the input vectors, output vectors
%   are returned as row vectors.
%
function fk1=expand(fk, h, M);
%
%   A default value of two is imposed on "M."
%
if exist('M') ~= 1
    M=2;
end
%
%   The sequences "fk" and "h" are reshaped as row vectors.
%

```

```

fk=reshape(fk,l,length(fk));
h=reshape(h,l,length(h));
%
%   Zero-insertion is performed on the input sequence "fk."
%   The result is assigned to "fk1."
%
fk1=zeros(1,M*length(fk)-1);
fk1(1:M:length(fk1))=fk;
%
%   The sequence "fk" is filtered with "h" and the result is
%   assigned to "fk1."
%
fk1=conv(fk1,h);
%

%   This function performs numerical integration of a
%   vector in accordance with Simpson's Rule. The function
%   arguments are:
%
%       "x"--the domain of the argument function
%       "y"--the range of the argument function.
%
%   The function's syntax is:
%
%       Y=simpson(x,y)
%
%   A regular partition is assumed.
%
function Y=simpson(x,y)
%
%   Vectors are checked for row- or column-vector format. Column
%   vectors are converted to row vectors.
%
dims=size(x);
N=max(dims);
if dims(1) == N,
    x=x';
    y=y';
end
%
%   The partition width is determined and the argument range vector
%   is multiplied by the partition width.
%
y=y*((max(x)-min(x))/max(size(x)));

```

```

%
%   The integral is evaluated.
%
Y(1)=y(1);
for k=2:N
    Y(k)=y(1:k)*ones(y(1:k)');
end
%

%
%   Given two, equal-length vectors, this MATLAB function
%   GENERATES HISTOGRAMS AND CONVERTS THEM TO RECEIVER
%   OPERATING CHARACTERISTICS.
%
%   The function syntax is:
%       [PFA, PD]=roc(H0, H1)
%   where: "H0" is a vector containing "hypothesis false"
%           realizations of a random process.
%           "H1" is a vector containing "hypothesis true"
%           realizations of a random process.
%           "PFA" is a vector representing the probability
%           of false alarm
%           "PD" is a vector representing the probability
%           of detection.
%
function [PFA, PD]=roc(H0, H1, Nobins)
%
%   The minimum and maximum bin locations are identified.
%
Bmin=min(min([H0;H1]));
Bmax=max(max([H0;H1]));
%
%   A vector is created representing the bin locations.
%
if exist('Nobins')== 0
%
    Nobins=length(H0)/25;
%
end
B=Bmin:(Bmax-Bmin)/Nobins:Bmax;
%
%   The MATLAB function "HIST" is invoked to produce histograms
%   of the realization vectors.

```

```

%
[pfa,X]=hist(H0,B);
[pd,X]=hist(H1,B);
%
%   The histograms are integrated using function "SIMPSON."
%
PFA=simpson(X,pfa);
PD=simpson(X,pd);
%
%   The integrals are normalized for maximum values of unity.
%
PFA=PFA/max(PFA);
PD=PD/max(PD);
%
%   The actual probability detect probability false-alarm
%   plots are the complements of the probability distribution
%   functions.
%
PFA=1-PFA;
PD=1-PD;

```

REFERENCES

- [1] *Webster's Unabridged Dictionary of the English Language*, Dilithium Press, Ltd. New York, 1989.
- [2] Reddy, J. N., *Applied Functional Analysis and Variational Methods in Engineering*, Krieger Publishing Co., Malabar, FL, 1991.
- [3] Riesz, Frigyes and Béla Sz.-Nagy, *Functional Analysis*, Dover Publications, Inc., New York, 1990.
- [4] Haaser, Norman B. and Joseph A. Sullivan, *Real Analysis*, Dover Publications, Inc., New York, 1991.
- [5] Taylor, Angus E. and David C. Lay, *Introduction to Functional Analysis*, Krieger Publishing Company, Malabar FL, 1980.
- [6] Daubechies, Ingrid, "The Wavelet Transform, Time-Frequency Localization and Signal Analysis," *IEEE Transactions on Information Theory*, Vol. 36, No. 5, September 1990.
- [7] Ahmed, Nasir, Heinz H. Schreiber and Philip V. Lopretsi, "On Notation and Definition of Terms Related to a Class of Complete Orthogonal Functions," *IEEE Transactions on Electromagnetic Compatibility*, Vol. 15, 1973, pp. 75-80.
- [8] Duffin, R. J. and A. C. Schaeffer, "A Class of Nonharmonic Fourier Series," *Transactions of the American Mathematical Society*, Vol. 72, No. 2, March 1952.
- [9] Cohen, Albert, "Biorthogonal Wavelets," *Wavelets: A Tutorial in Theory and Applications*, Academic Press, San Diego, CA, 1992, pp. 123-152.
- [10] Vetterli, Martin, "A Theory of Multirate Filter Banks," *IEEE Transactions on Acoustics, Speech, and Signal Processing*, Vol. ASSP-35, No. 3, March 1987, pp. 356-372.
- [11] Vaidyanathan, P. P., "Theory and Design of M -Channel, Maximally Decimated, Quadrature Mirror Filters with Arbitrary M , Having the Perfect-Reconstruction Property," *IEEE Transactions on Acoustics, Speech and Signal Processing*, Vol. ASSP-35, No. 4, April 1987.
- [12] Vaidyanathan, P. P., *Multirate Systems and Filter Banks*. Prentice Hall, Englewood Cliffs, N. J., 1993.

- [13] Vaidyanathan, P. P., Troung Q. Nguyen, Zinnur Doganata, and Tapio Saramäki, "Improved Technique for Design of Perfect Reconstruction FIR QMF Banks with Lossless Polyphase Matrices," *IEEE Transactions on Acoustics, Speech, and Signal Processing*, Vol. 37, No. 7, July 1989.
- [14] Gabor, D., "Theory of Communication," *Journal of the Institution of Electrical Engineers* (London), Vol. 193, Part III, No. 26, November 1946, pp. 429-457.
- [15] Heil, Christopher E., and David F. Walnut, "Continuous and Discrete Wavelet Transforms," *SIAM Review*, Vol. 31, No. 4, December 1989, pp. 628-666.
- [16] Beyer, William H., editor, *CRC Handbook of Mathematical Sciences*, sixth edition, CRC Press, Inc., Boca Raton, FL, 1987.
- [17] Chaiyasena, A. P. and L. H. Sibul, "Wavelet Transforms, Wideband Ambiguity Function and Group Theory," *Proceedings of the Twenty-Sixth Annual Asilomar Conference on Signals, Systems & Computers*, Pacific Grove, CA, 1992.
- [18] Daubechies, Ingrid, "Painless Nonorthogonal Expansions," *Journal of Mathematical Physics*, Vol. 27, No. 5, May 1986, pp. 1271-1283.
- [19] Rioul, Oliver and Martin Vetterli, "Wavelets and Signal Processing," *IEEE Signal Processing Magazine*, October 1991, pp. 14-38.
- [20] Kronland-Martinet, R., J. Morlet, and A. Grossman, "Analysis of Sound Patterns through Wavelet Transforms," *International Journal of Pattern Recognition and Artificial Intelligence*, Vol. 1, No. 2, 1987, pp. 273-302.
- [21] Daubechies, Ingrid, "Orthonormal Bases of Compactly Supported Wavelets," *Communications on Pure and Applied Mathematics*, Vol. XLI, 1988, pp. 909-996.
- [22] Mallat, Stephane G., "A Theory for Multiresolution Signal Decomposition: The Wavelet Representation," *IEEE Transactions on Pattern Analysis and Machine Intelligence*, Vol. 11, No. 7, July 1989, pp. 674-693.
- [23] Mallat, Stephan G., "Multiresolution Approximations and Wavelet Orthonormal Bases of $L^2(\mathbb{R})$," *Transactions of the American Mathematical Society*, Vol. 315, No. 1, September 1989, pp. 69-87.
- [24] Legaspi, Joseph E., *One- and Two-Dimensional Discrete Wavelet Transforms*, Masters Thesis, Naval Postgraduate School, Monterey, CA, September 1992.

- [25] Vetterli, Martin, "Wavelets and Filter Banks: Theory and Design," *IEEE Transactions on Signal Processing*, Vol. 40, No. 9, September 1992, pp. 2207-2232.
- [26] Daubechies, Ingrid and Jeffrey C. Lagarias, "Two-Scale Difference Equations: I. Existence and Global Regularity of Solutions," *SIAM Journal of Mathematical Analysis*, Vol. 22, No. 5, September 1991, pp. 1388-1410. "Two-Scale Difference Equations: II. Local Regularity, Infinite Products of Matrices and Fractals," *SIAM Journal of Mathematical Analysis*, Vol. 23, No. 4, July 1992, pp. 1031-1079
- [27] Strang, Gilbert, "Wavelets and Dilation Equations: A Brief Introduction," *SIAM Review*, Vol. 31, No. 4, pp. 614-627, December 1989
- [28] Shimbo, Osamu, *Transmission Analysis in Communication Systems*, Volume 1, Computer Science Press, Rockville, MD, 1988.
- [29] Unser, Michael, "An Improved Least Squares Laplacian Pyramid for Image Compression," *Signal Processing*, Vol. 27, 1992, pp. 187-203.
- [30] Burt, Peter J., and Edward H. Adelson, "The Laplacian Pyramid as a Compact Image Code," *IEEE Transactions on Communications*, Vol. COM-31, No. 4, April 1983, pp. 532-540.
- [31] Shensa, Mark J., "The Discrete Wavelet Transform: Wedding the À Trous and Mallat Algorithms," *IEEE Transactions on Signal Processing*, Vol. 40, No. 10, October 1992, pp. 2464-2482.
- [32] Mintzer, Fred, "On Half-Band, Third-Band and N^{th} -Band FIR Filters and Their Design," *IEEE Transactions on Acoustics, Speech and Signal Processing*, Vol. ASSP-30, No. 5, October 1982, pp. 734-738.
- [33] Brooks, William A., *Ultra-Wideband Radar Transient Signal Detection Using Time-Frequency and Wavelet Transforms*, Masters Thesis, Naval Postgraduate School, December 1992.
- [34] Koipillai, R. David and P. P. Vaidyanathan., "Cosine Modulated FIR Filter Banks Satisfying Perfect Reconstruction," *IEEE Transactions on Signal Processing*, Vol. 40, No. 4, April 1992.
- [35] Gopinath, R. A. and C. S. Burrus, "Wavelet Transforms and Filter Banks," *Wavelets: A Tutorial in Theory and Applications*, Academic Press, San Diego, CA, 1992, pp. 603-654.

- [36] Unser, Michael and Akram Aldroubi, "Polynomial Splines and Wavelets," *Wavelets: A Tutorial in Theory and Applications*, Academic Press, San Diego, CA, 1992, pp. 91-122.
- [37] Cohen, A., Ingrid Daubechies and J. C. Feauveau, "Biorthogonal Bases of Compactly Supported Wavelets," *Communications on Pure and Applied Mathematics*, Vol. XLV, 1992, pp. 485-560.
- [38] Tewfik, Ahmed H., Deepen Sinha and Paul Jorgensen, "On the Optimal Choice of a Wavelet for Signal Representation," *IEEE Transactions on Information Theory*, Vol. 38, No. 2, March 1992.
- [39] Pollen, David, "Daubechie's Scaling Function on $[0, 3]$," *Wavelets: A Tutorial in Theory and Applications*, Academic Press, San Diego, CA, 1992, pp. 3-13.
- [40] Tuma, Jan J., *Engineering Mathematics Handbook*, Third Edition, McGraw Hill, New York, NY, 1987.

INITIAL DISTRIBUTION LIST

	No. of Copies
1. Defense Technical Information Center Cameron Station Alexandria, VA 22304-6145	2
2. Library, Code 52 Naval Postgraduate School Monterey, CA 93943-5000	2
3. Chairman, Code EC Department of Electrical and Computer Engineering Naval Postgraduate School Monterey, CA 93943-5000	1
4. Professor Ralph Hippenstiel, Code EC/Hi Department of Electrical and Computer Engineering Naval Postgraduate School Monterey, CA 93943-5000	2
5. Professor Monique P. Fargues, Code EC/Fa Department of Electrical and Computer Engineering Naval Postgraduate School Monterey, CA 93943-5000	2
6. Professor Charles Therrien, Code EC/Ti Department of Electrical and Computer Engineering Naval Postgraduate School Monterey, CA 93943-5000	1
7. Professor Michael A. Morgan, Code EC/Mw Department of Electrical and Computer Engineering Naval Postgraduate School Monterey, CA 93943-5000	1
8. Dr. Charles Persons NCCOSC, RDT&E Division Code 732 San Diego, CA 92152-5000	1

- 9. Dr. Marc J. Shensa 1
NCCOSC, RDT&E Division
Code 782
San Diego, CA 92152-5000

- 10. Commander, Space and Naval Warfare Systems Command 1
SPAWAR 44
Attn: LT Neil A. Hamlett
Washington, DC 20363-5100